Evaluation of the Potential of ALOS PALSAR L-band Quadpol Radar Data for the Retrieval of Growing Stock Volume in Siberia

Dissertation

Zur Erlangung des akamedischen Grades doctor rerum naturalium
(Dr. rer. nat.)

vorgelegt dem Rat der Chemisch-Geowissenschaftlichen Fakultät der
Friedrich-Schiller-Universität Jena

von M.Sc.- Ing. Tanvir Ahmed Chowdhury
geboren am 01. Juli. 1980 in Chittagong, Bangladesch

Gutachter:

1. Prof. Dr. Christiane Schmullius, Friedrich-Schiller-Universität Jena

2. Dr. Christian Thiel, Friedrich-Schiller-Universität Jena

Tag der öffentlichen Verteidung: 04.09.2013

Abstract

Because of the massive wood trade, illegal logging and severe damages due to fires, insects and pollution, it is necessary to monitor Siberian forests on a large-scale, frequently and accurately. One possible solution is to use synthetic aperture radar (SAR) remote sensing technique, in particular by combining polarimetric technique. In order to evaluate the potentiality of ALOS PALSAR L-band full polarimetric radar for estimation of GSV, a number of polarimetric parameters are investigated to characterise the polarisation response of forest cover.

Regardless of the weather conditions, a high correlation (R=-0.87) is achieved between polarimetric coherence and GSV. The coherence in sparse forest is always higher than in dense forest. The coherence level and the dynamic range strongly depends on the weather conditions.

The four-component polarimetric decomposition method has been applied to the ALOS PALSAR L-band data to compare the decomposition powers with forest growing stock volume (GSV). Double-bounce and volume scattering powers show significant correlation with GSV. The correlation between polarimetric decomposition parameters and GSV is enhanced if the ratio of ground-to-volume scattering is used instead of considering polarimetric decomposition powers separately.

Two empirical models have been developed that describe the ALOS PALSAR L-band polarimetric coherence and ground-to-volume scattering ratio as a function of GSV. The models are inverted to retrieve the GSV for Siberian forests. The best RMSE of 38 m^3/ha and R^2=0.73 is obtained based on polarimetric coherence. On the other hand, using the ratio of ground-to-volume scattering the best retrieval accuracy of 44 m^3/ha and R^2=0.62 is achieved. The best retrieval results for both cases are observed under unfrozen condition. Saturation effects for estimated GSV versus ground-truth GSV are not observed up to 250 m^3/ha.

Zusammenfassung

Die Wälder Sibiriens stellen eine ökonomisch und ökologisch enorm wichtige natürliche Ressource dar. Sowohl Russland als auch dem Rest der Welt dienen sie als eminente Holzquelle, sind gleichzeitig aber auch ein Symbol wilder, unberührter Natur und als Stabilisator des weltweiten Klimas unentbehrlich. Die sibirischen Waldgebiete umfassen nahezu die Hälfte der weltweiten Nadelholzreserven und sind somit eine wertvolle wirtschaftliche und ökologische Ressource. Mit einem Anteil von 43 % bzw. 42 % am weltweiten Export von Nadel- bzw. Laubhölzern ist Russland der größte Exporteur von Rundhölzern. Außerdem kommt den ausgedehnten Waldflächen Sibiriens in ihrer Rolle als Kohlenstoffsenke eine immense Bedeutung zu.

Der massive industrielle Handel mit Holz, die illegale Abholzung sowie die umfangreichen Schäden durch Waldbrände, Insektenbefall und Luftverschmutzung erfordern eine großflächige, regelmäßige und genaue Kartierung der sibirischen Waldbestände. Traditionelle Waldinventuren sind eine sinnvolle Methode zur lokalen Untersuchung der Wälder, können aber aufgrund der räumlichen Ausdehnung und der Abgelegenheit der sibirischen Wälder sowie der schwach entwickelten Infrastruktur nicht regelmäßig großflächig durchgeführt werden, um allein als zuverlässige Informationsquelle für den Zustand des Ökosystems zu fungieren. Überdies sind diese zu kosten- und zeitaufwändig. Einen möglichen Lösungsansatz für ein flächendeckendes Monitoring bieten satellitenbasierte Fernerkundungstechniken. Diese können zur Kartierung des Waldbestandes, der Ausweisung von Kahlschlags- und Brandflächen sowie der Erfassung von Störungen des Ökosystems verwendet werden. Grundsätzlich sind optische Fernerkundungsdaten zur Ausweisung der zuvor genannten Flächen geeignet. Für Sibirien sind diese Daten jedoch stark durch Wolkenbedeckung, Nebel, Dunst und Dunkelheit über lange Zeiträume des Jahres beeinträchtigt. Mikrowellenbasierte Fernerkundungstechniken langwelliger Radarsensoren (SAR; *Synthetic Aperture Radar*) sind hingegen nicht sensitiv gegenüber der Wolkenbedeckung und stellen somit eine effiziente Möglichkeit, insbesondere durch die Kombination von Polaristationstechniken, zur Bearbeitung der Fragestellungen dar.

Ziel der vorliegenden Arbeit ist die Entwicklung neuer quantitativer Fernerkundungstechniken zum Monitoring von Wäldern, im Besonderen zur Ableitung der vorhandenen Holzbestände (GSV; *growing stock volume*). Infolge ihrer Sensitivität gegenüber den geometrischen Eigenschaften der zu untersuchenden Objekte sind Radardaten gut zur Bemessung der vorhandenen Waldbiomasse geeignet. Durch zahlreiche Studien, deren Focus auf verschiedenste Regionen der Erde und Waldtypen gerichtet ist, konnte ein hoher korrelativer Zusammenhang zwischen der Radarrückstreuung bzw. der interferometrischen Kohärenz und der überirdisch wachsenden Biomasse (AGB; *above ground biomass*; hier: Biomasse) aufgezeigt werden. Besonders für die homogenen, karg besiedelten Waldareale der borealen Zone konnten hohe Korrelationen nachgewiesen werden. Im Hinblick auf die polarimetrischen Eigenschaften des Radarsignals, wurde außerdem ein Zusammenhang zwischen Waldbiomasse und den polarimetrischen Phasenunterschieden von SAR-Daten entdeckt.

Radar-Rückstreuintensitäten weisen hingegen im Allgemeinen eine unzureichende Sensitivität gegenüber der Biomasse auf und sind durch eine frühzeitige Sättigung des Signals bereits bei niedrigen Biomassewerten gekennzeichnet. Ansätze, die SAR-Interferometrie nutzen, sind aufgrund ihrer Abhängigkeit von der Basislinie der Datenpaare und den vorherrschenden Wetterbedingungen zum Aufnahmezeitpunkt, wenig robust. Eine Implementierung sehr hochfrequenter (VHF; *very high frequency*) SAR-Sensoren sowie global aufnehmender *light detection and ranging* (LiDAR) Satelliten ist technisch bis dato nicht praktikabel. Umfassende Untersuchungen zu dem Potential, das Radarpolarimetrie für Waldapplikationen bietet, stehen noch aus. Dennoch konnten in einige Grundlagenstudien potentielle Möglichkeiten dieser Technik herausgearbeitete werden. Da es sich dabei jedoch lediglich um erste Untersuchungen für einige wenige Testgebiete handelt, ist eine Ableitung allgemeingültiger Aussagen über die Sensitivität, das Sättigungslevel und die Robustheit polarimetrischer Parameter bisher nicht möglich. Die Untersuchung dieser Aspekt steht somit noch aus.

Seit nunmehr fast 15 Jahren wird das Potential von POLINSAR-Techniken für Waldanwendungen eingehend untersucht. Im Rahmen dieser Arbeit erfolgt eine ausschließliche Konzentration auf polarimetrische Informationen. Der Grund dafür ist das Fehlen eines geeigneten globalen interferometrischen POLSAR-Datensatzes (L- oder P-Band, *single pass*), während polarimetrische Datensätze (z.B. ALOS PALSAR L-Band) für weite Teile der Erde existieren.

Der Fokus dieser Arbeit liegt auf folgenden Forschungsfragen:

- Können polarimetrische Parameter effektiv zur Erweiterung der (SAR-) Datengrundlage zur Ableitung des Holzbestandes beitragen?
- Kann mit Hilfe polarimetrischer Informationen eine Abschätzung des GSV verbessert und somit das bisher aufgrund der Sättigung erreichbare Level erhöht werden?

Im Rahmen der dritten Phase der *Advanced Land Observing Satellite* (ALOS) *Kyoto & Carbon Initiative*, die durch das *Earth Observation Research Centre* (EORC) der *Japanese Aerospace Exploration Agency* (JAXA) geleitet wird, werden insgesamt elf Waldterritorien genutzt. Für die polarimetrischen Analysen wurden die vier Gebiete Bolshe-Murtinsky, Chunsky, Primorsky und Shestakovsky als Untersuchungsgebiete ausgewählt, welche Teil der südlichen Taiga in der borealen Zone sind und zu den Verwaltungsdistrikten Krasnoyarsk Kray und Irkutsk Oblast gehören. Die Wahl fiel aus mehrerlei Gründen auf diese Gebiete: neben SAR-Daten, stehen Waldinventur- und meteorologischen Daten zur Verfügung und die Waldgebiete sind durch eine hohe Diversität gekennzeichnet. Aus jedem der vier Territorien wurden wiederum ein bis zwei Teilgebiete für die durchgeführten Analysen ausgewählt. Die Größe dieser variiert zwischen 50 und 200 km² und sie wurden entsprechend der geographischen Lage innerhalb des jeweiligen Territoriums bezeichnet (Shestakovsky-N, Primorsky-E, Chunsky-E, Chunsky-N & Bolshe-NE).

Die Inventurdaten umfassen eine Vielzahl von Waldparametern, wie z.B. die Identifikationsnummer, GSV (in 10 m^3/ha pro Klasse) oder die relative Bestandsdichte (RS; *relative stocking*). Der Holzbestand (GSV) repräsentiert das Volumen der Baumstämme aller Pflanzenspezies pro Flächeneinheit inklusive der Baumrinde. Äste und Baumstümpfe finden hingegen keine Berücksichtigung. Die relative Bestandsdichte setzt den aktuell betrachteten Bestand ins Verhältnis zu einem idealen Waldbestand unter perfekten Bewirtschaftungsbedingungen. Innerhalb der Testgebiete variiert das GSV zwischen 0 und ca. 450 m^3/ha. Kahlschläge und Sümpfe werden durch ein GSV von 0 m^3/ha gekennzeichnet. Bemerkenswert ist der große Anteil an den untersuchten Flächen von Waldbeständen, die eine Störung aufweisen. Weite Teile der sibirischen Wälder sind unbewirtschaftet, weshalb natürliche Mischwälder vorherrschend sind. Espen (*Populus tremula*), Birken (*Betula pendula*), Tannen (*Abies sibirica*), Lärchen (*Larix dahurica* und *Larix sibirica*), Kiefern (*Pinus sylvestris*) und Fichten (*Picea sibirica*) sind die am häufigsten vorkommenden Baumarten im Untersuchungsgebiet. Koniferen sind häufig ein Zeiger für Wälder, welche den Klimaxzustand erreicht haben (dies entspricht ca. 60 % der sibirischen Wälder). Im Gegensatz dazu sind für junge Wälder Pionierarten, wie Birken und Espen, charakteristisch.

Der größte Teil der Wintermonate ist durch Temperaturen unterhalb des Gefrierpunktes und Schneeakkumulation gekennzeichnet. In den Sommermonaten liegen die Temperaturen über 0 °C. Daher, können im Allgemeinen, Datenakquisitionen unter gefrorenen Bedingungen dem Winter und unter ungefrorenen Bedingungen dem Sommer zugeschrieben werden. Als Tauwetter wurden Situationen bezeichnet, in denen die Temperatur knapp oberhalb des Gefrierpunktes liegt. Die maximale Regenmenge im Akquisitionszeitraum betrug 1.6 cm.

Um das Ziel dieser Untersuchungen bestmöglich umsetzten zu können, wurden vollpolarimetrische L-Band SAR-Daten für das Untersuchungsgebiet durch die JAXA mithilfe von ALSO PALSAR akquiriert. In Übereinstimmung mit der Akquisitionsstrategie der JAXA wurden die polarimetrischen Daten einmal innerhalb von

zwei Jahren mit einem Blickwinkel von 21.5° und zweimal in zwei Jahren mit einem Blickwinkel von 23.1° aufgenommen. Daher ist es nicht möglich, große multitemporale Datensätze zusammenzustellen.

Für die Analysen wurden *Single Look Complex* (SLC) Level 1.1 PALSAR-Daten verwendet. Als erstes wurden die Daten polarimetrisch kalibriert. Anschließend wurde die Kohärenzmatrix berechnet. Im Zuge dessen wurden die Daten räumlich mit 7 *looks* in *Azimuth* und 1 *look* in *Range* gemittelt und Speckle-Effekte mit einem 3x3 *Lee Sigma Filter* reduziert. Durch die räumliche Mittelung (*Multi-Looking*) wurden annähernd quadratische Pixel erzeugt. Der Faraday-Effekt wurde ebenfalls berechnet und eliminiert. Außerdem erfolgte eine Korrektur der polarimetrischen SAR-Daten hinsichtlich des Einfluss der Neigung in *Azimuth*-Richtung. Um diesen Neigungseffekt zu kompensieren, wurden die Orientierungswinkel (OA; *orientation angles*) durch den Kreispolarisationsalgorithmus abgeleitet. Abschließend wurden die Bilder unter Zuhilfenahme des *Shuttle Radar Topography Mission-3 Digital Elevation Models* (SRTM-3 DEM) orthorektifiziert.

Vor der Abschätzung des GSV wurde das Potential verschiedener polarimetrischer Parameter, wie der polarimetrischen Signaturen, des Grades der Polarisation, der Phasenunterschiede, der polarimetrischen Kohärenz und der Intensität polarimetrischer Dekompositionen zur Charakterisierung der polarimetrischen Resonanz von Waldbedeckung unter variierenden Wetterbedingungen, Waldbestandsstrukturen und Baumarten untersucht. Aus den gegebenen polarimetrischen Signaturen wurden Rückstreuparameter wie z.B. die Art der Polarisation (linear, kreisförmig oder elliptisch) und der Orientierungswinkel des Rückstreuers extrahiert. Mithilfe der dreidimensionalen, ko-polarisierten Signaturen, welche aus der Sockelhöhe (pedestal height), können bewaldete und nicht bewaldete Flächen eindeutig getrennt werden. Die Rückstreumechanismen von Espen-, Birken-, Lärchen- und Kiefernbeständen sind, aufgrund des ähnlichen Streuverhaltens nicht geeignet, um diese Baumarten voneinander zu unterscheiden. In diesem Fall ist die polarimetrische Signatur gegenüber der Struktur des Rückstreuers nicht sensitiv. Eine deutliche Trennung der GSV-Klassen kann basierend auf den Grad der Polarisation vorgenommen werden, da die beiden Parameter negativ ($R = -0.80$) korreliert sind.

Die polarimetrischen Phasenunterschiede eignen sich für die Trennung von Kahlschlägen und Sumpfgebieten von bewaldeten Arealen. Das Rückstreuverhalten (Volumenstreuung, Oberflächenstreuung) wird durch die polarimetrischen Phasenunterschiede zwischen bewaldeten und nicht bewaldeten Flächen erfasst. Die größer werdenden Mittelwerte und Standardabweichungen der polarimetrischen Phasenunterschiede suggerieren eine hohe Variabilität in den Rückstreueigenschaften, die durch den Beitrag der Äste zum Signal bei ungefrorenen im Gegensatz zu gefrorenen Bedingungen entstehen. Lärchen weisen im Vergleich zu anderen Baumarten eine deutlich geringere Variabilität sowohl bei gefrorenen als auch bei nicht gefrorenen Verhältnissen auf. Des Weiteren konnte ein deutlicher Anstieg der mittleren polarimetrischen Phasenunterschiede, bei einem gleichzeitig lediglich geringen Anstieg der

Standardabweichung für größer werdende GSV-Werte bis zu 180 m^3/ha festgestellt werden. Für höhere GSV-Werte verliert die polarimetrische Phasendifferenz ihre Sensitivität.

Weiterhin wurde die Beziehung zwischen GSV und der polarimetrischen Kohärenz der ALOS PALSAR L-Band Daten für die sibirischen Waldgebieten untersucht. Unabhängig von den Wetterbedingungen konnte dabei eine starke Korrelation (R = -0.87) zwischen den beiden Parametern festgestellt werden. Topographische Effekte, wie z.B. die Exposition von geneigten Hängen konnten in den Daten nicht beobachtet werden. Die Korrelation zwischen der HHVV-Kohärenz und des GSV ist unabhängig von der Größe der Waldbestände. Es konnte weder ein an- noch absteigender Trend der Abhängigkeit von der Größe der Bestände festgestellt werden. Eine geringfügig höhere Korrelation zwischen der polarimetrischen Kohärenz und dem GSV wurde für vollständig bestandene Waldflächen ermittelt.

Die Kohärenz ist in spärlich besiedelten Waldarealen immer höher als in dichten Beständen. Das Kohärenzlevel und die Spannweite, d.h. die Differenz zwischen der Kohärenz in dünn und dicht besiedelten Arealen, hängen stark von den Wetterbedingungen ab, da diese die dielektrischen Eigenschaften des Waldbodens und der Vegetation beeinflussen. Die mittlere Kohärenz ist sowohl bei dicht- als auch bei dünnbesiedelten Beständen unter gefrorenen Bedingungen stets am höchsten und unter nicht gefrorenen Bedingungen stets am niedrigsten.

Die Vier-Komponenten Dekompositionsparameter wurden auf die ALOS PALSAR L-Band Daten angewendet, um die so erhaltenen Anteile mit dem GSV vergleichen zu können. Für den Vergleich wurden die Rückstreuanteile der Volumenstreuung, der Oberflächenstreuung und des *double-bounce*, abgeleitet mit und ohne Rotation der Kohärenzmatrix, herangezogen. Zur Kompensation topographischer Effekte wurde eine adaptive Rotation der Kohärenzmatrix verwendet. Die Korrelation zwischen GSV und *double-bounce* kann so signifikant erhöht werden. Währenddessen bleibt der Wert für die Volumenstreuung unverändert und die Korrelation mit der Oberflächenstreuung verringert sich leicht. Im Allgemeinen steigen die Rückstreuanteile der Volumenstreuung und des *double-bounce* mit steigendem GSV, während der Anteil der Oberflächenstreuung sinkt. Diese Zusammenhänge lassen sich wie folgt physikalisch erklären: i) Bei niedrigen GSV-Werten existieren zahlreiche Lücken im Kronendach, die einen höheren Rückstreuanteil des Bodens zulassen. ii) Das Wachstum der Vegetation geht mit einem allmählichen Schließen des Kronendaches einher, was zu einem Anstieg des Anteils der Volumenstreuung und einem sinken des Anteil der Oberflächenstreuung führt. iii) Das Wachstum des Baumstammes führt zu einer Erhöhung des *double-bounce*-Anteils. Diese Zusammenhänge zwischen GSV und den unterschiedlichen Rückstreumechanismen können zur Abschätzung des GSV genutzt werden.

Die Korrelation zwischen den polarimetrischen Dekompositionsparametern und dem GSV kann erhöht werden, indem die Verhältniszahl zwischen Boden- und Volumenstreuung, welche als Ratio aus dem Produkt der Anteile der Volumenstreuung

und des *double-bounce* und dem Anteil der Oberflächenstreuung definiert ist, verwendet wird, anstatt die Dekompositionsanteile einzeln zu betrachten. Diese Idee wurde in Verbindung mit dem Zwei-Schichten-Ansatz von Oberflächen- und Volumenstreuung im Wald entwickelt. Ein großer Zahlenwert für das Verhältnis von Boden- zu Volumenstreuung steht für ein geringes GSV, was auf die Lücken im Kronendach zurückzuführen ist. Ist umgekehrt das Verhältnis von Boden- zu Volumenstreuung niedrig, ist das GSV hoch. Die Sensitivität des Verhältnisses von Boden- zu Volumenstreuung gegenüber dem GSV wurde erhöht und somit eine relativ hohe Korrelation erreicht (R^2 variiert zwischen 0.65 und 0.82 innerhalb der Testgebiete). Allerdings konnte auch eine relative Vergrößerung der Spannweite der Daten für alle Testgebiete beobachtet werden.

Unter nicht gefrorenen Bedingungen ist die Oberflächenstreuung in dünn bestandenen Wäldern generell höher als die Volumenstreuung, während letztere für dichte Wälder dominant ist. Unter gefrorenen Bedingungen verhalten sich die Streumechanismen deutlich anders. Für dichte Wälder ist die Oberflächenstreuung dann höher als die Volumenstreuung. Die polarimetrische Dekomposition würde suggerieren, dass Oberflächen- und Volumenstreuung die dominierenden Rückstreumechanismen für die Sibirischen Wälder sind. Der Anteil des *double-bounce* am gesamten Rückstreusignal wäre hingegen nur sehr gering.

Der Einfluss verschiedener Baumarten auf die polarimetrischen Dekompositionsanteile, die polarimetrische Kohärenz und den Grad der Polarisation wurde unter drei unterschiedlichen meteorologischen Bedingungen untersucht: nicht gefroren (nass und trocken), gefroren und Tauwetter. Im Rahmen der vorliegenden Arbeit wurden dahingehend die vier Baumarten Espe, Birke, Lärche und Kiefer untersucht. Vor allem Lärchen unterscheiden sich von anderen Baumarten, was anhand eines erhöhten Anteils an Oberflächenstreuung um +2 dB bei nicht gefrorenen Bedingungen quantifiziert werden kann. Der höhere Anteil der Oberflächenstreuung bei Lärchenwäldern kann darauf hinweisen, dass das Kronendach für die elektromagnetische Welle transparenter erscheint und daher ein großer Anteil des Rückstreusignals vom Waldboden stammt. Weiterhin kann dies durch unterschiedliche Kronenstrukturen, eine andere Anordnung der Nadeln, ein weniger dichtes Kronendach sowie eine geringere Anzahl an Unterholzschichten begründet werden. Der Einfluss unterschiedlicher Baumarten auf die polarimetrischen Rückstreuanteile ist unter gefrorenen Bedingungen sehr gering. Lärchen unterscheiden sich bei nicht gefrorenen Bedingungen mit einem Wert von + 0.17 in der polarimetrischen Kohärenz wiederum von anderen Baumarten. Espen, Birken, Lärchen und Kiefern hingegen beeinflussen den Grad der Polarisation nicht, unabhängig von den vorherrschenden Wetterverhältnissen.

Auf der Basis der Erkenntnisse über die sibirischen Wälder wurden zwei empirische Modelle entwickelt, mit deren Hilfe die polarimetrische Kohärenz von ALOS PALSAR L-Band Daten und das Verhältnisses von Boden- zu Volumenstreuung als eine Funktion des GSV des Waldes beschrieben werden kann. Die Modellparameter wurden durch eine Regression zwischen der polarimetrischen Kohärenz und des GSV mithilfe eines Trainingsdatensatzes berechnet.

Um die Genauigkeit der abgeleiteten GSV-Werte zu bestimmen, wurden der mittlere quadratische Fehler (RMSE; *root mean square error*), der relative RSME, das Bestimmtheitsmaß (R^2) und der systematische Fehler (Bias) berechnet. Als bester Wert konnte auf der Basis der polarimetrischen Kohärenz ein RMSE von 38 m³/ha und $R^2 = 0.73$ erzielt werden. Unter Verwendung des Verhältnisses von Boden- zu Volumenstreuung konnte eine maximale Genauigkeit mit einem RMSE von 44 m³/ha und $R^2 = 0.62$ erreicht werden. Die besten Ergebnisse für beide SAR-Parameter wurden unter nicht gefrorenen Bedingungen im Testgebiet Shestakovsky-N abgeleitet. Unabhängig von den Wetterbedingungen konnten für dieses Testgebiet die Resultate mit den geringsten Ungenauigkeiten erreicht werden. Außerdem war es möglich für Shestakovsky-N auf der Waldbestandebene GSV bis zu einem Wert von 250 m³/ha mit einer Genauigkeit von 38 m³/ha (relativer RMSE = 18 %) abzuleiten. Da die ALOS PALSAR L-Band Daten nicht für alle Wetterverhältnisse in allen Testgebieten vorliegen, ist eine Aussage über die am besten geeignetsten Wetterbedingungen zur Ableitung von GSV schwierig.

Der Fehler bei der GSV-Ableitung ist stark vom betrachteten Gebiet abhängig. Shestakovsky-N liefert die besten Resultate, während Bolshe-NE am schlechtesten abschneidet. Die Gründe für die großen Abweichungen sind in den unterschiedlichen Eigenschaften der Testgebiete sowie in den unterschiedlichen Genauigkeiten der Referenzdaten zu suchen. Für Sibirien könnten die Heterogenität der dielektrischen Eigenschaften, Effekte unterschiedlicher struktureller Elemente auf die Beziehung zwischen Radar-Rückstreuung und GSV sowie Ungenauigkeiten innerhalb der Referenzdaten die teilweise hohen Fehlerraten erklären. Für das Trainieren des Modells sollte daher eine bestmögliche Verteilung des GSV innerhalb des Untersuchungsgebietes angestrebt werden. Trotz der unterschiedlichen Genauigkeiten der abgeleiteten GSV-Werte, die für Sibirische Wälder erreicht wurden, könnte die Genauigkeit verbessert werden, wenn Informationen über das Untersuchungsgebiet einbezogen werden.

Die auf das Verhältnis der Boden- zu Volumenstreuung basierende Abschätzung des GSV wurde in Abhängigkeit von Strukturmerkmalen der Waldbestände, wie z.B. der Bestandsgröße und des Bestockungsgrad durchgeführt. Um eine bessere Vorstellung von den erreichten Genauigkeiten für alle Testgebiete unter Berücksichtigung der jeweiligen Verteilung des GSV zu erhalten, wurde der relative RMSE berechnet. Der relative Bewuchs hat einen positiven Einfluss auf die Ableitung des GSV. Mit steigender Bestandsgröße und steigendem relativen Bewuchs sinkt der Fehler bei der Abschätzung des GSV. Die Ergebnisse sind für alle Wetterbedingungen und für alle Testgebiete konsistent, mit Ausnahme von Chunsky-N. Für sibirische Wälder mit einer relativen Bestandsdichte von mindestens 70 % ist bei der Datenerhebung von einem effektiven Fehler von 17-40 % (relativer RMSE) auszugehen. Die vergleichsweise niedrigen relativen RMSE für intensiv bewirtschaftete Wälder zeigen, dass mit diesem Verfahren die besten Ergebnisse für eben solche Gebiete erzielt werden können. Weiterhin konnte beobachtet werden, dass die Bestandsgröße einer der wesentlichsten Faktoren für eine genaue GSV-Ableitung ist. Die Ergebnisse zeigen, dass ein relativer RMSE von 16-40 % für Bestände mit einer Fläche von > 40 ha erreicht werden kann. Die Auswertung aller Modelldaten

zeigt, dass mithilfe polarimetrischer Daten vor allem für große, bewirtschaftete Bestände genaue Ergebnisse erzielt werden können.

Für die sibirischen Wälder wurde außerdem festgestellt, dass die Genauigkeit der abgeleiteten GSV-Werte für Lärchenbestände besonders sensitiv gegenüber den Wetterverhältnissen ist. So wurden hohe Genauigkeiten unter nicht gefrorenen Bedingungen erzielt, im Gegensatz zu den niedrigen Genauigkeiten unter gefrorenen Bedingungen.

Die Auswahl der Trainingsgebiete zur Messung der Modellparameter ist der größte Nachteil beider Ableitungsmethoden. Dies gilt insbesondere für die polarimetrische Kohärenz. Die Verteilung des GSV sollte für die Bestände zum Training und zur Validierung des Modells möglichst ähnlich sein. Der Parameter, des auf dem Verhältnis von Boden- zu Volumenstreuung basierenden Modells, wird anhand einer Regression zwischen HV-Rückstreuung und des GSV aus dem Trainingsdatensatz hergeleitet. Dieser Nachteil kann durch die Verwendung der *Entropy* kompensiert werden, da diese ein gutes Trennbarkeitsmaß für bewaldete und nicht bewaldete Flächen liefert.

Zusammenfassend ist zu den vorliegenden Untersuchungen zu sagen, dass die erhaltenen Ergebnisse die Hypothese bestätigen, dass ALOS PALSAR L-Band *quadpol* Daten zur Ableitung von GSV mit annehmbarer Genauigkeit für sibirische Wälder auf der Bestandsebene geeignet sind. Wenngleich zu beachten ist, dass die Gegebenheiten im Untersuchungsgebiet zentral für die letztendlich zu erreichenden Genauigkeiten sind. Die Ableitung des GSV auf der Basis polarimetrischer Daten setzt keine multi-temporalen Datensätze voraus, wie dies z.B. bei Methoden der polarimetrischen Interferometrie (POLINSAR) der Fall ist und macht so eine bessere Kartierung der temporalen Veränderungen des GSV möglich. Ein weiterer Vorteil ist, dass ALOS PALSAR L-Band Daten für große Teile der Erde bereits zur Verfügung stehen, während vergleichbare POLINSAR-Datensätze bisher nicht vorhanden sind.

Table of Contents

Abstract i

Zusammenfassung ii

Table of Contents x

Acronyms and Symbols xiv

Chapter 1 - Introduction 1

1.1 Introduction and background 1

1.2 ALOS PALSAR mission 3

1.3 Potential of radar data for forest biomass derivative 4

1.3.1 Backscattering intensities 4

1.3.2 Interferometry 5

1.3.3 Polarimetry 7

1.3.4 Polarimetric interferometry 9

1.4 Scope of the thesis 10

1.5 Outline of the thesis 11

Chapter 2 - Radar Polarimetry 12

2.1 Polarimetry 12

2.1.1 Wave polarimetry 12

2.1.2 The Jones vector and Stokes vector 14
2.2 Partially polarised waves 15
2.2.1 Degree of polarisation 16
2.3 Scattering matrix 16
2.4 Non-deterministic scatterers 19
2.5 Line of sight rotation 20
2.5.1 Rotation of the scattering matrix 20
2.5.2 Rotation of the coherency matrix 21
2.6 Polarimetric target decomposition 22
2.6.1 Eigenvector based decomposition 22
2.6.2 Model based decomposition 24
2.6.2.1 Four-component Yamaguchi decomposition 24
2.7 Polarimetric parameters 30
2.7.1 Polarisation signatures 30
2.7.2 Polarimetric coherence 31
2.7.3 Polarisation phase difference 31
Chapter 3 – Site Description and Data Sources 32
3.1 Test sites 32
3.1.1 Bolshe Murtinsky 32
3.1.2 Chunsky 34
3.1.3 Primorsky 36
3.1.4 Shestakovsky 37
3.2 Ground data 37
3.3 Weather data 40
3.4 PALSAR data 42

3.5 Necessary pre-processing thoughts 42
3.5.1 In-situ data pre-processing 42
3.5.2 PALSAR data pre-processing 44
3.5.2.1 Correction of Faraday rotation (FR) effects 45
3.5.2.2 Polarisation orientation angle compensations 49
3.6 Conclusions 52
Chapter 4 - Polarimetry in Siberian Forests 53
4.1 Polarimetric signatures 53
4.2 Polarisation phase difference 56
4.3 Polarimetric coherences 59
4.3.1 Multi-temporal consistency 63
4.3.2 Seasonal variations 64
4.4 Polarimetric decomposition powers 68
4.4.1 Impact of line of sight rotation 68
4.4.2 Growing stock volume and polarimetric decomposition powers . . 70
4.4.3 Impact of weather conditions 75
4.5 Impact of tree species on polarimetric parameters 79
4.6 Conclusions 83
Chapter 5 – Growing Stock Volume Retrieval 86
5.1 Polarimetric coherence modelling 86
5.1.1 Model selection 86
5.1.2 Model training 87
5.1.3 Model parameters estimation 87
5.2 Polarimetric decomposition modelling 90
5.2.1 Model selection 90

5.2.2 Model training and model parameters estimation 93
5.3 GSV retrieval procedure 96
5.4 Assessment of GSV retrieval 98
5.5 Conclusions 106
Chapter 6 - Conclusions 109
6.1 Summary of the results 109
6.2 Future Outlook 114
Chapter 7 - References 115
Appendix A 127
Appendix B 130
Appendix C 137
Acknowledgements 146
Curriculum Vitae 147
Selbständigkeitserklärung 149

Acronyms and Symbols

AIRSAR	Airborne Synthetic Aperture Radar
ALOS	Advanced Land Observing Satellite
ASAR	Advanced Synthetic Aperture Radar
AVNIR-2	Advanced Visible and Near Infrared Radiometer type 2
BSA	Back Scattering Alignment
DEM	Digital Elevation Model
DoP	Degree of polarisation
DWD	Deutsche Wetter Dienst (German Weather Service)
ERS	European Remote Sensing
ESA	European Space Agency
FIP	Forest Inventory Planning
FR	Faraday rotation
FSA	Forward Scattering Alignment
GIS	Geographical Information System
GSV	Growing Stock Volume
HH	Horizontal Horizontal Polarisation
HV	Horizontal Vertical Polarisation
IIASA	International Institute for Applied System Analysis
JAXA	Japanese Aerospace Exploration Agency
JERS	Japanese Earth Resources Satellite
JPL	Jet Propulsion Laboratory
KOMPSAT-2	Korea Multi-Purpose Satellite-2
LIDAR	Light Detection And Ranging
LOS	Line of Sight
NASA	National Aeronautics and Space Administration
POA	Polarisation Orientation Angle
PALSAR	Phased Array type L-band Synthetic Aperture Radar
POLINSAR	Polarimetric Interferometry Synthetic Aperture Radar
POLSAR	Polarimetric Synthetic Aperture Radar
PPD	Polarisation phase difference

PRISM	Panchromatic Remote-sensing Instrument for Stereo Mapping
Radar	Radio Detection and Ranging
RS	Relative Stocking
RVoG	Random Volume over Ground
SAR	Synthetic Aperture Radar
SLC	Single Look Complex
SRTM	Shuttle Radar Topography Mission
TEC	Total electron content
VH	Vertical Horizontal Polarisation
VHF	Very High Frequency
VV	Vertical Vertical Polarisation

Symbols

Chapter 2

α	Scattering alpha angle
β	Scattering beta angle
δ	Relative phase difference between electric field
ω	Angular frequency
ψ	Orientation angle
χ	Ellipticity angle
A_0	Amplitude wave
A	Anisotropy
$\overrightarrow{E}$	Electric field vector (complex)
$\overrightarrow{E}(\vec{r},t)$	Electric field vector (real)
H	Scattering entropy
$\vec{k}$	Propagation vector
$\overrightarrow{k_L}$	Scattering vector (Lexicographic basis)
$\overrightarrow{k_P}$	Scattering vector (Pauli basis)
R_h	Bragg coefficient (horizontal)
R_v	Bragg coefficient (vertical)
TP	Total power
φ_0	Absolute phase reference
$[S]$	Sinclair matrix
$[T]$	Coherency matrix
$[C]$	Covariance matrix
$[J]$	Jones matrix
p	Degree of polarisation
ρ	Complex coherence
φ	Polarisation phase difference

Chapter 3

σ^0	Sigma-nought radar backscatter
γ^0	Gamma-nought normalized radar backscatter
Ω	Faraday rotation angle

θ	Polarisation orientation angle

Chapter 4

φ_{HHVV}	Polarisation phase difference between HH and VV
θ_{sat}	Saturated slope
P	Four-component decomposition power
$P(\theta)$	Four-component decomposition power (rotation of $[T]$)
P_d	Double-bounce scattering power
P_s	Surface scattering power
P_v	Volume scattering power
P_h	Helix scattering power
R	Pearson's linear coefficient of correlation
σ_0	Backscattering coefficient for sparse forest
σ_∞	Backscattering coefficient for dense forest

Chapter 5

γ_{gr}	Coherence value of sparse forest
γ_∞	Coherence value of dense forest
m_s	Surface scattering component
m_d	Double-bounce component
m_v	Volume scattering component
φ	Scattering phase
α	Dominant scattering mechanism
F_P	Volume shape parameter
μ	Ground-to-volume scattering ratio
σ_{gr}^0	Backscatter coefficient for sparse forest
σ_∞^0	Backscatter coefficient for dense forest
β	Two-way forest transmissivity
R^2	Coefficient of determination
RMSE	Root Mean Square Error
RRMSE	Relative Root Mean Square Error

Units

°C	Degree Celsius
cm	Centimetre
dB	decibel
ha	hectare
hrs	hours
km	kilometre
m	Meter
s	second

Chapter 1

Introduction

This chapter presents the role of synthetic aperture radar (SAR) for monitoring forest. Emphasis is given on the problem, in particular sensitivity to forest biomass, which in turn motivates my Ph.D. work. The importance of Siberian forests will be discussed briefly in section 1.1. A general review of the most important space-borne ALOS PALSAR L-band sensor will be presented in section 1.2. Section 1.3 summarises the potential of radar remote sensing techniques: backscatter intensities, interferometry and polarimetry for forestry applications, particularly for biomass estimation. It is not intended to give a comprehensive presentation of these arguments, but rather to provide the reader with the boundaries of this research work. Section 1.4 discusses the research gaps and mentions the objectives and the innovations introduced by this study in the field of SAR growing stock volume estimation which is the major predictor for assessing the forest biomass. Finally, section 1.5 concludes the chapter with an outline of this dissertation.

1.1 Introduction and background

The title "Evaluation of the Potential of ALOS PALSAR L-band Quadpol Radar Data for the Retrieval of Growing Stock Volume in Siberia" apparently relates the topic of microwave remote sensing to forests in boreal zone. This work essentially merges two fields of science: synthetic aperture radar (SAR) "polarimetry" and growing stock volume estimation in Siberian "forests". The growing stock volume (GSV) is the important forest parameter in relation to the forest resource management and global change issues. It is the key indicator for assessing the above ground biomass (Häme *et al.* 1992; Shivdenko *et al.* 2007) which is the essential variable for estimating the net carbon dioxide exchange between the land surface and the atmosphere.

The boreal forest is the northernmost forest zone on earth and stretches all around the globe at latitudes 60° - 70° N in Alaska and northern Europe, 55° - 70° in western Canada, 45° - 60° in eastern Canada, and all the way from 45° to above 70° in Siberia (Treter, 1993). Siberian forests are a natural resource of global importance, both economically and

ecologically. They already serve Russia and the world as a source of wood, a symbol of wilderness, and a critical stabilizer of the global climate. Siberian forests contain roughly half of the world's growing stock volume of coniferous species, making them commercially and environmentally precious resource. Russia is the world's largest exporter of round wood, accounting for 43% coniferous and 42% non-coniferous exports in international markets and the industries employee almost 900,000 workers, with more than three-quarters of its employees in Siberia (Thornton & Ziegler, 2002). Several countries provide a growing market for the forest sectors located in East and West Siberia. Many non-wood products such as gum or resin, stumps, bark, twigs, hay, tree saps, wild fruits, mushrooms, berries, etc. come from the forests are of substantial economic importance for the Russian society.

It is known that forest biomass, i.e. the amount of living organic matter in a given forested area, represents an important sink of carbon in the carbon budget. However, there are still large uncertainties in quantifying its spatial distribution and variation over the time (Davidson, 2008). The vast forests of Asian Russia act as reservoirs for one seventh of the global carbon pool (Lebedev, 2005). Russia's forests comprise approximately one-fifth of the world's total forests. Therefore, a better understanding of the Russian carbon balance is not only importance in itself, but is also critical to better understanding of the global carbon balance. Therefore, vast forests of Siberia play an important role as a carbon sink (Nilsson *et al.* 2000, Beer *et al.*, 2006). Siberia's forests contain 40 million tons of stored carbon (Trexler, 1991). Forests are a vitally important tool for protection of soils against erosion and protection and regulation of water resources – practically all accessible freshwater comes from forested catchments.

Siberia's forests suffer from severe ecological degradation. Much of this damage is caused by careless logging practices, including over logging, excessive forest fires, acid rain and air particulate pollution also contribute to the damage. The forest degradation or deforestation has an impact on climate change. Therefore, forest needs to be continuously monitored. The traditional ground survey is useful for the local investigations but taking into account of the vastness and remoteness of Siberian forests and also the less developed infrastructure, forest inventories are not carried out frequently enough to provide the information about the ecosystem. Moreover, ground-based surveys are too expensive and time consuming. Possible solution to overcome this problem is to use remote sensing, in particular space-borne remote sensing technique. The technique can be used for forest cover mapping, clear-cut or burned area monitoring and the detection of forest disturbances (White *et al.* 2005; Healy *et al.* 2005; Fraser & Li, 2002; Rignot *et al.* 1997; Lozano *et al.* 2008; Saska *et al.* 2003; Kasischke *et al.* 1992; Yatabe & Leckie, 1995; Rignot *et al.* 1997; Thiel *et al.* 2006). The optical remote sensing data are useful for the identification of clear-cuts, fires scars or other disturbances (White *et al.* 2005; Healy *et al.* 2005; Lozano *et al.* 2008; Saska *et al.* 2003). In Siberia, the optical remote sensing data are affected by frequent cloud cover, fog, mist, or darkness over the long periods of the year. Microwave remote sensing technique of longer wavelength radar sensor which is not sensitive to cloud cover provides efficient means to accomplish this task, especially by

combining polarimetric techniques. The goal is to apply SAR polarimetry remote sensing technique to provide accurate, reliable and complete information in terms of sensitivity, saturation level and robustness about the estimation of growing stock volume in Siberian forests.

1.2 ALOS PALSAR mission

The Advanced Land Observing Satellite (ALOS), first L-band polarimetric SAR, was launched by the Japanese Space Exploration Agency (JAXA) on January 24, 2006. ALOS carries three remote sensing instruments: the along-track 2.5 m resolution Panchromatic Remote-sensing Instrument for Stereo Mapping (PRISM), the 10-m resolution Advanced Visible and Near-Infrared Radiometer type 2 (AVNIR-2), and the variable resolution polarimetric Phased Array L-band Synthetic Aperture Radar (PALSAR). In this thesis only PALSAR data is used for the investigation because it operates only on polarimetric mode. PALSAR aimed at spatially and temporally consistent, global coverage on a repetitive basis, to accommodate geo- and bio-physical parameter retrieval over semi-continental scales. ALOS is placed in a sun-synchronous orbit at 691 km with a repeat pass cycle of 46 days. Table 1.1 summarises the principal aspects of ALOS PALSAR mission and illustrates some technical details of the SAR on board satellites.

Mission	ALOS PALSAR
Duration	2006-2011
Altitude	691.65 km
Repeat cycle	46 days
Polarisation	HH/HV/VH/VV
Incidence angle	21.5°
Swath width	30 Km
Ground resolution:	
Range(1 look)	31 m
azimuth (2 looks)	10 m
Pass direction	Ascending
Application	Biophysical parameter retrieval, monitoring damage assessment

Table 1.1 Main features ALOS PALSAR mission.

PALSAR is operated in five different observation modes: Fine Beam Single polarisation (FBS), Fine Beam Dual polarisation (FBD), Polarimetric mode (POL), ScanSAR mode, and Direct Transmission (DT) mode. In FBS mode, PALSAR is operated with either HH or VV polarisation and in FBD mode, the polarisation options are HH/HV or VV/VH. The look angle is between 9.9° and 50.8° off-nadir. The POL mode is functioned with HH/HV/VH/VV with 12 alternative off-nadir angles between 9.7° and

26.2°. The default off-nadir angle is 21.5°. This mode yield a swath width of 30 km and 30 × 10 m ground resolution.

Due to the compromise between scientific requirements, user requests, and programmatic and satellite operational constraints the four modes are initially chosen as default modes:

a) FBS (HH) at 34.3°;

b) FBD (HH/HV) at 34.3°;

c) POL (HH/HV/VH/VV) at 21.5°;

d) ScanSAR five-beam (HH) 14 MHz.

To avoid the conflict with the optical sensors, which only perform during descending passes, PALSAR operations on FBS, FBD, and POL mode are performed during ascending passes. In the observation plan, the earth has been divided into some 80 adjacent non-overlapping geographical polygons which cover all land areas and coastal regions. All passes within each polygon are then acquired in groups of eight (46-day) unit cycles that are repeated on an annual (368 days) basis. In POL (at 21.5°) mode the selected regions are acquired every two years within two consecutive 46-day cycles. Due to the narrow swath width (30 km) in the POL, however, regional acquisition below N60° are not spatially contiguous but have gaps between the passes.

1.3 Potential of radar data for forest biomass derivative

Due to their sensitivity for the geometric properties of the targets, radar data proved to have potential for forest biomass assessment. In numerous studies and for diverse regions and forest types an in part high sensitivity of backscattering intensity (Saatchi & Moghaddam, 2000; Harrell *et al.* 1995; Harrell *et al.* 1997; Ranson & Sun 1997; Kuplich *et al.* 2000; Tsolmon *et al.* 2002; Balzter *et al.* 2003; Santos *et al.* 2003) and interferometric coherence (Santoro *et al.* 2002; Wagner *et al.* 2003; Tansey *et al.* 2004) for forest biomass has been verified. Particular high correlations are found for the homogeneous and frugal structured forests of the boreal zone. With regard to polarimetric systems, a link between forest biomass and polarimetric phase difference has been discovered (Le Toan *et al.* 1992).

In the following sub-sections, a thorough literature review pointing out the state of the art is summarised. However, the major focus will be concentrated on the discussion of the potentiality of radar remote sensing and especially on the radar polarimetry for forest biomass assessment.

1.3.1 Backscattering intensities

Active microwave system is of particular interest of forest monitoring because they can penetrate clouds. A SAR (Synthetic Aperture Radar) sends out electromagnetic signal and the signal, scattered back towards the radar, contains information about the geometrical

properties of the scatterer. The backscattered signal or backscatter intensities from SAR have high sensitivity over the forest areas. Generally, backscatter intensities increases with increase of forest biomass. This positive correlation has been simulated by means of simple empirical, semi-empirical, and complex physical models (Harrell et al. 1997; SMITH & Ulander, 1998; Wang *et al.* 1998; Smith & Ulander 2000; Santos *et al.* 2003, Watanabe *et al.* 2006; Santoro *et al.* 2006; Lucas *et al.* 2006;). The two most important properties of the radar for determining the forest biophysical parameters are dynamic range i.e. the intensity contrast between the forest and bare surface, and the saturation level at which further growth of a forest does not result in any change in backscatter. Both dynamic range and saturation level have been found to be a function of radar wavelength and polarisation. Radar backscatter has been shown to be positively correlated with forest biomass until it becomes saturated at a level which is higher with increasing radar wavelengths i.e. saturation level of forest biomass depends on the radar frequency. Lower frequencies (L-band and P-band) are more preferable than higher frequencies (X-band and C-band) for increasing saturation level at higher biomass (Le Toan *et al.* 1992; Luckman *et al.* 1997; Hoekman & Quinones, 2000). Radar backscattering at high frequencies is dominated by the scattering process in the crown layer of small branches, needles, twigs in the crown, and therefore, it does not penetrate and scatter significantly from the stem, while backscatter at lower frequencies is dominated by the scattering process from the trunks and large branches.

In addition to the radar frequency radar polarisation (Yanasse *et al.* 1997; Kellendorfer *et al.* 2003), forest characteristics (Lucas *et al.* 2004; Lucas *et al.* 2006), and environmental conditions (Harrell *et al.* 1997; Wang *et al.* 1998; Pulliainen *et al.* 1999; Ranson & Sun, 2000; Townsend, 2002) such as weather, seasonal changing parameters: snow cover, soil moisture, soil roughness, and total water content of the vegetation canopy have also great impacts on saturation level of biomass. The scattering mechanisms depend upon the environmental conditions at the time of the acquisition, indicating seasonal variations and temporal consistency of the backscatter. Both radar frequencies and radar polarisation have been used together to achieve higher saturation level. Furthermore, it has been proved that superimposed of multiple SAR scenes (time series SAR data) can increase the sensitivity of radar backscatter for forest biomass and the saturation level (Kurvonen *et al.* 1999; Santoro *et al.* 2007a; Rauste *et al.* 2005). Very High Frequency (VHF) seems to be optimal for the estimation of forest biomass. So far, no saturation level for forest biomass has been found (Fransson *et al.* 2000; Smith & Ulander, 2000; Melon *et al.* 2001). However, the sensitivity of backscattering intensity over the forest areas is much higher than the shorter wavelengths (Fransson *et al.* 2000; Imhoff *et al.* 2000; Manninen & Ulander, 2001; Ulander *et al.* 2002). But due to technical restrictions the space borne operation of VHF-SAR is used only for local forest (Imhoff *et al.* 2000; Fransson *et al.* 2000; Kononov & Ha, 2008).

1.3.2 Interferometry

When two or more coherent SAR images of the same scene are from different look directions, the complex correlation between pairs of images can be evaluated and the

system is said to operate as a SAR interferometer (INSAR). Additional to the backscattering intensity, the SAR interferometry studies the interferometric phase. The basic principle of SAR interferometry was first introduced by Graham (Graham, 1974). Zebker and Goldstein (Zebker & Goldstein, 1986; Zebker *et al.* 1992) first attempted to apply single pass interferometry using the AIRSAR system. With the launch of ERS-1 and ERS-2 satellite by European Space Agency (ESA), a large amount of data are available for the purpose of this technique. ERS SAR interferometry is used for the determination of complete topography map of the Earth surface with high accuracy and high resolution.

SAR interferometry is used mainly in three different ways. First, the phase difference between the SAR images provide information about the topographic height and hence to generate the Digital Elevation Model (DEM). Secondly, the differential interferometry, using at least two images, which has been successfully, applied for the detection of surface movements due to earthquakes, volcanic events, ice and glacier dynamics (Zebker *et al.* 1994; Massonnet *et al.* 1993). Third method, a measure called interferometric coherence (Luckman *et al.* 2000; Gaveau 2002; Eriksson *et al.* 2003; Askne & Santoro *et al.* 2005) for the quantitative retrieval of vegetation remote sensing. It is a measure for the complex correlation of two SAR images. The selection of SAR images depend on the temporal baseline and the environmental conditions i.e. precipitation, snow cover, wind speed, soil moisture etc. (Castel *et al*. 2000; Koskinen *et al.* 2001; Santoro *et al.* 2002; Askne *et al.* 2003; Eriksson *et al*. 2003; Pulliainen *et al.* 2003; Askne & Santoro 2007; Santoro *et al.* 2007b). The very cold winters (frozen conditions) combined with long temporal baselines (weeks or months) are found to be stable conditions in the boreal zone for forest parameters retrieval. Otherwise short temporal baselines are preferable (days) due to the less effect of rain, snowmelt, soil moisture etc. In addition to this, the shorter the wavelength, the more sensitive is the coherence to change and the shorter is the required temporal baseline. The spatial baseline within a critical value is of particular relevance (Askne *et al.* 2005; Askne & Santoro, 2007) for the selection of appropriate SAR images.

Growing stock volume retrieval or forest biomass estimation by means of SAR interferometric coherence has been discussed in a large number of publications (Luckman *et al.* 2000; Koskinen *et al.* 2001; Askne *et al.* 2003; Eriksson *et al*. 2003; Wagner *et al*. 2003; Tansey *et al.* 2004; Askne & Santoro, 2005). The coherence decreases with increasing biomass. The reason for this relationship is the volume decorrelation which is coupled to biomass (Gaveau 2002; Askne *et al.* 2003; Askne & Santoro, 2005). In addition, high forest biomass promotes temporal decorrelation (Gaveau 2002; Askne *et al.* 2003; Askne & Santoro, 2005) which is mainly caused by the movements of the scatterers. Wind speed is considered the critical parameter determining temporal decorrelation over forest. The relationship between forest biomass and interferometric coherence has already been described by empirical and physically based models (Sarabandi & Lin, 2000; Gaveau 2002; Santoro *et al.* 2002; Askne *et al.* 2003; Pulliainen *et al.* 2003, Wagner *et al.* 2003; Askne & Santoro, 2005, 2007). Under optimal conditions saturation occurs only at a high biomass level (at about 250-300 t/ha) (Koskinen *et al.* 2001; Askne & Santoro, 2005, 2007; Santoro *et al.* 2007b). The saturation level of biomass dropped significantly during rain,

thaw or snow melt conditions. Although saturation typically occurs at lower biomass levels, the saturation level is in general higher compared to the ones for the backscattering intensities (except VHF-SAR). However, saturation of coherence depends on the meteorological conditions during the time of the image acquisition. Similar to the backscattering intensities multi-temporal stack of images and combining the single images improve the retrieval results (Santoro *et al.* 2002; Askne *et al.* 2003; Eriksson *et al.* 2003, Askne & Santoro, 2007). The SAR interferometric coherence is expected to differ on the tree species as the different geometrical structure of crown movement or oscillation induced by the wind. Growing stock volume with high relative stocking are retrieved more accurately than stands with low relative stocking in Siberian boreal forests. One should note that forest stands with higher relative stocking represents a more homogeneous and managed type of forest.

The other approach of SAR interferometry for forest biomass retrieval aims at the generation of digital height models. The respective height is determined by the specific position of the scattering centre of the electromagnetic wave (Balzter *et al.* 2007; Walker *et al.* 2007). Depending on the penetration depth of the EM wave into the vegetation the scattering centre can be located within the upper canopy layer (e.g. at X-band) (Hoekman & Varekamp, 2001; Neeffs *et al.* 2005; Izzawati *et al.* 2006; Balzter *et al.* 2007; Rowland & Balzter, 2007) or close to the forest floor (e.g. at P-band) (Neeffs *et al.* 2005; Balzter *et al.* 2007; Hyde *et al.* 2007). Therefore, in particular at short wave SAR data the vegetation height is incrementally integrated into the digital height model (Kobayashi *et al.* 2000; Izzawati *et al.* 2006). The delineation of the vegetation height could now be easily conducted by subtracting a digital elevation model representing the surface of the terrain (Kobayashi *et al.* 2000; Izzawati *et al.* 2006; Balzter *et al.* 2007; Rowland & Balzter, 2007). If no digital surface model is available, the analysis of the height discontinuity within the digital height model at the edge of a forest can provide an assessment of the forest height at this specific location (Kellndorfer *et al.* 2004; Thiel, 2004; Santoro *et al.* 2005). However, this method only delivers for flat areas with reasonable results.

1.3.3 Polarimetry

Radar polarimetry analyses POLSAR (polarimetric Synthetic Aperture Radar) data including the polarimetric phase. One fully polarimetric dataset comprises both, co- and cross-polarisation defined in an orthogonal polarisation basis. Superior objective of polarimetric data exploration is the analysis of backscattering mechanisms of scattering objects and thus to gain insight into their physical characteristics. Basic data examination techniques analyse polarimetric coherence or polarimetric phase difference. Both parameters allow first implications on the scattering processes (Van Zyl, 1989) and are, therefore, sensitive for forest biomass (Le Toan *et al.* 1992). The single components of the backscattering signal can be decomposed into scattering processes such as surface scattering, volume scattering and double-bounce. A number of decomposition approaches have been already designed (Cloud & Pottier, 1996; Freeman & Durden, 1998; Krogager, 1990; Krogager and Madsen, 1996). Although the SAR data based delineation of forest cover and forest biomass maps is object of many published studies, and polarimetric SAR

datasets are available for many years, polarimetric data exploration techniques have rarely been used for this scientific problem. So far, the effort has been focused on land cover classification (Krogager & Madsen, 1996; Cloud & Pottier 1997; Ito & Omatu 1998; Hellmann 2000; Lee *et al,* 2001) and the delineation of physical land surface parameters such as soil moisture and surface roughness (Schuler *et al*. 2002; Hajnsek *et al*. 2003; Thiel, 2004).

Boerner *et al.* (1987) and Ulaby *et al.* (1987) analysed polarisation phase differences obtained by JPL (Jet Propulsion Laboratory) sensor. It has been shown that corn fields definitely displayed a polarisation phase difference markedly different from that of bare fields. Wang *et al*. (1990) investigated polarisation phase differences and differentiated orchard trees from the bare fields and fields covered with other crops.

In one of the first studies Le Toan *et al.* (1992) applied polarimetric SAR data to maritime pine forest for biomass assessment. However, development of polarimetric data exploration techniques are out of the main consideration, the relationship between biomass and polarimetric phase difference has been described. Based on the reported results, Karam *et al.* (1995) has developed a backscattering model for forest. This model also considers polarimetric phase difference and polarimetric coherence. For both polarimetric variables the modelled and measured values are in good agreement. Nevertheless, the complex model structure results in the unfeasibility of the model's inversion. In addition, one should note that the test site comprised only intensively managed and homogeneous forest stands. In the following studies, for example Balzter *et al.* (2002) has investigated the impact of varying forest biomass on backscattering intensities and polarimetric parameters for a test site in Finland. It is stated that the sensitivity and the saturation level for biomass increase with increasing biomass and are the greatest when cross-polarisations are used. The authors have developed simple regression models, in which polarimetric phase difference and polarimetric coherence are integrated. By the implementation of both polarimetric parameters the accuracy of the delineated forest biomass has been improved significantly. Mougin *et al.* (1999) and Proisy *et al.* (2000) have investigated the capabilities of polarimetric SAR data for the delineation of forest parameters at mangrove forests in French-Guiana. Besides the backscatter intensities they also have employed diverse polarisation ratios. Proisy *et al.* (2000) incorporates both polarimetric phase difference and polarimetric coherence into the investigations. The implementation of multiple SAR frequencies and polarisations permitted the assessment of forest biomass up to 240 t/ha for that specific forest type. In particular, the polarimetric coherence has revealed a distinct sensitivity for forest biomass. Hoekman *et al.* (2002) has derived diverse forest parameters by using a polarimetric classification method. Moreover, the authors developed a specific approach for interpretation of the complex polarimetric coherence across various radar frequencies. Thus, the authors are able to link these specific polarimetric coherence signatures to diverse forest types and biomass classes. Quinones *et al*. (2004) has introduced a LIFEFORM model which covers forest structural differences, terrain roughness, and soil moisture variation to estimate forest biomass up to 340 t/ha in tropical forest. But the model is applied only in homogenous forest with broad-leaved plants.

Natural tropical forests have larger complexity and may feature considerable amounts of other life forms. McNeill *et al.* (2005) systematically explored the capabilities of polarimetric parameters for the delineation of the forest stand age in the largest production forest in New Zealand. As the age of forest stand is considerably correlated with its biomass (as described by well-known allometric scaling laws), it is a strong indicator for this forestry parameter. Besides intensities, polarimetric phase difference and polarimetric coherence, McNeill *et al.* (2005) has considered also polarimetric indices of the Cloud decomposition (Cloude & Pottier, 1996) and further proprietary developed polarimetric parameters. Diverse combinations of these parameters have been correlated with forest stand age by employing a principle component regression approach. It has been found that the use of the polarimetric information significantly minimizes the standard error for the delineated forest stand age. Garestier *et al.* (2009) used an eigenvector decomposition scheme that shows linear correlation between anisotropy and tree height using P-band over pine trees. The other eigenvector parameters alpha and entropy have been saturated very early. Goncalves *et al*. (2011) used airborne L-band SAR data to apply the backscattering coefficient HH polarisation, cross polarised ratio, HH-VV phase difference, HH-VV coherence and the volume scattering component of the Freeman and Durden decomposition method (Freeman & Durden, 1998) in tropical forest. The authors modelled the stem volume using multi-linear regression analysis of these POLSAR attributes based on airborne L-band SAR data. Different trend of correlation between forest growing stock volume and decomposition powers is observed. It has been presented that all the decomposition scattering powers are positively correlated to the forest growing stock volume of tropical forest.

In the most recent publication, Kobayashi *et al.* (2012) applied Yamaguchi's four-component decomposition scheme to ALOS PALSAR L-band data to compare decomposition powers with the forest parameters tree height, tree diameter, and stand volume in tropical forest. The authors have showed that surface and volume scattering are slightly better positively correlated with the forest parameters after the rotation of coherency matrix. The surface scattering is negatively correlated whereas volume scattering is positively correlated with forest parameters. No correlation has been observed between double-bounce and forest parameters.

1.3.4 Polarimetric interferometry

The basic idea of POLINSAR technique is the discrimination between the canopy phase centre and the ground phase centre by using different polarisations and the subsequent estimation of vegetation height by means of the interferometric height. The reference model which combines this idea is called Random Volume over Ground (RVoG) model. Polarimetric interferometry requires at least two polarimetric or multiple single polarisation data sets respectively. The coherence between all scenes must be as high as possible. This precondition demands for an acquisition of all SAR data within a short time span. Moreover, the environmental conditions must be stable for keeping the temporal decorrelation as minor as possible. The technical feasibility of polarimetric SAR interferometry and SAR tomography could already be proven by means of experimental

airborne datasets. However, presently there is no prospective space borne sensor constellation existing providing the required data base for both SAR data exploration techniques. Experimental results using polarimetric ALOS PALSAR data nevertheless proved the potential of the polarimetric interferometry (Papathanassiou *et al.* 2007).

1.4 Scope of the thesis

Currently, there is no operational procedure exists for the derivation of global forest biomass. For optical data and SAR backscatter intensities, generally the sensitivity to biomass is insufficient and the signal is already saturated with too low values. SAR interferometric approaches are less robust due to the dependency on baseline and weather conditions. The space borne implementation of VHF SAR and LIDAR for global measurements is technically not practicable. For complex but operational applicable SAR data examination techniques, such as polarimetric interferometry or SAR tomography, the required sensor constellations do not exist, although with regards to polarimetric interferometry a tandem constellation of two polarimetric L-band satellites (such as ALOS PALSAR I and II) could be easily realised from the technical point of view. The potentiality of radar polarimetry for forestry applications has been rarely investigated so far. However, several studies (Le Toan *et al*. 1992; Krogager, 1990; Cloud & Pottier, 1996; Krogager & Madsen, 1996; Durden *et al.* 1989; Freeman & Durden, 1998; Proisy *et al*. 2000; Balzter *et al.* 2002; Hoekman & Quiñones, 2002; McNeill & Pairman, 2005; Thiel *et al.* 2007; Kobayashi *et al.* 2012) have discovered some potential of SAR polarimetry technique. The studies have no conclusions about the sensitivity, saturation level and robustness of the polarimetric parameters. Such investigations are still pending. So far, however, lack of depth investigations that are related to the forest biomass and polarisation phase difference has been found. There are only initial results for a few test areas. By sensitivity, saturation level, or robustness of the polarimetric phase difference and also polarimetric coherence as regards the disposal of forest biomass so far there is no knowledge. The previous studies had other priorities.

During almost past 15 years much effort has been made in regard to the forestry applications using POLINSAR (Polarimetric Interferometry SAR) technique (Israelsson *et al.* 1997; Cloude & Papathanassiou *et al.* 2003; Parks *et al.* 2007; Neumann *et al.* 2012). However, in this study we solely concentrate on the polarimetric information. Rationale is the absence of an adequate global POLINSAR dataset (L- or P-band, single pass), while polarimetric ALOS PALSAR L-band data exist for a high percentage of the globe.

The scope of this thesis is to find the answer of these two questions:

- **Can polarimetric parameters effectively extend the SAR data base for the retrieval of forest growing stock volume?**

- **Can the saturation level of estimating forest growing stock volume improve by means of polarimetric information?**

To answer these questions the following tasks are formulated

- Analysis of the variations of polarimetric parameters due to
    - Weather conditions
    - Forest stand structures
    - Different tree species

The importance is put only on growing stock volume because (a) it is the most valuable parameter in Russian forest inventories and for planning forest enterprise operations; and (b) compared to other parameters collected by the Russian forest inventory, growing stock volume appears to be the one most directly related to the radar parameters (Wagner *et al.* 2003).

1.5 Outline of the thesis

The work of this thesis is comprised of seven chapters as follows:

Chapter 1 discusses the state of the art and the objective of the thesis. The state of the art summarises the potentiality of remote sensing techniques, to make a scientific contribution to the operational detection of global forest biomass. The focus of the discussion is on the radar remote sensing and especially on the radar polarimetry for forest biomass assessment.

Chapter 2 presents the basic concepts for understanding polarimetric measurements and the polarimetric parameters which will be used for the investigations.

Chapter 3 addresses the brief description of the investigated areas and the data which will be used for the analysis. Processing of SAR data and forest inventory data will also be presented.

Chapter 4 presents the detail analysis of the behaviour of polarimetric parameters in Siberian forests special focus on forest growing stock volume. The analysis considers the impact of weather conditions, topography of the areas, forest stand structures and the impact of tree species on polarimetric parameters.

Chapter 5 describes the model selection, model training and accuracy assessment of the estimation of growing stock volume.

Chapter 6 addresses the summary of the major findings of this research work and future lines of studies outlined. In the outlook, topics that need further investigation are discussed and some promising new techniques and future mission are mentioned.

Chapter 7 lists the publications of journals, conference proceedings and books which are referred in this thesis.

Chapter 2

Radar Polarimetry

The objective of this chapter is to provide the reader with basic concepts for understanding polarimetric measurements and scattering process in random media. It is important in polarimetry to have knowledge on electromagnetic waves and the scattering matrices. The mathematics is necessary to present these concepts. The polarimetric electromagnetic waves, the monochromatic wave represented by a Jones vector and Stokes vector and quasi monochromatic wave or partially polarised wave which varies in time will be described in Section 2.1. All combination of polarisation states will be also presented in section 2.1. Polarimetric scattering matrix which leads to the coherence and covariance matrices for the data representation of distributed targets will be derived in section 2.3 and 2.4. Section 2.5 concerns the transformation caused by rotating the scattering object or the antenna used for transmission and reception about the Line-of-sight (LOS). Polarimetric target decomposition in particular, Yamaguchi four-component decomposition for separating radar measurements into basic scattering mechanisms will be described in section 2.6. Polarimetric parameters used for the investigations in this thesis will be presented in section 2.7.

2.1 Polarimetry

Radar polarimetry (Polar: polarisation Metry: measure) is the science of acquiring, processing and analysing the polarisation state of an electromagnetic field (Lee & Pottier, 2006). Radar polarimetry deals with the full vector nature of polarised electromagnetic waves. When the wave passes through a medium strikes an object, it is reflected; then, characteristic information about its geometrical structure such as reflectivity, shape and orientation and its geophysical properties can be obtained. The following sections provide mathematical formulations to describe the polarimetry.

2.1.1 Wave polarimetry

The fundamental relations of radar polarimetry are obtained directly from Maxwell's equations (Stratton, 1941). It is found in Maxwell's equations that an electromagnetic field is a travelling wave with an electric field vector and magnetic field vector orthogonal to

each other and of constant amplitude on a plane orthogonal to the direction of propagation. The electric field vector of such a wave $\overrightarrow{E}(\vec{r},t)$ propagating into the direction of $\vec{k}$ at a given location, defined by the position vector $\vec{r}$ and a given time *t,* can be expressed as (Boerner & El-Arini, 1981):

$$\overrightarrow{E}(\vec{r},t) = \overrightarrow{E}(\vec{r})\cos(\omega t) \tag{2.1}$$

where $\overrightarrow{E}(\vec{r})$ is the real amplitude of the electric vector and ω is the angular frequency of the travelling wave. The complex representation of electric field vector is given by

$$\overrightarrow{E}(\vec{r}) = \overrightarrow{E}e^{(i\vec{k}\vec{r})} \tag{2.2}$$

$\overrightarrow{E}$ is the constant amplitude of the electric field. The complex amplitude vector can be decomposed into two orthogonal complex components E_h and E_v, as shown in Equation 2.2:

$$\overrightarrow{E} = E_h\overrightarrow{h} + E_v\vec{v} \tag{2.3}$$

The complex electric field vector varies in time with single angular frequency. The electromagnetic wave, which describes the orientation (horizontal and vertical polarisations) of the electric field vector and moves in the direction of perpendicular to the propagation in time along an ellipse is called monochromatic wave. This ellipse is known as polarisation ellipse. The monochromatic wave has potentially of four degrees of freedom. Two of them are needed to describe the polarisation state of the wave and others are the wave amplitude, A_0 and absolute phase reference, φ_o.

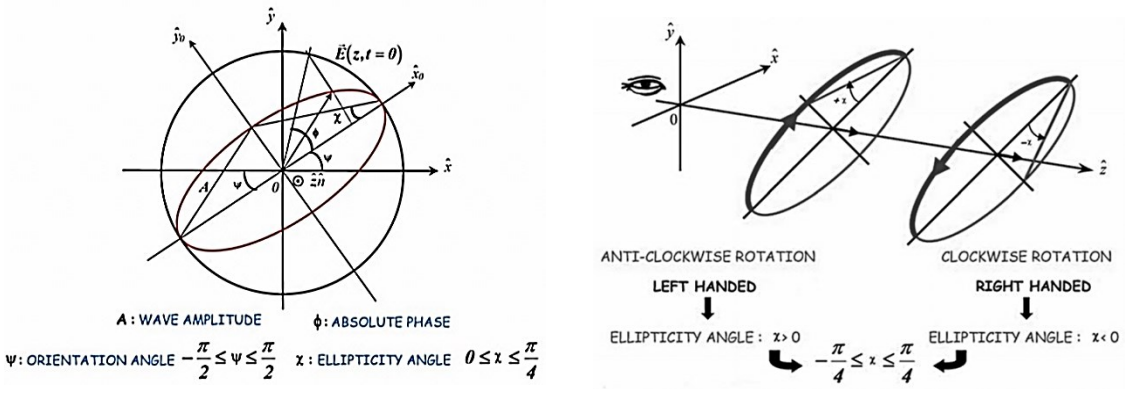

(a) (b)

Figure 2.1 (a) Polarisation ellipse. (b) Left hand and right elliptical polarisations (Lee & Pottier, 2006).

The shape of the polarisation ellipse is defined by the polarisation state. It can be described completely in terms of two angles, orientation angle ψ, and the ellipticity angle χ. The horizontal and vertical polarisations are physically realized by changing the antenna effective length, and the normalized antenna effective length is called the polarisation state.

The polarisation ellipse shape is characterised by using four parameters as shown in Figure 2.1(a). The orientation angle, ψ, varies between -90° and +90° and the ellipticity angle, χ, spans between -45° and 45°. At $\chi = 0°$ the ellipse becomes linear state and in this case $\psi = 0°$ defines horizontally polarised waves, while $\psi = 45°$ presents vertically polarised waves. The ellipse becomes circular if $\chi = \pm 45°$ and refers circular polarisation state. The positive or negative sign of the ellipticity angles defines the sense of the rotation of electric field *E,* vector. Figure 2.1(b) illustrates the rotation sense of rotation of *E* vector. If $\chi > 0°$, the rotation is left-handed, otherwise, for $\chi < 0°$, the rotation is right-handed (IPU system convention). A canonical polarisation states are listed in Table 2.1.

	Horizontal (H)	Vertical (V)	Liner +45°	Liner -45°	Left circular	Right circular
Jones vector	$\begin{bmatrix}1\\0\end{bmatrix}$	$\begin{bmatrix}0\\1\end{bmatrix}$	$\frac{1}{\sqrt{2}}\begin{bmatrix}1\\1\end{bmatrix}$	$\frac{1}{\sqrt{2}}\begin{bmatrix}-1\\1\end{bmatrix}$	$\frac{1}{\sqrt{2}}\begin{bmatrix}1\\j\end{bmatrix}$	$\frac{1}{\sqrt{2}}\begin{bmatrix}1\\-j\end{bmatrix}$
Stokes vector	$\begin{bmatrix}1\\1\\0\\0\end{bmatrix}$	$\begin{bmatrix}1\\-1\\0\\0\end{bmatrix}$	$\begin{bmatrix}1\\0\\1\\0\end{bmatrix}$	$\begin{bmatrix}1\\0\\-1\\0\end{bmatrix}$	$\begin{bmatrix}1\\0\\0\\1\end{bmatrix}$	$\begin{bmatrix}1\\0\\0\\-1\end{bmatrix}$
Orientation angle (ψ)	0°	±90°	45°	-45°	-90° to 90°	-90° to 90°
Ellipticity angle (χ)	0°	0°	0°	0°	45°	-45°

Table 2.1 Representation of canonical polarisation states.

2.1.2 The Jones vector and Stokes vector

The polarisation state can be derived from the Jones vector. The Jones vector is expressed by the orientation angle ψ, ellipticity angle χ, the amplitude of the wave A_0 and the initial phase φ_0 as shown in Equation 2.4 (Huynen, 1970; Kostinski & Boerner, 1986):

$$\vec{E} = \begin{bmatrix}E_x\\E_y\end{bmatrix} \tag{2.4}$$

$$\vec{E} = A_0 e^{-i\varphi_0}\begin{bmatrix}\cos\psi & -\sin\psi\\ \sin\psi & \cos\psi\end{bmatrix}\begin{bmatrix}\cos\chi\\ -i\sin\chi\end{bmatrix} \tag{2.5}$$

The parameters of Equation 2.5 can be defined as:

$$A = \sqrt{E_x^2 + E_y^2} \tag{2.6}$$

$$\sin 2\chi = \frac{2E_x^2 E_y^2}{E_x^2 + E_y^2}\sin\delta \tag{2.7}$$

$$\tan 2\psi = \frac{2E_x^2 E_y^2}{E_x^2 - E_y^2}\cos\delta \tag{2.8}$$

where $\delta = \delta_y - \delta_x$ with $0 < \delta < 2\pi$ is the relative phase between x and y electric field components. An alternative way of representing polarisation information is second order statistics of Stokes vector which can be expressed as (Stokes, 1852; Huynen, 1970; Huynen, 1990):

$$\vec{S} = \begin{bmatrix} s_0 \\ s_1 \\ s_2 \\ s_3 \end{bmatrix} = \begin{bmatrix} |E_x|^2 + |E_y|^2 \\ |E_x|^2 - |E_y|^2 \\ 2Re\{E_x E_y^*\} \\ -2Im\{E_x E_y^*\} \end{bmatrix} \tag{2.9}$$

The first term, s_o, of the Stokes vector is proportional to the power density of the wave, s_1 is the difference between the densities powerrelated to the horizontal and vertical polarisations. Parameters s_2 and s_3 are related to the phase difference between the h and v components of the electric field. The Stokes vector is expressed also by the three parameters of the Jones vector (Huynen, 1970; Huynen, 1990):

$$\vec{S} = \begin{bmatrix} s_0 \\ s_1 \\ s_2 \\ s_3 \end{bmatrix} = \begin{bmatrix} A^2 \\ A^2\cos(2\psi)\cos(2\chi) \\ A^2\sin(2\psi)\cos(2\chi) \\ A^2\sin(2\chi) \end{bmatrix} \tag{2.10}$$

The Stokes parameter s_0 is always equal to the total power (density) of the wave which can be expressed as:

$$s_0^2 = s_1^2 + s_2^2 + s_3^2 \tag{2.11}$$

s_1 is equal to the power in the linear horizontal or vertical polarised components; s_2 is equal to the power in the linearly polarised components at tilt angles ψ = 45° or 135°; and s_3 is equal to the power in the left-handed and right-handed circular polarised component in the plane wave. If any of the parameters $\{s_0, s_1, s_2, s_3\}$ has a nonzero value, it indicates the presence of a polarised component in the plane wave. The electromagnetic wave can be fully polarised, partially polarised or completely unpolarised.

2.2 Partially polarised waves

Until now completely polarised monochromatic waves are discussed. The amplitude and phase of the electric field of the polarised wave are independent of time and space. In natural media cause random scattering which produces partially polarised waves. In contrast to the completely polarised waves, the amplitude, phase and polarisation of electric field of the partially polarised waves are varying in time and space. Because of this, polarisation can be defined only of statistical average over time. The wave coherency matrix is defined by the Jones vector averaged over coherency time as (Huynen, 1970; Lüneburg, 1995):

$$[J] = \langle \vec{E}.\vec{E}^{*} \rangle = \begin{bmatrix} \langle |E_x|^2 \rangle & \langle |E_x E_y^{*}| \rangle \\ \langle |E_y E_x^{*}| \rangle & \langle |E_y|^2 \rangle \end{bmatrix} \tag{2.12}$$

Where <> denotes the ensemble averaging. The matrix *J* is hermitian positive semi definite which have real, non-negative eigenvalues and orthogonal eigenvectors. The diagonal elements of the matrix resemble to the intensities of the wave and the trace of *J* is equal to the total intensities of the wave. The off diagonal elements corresponds to the cross correlation between the elements of the Jones vector.

2.2.1 Degree of polarisation

If the electromagnetic wave is partially polarised, it can be expressed as the sum of a completely polarised wave and a completely unpolarised or noise-like wave. The degree of polarisation p, of the wave is defined as the power density of the polarised part of the wave divided by the total power density (Lee & Pottier, 2006).

$$p = \frac{\sqrt{s_1^2 + s_2^2 + s_3^2}}{s_0} \tag{2.13}$$

where $s_0^2 > s_1^2 + s_2^2 + s_3^2$. If $p = 1$, the wave is polarised: $s_0^2 = s_1^2 + s_2^2 + s_3^2$ and if p =0, the wave is unpolarised: $s_1^2 + s_2^2 + s_3^2 = 0$. For partially polarised waves, not all the density powers are contained in the polarised components and therefore the total intensity of the wave is greater than the polarised components.

2.3 Scattering matrix

If a fully polarised monochromatic plane wave $\vec{E}^{i}$ is radiated by the transmitted antenna with a defined polarisation state (horizontal or vertical polarisations) propagates in direction of $\vec{k}_i$ towards the target, the transmitted wave can be written as:

$$\overrightarrow{E^{i}} = {E_h}^{i}\vec{h}_i + {E_v}^{i}\vec{v}_i \tag{2.14}$$

The right-handed orthogonal coordinate $(\overrightarrow{h_i}, \overrightarrow{v_i}, \overrightarrow{k_i})$ system is used for the transmitting antenna. The transmitted wave is scattered by the target and change its polarisation or degree of polarisation. Consider the right-handed orthogonal coordinate system $(\overrightarrow{h_s}, \overrightarrow{v_s}, \overrightarrow{k_s})$, the receiving antenna located in the direction of $\vec{k}_s$ receives the scattered wave $\vec{E}^{s}$ is expressed as:

$$\overrightarrow{E^{s}} = {E_h}^{s}\vec{h}_s + {E_v}^{s}\vec{v}_s \tag{2.15}$$

Two conventions are used to define the scattered wave coordinate $(\overrightarrow{h_s}, \overrightarrow{v_s}, \overrightarrow{k_s})$ system with respect to transmitted wave coordinate $(\overrightarrow{h_i}, \overrightarrow{v_i}, \overrightarrow{k_i})$ system. One is known as the Forward Scattering Alignment (FSA) convention and mainly used for the bi-static scattering problems. Another one is known as the Back-Scattering Alignment (BSA) convention is used for the radar backscattering problems (Lee & Pottier, 2006).

The antenna of the radar is configured in such a way that the system first transmitting a horizontally (H) polarised wave and receiving the horizontally and vertically (V) polarised backscatter wave simultaneously and then transmitting a vertically polarised wave and receiving the horizontally and vertically polarised backscatter wave simultaneously. Under this antenna configuration a complex scattering matrix [*S*], called the Sinclair matrix (Henderson & Lewis, 1998), can be defined as follows:

$$[S] = \begin{bmatrix} S_{HH} & S_{HV} \\ S_{VH} & S_{HH} \end{bmatrix} \tag{2.16}$$

The scattering process can be regarded as a transformation of the incident wave into the scattered wave backscattered by the target. This transformation can be represented by (Henderson & Lewis, 1998):

$$\vec{E}^s = \frac{e^{jkr}}{r} \begin{bmatrix} S_{HH} & S_{HV} \\ S_{VH} & S_{HH} \end{bmatrix} \begin{bmatrix} E_h^i \\ E_v^i \end{bmatrix} \tag{2.17}$$

The 2×2 complex matrix of Equation 2.17 is the radar scattering matrix. r is the distance between antenna and the target. The term e^{jkr}/r denotes the wave attenuation occurs during the travel time from antenna to the target. The four elements of the scattering matrix S_{IJ} (*I, J = H or V*) are knows as the complex scattering amplitudes:

$$\begin{aligned} S_{HH} &= c.e^{-i\varphi_{HH}}\sqrt{\sigma_{HH}^0} \\ S_{HV} &= c.e^{-i\varphi_{HV}}\sqrt{\sigma_{HV}^0} \\ S_{VH} &= c.e^{-i\varphi_{VH}}\sqrt{\sigma_{VH}^0} \\ S_{VV} &= c.e^{-i\varphi_{VV}}\sqrt{\sigma_{VV}^0} \end{aligned} \tag{2.18}$$

where c is the calibration factor. The total power of the scattered by the scatterer can be defined as:

$$TP = |S_{HH}|^2 + |S_{HV}|^2 + |S_{VH}|^2 + |S_{VV}|^2 \tag{2.19}$$

Once the Sinclair matrix is measured for a given transmit or receive configuration, it can be transformed into the basis of any desired polarisation state. This is called polarisation basis transformation (Lüneburg, 1995). The basis transformation of the scattering matrix $[S]_{HV}$ from $\{\overrightarrow{\varepsilon_H}, \overrightarrow{\varepsilon_V}\}$ basis to the desired scattering matrix of $[S]_{IJ}$ into $\{\overrightarrow{\varepsilon_I}, \overrightarrow{\varepsilon_J}\}$ polarisation basis can be defined as:

$$[S]_{IJ} = [U_2][S]_{HV}[U_2]^T \tag{2.20}$$

where $U_2(\psi,\chi) = \begin{bmatrix} \cos\chi & -j\sin\chi \\ -j\sin\chi & \cos\chi \end{bmatrix}\begin{bmatrix} \cos\psi & \sin\psi \\ -\sin\psi & \cos\psi \end{bmatrix}$ is a 2×2 unitary matrix. ψ and χ are the orientation angle and ellipticity angle respectively.

The $[S]_{IJ}$ is changed here to other orthonormal polarisation basis. This can be done only for polarimetric radar systems over conventional radar operating with single or dual polarisation mode. One of the most frequent examples, the transformation of Sinclair matrix from the linear polarisation $\{\overrightarrow{\varepsilon_H}, \overrightarrow{\varepsilon_V}\}$ basis into the circular polarisation $\{\overrightarrow{\varepsilon_L}, \overrightarrow{\varepsilon_R}\}$ basis which can be expressed as (Lee & Pottier, 2006; Henderson & Lewis, 1998):

$$\begin{bmatrix} S_{RR} & S_{LR} \\ S_{RL} & S_{LL} \end{bmatrix} = \begin{bmatrix} 1 & j \\ j & 1 \end{bmatrix}\begin{bmatrix} S_{HH} & S_{HV} \\ S_{VH} & S_{HH} \end{bmatrix}\begin{bmatrix} 1 & j \\ j & 1 \end{bmatrix} \tag{2.21}$$

where L and R denote the left and right oriented circular polarisation. S_{XX} is defined as the cross polarisation (S_{HV} or S_{VH}). The elements of the left-/right-handed circular polarisation basis can be measured as:

$$\begin{aligned} S_{LL} &= \frac{1}{2}[S_{HH} + 2jS_{XX} - S_{VV}] \\ S_{LR} &= \frac{1}{2}[j(S_{HH} + S_{VV}] \\ S_{RR} &= \frac{1}{2}[-S_{HH} + 2jS_{XX} + S_{VV}] \end{aligned} \tag{2.22}$$

The scattering matrix $[S]$ can be vectored by transforming it into a four-dimensional complex vector $\overrightarrow{k_4}$ in order to understand the scattering behaviour of the target (Cloude, 1986; Ziegler *et al.* 1992; Lüneburg, 1995; Lüneburg, 1996).

$$\overrightarrow{k_4} = \frac{1}{2}Trace([S]\psi) = [k_0, k_1, k_2, k_3]^T \tag{2.23}$$

where *trace*($[S]$) is the sum of the diagonal elements of $[S]$ and ψ is 2×2 complex basis matrices under a hermitian inner product. T is the transpose operator. There are two options for choosing the structure of ψ from ψ_L or ψ_P. The first one ψ_L is known as the Lexicographic basis, which corresponds (Cloude, 1986; Cloude & Pottier, 1996):

$$\psi_L = \left\{2\begin{bmatrix} 1 & 0 \\ 0 & 0 \end{bmatrix}, 2\begin{bmatrix} 0 & 1 \\ 0 & 0 \end{bmatrix}, 2\begin{bmatrix} 0 & 0 \\ 1 & 0 \end{bmatrix}, 2\begin{bmatrix} 0 & 0 \\ 0 & 1 \end{bmatrix}\right\} \tag{2.24}$$

Applying ψ_L into Equation 2.24, the corresponding Lexicographic scattering vector is

$$\overrightarrow{k_L} = [S_{HH}, S_{HV}, S_{VH}, S_{VV}]^T \tag{2.25}$$

The second one ψ_P is defined as the Pauli spin matrices as (Cloude & Pottier, 1997):

$$\psi_P = \left\{\sqrt{2}\begin{bmatrix} 1 & 0 \\ 0 & 1 \end{bmatrix}, \sqrt{2}\begin{bmatrix} 1 & 0 \\ 0 & -1 \end{bmatrix}, \sqrt{2}\begin{bmatrix} 0 & 1 \\ 1 & 0 \end{bmatrix}, \sqrt{2}\begin{bmatrix} 0 & -j \\ j & 1 \end{bmatrix}\right\} \tag{2.26}$$

The complex vector corresponding to Pauli basis is:

$$\overrightarrow{k_P} = \frac{1}{\sqrt{2}}[S_{HH} + S_{VV}, S_{HH} - S_{VV}, S_{HV} + S_{VH}, j(S_{HV} - S_{VH})]^T \tag{2.27}$$

The norm of the scattering vector $\vec{k}$ is equal to the total scattered power, as shown in Equation 2.28:

$$\begin{aligned} \left|\vec{k}\right|^2 &= \overrightarrow{k_P} * \overrightarrow{k_P}^T = \overrightarrow{k_L} * \overrightarrow{k_L}^T \\ &= (|S_{HH}|^2 + |S_{HV}|^2 + |S_{VH}|^2 + |S_{VV}|^2) \end{aligned} \tag{2.28}$$

where $\overrightarrow{k_L} = \left[S_{HH}, \sqrt{2}S_{HV}, S_{VV}\right]^T$ and $\overrightarrow{k_P} = \frac{1}{\sqrt{2}}[S_{HH} + S_{VV}, S_{HH} - S_{VV}, 2S_{HV})]^T$

2.4 Non-deterministic scatterers

For geoscience or remote sensing application the scatterer are affected by spatial and time variations. Therefore, the assumption of pure deterministic is not valid. A resolution cell in the SAR image is bigger than the wavelength of the radar and the cell is composed by many distributed deterministic scatterers. Each of the scatterer is represented by an individual Sinclair matrix, $[S]_i$. Therefore, the matrix $[S]$ is formed by the coherent addition of the individual $[S]_i$ matrices for all the distributed scatterers within a resolution cell. To deal with the analysis of non-deterministic scatterers the concept of a scatterer covariance matrix or coherency matrix are introduced. The covariance matrix $[C]$ is formed by the outer product $\langle \overrightarrow{k_L}.\overrightarrow{k_L}^+ \rangle$ of the Lexicographic scattering vector $\langle \overrightarrow{k_L} \rangle$ with its conjugate transpose vector $\langle \overrightarrow{k_L}^+ \rangle$ (Lüneburg, 1995; Lüneburg, 1996).

$$[C] = \langle \overrightarrow{k_L}.\overrightarrow{k_L}^+ \rangle = \begin{bmatrix} \langle |S_{HH}|^2 \rangle & \sqrt{2}\langle S_{HH}S_{HV}^* \rangle & \langle S_{HH}S_{VV}^* \rangle \\ \sqrt{2}\langle S_{HV}S_{HH}^* \rangle & \langle |S_{HV}|^2 \rangle & \sqrt{2}\langle S_{HV}S_{VV}^* \rangle \\ \langle S_{VV}S_{HHVV}^* \rangle & \sqrt{2}\langle S_{VV}S_{HV}^* \rangle & \langle |S_{VV}|^2 \rangle \end{bmatrix} \tag{2.29}$$

where $\langle\rangle$ represents ensemble averaging assuming that the spatial scattering medium to be averaged is homogenous. The diagonal elements correspond to the backscattered intensities. The off diagonal elements represent the complex covariance of the respective polarisation configurations. Similar way, the coherency matrix $[T]$ is defined by the other product $\langle \overrightarrow{k_P}.\overrightarrow{k_P}^+ \rangle$ of Pauli scattering vector (Lüneburg, 1995; Lüneburg, 1996):

$$[T] = \langle \overrightarrow{k_P}.\overrightarrow{k_P}^+ \rangle$$

$$= \begin{bmatrix} \langle |S_{HH} + S_{VV}|^2 \rangle & \langle (S_{HH} + S_{VV})(S_{HH} - S_{VV})^* \rangle & 2\langle (S_{HH} + S_{VV}){S_{HV}}^* \rangle \\ \langle (S_{HH} - S_{VV})(S_{HH} + S_{VV})^* \rangle & \langle |S_{HH} - S_{VV}|^2 \rangle & \sqrt{2}\langle S_{HV}S_{VV}^* \rangle \\ 2\langle S_{HV}(S_{HH} + S_{VV})^* \rangle & 2\langle S_{HV}(S_{HH} - S_{VV})^* \rangle & 4\langle |S_{HV}|^2 \rangle \end{bmatrix} \tag{2.30}$$

$[C]$ and $[T]$ matrices are by definition hermitian positive semi definite and have the real non-negative eigenvalues but different eigenvectors. Both matrices have rank 3 and contain

the same information. Without ensemble averaging both matrices have rank 1 and characterise a deterministic scattering process. The sum of the diagonal elements (the trace) for both matrices is same and represents the total power of the scattered wave if the incident wave has unit power.

One has to keep in mind that coherency or covariance matrix data have reduced resolution because of the spatial averaging needed for the formation of $[T]$ or $[C]$ matrix. The resolution loss can be critical for point targets but not for the distributed scatterers such as forest areas.

2.5 Line of sight rotation

The following section concerns the transformation caused by the rotating the scattering object or the antenna used for transmission and reception about the line-of-sight (LOS). The LOS is defined as the line which connects the antenna phase centre with the scatterer.

2.5.1 Rotation of the scattering matrix

The scattering matrix data set of the imaging pixel area is defined as:

$$[S] = \begin{bmatrix} S_{HH} & S_{HV} \\ S_{VH} & S_{HH} \end{bmatrix} \tag{2.31}$$

If the scattering matrix $[S]$ is rotated along line of sight (LOS) by an angle θ, the rotated scattering matrix $[S(\theta)]$ can be defined as (Huynen, 1970; Cloude & Pottier, 1996):

$$[S(\theta)] = [R_2(\theta)][S][R_2(\theta)]^{-1} \tag{2.32}$$

where $[R_2(\theta)]$ is a unitary rotation matrix given by

$$[R_2(\theta)] = \begin{bmatrix} \cos\theta & \sin\theta \\ -\sin\theta & \cos\theta \end{bmatrix} \tag{2.33}$$

Then, the scattering matrix is rotated by an angle θ along the line of sight of the radar leads to:

$$[S(\theta)] = \begin{bmatrix} S_{HH}(\theta) & S_{HV}(\theta) \\ S_{VH}(\theta) & S_{HH}(\theta) \end{bmatrix}$$

$$= \begin{bmatrix} \cos\theta & \sin\theta \\ -\sin\theta & \cos\theta \end{bmatrix} \begin{bmatrix} S_{HH} & S_{HV} \\ S_{VH} & S_{HH} \end{bmatrix} \begin{bmatrix} \cos\theta & -\sin\theta \\ \sin\theta & \cos\theta \end{bmatrix} \tag{2.34}$$

The elements of the $[S(\theta)]$ can be obtained as:

$$S_{HH}(\theta) = S_{HH}\cos^2(\theta) + S_{HV}\cos\theta\sin\theta + S_{VH}\cos\theta\sin\theta + S_{VV}\sin^2(\theta)$$

$$S_{HV}(\theta) = -S_{HH}\cos\theta\sin\theta + S_{HV}\cos^2(\theta) - S_{VH}\sin^2(\theta) + S_{VV}\cos\theta\sin\theta$$

$$S_{VH}(\theta) = -S_{HH}\cos\theta\sin\theta - S_{HV}\cos^2(\theta) + S_{VH}\sin^2(\theta) + S_{VV}\cos\theta\sin\theta$$

$$S_{VV}(\theta) = S_{HH}\sin^2(\theta) - S_{HV}\cos\theta\sin\theta - S_{VH}\cos\theta\sin\theta + S_{VV}\cos^2(\theta) \quad (2.35)$$

For the case of backscattering from reciprocal media $S_{HV} = S_{VH}$ and $S_{HV}(\theta) = S_{VH}(\theta)$ the Equation 2.35 becomes:

$$S_{HH}(\theta) = S_{HH}\cos^2(\theta) + S_{XX}\cos\theta\sin\theta + S_{VV}\sin^2(\theta)$$

$$S_{XX}(\theta) = -S_{HH}\cos\theta\sin\theta + S_{XX}(\cos^2(\theta) + \sin^2(\theta)) + S_{VV}\cos\theta\sin\theta$$

$$S_{VV}(\theta) = S_{HH}\sin^2(\theta) - S_{XX}\cos\theta\sin\theta + S_{VV}\cos^2(\theta) \quad (2.36)$$

2.5.2 Rotation of the coherency matrix

The rotation by an angle θ Pauli scattering vector along the LOS leads to:

$$\vec{k}_p(\theta) = \begin{bmatrix} S_{HH}(\theta) + S_{VV}(\theta) \\ S_{HH}(\theta) - S_{VV}(\theta) \\ 2S_{XX}(\theta) \end{bmatrix}$$

$$= \begin{bmatrix} S_{HH} + S_{VV} \\ (S_{HH} - S_{VV})\cos 2\theta - 2S_{XX}\sin 2\theta \\ (S_{HH} - S_{VV})\sin 2\theta + 2S_{XX}\cos 2\theta \end{bmatrix}$$

$$= \begin{bmatrix} 1 & 0 & 0 \\ 0 & \cos 2\theta & \sin 2\theta \\ 0 & -\sin 2\theta & \cos 2\theta \end{bmatrix} \begin{bmatrix} S_{HH} + S_{VV} \\ (S_{HH} - S_{VV}) \\ 2S_{XX} \end{bmatrix}$$

$$\vec{k}_p(\theta) = [R_3(\theta)]\vec{k}_p \quad (2.37)$$

where $[R_{3p}(\theta)] = \begin{bmatrix} 1 & 0 & 0 \\ 0 & \cos 2\theta & \sin 2\theta \\ 0 & -\sin 2\theta & \cos 2\theta \end{bmatrix}$. The LOS rotation of θ angle for the coherency matrix $[T]$ can be written using Equation 2.37:

$$[T(\theta)] = \langle \vec{k}_p(\theta).\vec{k}_p(\theta)^* \rangle$$
$$= \left[R_{3p}(\theta)\right] \langle \overrightarrow{k_P}.\overrightarrow{k_P}^* \rangle \left[R_{3p}(\theta)\right]^{-1}$$
$$= \left[R_{3p}(\theta)\right][T]\left[R_{3p}(\theta)\right]^{-1} \quad (2.38)$$

2.6 Polarimetric target decomposition

In radar remote sensing application, targets of interest require a multivariate statistical description due to combination of coherent speckle noise and random vector scattering effects from surface and volume. For classification purpose or inversion of scattering data it is necessary to identify the average or dominant scattering mechanism from the targets. This averaging process indicates the concept of the distributed target. The main aim of the target decomposition is to decompose the coherency matrix or covariance matrix into a sum of independent matrices which represent independent scatterers associated with different physical scattering mechanisms such as surface scattering, double-bounce and volume scattering.

The target decomposition is divided into two parts. The first one is coherent decomposition (Cameron, 1990; Krogager, 1990; Touzi *et al.* 2002) which is appropriate if only if one or two dominant scattering mechanisms are expected. This cannot be the case for most natural targets. In addition, coherent averaging is affected by the speckle noise.

The second one is incoherent decomposition which provides a statistically smoother description of the behaviour of the scatterers. The incoherent decomposition is divided into Huynen based (Huynen, 1970), eigenvector based (Cloude, 1986; Cloude & Pottier, 1996) and model based decomposition (Freeman & Durden, 1998; Yamaguchi, 2005) methods.

2.6.1 Eigenvector based decomposition

The eigenvector based decomposition is based on the eigenvector analysis of the coherency matrix. Since coherency matrix $[T]$ is a hermitian, positive, semi-definite matrix, it can always be diagonalised using unitary similarity transformations. The coherency matrix is defined as (Cloude & Pottier, 1996):

$$[T] = [U_3][\Lambda\Lambda][U_3]^{-1} = [U_3]\begin{bmatrix}\lambda_1 & 0 & 0\\ 0 & \lambda_2 & 0\\ 0 & 0 & \lambda_3\end{bmatrix}[U_3]^{-1} \quad (2.39)$$

where

$$U_3 = [\overrightarrow{e_1}\overrightarrow{e_2}\overrightarrow{e_3}] = \begin{bmatrix}\cos\alpha_1 & \cos\alpha_2 & \cos\alpha_3\\ \sin\alpha_1\cos\beta_1 e^{i\delta_1} & \sin\alpha_2\cos\beta_2 e^{i\delta_2} & \sin\alpha_3\cos\beta_3 e^{i\delta_3}\\ \sin\alpha_1\cos\beta_1 e^{i\gamma_1} & \sin\alpha_2\cos\beta_2 e^{i\gamma_2} & \sin\alpha_3\cos\beta_3 e^{i\gamma_3}\end{bmatrix} \quad (2.40)$$

and where $[\Lambda\Lambda]$ is the diagonal eigenvalue matrix of $[T]$. $\lambda_1 \geq \lambda_2 \geq \lambda_3 \geq 0$ are real eigenvalues and $[U_3]$ is a unitary matrix whose column corresponds to orthonormal eigenvectors $\overrightarrow{e_1}, \overrightarrow{e_2}, \overrightarrow{e_3}$ of $[T]$. Hence, the coherency matrix can be expressed as:

$$T = \lambda_1\left(\overrightarrow{e_1}\overrightarrow{e_1}^{+}\right) + \lambda_2\left(\overrightarrow{e_2}\overrightarrow{e_2}^{+}\right) + \lambda_3\left(\overrightarrow{e_3}\overrightarrow{e_3}^{+}\right) \tag{2.41}$$

The eigenvalues and eigenvectors are considered as the primary parameters of the eigen decomposition of $[T]$. The sum of the three eigenvalues expresses the total power TP received form the scatter:

$$TP = \lambda_1 + \lambda_2 + \lambda_3 \tag{2.42}$$

In order to simplify the analysis of the physical information provided by this eigen decomposition, three secondary parameters are defined as a function of eigenvalues and the eigenvectors of $[T]$. These are as follow:

(i) Scattering Entropy, *H*:

The degree of randomness of target scattering is represented by *H*. The polarimetric scattering entropy, *H*, is defined by the logarithmic sum of the eigenvalues of $[T]$ (Cloude & Pottier, 1996).

$$H = \sum_{i=1}^{3} -P_i \log_3 P_i \tag{2.43}$$

where P_i is the probability of the eigenvalue λ_i , represents the relative importance of this eigenvalue respective to the total scattered power:

$$P_i = \frac{\lambda_i}{\sum_{j=1}^{3} \lambda_j} = \frac{\lambda_i}{\lambda_1 + \lambda_2 + \lambda_3} \tag{2.44}$$

The entropy ranges from 0 to 1. It can be interpreted as the number of effective scattering processing occurs. An entropy of $H = 0$ indicates that $[T]$ has one nonzero eigenvalue i.e. $\lambda_2 = \lambda_3 = 0$ and represents one deterministic scattering process while an entropy $H = 1$ means that all eigenvalues are equal i.e. $\lambda_1 = \lambda_2 = \lambda_3$. This indicates that the target depolarizes all the incident waves.

(ii) Anisotropy, *A*:

The anisotropy is defined as a measure of the relative difference between the second and third eigenvalues of the target decomposition (Cloude & Pottier, 1996):

$$A = \frac{P_2 - P_3}{P_2 + P_3} = \frac{\lambda_2 - \lambda_3}{\lambda_2 + \lambda_3} \tag{2.45}$$

A ranges also from 0 to 1. For high entropy the eigenvalues are nearly equal to the anisotropy contains no additional information. Also for low entropy the minor eigenvalues λ_2 and λ_3 are close to zero and the anisotropy yields no information. For medium entropy values, the high anisotropy indicates the presence of secondary scattering process, while a low anisotropy indicates that the third scattering mechanism plays an important role.

(iii) Alpha angle, α:

The α angle provides information about dominant scattering mechanism. It is computed as the weighted α_i values of Equation 2.46 (Cloude & Pottier, 1996):

$$\alpha = P_1\alpha_1 + P_2\alpha_2 + P_3\alpha_3 \tag{2.46}$$

where P_i is defined in Equation 2.44 and α_i is extracted from the respected eigenvectors in Equation 2.40. The α is a continuous angle with a range from 0° to 90°. For $\alpha = 0°$ the scattering corresponds to single bounce scattering created by the rough surface and $|HH| = |VV|$. As α increases the surface becomes anisotropic and $|HH| \neq |VV|$. If $\alpha = 45°$ the scattering mechanism represents dipole or volume scattering and either $|HH|$ or $|VV|$ is zero which can be determined by the target orientation angle β. The dihedral scattering occurs when α approaches to 90°.

2.6.2 Model based decomposition

Model based decompositions such as the Freeman–Durden decomposition (Freeman & Durden, 1998; Freeman, 2007) or the four-component Yamaguchi decomposition (Yamaguchi, 2005), decompose the covariance or coherency matrices into different scattering types, such as surface scattering, double bounce scattering, volume scattering, and helix scattering.

2.6.2.1 Four-component Yamaguchi decomposition

Yamaguchi *et al.* (2005) extended the Freeman–Durden model (Freeman & Durden, 1998) by allowing a certain degree of orientation inside the vegetation and introduced a helix component corresponds to non-reflection symmetric cases $\langle S_{HH}S^*{}_{HV}\rangle \neq 0$ and $\langle S_{HV}S^*{}_{VV}\rangle \neq 0$. The distribution of orientation angles is taken to follow a sine function and a set of covariance matrices are computed.

The scattering matrix data set of the imaging pixel area is defined as:

$$[S] = \begin{bmatrix} S_{HH} & S_{HV} \\ S_{VH} & S_{HH} \end{bmatrix} \tag{2.47}$$

Then, the scattering matrix is rotated by an angle θ along the line of sight of the radar leads to

$$[S(\theta)] = \begin{bmatrix} \cos\theta & \sin\theta \\ -\sin\theta & \cos\theta \end{bmatrix} \begin{bmatrix} S_{HH} & S_{HV} \\ S_{VH} & S_{HH} \end{bmatrix} \begin{bmatrix} \cos\theta & -\sin\theta \\ \sin\theta & \cos\theta \end{bmatrix} \tag{2.48}$$

The coherency matrix from the scattering matrix data set of the image pixel area is created by the mathematical averaging with probability density function $p(\theta)$ given by (Yamaguchi *et al.* 2005):

$$T(\theta) = \int_0^{2\pi} S.S^*(\theta)\, p(\theta) d\theta \tag{2.49}$$

Assume the probability function is uniform i.e. $p(\theta) = 1/2\pi$. The measured coherency matrix can be decomposed into four sub matrices which correspond to surface scattering, double-bounce scattering, volume scattering and helix scattering mechanisms:

$$\langle [T] \rangle = f_s \langle [T] \rangle_{surface} + f_d \langle [T] \rangle_{double} + f_v \langle [T] \rangle_{volume} + f_h \langle [T] \rangle_{helix} \tag{2.50}$$

where f_s, f_d, f_v and f_h are the expansion coefficients to be evaluated, and $\langle [T] \rangle_{surface}$, $\langle [T] \rangle_{double}$, $\langle [T] \rangle_{volume}$, and $\langle [T] \rangle_{helix}$ are the scattering models for the surface, double-bounce, volume and helix scatterings respectively (Figure 2.2). The four terms in Equation 2.50 have been derived from the physical scattering models.

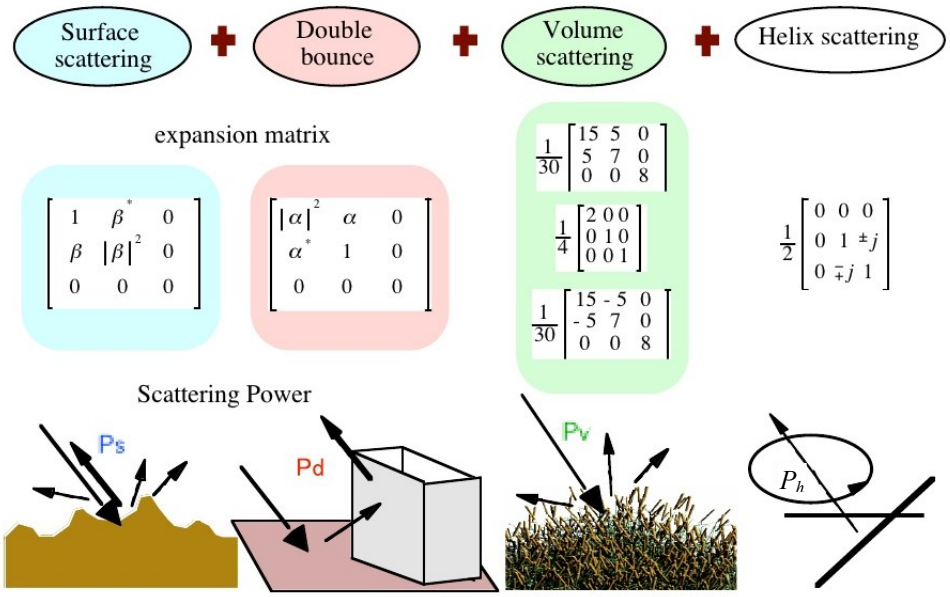

Figure 2.2 Four-component decomposition scattering powers P_s, P_d, P_v and P_h (Yamaguchi *et al.* 2011)

The single-bounce model is represented by the surface scattering mechanisms from slightly rough surface or Bragg surface. The cross polarised (HV-polarisation) is neglected in this model. The expansion matrix from the surface scattering coherency matrix is defined as (Yamaguchi *et al.* 2005):

$$[T]_{surface} = \begin{bmatrix} 1 & \beta^* & 0 \\ \beta & |\beta|^2 & 0 \\ 0 & 0 & 0 \end{bmatrix} \text{ with } \beta = \frac{R_h - R_v}{R_h + R_v} \tag{2.51}$$

The Bragg coefficient for the horizontally and vertically polarised wave is:

$$R_h = \frac{\cos\theta - \sqrt{\varepsilon_r - \sin^2\theta}}{\cos\theta + \sqrt{\varepsilon_r - \sin^2\theta}} \tag{2.52}$$

$$R_v = \frac{(\varepsilon_r - 1)\{\sin^2\theta - \varepsilon_r(1 + \sin^2\theta)\}}{(\varepsilon_r \cos\theta + \sqrt{\varepsilon_r - \sin^2\theta})^2} \tag{2.53}$$

where θ is the incidence angle and ε_r is the relative dielectric constant of the surface. The double-bounce model is based on the dihedral to be formed by two orthogonal Bragg scattering planes with the same or different dielectric properties. In this case the coherency matrix can be written as:

$$[T]_{double} = \begin{bmatrix} |\alpha|^2 & \alpha & 0 \\ \alpha^* & 1 & 0 \\ 0 & 0 & 0 \end{bmatrix} \tag{2.54}$$

Assume $\alpha = (|S_{HH} + S_{VV}|)/(|S_{HH} - S_{VV}|)$ with $|\alpha| < 1$. The third scattering component of the model is a randomly oriented volume of dipole. The corresponding coherency matrix according to the magnitude balance of $\langle|S_{HH}|^2\rangle$ and $\langle|S_{VV}|^2\rangle$:

$$[T]_{volume} = \frac{1}{30}\begin{bmatrix} 15 & 5 & 0 \\ 5 & 7 & 0 \\ 0 & 0 & 8 \end{bmatrix} \tag{2.55}$$

for $10\log\left(\frac{\langle|S_{VV}|^2\rangle}{\langle|S_{HH}|^2\rangle}\right) < -2\text{dB}$

$$[T]_{volume} = \frac{1}{4}\begin{bmatrix} 2 & 0 & 0 \\ 0 & 1 & 0 \\ 0 & 0 & 1 \end{bmatrix} \tag{2.56}$$

for $10\log\left(\frac{\langle|S_{VV}|^2\rangle}{\langle|S_{HH}|^2\rangle}\right) < 2\text{dB}$

$$[T]_{volume} = \frac{1}{30}\begin{bmatrix} 15 & -5 & 0 \\ -5 & 7 & 0 \\ 0 & 0 & 8 \end{bmatrix} \tag{2.57}$$

for $10\log\left(\frac{\langle|S_{VV}|^2\rangle}{\langle|S_{HH}|^2\rangle}\right) > 2\text{dB}$

The helix scattering model is developed from Krogager, (1990). The corresponding helix coherency matrix is:

$$[T]_{helix} = \frac{1}{2}\begin{bmatrix}0 & 0 & 0\\ 0 & 1 & \pm j\\ 0 & \pm j & 1\end{bmatrix}$$

$$[T]_{right-helix} = \frac{1}{2}\begin{bmatrix}0 & 0 & 0\\ 0 & 1 & +j\\ 0 & -j & 1\end{bmatrix}$$

$$[T]_{left-helix} = \frac{1}{2}\begin{bmatrix}0 & 0 & 0\\ 0 & 1 & -j\\ 0 & +j & 1\end{bmatrix} \tag{2.58}$$

From Equation 2.50 the expanded coherency matrix is defined by using four scattering coherency matrices as:

$$[T] = f_s\begin{bmatrix}1 & \beta^* & 0\\ \beta & |\beta|^2 & 0\\ 0 & 0 & 0\end{bmatrix} + f_d\begin{bmatrix}|\alpha|^2 & \alpha & 0\\ \alpha^* & 1 & 0\\ 0 & 0 & 0\end{bmatrix}$$

$$+\frac{f_v}{4}\begin{bmatrix}2 & 0 & 0\\ 0 & 1 & 0\\ 0 & 0 & 1\end{bmatrix} + \frac{f_c}{2}\begin{bmatrix}0 & 0 & 0\\ 0 & 1 & \pm j\\ 0 & \pm j & 1\end{bmatrix} \tag{2.59}$$

Comparing the elements of coherency matrix $[T]$ in Equation 2.30, the following equations with six unknowns $\alpha, \beta, f_s, f_d, f_v$ and f_h are stated:

$$|Im\langle S_{HV}{}^*(S_{HH} - S_{VV})\rangle| = \frac{f_c}{2} \tag{2.60}$$

$$2\langle|S_{HV}|^2\rangle = \frac{f_v}{4} + \frac{f_c}{2} \tag{2.61}$$

$$\frac{1}{2}\langle|S_{HH} - S_{VV}|^2\rangle = f_s|\beta|^2 + f_d + \frac{f_v}{4} + \frac{f_c}{2} \tag{2.62}$$

$$\frac{1}{2}\langle|S_{HH} + S_{VV}|^2\rangle = f_s + f_d|\alpha|^2 + \frac{f_v}{4} \tag{2.63}$$

$$\frac{1}{2}\langle(S_{HH} + S_{VV})(S_{HH} - S_{VV})^*\rangle = f_s\beta^* + f_d\alpha \tag{2.64}$$

To a reasonable degree of coherency matrix the term $\langle|S_{HH} + S_{VV}|^2\rangle/2$ represents the single bounce power and the term$\langle|S_{HH} - S_{VV}|^2\rangle/2$ corresponds to double-bounce power. From Equation 2.60 the f_c can determine directly, as shown in Equation 2.65

$$2|Im\langle S_{HV}{}^*(S_{HH} - S_{VV})\rangle| = f_c \tag{2.65}$$

The sense of rotation can be determined from the sign of the Equation 2.58 referring to 2.60.

Right circular polarisation:

$$Im\langle {S_{HV}}^{*}(S_{HH} - S_{VV})\rangle > 0 \tag{2.66}$$

Left circular polarisation:

$$Im\langle {S_{HV}}^{*}(S_{HH} - S_{VV})\rangle < 0 \tag{2.67}$$

Put the value of f_c into Equation 2.61, the f_v can be determined.

$$f_v = 8\langle|S_{HV}|^2\rangle - 4|Im\langle {S_{HV}}^{*}(S_{HH} - S_{VV})\rangle| \tag{2.68}$$

The remaining four unknowns f_s, f_v, α, β, can be obtained as follows. If $Re\langle S_{HH}{S^*}_{VV}\rangle > 0$ for the area of interest then $\alpha = 0$ (zero double bounce) because $Re\langle S_{HH}{S^*}_{VV}\rangle > 0$ indicates dominant of surface scattering mechanism. Then four unknowns can be determined by:

$$f_s = B \quad \beta^* = \frac{C}{B} f_d = A - \frac{|C|^2}{B} \tag{2.69}$$

α is not determined yet. If $Re\langle S_{HH}{S^*}_{VV}\rangle < 0$ the double-bounce scattering is dominant and $\beta^* = 0$ which neglects the term $\frac{|C|^2}{B}$. Therefore, the Equation 2.69 remains:

$$f_d = A \quad \alpha = \frac{C}{A} f_s = B \; - \frac{|C|^2}{A} \tag{2.70}$$

where A, B, C, are given by:

$$A = \frac{1}{2}\langle|S_{HH} - S_{VV}|^2\rangle - 2\langle|S_{HV}|^2\rangle \tag{2.71}$$

$$B = \frac{1}{2}\langle|S_{HH} - S_{VV}|^2\rangle - 4\langle|S_{HV}|^2\rangle + 2|Im\langle {S_{HV}}^{*}(S_{HH} - S_{VV})\rangle| \tag{2.72}$$

$$C = \frac{1}{2}\langle(S_{HH} + S_{VV})(S_{HH} - S_{VV})^*\rangle \tag{2.73}$$

The scattering powers P_s, P_d, P_v and P_h corresponds to surface, double-bounce, volume and helix scattering power are measured by the expansion coefficients f_s, f_d, f_v and f_h and the traces of the four sub matrices (Equation 2.59). The scattering powers are expressed as:

$$P_s = f_s(1 + |\beta|^2),\ P_d = f_d(1 + |\alpha|^2) \text{ and}$$

$$P_v = f_v, P_c = f_c \tag{2.74}$$

For quantitative analysis, the term in Equation 2.74 is compared with actual data in Chapter 4 (section 4.4).

Figure 2.3 illustrates an example of ALOS PALSAR L-band RGB (R=double-bounce, G=volume and B=surface scattering) image of four-component decomposition powers in Shestakovsky-N. Helix scattering is not presented here. Buildings, bare surfaces, and areas with low vegetation are shown in the lower part of the Shestakovsky-N. The areas in upper part of the image are covered with forest of different tree species: aspen, birch, larch and pine. Forested and dense vegetated areas are characterised by dominant volume (shown in green/yellow), a reasonably double-bounce (shown in red) and a small amount of surface (shown in blue) scattering. The amount of contribution of scattering powers in the forest areas greatly depends on the weather conditions, tree species and different density of forest such as sparse forest or dense forest. This will be discussed in details in Chapter 4 (section 4.4 and section 4.5).

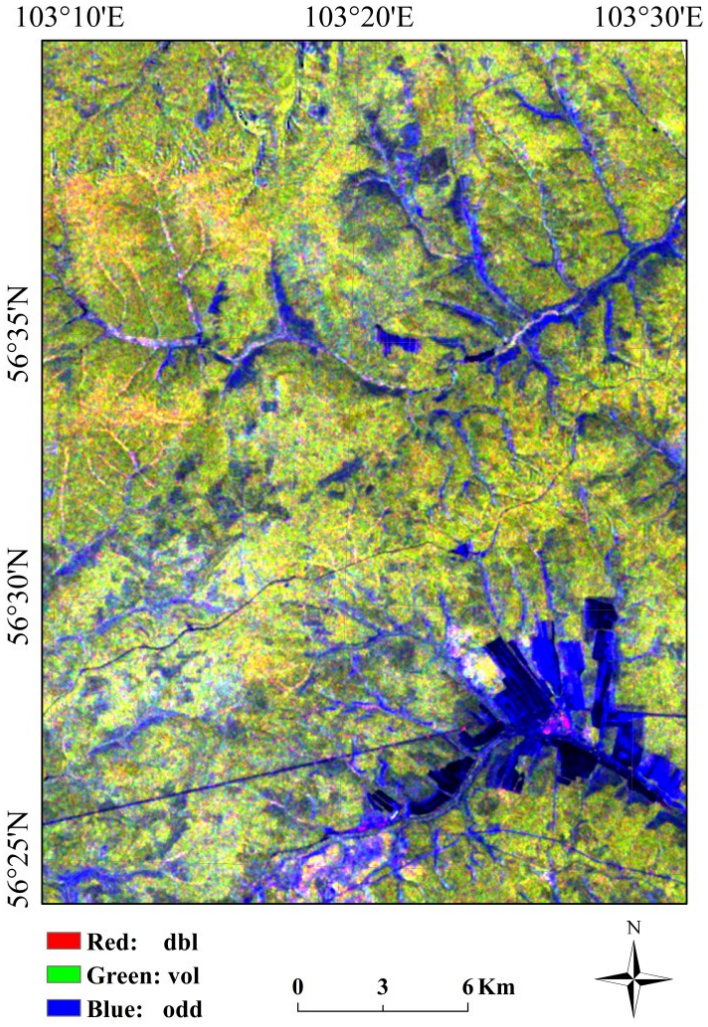

Figure 2.3 Composite image of Yamaguchi four-component decomposition powers (RGB=double-bounce/volume/surface scattering) in Shestakovsky-N.

2.7 Polarimetric parameters

The polarimetric parameters of natural targets can be described from the elements of Sinclair, Jones and coherency or covariance matrices. These parameters are derived directly from polarisation diversity of power measurements and also from phase relationships. The following sections describe how these parameters are determined and which information they provide about the nature of the scatterer.

2.7.1 Polarisation signatures

Polarisation signature is defined as the graphical representation of the variation of received power as a function of both different polarisation and all combinations of orientation angles and elliptical angles of the transmitted antenna (Van Zyl *et al.* 1987). The radar backscatter from distributed scatterers within a resolution cell or pixel consists of superposition of number of waves of different polarisations. The polarisation signature of a given pixel in radar image is the sum of polarisation signatures of many individual scatterers. The polarisation signatures of different scatterers may not be identical therefore their backscatter maxima and minima powers occur at different polarisations. The more the polarisation signature differs the less the difference of maximum and minimum backscatter power of resultant polarisation signatures. The ratio of minimum backscatter power to the maximum backscatter power is called coefficient of variation (Van Zyl *et al.* 1987). The higher coefficient of variation indicates the scattering mechanisms within the pixel vary. Vegetation areas have higher coefficients of variation because of multiple scattering. Water surface such as ocean has the smaller coefficient of variation.

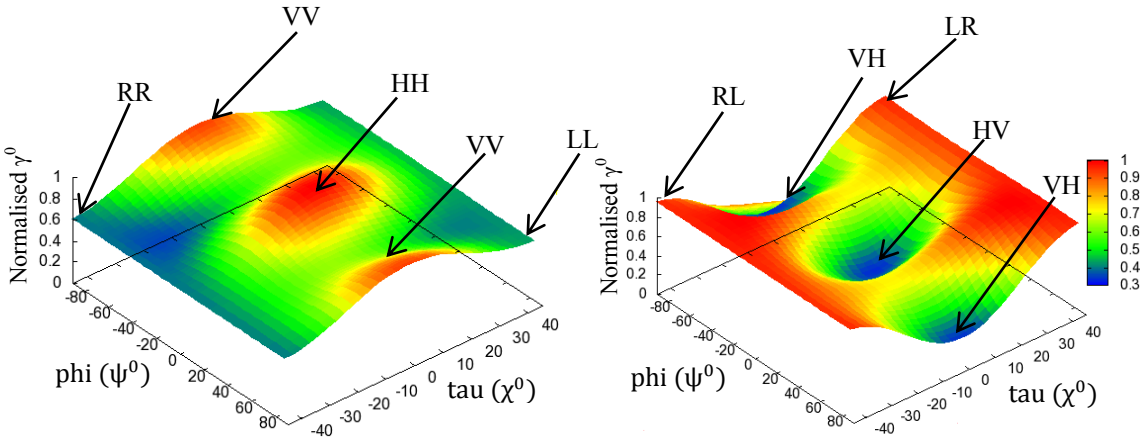

(a) (b)

Figure 2.4 Observed ALOS PALSAR L-band three-dimensional (a) co-polarisation and (b) cross-polarisation signatures for 90 years old birch forest stand in Shestakovsky-N, Siberia.

When same polarisation is used for both transmitting and receiving, the signature plot is referred to as the co-polarised signature. On the other hand, when transmit and receive polarisations are orthogonal; the plot is mentioned cross-polarised signature. An ellipticity

$\chi = 0^0$ corresponds to linear polarisation whereas ellipticity $\chi = \pm 45°$ corresponds to circular polarisation. For an ellipticity of $\chi = 0^0$, an orientation angle $\psi = 0^0$corresponds to horizontal (HH) polarisation and an orientation angle of $\psi = \pm 90^0$ corresponds to vertical (VV) polarisation. Figure 2.4 illustrates the co- and cross-polarisation signatures of 90 years old birch forest stand in Shestakovsky-N.

The polarisation signature is useful to describe the polarisation properties of point and distributed targets. The shape of the polarimetric signatures provides information on the dominant scattering mechanism as well as the type of the polarisation (linear, circular) and also the target of the orientation by means of orientation angle.

2.7.2 Polarimetric coherence

The complex coherence of between the two co-polarised channels (Henderson & Lewis, 1998):

$$\rho_{xx-yy} = \langle \frac{S_{xx}S^*{}_{yy}}{\sqrt{\langle S_{xx}S^*{}_{xx}\rangle\langle S_{yy}S^*{}_{yy}\rangle}} \rangle \tag{2.75}$$

where ρ is the complex coherence and <> denotes an ensemble averaging. The subscript x=H and y=V. S_{xx} or S_{yy} are the elements of Sinclair matrix (Equation 2.19). The magnitude of $\rho_{xx\text{-}yy}$ is between 0 and 1. When $|\rho_{xx\text{-}yy}|$=1 the electromagnetic wave is completely polarised and if $|\rho_{xx\text{-}yy}|$=0 the wave is unpolarised. Between these two extreme cases ($0 < |\rho_{xx\text{-}yy}| < 1$), the waves carry part of the energy in polarised form with the remainder in an unpolarised form.

A high degree of coherence between two channels indicates that there is a little difference in scattering behaviour between the two polarization configurations. On the other hand, a low degree of coherence indicates significantly different scattering behaviour between the two polarization configurations. This gives insight into the nature of the scatterer which may be valuable for target discrimination.

2.7.3 Polarisation phase difference

The polarisation phase difference between two co-polarised channels (Henderson & Lewis, 1998):

$$\varphi_{xx-yy} = \langle \tan^{-1}\left(\frac{Im(S_{xx})}{Re(S_{xx})}\right) - \tan^{-1}\left(\frac{Im(S_{yy})}{Re(S_{yy})}\right) \rangle \tag{2.76}$$

The cross-polarised phase difference:

$$\varphi_{xx-xy} = \langle \tan^{-1}\left(\frac{Im(S_{xx})}{Re(S_{xx})}\right) - \tan^{-1}\left(\frac{Im(S_{xy})}{Re(S_{xy})}\right) \rangle \tag{2.77}$$

where φ is the complex coherence. The co-polarization phase difference (PPD) is useful for understanding the scattering behaviour of forest and non-forest.

Chapter 3

Site Description and Data Sources

This chapter briefly describes the test sites, ground-truth data used for validation and remote sensing polarimetric SAR data. The forests in Siberia are chosen as test sites for the investigations. The characteristics of these test sites in terms of areas, tree species composition, and topography will be discussed briefly in section 3.1. A brief overview of ground-truth data and the relation between forest parameters will be presented in Section 3.2. The weather data and the available satellite data will be described in section 3.3 and section 3.4 respectively. Since errors in the ground-truth database can distort the interpretation of polarimetric parameters and also the assessment of the growing stock volume retrieval accuracy, the screening of ground-truth data will be suggested in section 3.5.1. As the low frequency SAR data is affected by Faraday rotation in ionosphere and also the polarimetric SAR data is affected by the terrain slopes in forest areas, the SAR data needs to be corrected. The compensation of the SAR data will be described in Section 3.5.2. Finally, a brief conclusion will be presented in section 3.6.

3.1 Test sites

Among the eleven forest territories used in the ALOS Kyoto & Carbon Initiative phase 3, led by JAXA Earth Observation Research Centre (EORC), the four forest territories Bolshe-Murtinsky, Chunsky, Primorsky and Shestakovsky are selected as the test sites for the investigation of polarimetric analysis (Figure 3.1). These areas belong to the southern taiga sub-zone of the boreal forest and belong to two Russian Siberian Federal Districts: Krasnoyarsk Kray and Irkutsk Oblast. These areas are chosen for a number of reasons: availability of the SAR data, forest inventory data as well as diversity of forest and meteorological data. The forests are characterised by the homogenous and mixed tree species stands and also disturbances such as clear-cuts and fire-scars.

3.1.1 Bolshe Murtinsky

Bolshe Murtinsky (centre coordinates 92.8° E 57.0° N) forest territory is located on both sides of the river named Yenisey. There are four forest compartments in this forest

territory. Two forest compartments are situated at eastern bank of the river and others two are at western side of the river. The forest compartments are named here Bolshe-NE, Bolshe-SE, Bolshe-NW and Bolshe-SW by means of their geographical location. Because of the availability of multi-temporal images, Bolshe-NE forest compartment is investigated

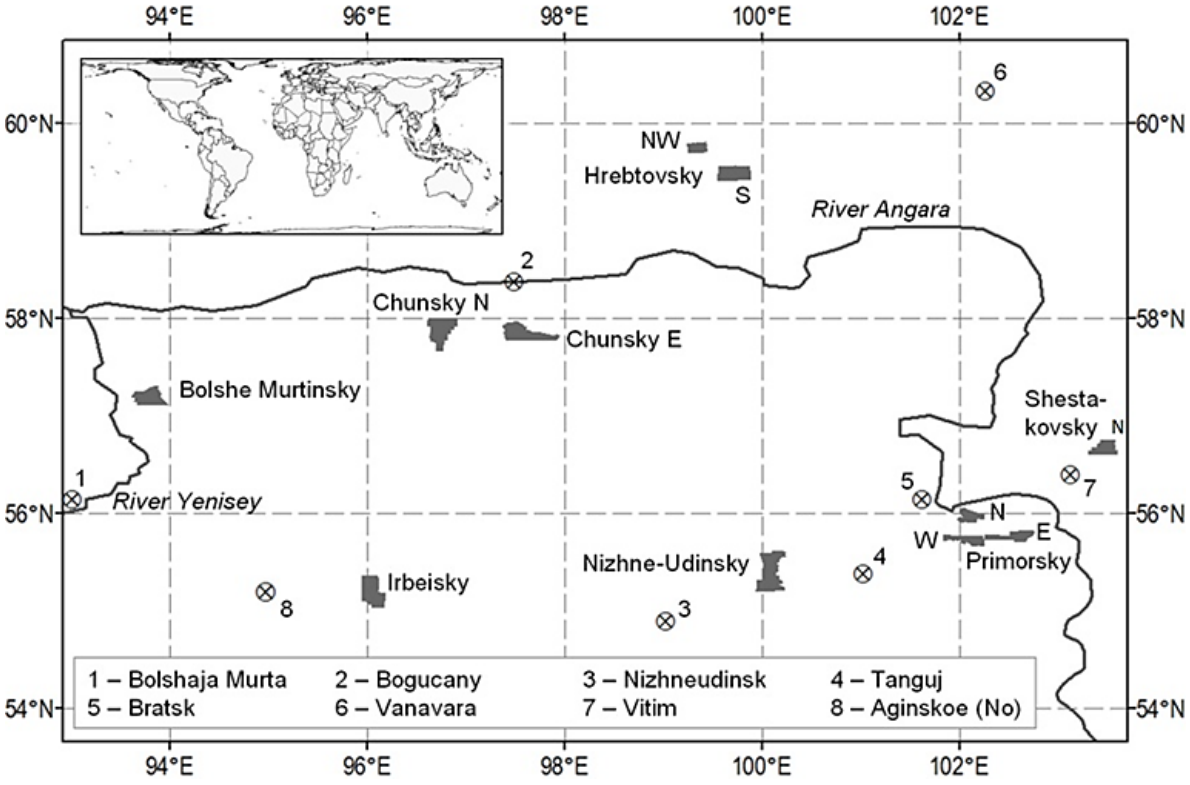

Figure 3.1 Test sites in Central Siberia including forest inventory and weather stations. The four forest territories: Bolshe Murtinsky, Chunsky, Primorsky and Shestakovsky are investigated in this study. Satellite imagery covered all these forest territories

only for the polarimetric analysis. The size of the forest compartment is 43km². Bolshe-NE comprises 484 stands with a mean area of 26ha. The detailed information about stands, and growing stock volume (GSV) of the test areas are given in Table 3.1.

Figure 3.2 depicts the tree species composition in Bolshe-NE. Aspen (*Populus tremula*), birch (*Betula pendula*), fir (*Abies sibirica*), pine (Pinus sylvestris), and spruce (*Picea sibirica*) are the main tree species. Aspen and pine have been found in the stands with lower GSV. Young and mature forests are dominant in the compartment (Figure 3.3) where the intermediate stages of forests are very few. Since Bolshe-NE is located on the mountainous area, the forests are here more heterogeneous and less affected by human activities.

Bolshe-NE is hilly terrain areas except some valleys along the riverbeds. The elevation ranges between 400m and 460m with slopes up to 10° at the south-east corner. 70% of the stands have slope up to 5°. Detailed topographic information of all the investigated areas is given in Table 3.2.

3.1.2 Chunsky

The forest territory, Chunsky (centre coordinates 96.40° E 57.40° N), is located on the southern side of the river Angara. There are four forest compartments in this forest territory and are referred as Chunsky-N, Chunsky-S, Chunsky-E and Chunsky-W. In this thesis, Chunsky-N and Chunsky-E are investigated. The size of the test area is between 146km² and 200km². Each compartment has between 336 stands and 354 stands with mean area between 59ha and 41ha. In Chunsky, the forest stands sizes are bigger than the stands in Bolshe-Murtinsky.

	Bolshe-NE	Chunsky-E	Chunsky-N
Area (km²)	43	146	200
Number of Stands	484	354	336
Stands size: min-mean-max-stdv (ha)	5-26-250-26	5-41-468-40	5-59-327-44
Stem volume (m³/ha)	0 – 430	0 – 430	0 – 350
Mean/ Stdv (m³/ha)	157/ 111	133/ 114	107/ 106

	Shestakovsky-N	Primorsky-E
Area (km²)	186	192
Number of Stands	683	536
Stands size: min-mean-max-stdv (ha)	2-27-171-24	2-36-138-19
Stem volume (m³/ha)	0 – 350	0 – 470
Mean/ Stdv (m³/ha)	185/ 92	184/ 112

Table 3.1 Forest stands summary statistics for the test sites under investigations.

Aspen, birch, larch (*Larix sibirica*), and pine are the main tree species in both compartments in Chunsky. Fir and spruce are only found in Chunsky-E. Young forests are dominated by deciduous trees in Chunsky-N and Chunsky-E. The histogram of growing stock volume distribution of all the forest compartments in Chunsky is similar to the Bolshe-Murtinsky (Figure 3.3). The greater number of stands with lower GSV has been noticed in Chunsky-N and Chunsky-E. In both forest compartments either very young or dense forests are dominant, whereas the intermediate growth stage between 50 m³/ha and 100 m³/ha is rarely found. Remarkable for all the investigated areas is the large amount of forest stands represent disturbed areas. The Siberian forests are commonly unmanaged, thus natural mixed forest is prevalent.

In Chunsky-N and Chunsky-E the topography is mostly flat. The elevation in Chunsky-N is about 200m above the seal level in the southern part, where steep slopes are located along the river basins. In the northern part the elevation increases to 400m. In Chunsky-N,

the topography is varying between 200m and 250m. Few peaks reach altitudes up to 340m. In 90% of the areas of Chunsky-N and Chunsky-E the slopes are smaller than 5°.

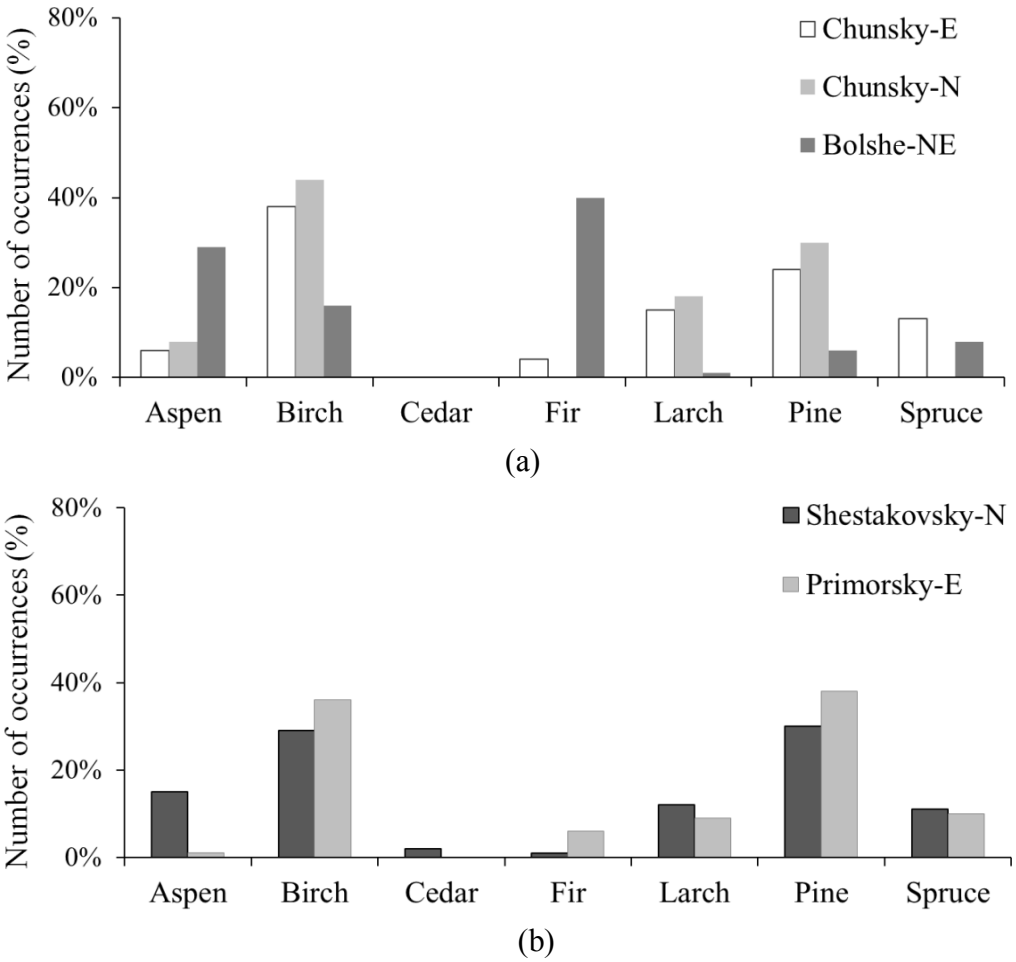

Figure 3.2 Tree species composition for (a) Chunsky-N, Chunsky-E, Bolshe-NE and (b) Shestakovsky-N, Primorsky-E.

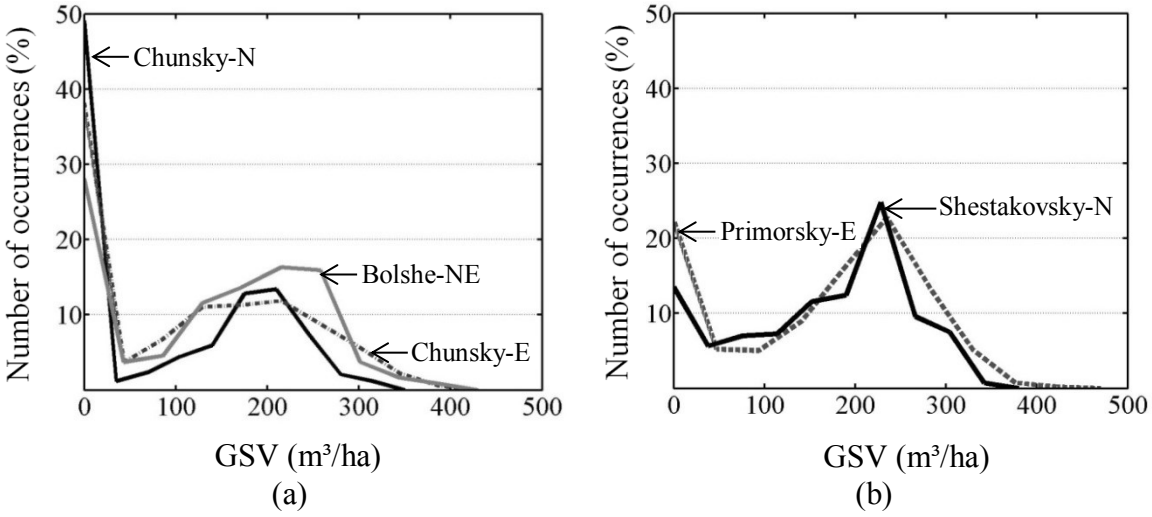

Figure 3.3 Histogram of growing stock volume (GSV) distribution for (a) Chunsky-N, Chunsky-E, Bolshe-NE and (b) Shestakovsky-N, Primorsky-E.

Test sites	Slope (°)	Topographic height (m)
Shestakovsky-N	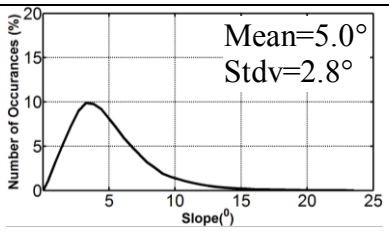	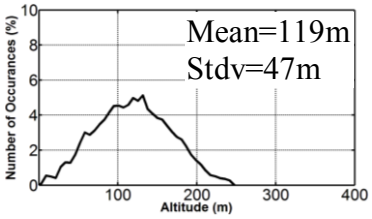
Primorsky-E	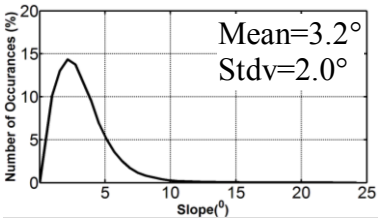	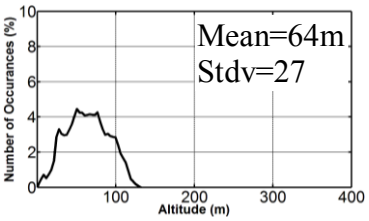
Chunsky-E	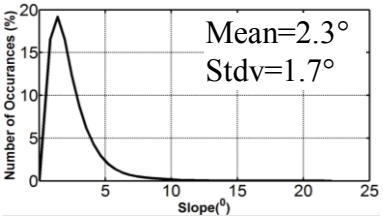	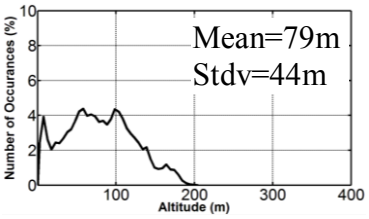
Chunsky-N	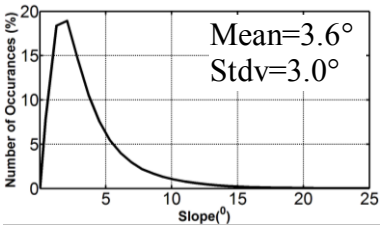	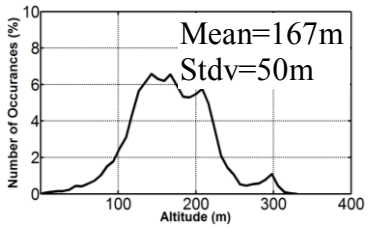
Bolshe-NE	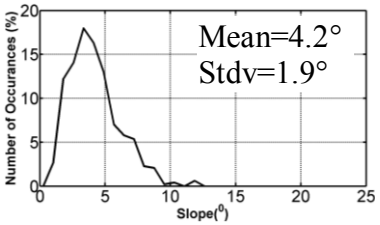	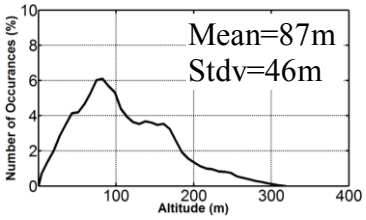

Table 3.2 Distribution of slope angles and topographic heights for the test sites in Siberia. The slope angles and altitude are segmented into 40 bins.

3.1.3 Primorsky

The two compartments in Primorsky (centre coordinates 102.20° E 55.50° N) forest territory are located on the southern bank of the Bratskove reservoir. The size of the Primorsky-E and Primorsky-W is 192km² and 195km² respectively. Primorsky-E contains 536 stands with mean size of 36ha and Primorsky-W contains 672 stands with mean stand size of 28ha.

Aspen, birch, larch, pine and spruce are the main tree species in Primorsky-E. The tree species composition is very similar to that at the Chunsky test sites. However, in

Primorsky-E aspen is the dominant tree type at young forests, whereas birch dominates the young stands in Chunsky. The distribution of GSV for Primorsky-E is similar to the GSV distribution of Shestakovsky-N (Figure 3-3 (b)).

Topography is rather gentle in Primorsky-E with few steep slopes along the riverbeds. The elevations are 350m to 400m near the stream valleys and it increases to 600m at the centre of the compartments. The highway goes across the forest areas which indicate an extensive logging of the forests. The elevations range between 350m and 400m near the stream valleys and increase to 600m at the centre of the compartment. In Primorsky-N, 65% of the area features slope up to 5°.

3.1.4 Shestakovsky

Shestakovsky (centre coordinates 104.45° E 56.67° N) forest territory is 80km north from the Bratsk Reservoir and 10km west to the Llim river. Three compartments are included in this forest territory. The SAR images have been acquired only over Shestakovsky-N forest compartment. Its area is 186km². It comprises 683 stands with a mean size of 27ha.

The main tree species are aspen, birch, larch, pine and spruce. A few percentage of cedar (*Pinus sibirica*) stands are found only in Shestakovsky-N. Conifers are predominant in mature forests. The histogram (Figure 3.3(b)) of GSV is similar to the Primorsky-E. A large number of stands represent dense forests. The intermediate and young forests are uniform in Shestakovsky-N which is not observed in other forest compartments of different forest territories.

The topography varies across Shestakovsky-N. High altitudes are found from the south-east corner to the north-west corner. The elevation ranges between 550m and 700m above the sea level. In south-east side of this test area 50% of the slopes are larger than 7º. In the southern and western parts, the topography varies between 450m and 550m. The standard deviation of the elevation is 60m and like in Primorsky-E, 65% of the areas have slopes up to 5°. The highway passes through the forest area indicating the active exploitation of forest.

3.2 Ground data

Two types of inventory data have been used for Siberian forests. First one, survey of unmanaged forest through satellite images, aerial photographs or multistage sample design. Second one, the Forest Inventory Planning (FIP) for managed forests. Approximately 70% of the Russian forests have been inventoried by FIP method and completed every 10 to 20 years. Boundaries of inventory units named stand interpreted from aerial photos within scale 1:25000. Ground measurements are used for final estimation and verify the aerial photos interpretation.

The forest inventory data is available from regular forest surveys and are part of an extensive Geographical Information System (GIS) database updated on 1998 by

International Institute for Applied System Analysis (IIASA). The data consist of forest stand boundary maps in digital form at stand level. A stand is the primary forest inventory unit where the borders are calculated from the aerial photographs. The attributes of each stand are stem volume, relative stocking, age, height and depth breast height (dbh) of the dominant tree species, species composition etc. The short descriptions of forest parameters are as follow:

Area: vertical projection of the area of the stand as reported in the forest inventory. The area is measured in square meter.

Land Category: different land categories referred in four digits numeric number, of the entire test sites. Some of the examples of the land category are as follow:

1101 - natural stand

The trees in a stand grow from natural regeneration following forest disturbances. The relative stocking of natural stands are greater or equal to 10% for young age groups and greater than or equal to 30% for all other age groups.

1104 - low productivity forest

According to "All-Russia Manual", these are mature and over mature exploitable forests of site index *Va* and *V,* and forests of higher productivity if growing stock is less than 40 m^3/ha in European Russia and less than 50 m^3/ha in Siberia.

1108 - forest plantation

A stand of growing trees, raised artificially, either by sowing (seeds) or (most commonly) planting. A forest plantation must have at least a relative stocking of 30 for young trees and 20% for mature (less than this it is an unclosed forest plantation).

1400 - sparse forest

Forests with relative stocking of 10 to 40% for young age groups and 10 to 30% for all other age groups, however, this state is the result of natural (e.g. fire) or human-induced disturbances.

1503 - burned forest

The full name of this category is burned and dead forest. This is a land category that describes areas that have experienced a "stand replacing" fire. This means that the "surviving" trees have a relative stocking of less than or equal to 10. If between 10 and 30% (relative stocking) survive the fire then it is classed as a sparse forest (category 1400)

1509 - clear-cut areas

These are areas that are harvested under the clear-cut silvicultural system. They have a relative stocking of less than 10%. This is a system of regenerating even-aged forest stands in which new seedlings become established in fully exposed micro-environments after most (some individual trees may remain standing) of the

existing trees have been removed. Regeneration can originate naturally or artificially. Clear-cutting may be done in blocks, strips or patches. Once regrowth occurs the area could be classed into unclosed forest plantation.

Relative stocking: relative stocking is an expression of the suitability of tree cover on a basal area. A basal area is the cross section of a tree trunk measured usually 1.3m above the ground. Basal area is used to describe the areas occupied by the trees per hectare. Relative stocking is a comparison of the stocking of a particular stand to what the ideal stocking would be under perfect management conditions. The ideal conditions depend on the quality of the area in terms of tree species composition and age of the stand. Relative stocking also indicates the tree density. It is scaled to 0 to 100%.

Growing stock volume: the stem volume of all living trees in a stand. The trees must be greater than 6 cm at breast height (1.3 m) to be included in growing stock. It is expressed in cubic meters per hectare (m^3/ha).

Age: age of the dominant species expressed in years. It is not the stand age. The dominant species is not dominant by number, but in economic value. Cedar is the highest value, then pine, regardless their percentage in the stand. The age class is different for different species. Table 3.3 shows the tree species of five age groups.

Species	Young (years)	Middle-aged (years)	Immature (years)	Mature (years)	Over-mature (years)
Aspen & birch	1-20	21-50	51-60	61-70	>70
Cedar	1-80	81 - 160	161 - 200	201 - 240	>240
Pine, spruce, fir and larch	1-40	41-80	81-100	101-140	>140

Table 3.3 The age thresholds for the different tree species in Bolshe Murtinsky, Chunsky, Primorsky and Shestakovsky forest territories (Schmullius *et al.* 2001).

Species composition: proportion of the species of the trees in a stand. It is specified on a scale of 1 to 10. For example if a stand have 80% birch and 20% aspen then it is defined BIRCH_SC=8 and PINE_SC=2. The composition is listed separately for each tree species in a stand.

Height: estimate of the average height of the dominant tree species in a stand. Expressed in metre.

Diameter: estimate of the average tree diameter of the dominant tree species. The diameter measured at breast height (1.3 m). Expressed in decimetre.

The forest disturbance is an important factor for the investigated areas. Forest is disturbed by fires, wind, insects, and diseases and through human-caused activities (e.g. harvesting, pollution). The most frequent disturbances in the study area are clear-cut for harvesting and forest fires. The clear-cut is done in blocks and strips. Fire is occurred

everywhere, and the regeneration after fire or clear cutting is mostly natural. Burned areas generally have many standing dead trees. Wetlands may have similar physiognomic features to recently disturbed areas and may actually have "dry surfaces" during the summer months.

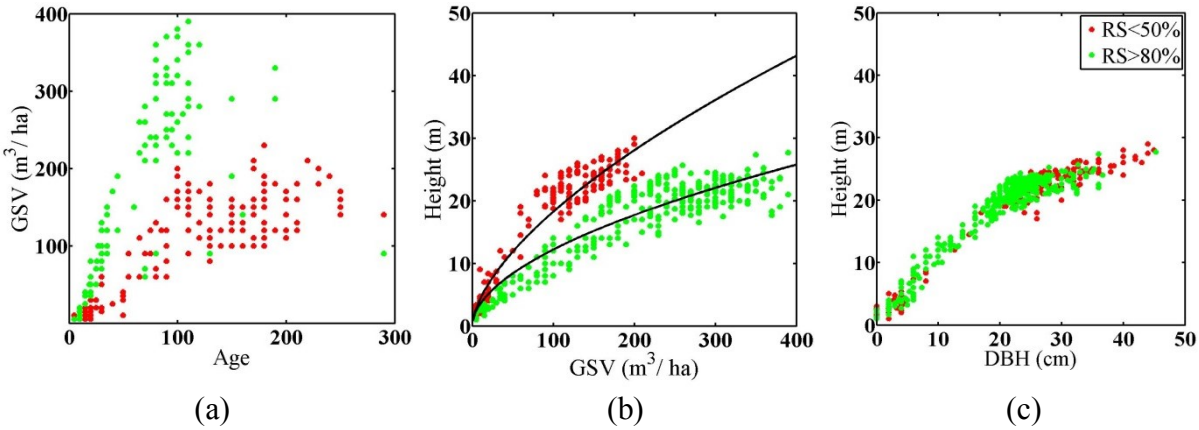

Figure 3.4 Scatter plots between forest structure parameters. The red and green colour represents the stands of relative stocking less than 50% and greater than 80% respectively.

The relationship between forests structure parameters are shown in Figure 3.4. It has been observed that the stands with relative stocking (RS) less than 50% hardly exceed growing stock volume (GSV) of 200 m³/ ha. On the other hand, fully stocked, relative stocking more than 80%, stands have up to 400 m³/ ha GSV. The age of the trees are less than 150 years in fully stocked stands. So, the relative stocking of mature forests are below 50%. Hence, the relationship between age and GSV depends on site quality. Also it has to be noted that in forest inventory list age refers economically the most valuable tree species in stand.. Figure 3.4(b) illustrated the tree heights increased with the increase of GSV in fully stocked stands than the stands of low relative stocking. This can be demonstrated that in fully stocked stands the trees grow upwards as well as depth breast height (dbh) of the trees increase. So the growing stem volume gets higher with the increase of tree height. The development is different for the stands with low relative stocking where either the forests are sparse or very dense enough that the trees remain thin (Santoro *et al.* 2007a). The relationship between diameter and height of the trees remain same regardless of the relative stocking. The observation on dbh-height relationship does not agree with the investigation by Pretzsch, (2002). The author found the dbh-height relation depends on species, site quality and climate conditions.

3.3 Weather data

Weather has immense influence on SAR data. It is important to know the environmental conditions for better interpretation of SAR images. The meteorological data is partly obtained from the German Weather Service (DWD). The other part is gathered from Weather Underground Website (www.wunderground.com). Four weather stations are located near the Bolshe Murtinsky, two stations near the Chunsky, two stations near the

Test Sites	Acquisition date	Temperature (ºC)			Weather conditions
		Min	Mean	Max	
Shestakovsky-N T-457 F-1130	21.05.2007	1	6	14	0.2 cm rain the day before (unfrozen, dry)
Shestakovsky-N T-457 F-1130	10.04.2009	-7	4	17	snowfall at 21:00 hrs last 2 days no snow; (thaw, wet)
Shestakovsky-N T-457 F-1130	26.05.2009	5	6	8	rainfall at 3:00 hrs and 21:00 hrs; last 2 days no rain; (unfrozen,wet)
Primorsky-E T-459 F-1120	09.05.2007	4	7	13	light rain showers at 23:00 hrs and 00:00 hrs; last 1 week no rainfall (unfrozen, dry)
Primorsky-E T-459 F-1120	24.03.2007	-8	-3	-1	snowfall at 9 hrs; last 20 days snowfall (frozen)
Primorsky-E T-460 F-1110	31.05.2009	4	17	22	last 3 days 1.6 cm rain (unfrozen, wet)
Chunsky-E T-467 F-1160	07.05.2007	-4	7	15	rain at 20:00 hrs; snowfall day before (thaw, wet)
Chunsky-E T-467 F-1160	19.09.2006	8	10	14	0.3 cm rain; 2 days before 1.1 cm rained. (unfrozen, wet)
Chunsky-N T-468 F-1160	06.10.2006	-4	-3	1	snowfall; last day 3 cm snow; snow depth 16 cm (frozen)
Chunsky-N T-468 F-1160	13.04.2009	-12	-7	-1	snowfall; snow depth 20 cm (frozen)
Chunsky-N T-468 F-1160	21.08.2006	7	11	14	0.15 cm rain at 08:00 hrs: 2 cm rain last 4 days (unfrozen, wet)
Chunsky-N T-468 F-1160	24.05.2007	3	12	17	3 days before 0.5 cm rain (unfrozen, dry)
Bolshe-NE T-474 F-1150	03.06.2007	6	13	18	4 days before 0.80cm rain (Unfrozen, wet)
Bolshe-NE T-474 F-1150	31.08.2006	6	9	18	3 days before 0.23cm rain (Unfrozen, dry)

Table 3.4 Weather observations on the day of the ALOS PALSAR L-band acquisitions for the forest territories in Shestakovsky-N, Primorsky-E, Chunsky- E and Chunsky-N. In first column "T" and "F" stands for the track and frame numbers for the PALSAR data. The time of the overpass of the satellite is 23:30 hrs (local time).

Primorsky and one station near the Shestakovsky. All the weather stations located between 50 km and 100 km distance from the forest compartments. Despite the distance from the weather stations to the investigated areas, it has been assumed that the weather conditions at the test sites are not significantly different. Daily measurements of temperature, precipitation, snow depth, wind speed, cloud cover, dew point, are available at all the stations. Four daily observations are recorded on every 6 hours by the stations in Bolshe Murtinsky, Chunsky and Primorsky. The stations near Shestakovsky measured two daily observations on every 12 hours. A brief summary of the weather conditions is provided in Table 3.4.

In the majority of cases, during the winter, the temperatures are below the freezing and snow accumulated on the ground. During the summer, the temperatures are above 0°C. Thus, in general, frozen conditions can be assigned to winter and unfrozen conditions to summer acquisitions. Thaw is defined as when the minimum temperature is above freezing. During the acquisitions no heavy rain is reported. The maximum amount of precipitation is 1.6cm. For most acquisition dates there is no precipitation.

3.4 PALSAR data

Fully polarimetric L-band SAR data have been acquired over the study areas by the Japanese Aerospace Exploration Agency (JAXA) using the Advanced Land Observing Satellite ALOS-PALSAR. The SAR data analysed in this research are listed in the Table 3.4. Fourteen SAR images are obtained from 2006 to 2009 at approximately 11:30 p.m. local time at different meteorological conditions. All images are acquired on ascending orbit. According to JAXA's ALOS acquisition strategy, the polarimetric data are acquired once every two years with a look angle of 21.5° and twice every two years with a look angle of 23.1º. Thus, it is not possible to gather a large multi-temporal dataset.

3.5 Necessary pre-processing thoughts

The pre-processing steps include in-situ data processing and ALOS PALSAR L-band data pre-processing. Errors in the forest inventory data either in the location of forest stands or the measured forest attributes may mislead the understanding of SAR polarimetric parameters as well as the assessment of the growing stock volume estimation accuracy. Therefore, error in the inventory data should be identified and excluded from the database. Since the low frequency SAR data is affected by Faraday rotation in ionosphere and the polarimetric SAR data is affected by the terrain slopes in forest areas, the SAR data needs to be corrected. The following sections present procedures of the screening of ground-truth data and the compensation of the ALOS PALSAR L-band data.

3.5.1 In-situ data pre-processing

To reduce the border effects and minimize the localization errors, the forest stands are buffered by 25 m. Also to limit the speckle effect and uncertainty on the forest inventory data, the stands size less than 2 ha are excluded. The stand-wise forest inventory data are converted to raster format and resampled to 25 m.

The polarimetric parameters can be influenced by the 8 to 11 years difference between the reference data set and acquisition of ALOS PALSAR images. Santoro & Cartus, (2010) introduced a growth model for Siberian forest to overcome the time gap between this reference data set and ASAR data. They were assumed that for the region of Central Siberia where the test sites are located forests grow annually on average by 5 m³/ha/year with decreasing rate for increasing age, reaching 1 m³/ha/year in mature forest. The updated GSV from the growth model has been done on a yearly basis using the value computed for the preceding year. Equation 3.1 illustrates the GSV update procedure.

$$GSV_1 = 0.9867 * GSV_{inv} + 5$$

$$GSV_2 = 0.9867 * GSV_1 + 5$$

……

$$GSV_{ref} = 0.9867 * GSV_{n-1} + 5 \quad (3.1)$$

where GSV_{inv} the original value from the inventory, GSV_1, GSV_2, GSV_{n-1} the yearly updated GSV and GSV_{ref} being the updated GSV. The proposed growth model does not consider for the different tree species and their growth rate which are found to be different in Siberian forest where mixed forests are prevalent (see Table 3.3). Moreover, it has been discussed previously (section 3.2 and Figure 3.4) that the relative stocking i.e. forest stand structure is very important parameter for the forest growing. Forest GSV reaches higher levels in case of fully stock stands. Low relative stocking (RS<50%) hardly exceeds a GSV of 200 m³/ha. The tree heights for low relative stocking stands are higher for a given stem volume than for fully stock stands. Therefore, it is not suitable to implement the growth model to the Siberian forests without any knowledge of the growth of the individual tree species.

During these 8 to 11 years, there could be a possibility for the forest disturbances such clear-cut for harvesting, forest fires, wind, insect outbreaks and diseases. As a result the forest became non-forest which is not updated in inventory data. The outdated forest inventory data are updated using high resolution optical data regarding recent logging and other disturbances. The Multi-Purpose Satellite (KOMPSAT-2) from the Korea Aerospace Research Institute (KARI) data is used for this purpose. If any mismatch is found between optical images and ground-truth data, the stands are excluded.

Based on the SAR data, for each stand mean and standard deviations of polarimetric coherence and decomposition power $P(\theta)$ have been computed. If the standard deviation of $P(\theta)$ is greater than 0.1, these stands are considered non-homogenous stands and thus are discarded. The number of remaining stands of each site is given in Table 3.1.

3.5.2 PALSAR data pre-processing

Single look complex (SLC) level 1.1 PALSAR data are used. First of all, the data is polarimetrically calibrated (Shimada *et al.* 2009). Afterwards, the coherency matrix $[T]$ is formed. In this step, the data is multi-looked with 7 azimuth and 1 range looks and speckle filtered using 3 × 3 Lee Sigma filter (Lee *et al.* 1999). The multi-looked factors result in approximately squared pixels. The Faraday rotation is calculated and eliminated which will be discussed more details in section 3.5.2.1. The polarimetric SAR data are corrected for impacts of the azimuth slope (see section 3.5.2.2). The multi-looked intensity images are terrain corrected and geocoded by using SRTM-3 DEM (Shuttle Radar Topography Mission-3 Digital Elevation Model) of the test sites. The size of the geocoded images is 25m × 25 m pixel and in sigma-nought σ^0 format. Geocoding has been done:

1. Generating an initial look-up table by using orbital information from the SAR data and elevation in the DEM. This look-up table describes the transformation between the radar and the map geometry (Wegmüller, 1999; Wegmüller *et al.* 2002).
2. For reducing inaccuracies in orbital information look-up table is refined by implementing cross correlation of a high number of image chips in the SAR intensity image in radar geometry and simulated SAR image from DEM. The image chips are distributed homogenously on the image data, with number and size being strictly dependent on the correlating features between the SAR image and simulated image.
3. The simulated image is re-projected into SAR geometry using the initial look-up table. With the refined transfer function from the cross correlation, the look-up table is updated to a refined look-up table and used for re-projecting the PALSAR image products in SAR geometry into map geometry. Quality of the refinement is given by the root mean square error between measured and estimated offset using the offset polynomial.

The geocoded SAR images are affected by the terrain areas. The slopes facing towards the radar appear brighter and enhance the backscatter. For correct interpretation of backscatter images, the correction for the effect of local incidence angle needs to be correct (Ulander, 1996). Otherwise the uncompensated radar backscatter images are induced by the topographic effects with a dispersion of 2-7 dB (Castel *et al.* 2001).

The sigma-nought σ^0 backscatter can be corrected to gamma-nought γ^0 according to Ulander, (1996) and Castel *et al.* (2001)

$$\gamma^0 = \sigma^0 \frac{A_{flat}}{A_{slope}} \left(\frac{\cos \theta_{ref}}{\cos \theta_{loc}} \right)^n \tag{3.2}$$

where A_{flat} and A_{slope} represent the local pixel area for a reference flat ground and the true pixel area, respectively. θ_{ref} and θ_{loc} denote the reference angle for the normalization of the backscatter and the local incidence angle respectively. The lack of detailed

information about optical depth of the forest canopies at the test sites, *n* is set equal to 1 (Santoro *et al.* 2009).

It is mentioned before that the data is speckle filtered using the 3 × 3 Lee filter (Lee *et al.* 1999). The impact of the filter is demonstrated in Figure 3.5. The black polygons indicate the boundaries of forest stands. Surface and volume scattering are smeared in the unfiltered image (Figure 3.5(a)). The result of the filtered image (Figure 3.5(b)) shows the positive effect of the filtering. The dominant scattering properties have been preserved. Double-bounce, surface, and volume scattering can be observed to produce peaks with less variance.

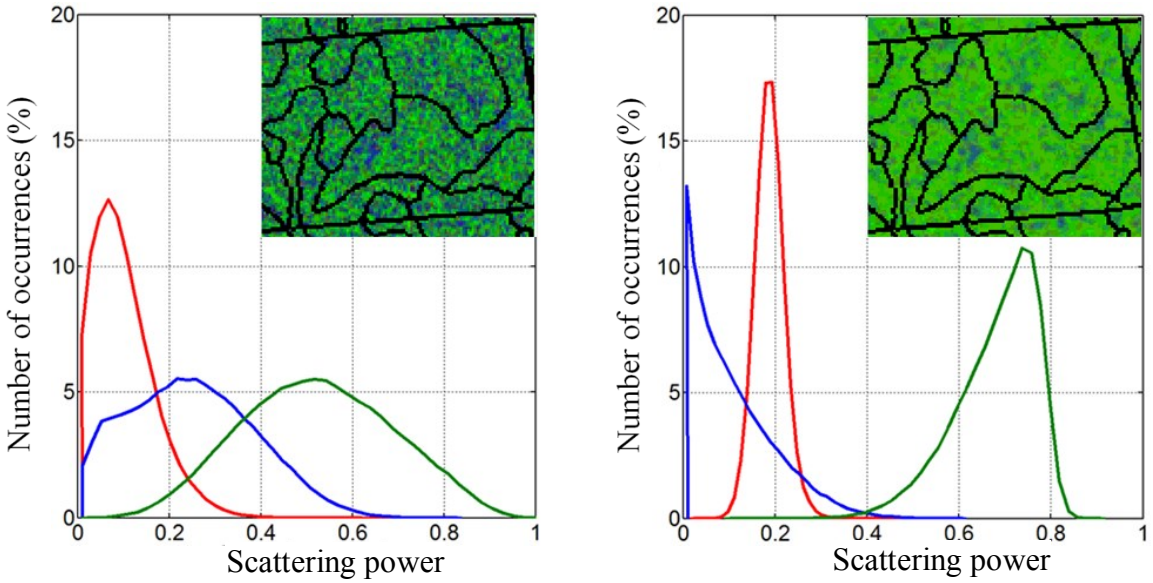

Figure 3.5 Distribution of decomposition powers (a) before and (b) after applying the 3 × 3 LEE filter. The red, green, and blue colours represent the double-bounce, volume, and surface scattering power respectively. The scattering powers are segmented into 40 bins.

3.5.2.1 Correction of Faraday rotation effects

Faraday rotation (FR) which rotates SAR polarisations during their two way transmission through ionosphere is one of the distortions for POLSAR data. The effect of FR on measurements of polarisation scattering matrix using monostatic radar is first addressed by Bickel & Bates, (1965). The authors formulated the relation between actual and measured scattering matrices and showed that FR is a nonreciprocal effect which means cross polarisation HV returns deviates from VH return, cause errors in estimation of polarimetric calibration parameters and therefore impact on current POLSAR application. Rignot, (2000) has investigated the effects of FR on L-band H polarisation Japanese Earth Resources Satellite 1 (JERS-1) SAR data. Rignot suggested that a FR of 30°-45° provides a reasonable explanation of some anomalous scattering behaviour observed in JERS-1 data collected over the Amazon rainforest. He also suggested that FR may be as large as 90° during periods of intense solar activity. Wright *et al.* (2003) proposed that FR angles for a

single path through the ionosphere may be as high as 30° during solar maximum. They also model the effects of Faraday rotation on HH, HV, and VV backscatter, with results indicating that values of FR>5° are likely to significantly affect the recovery of geophysical parameters from these three measures.

Electromagnetic waves traveling through the ionosphere interact with the electrons and the magnetic field with the result that the polarisation vector of the electric field is rotated by an angle, Ω, which is called the Faraday rotation (FR) angle (Davies, 1965).

$$\Omega = \frac{K}{f^2} B \cos(\theta)\,\mathrm{TEC} \tag{3.3}$$

where K is a constant of value 40.28 [m³/s²], B is the flux density of earth's magnetic field, θ is the angle between the magnetic field and the wave propagation and TEC is total electron content integrated along the vertical. The magnitude of the FR angle depends on the frequency of the wave, the direction of earth magnetic field and its total electron content. The degree of FR is proportional to the inverse square of the frequency so that the effects of the FR may be significant at longer wavelength or lower frequencies such as on L-band and P-band. TEC exhibits large variations depending on time of day, season, solar activity, geographical location and satellite orbital height. At night TEC value is low compare to the day time. FR is expected to increase during solar maximum around 2011. FR is significant near the equator. Intermediate latitude between 30° and 50º, largest FR expected. At higher latitudes TEC values tend to be low. It should be noted that the microwave signal is rotated by in the same sense each time it traverses the ionosphere. For SAR, the total FR will, therefore, be double the one-way FR experienced by a passive microwave sensor. L-band or P-band orbited in the ionosphere. If FR is the only disturbing effect on the SAR signal, the correct scattering matrix S^c can be written as:

$$\begin{bmatrix} S^c_{hh} & S^c_{hv} \\ S^c_{vh} & S^c_{vv} \end{bmatrix} = \begin{bmatrix} \cos\Omega & \sin\Omega \\ -\sin\Omega & \cos\Omega \end{bmatrix} \begin{bmatrix} S_{hh} & S_{hv} \\ S_{vh} & S_{vv} \end{bmatrix} \begin{bmatrix} \cos\Omega & \sin\Omega \\ -\sin\Omega & \cos\Omega \end{bmatrix} \tag{3.4}$$

which can be written as:

$$S^c_{hh} = \cos^2\Omega S_{hh} - \sin^2\Omega S_{vv} + \sin\Omega\cos\Omega(S_{hv} - S_{vh}) \tag{3.5}$$

$$S^c_{hv} = \cos^2\Omega S_{hv} + \sin^2\Omega S_{vh} - \sin\Omega\cos\Omega(S_{hh} + S_{vv}) \tag{3.6}$$

$$S^c_{vh} = \cos^2\Omega S_{vh} + \sin^2\Omega S_{hv} + \sin\Omega\cos\Omega(S_{hh} + S_{vv}) \tag{3.7}$$

$$S^c_{vv} = \cos^2\Omega S_{vv} - \sin^2\Omega S_{hh} + \sin\Omega\cos\Omega(S_{hv} - S_{vh}) \tag{3.8}$$

where Ω is the FR angle, S is the radar backscattering matrix. With fully polarimetric SAR data, several methods have been introduced to estimate the Faraday rotation angle (Freeman, 2004; Freeman & Saatchi, 2004; Bickel & Bates, 1965).

$$Z = T_{11} - T_{44} + i2Im(T_{14}) \tag{3.9}$$

$$\Omega = 0.25 * arg(Z) \tag{3.10}$$

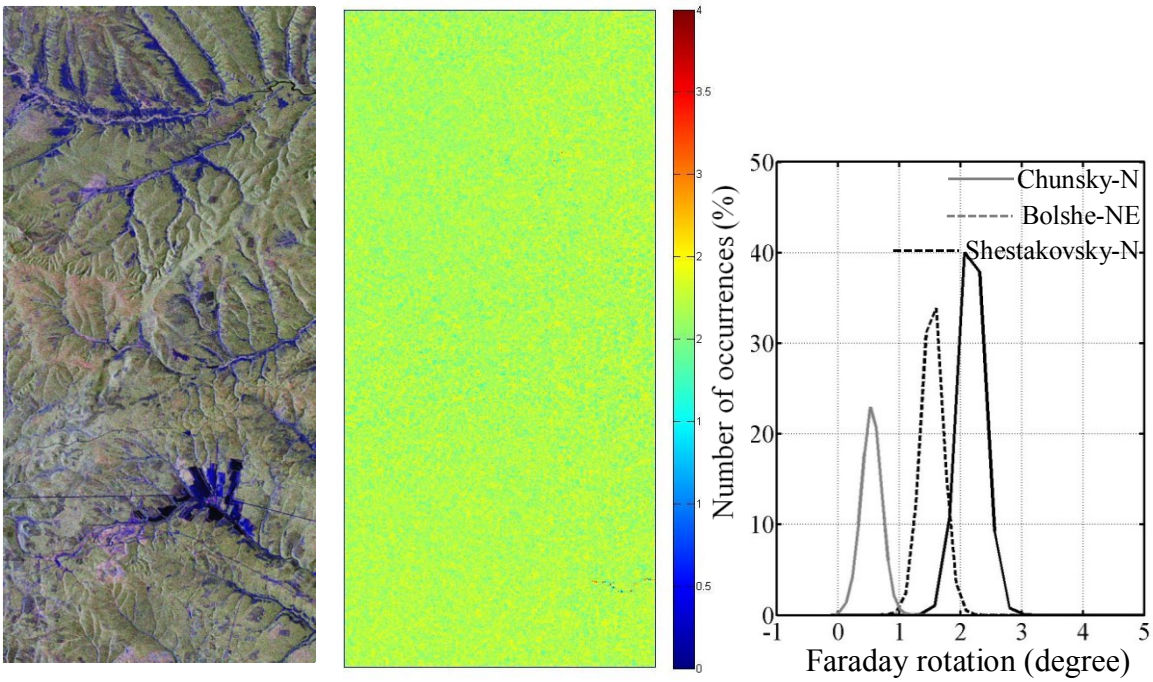

(a) (b) (c)

Figure 3.6 (a) Pauli RGB image acquired by ALOS-PALSAR L-band over Shestakovsky-N on 21.05.2007. (b) Spatial map of Faraday rotation angle span between 0° and 4°. (c) Distribution of Faraday rotation angle measured in Chunsky-N, Bolshe-NE and Shestakovsky-N.

The FR angles are estimated for all the ALOS PALSAR L-band datasets during 2006 to 2009. After multi-looking and filtering, FR angles are measured using Equation 3.10. Here one example has been provided for the FR estimation by using ALOS PALSAR L-band polarimetric data. The PALSAR data are imaged on 21.05.2007 in Shestakovsky-N. The image is shown in Figure 3.6(a) with Pauli RGB image: |HH-VV| in red, |HV|+|VH| in green and |HH+VV| in blue. The image illustrates the smooth areas in blue (surface scattering) and forest areas in green (volume scattering or multiple scattering). Figure 3.6(b) depicts the spatial distribution of FR angle estimation for polarimetric SAR data over Shestakovsky-N. The histogram distribution of Bolshe-NE, Shestakovsky-N and Chunsky-N are shown in Figure 3.6(c) where the FR angles are concentrated between 0.6º and 2.2º. The SAR image acquired on 21.05.2007 at Shestakovsky-N is mostly affected by the 2.2º (total rotation is 4.4°) FR (see Table 3.5). The FR estimation of other data sets are below ~1.7°. The small standard deviations (0.01º-0.02º) for all the test sites show that FR

angles are very uniform all over the images. The observed FR angle is smaller due to the following reasons: (i) solar minimum conditions during 2004-2008, (ii) SAR images acquired at night and (iii) all the investigated areas are in higher latitudes (56.5° N to 57.5° N). Only data set acquired on 21.05.2007 in Shestakovsky-N is compensated. The corrected HH, HV, VH and VV polarisations is computed by applying Equation 3.5-3.8.

Test Sites	Data	Mean	Stdv
Chunsky-N	13.04.2009	0.6º	0.01º
Bolshe-NE	31.08.2006	1.5º	0.02º
Shestakovsky-N	21.05.2007	2.2º	0.01º

Table 3.5 Mean and standard deviation of FR angles for Chunsky-N, Bolshe-NE and Shestakovsky-N.

The co-polarised backscattering coefficients are roughly equal over most of the forested areas. The compensating results indicate that FR reduces the co-polarised, HH and VV, backscatter power while increase the cross-polarised, HV and VH, power. The change of the co-polarised backscatter power after the correction of FR angle is between 0.2 and 0.3 dB. On the other hand, the cross polarised channels HV and VH are more severely affected than the co-polarised channels. One way FR of 2.2° (total FR of 4.4°), the differences are 1.6 dB and 1.2 dB for HV and VH respectively. The impact of FR on forest areas is indicated by the scatter plots shown in Figure 3.7. The co- and cross-polarisations become more correlated and less separable after compensating data with Faraday rotation. Therefore, the accuracies of retrieved vegetation are affected adversely once FR exceeds 4.4°.

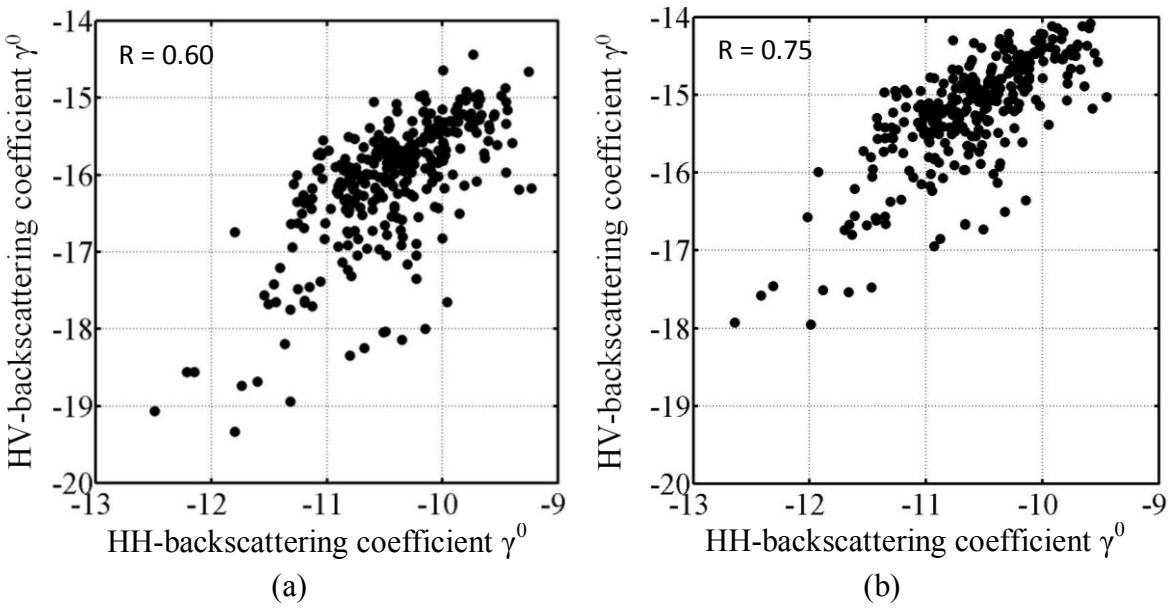

Figure 3.7 Comparison of ALOS PALSAR L-band HH- and HV-backscatter intensities at Shestakovsky-N forest areas. (a) Before FR correction and (b) after the 4.4° FR correction. The image is acquired on 21.05.2007.

3.5.2.2 Polarisation orientation angle compensations

When the SAR acquires images over the terrain areas, the images are affected by (i) the change of radar cross section per unit image area and (ii) change of polarisation state induced by azimuth slopes. The first affect is already compensated by radiometric slope correction. When the SAR transmits the signal, H-polarisation electric field is parallel to horizontal surface. But for the tilted surface H-polarisation is no longer parallel to the surface. So, HH-polarisation is affected by the tilted slope. VV-polarisation also can be affected.

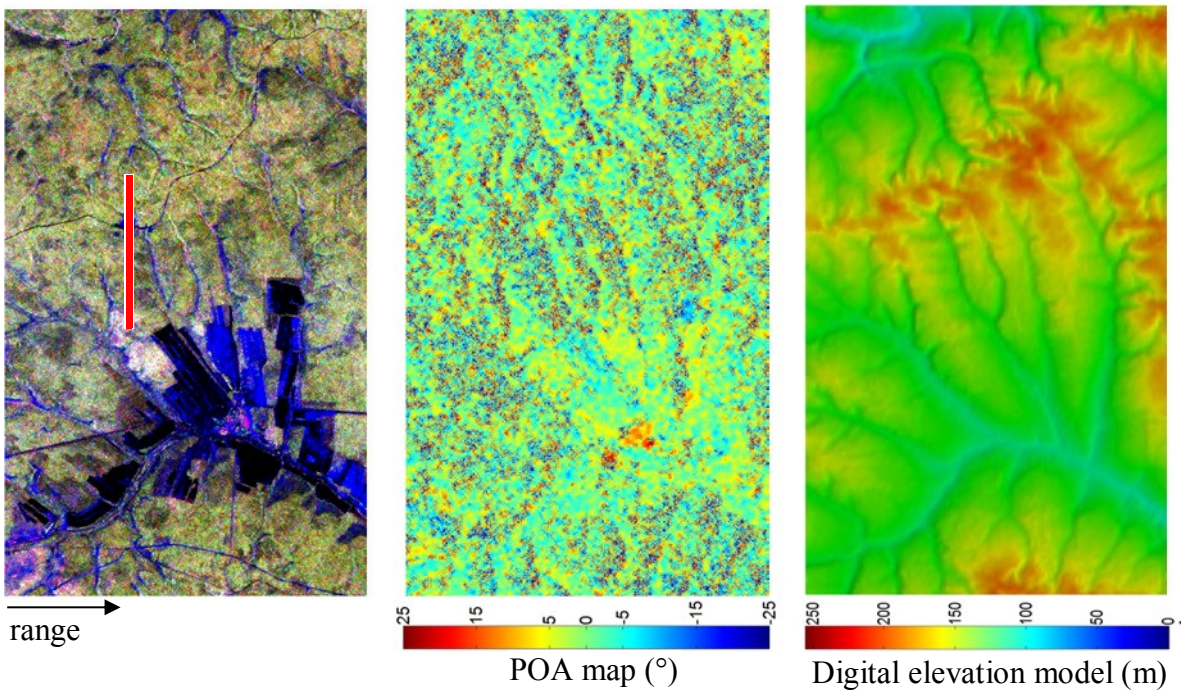

Figure 3.8 ALOS-PALASAR L-band PLR data of Shestakovsky-N for illustration. (a) The Pauli RGB image. R=|HH-VV|, G=|HV|+|VH| and B=|HH+VV|. (b) The POA derived from circular polarisation algorithm. (c) Digital Elevation Model (DEM) from SRTM-X. The vertical red line of 200 pixels by azimuth and 4 pixels by range will be used to show the profiles for Figure 3.9 and Figure 3.10.

The basic principle is to rotate the data about the line of sight by the negative of the polarisation orientation angle (POA) induced by topographical effects. Several methods have been established for estimating POA. Here circular polarisation algorithm has been used because of its effectiveness, simplicity and computational efficiency (Lee *et al.* 2000). This method is better than other methods: (i) orientation angle derived from DEM and (ii) orientation angle derived from POLSAR data. The polarimetric SAR data are corrected for the impacts of the azimuth slope. To compensate this slope affect, the POA are derived from the circular polarisation algorithm (Lee *et al.* 2002; Lee *et al.* 2011), as shown in Equation 3.11:

$$\theta = \frac{1}{4}\left[\tan^{-1}\left(\frac{-2Re[T_{23}]}{-T_{22}+T_{33}}\right)\right] \tag{3.11}$$

The circular polarisation algorithm is applied to all ALOS PALSAR L-band data. Figure 3.8 illustrates one example for Shestakovsky-N. Buildings, bare surfaces, and areas with low vegetation are shown in the lower part of the Shestakovsky-N. Figure 3.8(a) shows the POLSAR data with Pauli colour coding (|HH-VV| for red, |HV| for green and |HH+VV| for blue). The image size is 700 × 900 pixels (each pixels is 25m). The areas in upper part of the image are covered with forest of different tree species: aspen, birch, larch and pine. The POA map derived from the circular polarisation is depicted in Figure 3.8(b). The POA varies between -25° and +25°. The POA is noisier in forest areas, where much of the backscattered energy comes from the volume of the canopy. The areas with bare surfaces and buildings have meaningful orientation measurements. The SRTM DEM is shown in Figure 3.8(c).

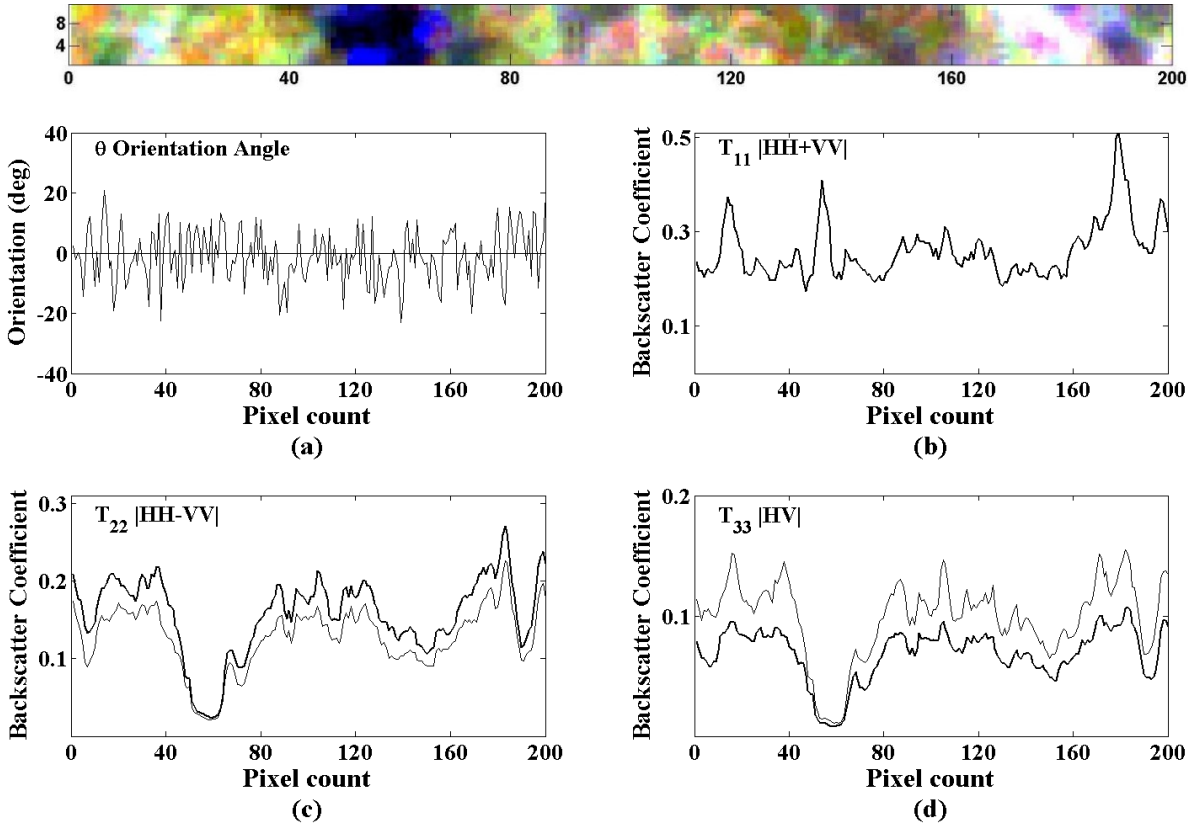

Figure 3.9 The top figure shows the profile plot of red line (200x4 pixels) from Figure 3.8. (a) The POA varies from -23° to 20°. (b) - (d) shows the POA compensation for diagonal elements of coherency matrix [T]. The thin lines indicate the value before compensation and coarse lines for the value after compensation. (b) T_{11} remains unchanged because of roll-invariant property. (c) T_{22} always increases and (d) T_{33} always decreases after compensation.

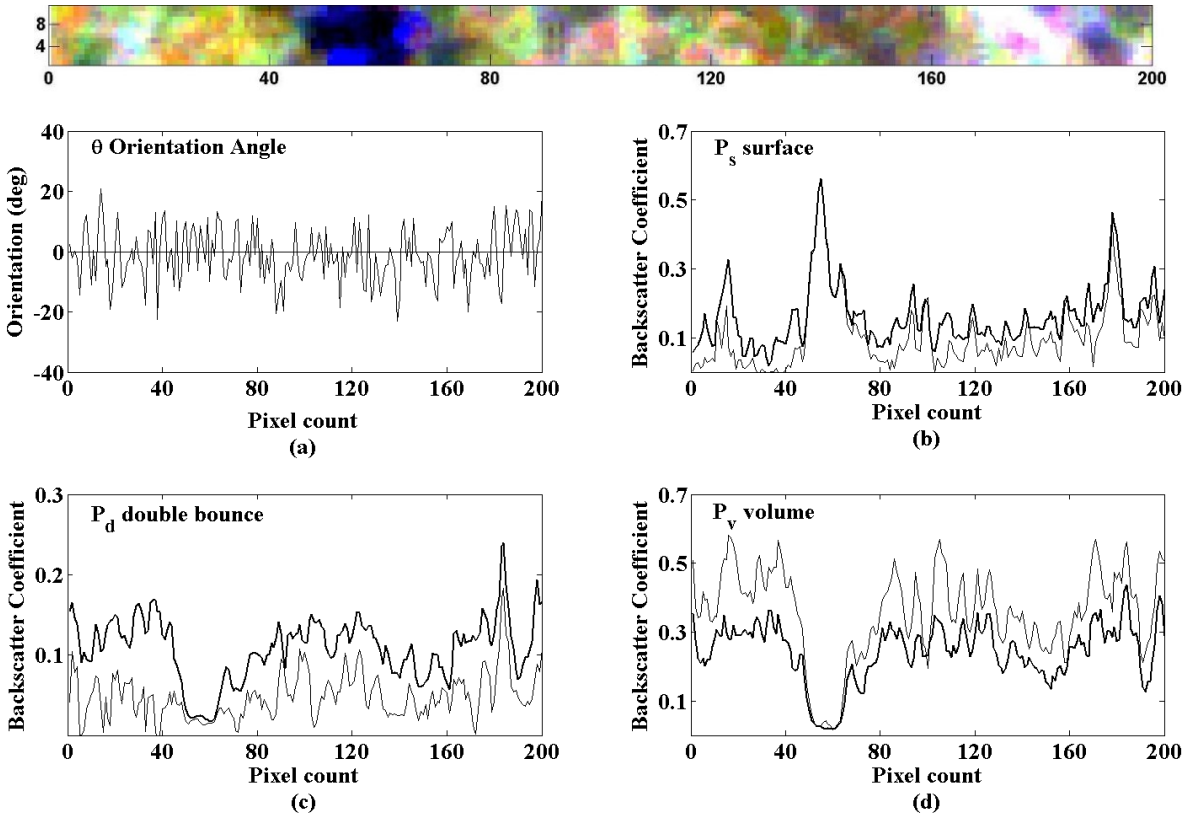

Figure 3.10 The profile plots of red line (200x4 pixels) of Figure 3.8. (a) The OA varies from -23° to 20°. (b) - (d) shows the POA compensation for the four-component decomposition powers. The thin lines indicate the value before compensation and coarse lines for the value after compensation. (b) Surface power remains unchanged. (c) Double-bounce power is consistently increased and (d) Volume scattering power is consistently decreased by compensation. Because of flat surface from pixel number 45 to 60 (blue areas), the volume power and double-bounce remains unchanged.

The effect of POA compensation on coherency matrix [T], and four-component decomposition powers (Yamaguchi *et al.* 2005) are investigated. The coherency matrix [T] is compensated by applying Equation 2.38. For the interpretation of compensation results a small cut of 200 pixels in azimuth and 4 pixels in range shown in red line in Figure 3.8 is made to show the profiles of the POA compensations in Figure 3.9 and Figure 3.10. The 4 pixels in range are averaged to make 200 × 1 lines of profile. The profile before orientation compensations are represented by thin lines, and after compensation, they are represented by thick lines. The POA of 200 pixels induced by azimuth slope are shown in Figure 3.9(a). The POA ranged between -23º to +20º. The POA in blue areas (Figure 3.9) of pixels 45 to 60 where surface scattering dominant, are relatively smaller. On the other hand, pixels of green and yellow areas, the POA is relatively larger. Figure 3.9(b)-(c) plots the three diagonal elements of the coherency matrix [T] before (thin line) and after (thick line) compensation. The vertical axis indicates the backscattering coefficient γ^0. T_{11} ($|S_{HH} - S_{VV}|$) is rotational invariant and remains unchanged. The other diagonal elements, T_{22} and T_{33}, are consistently increasing and decreasing respectively. Only pixel number from 45 to

60 shows no change because the surface is flat. The maximum power increased for T_{22} is -12dB observed on pixel number 38. On the other hand, the maximum power reduced to -12 dB for T_{33} on the same pixel. The amount of increased power in T_{22} is equal to the amount of the decreased power in T_{33}. The real and imaginary parts of the off diagonal elements of the coherency matrix $[T]$ are shown in Figure A.2.1 (Appendix A). The Yamaguchi four-component decomposition powers are applied to this new rotated coherency matrix $[T(\theta)]$ and calculated surface scattering $P_s(\theta)$, double-bounce $P_d(\theta)$, volume scattering $P_v(\theta)$ and helix scattering $P_h(\theta)$. Similar line of profile is plotted in Figure 3.10 to investigate the impact of applying POA compensation to four-component decomposition powers at Shestakovsky-N. The change of surface scattering power is very small due to its roll invariant property. The volume scattering power is consistently decreased after POA compensation and on the other hand double-bounce scattering power is increased. Unlike the coherency matrix, the volume scattering power is greater than double-bounce scattering power because the volume scattering model added more than the single T_{33} terms. As the helix power (not shown in Figure 3.10) is rotational invariant, it is not changed. The effect of POA compensation on Cloude and Pottier decompositions Alpha-Entropy-Anisotropy has not been investigated because of its roll invariant property.

3.6 Conclusions

To reduce the border effects, mismatches with the SAR data and errors in the delineation of the stand borders, the forest stands are buffered by 25 meters. The outdated forest inventory data are updated by using KOMPSAT-2 data for recent logging and disturbances, but no growth model is applied. The stand-wise mean values and standard deviations of polarimetric parameters are computed. If the standard deviations of polarimetric parameters are greater than 0.1, these stands are considered non-homogenous stand and thus are discarded. It has been found that between 15 and 20% stands are excluded. In Askne *et al.* (2003), a much larger standard error indicates very heterogeneous forest cover (e.g. partial clear-cut) for which the inventory data is probably erroneous.

The Faraday rotation angle is measured for all the test sites during 2006 to 2009. Highest 4.4° Faraday rotation is observed for ALOS PALSAR L-band image acquired on 21.05.2007 over Shestakovsky-N. It has been illustrated that Faraday rotation can be expected to reduce the quality of the ALOS PALSAR L-band data. The cross-polarised channel is much more likely to be distorted by the Faraday rotation than the co-polarised channels.

The impact of POA compensation on the coherency matrix and Yamaguchi four-component decomposition has been analysed. The POA is derived from the circular polarisation algorithm. The term T_{11} is roll invariant and there it remains unchanged. T_{22} term is increased by the same amount that T_{33} term is decreased. The four-component decomposition powers applied to rotated coherency matrix. It has been found that double-bounce scattering power is increased and the volume scattering power is decreased. Although surface scattering is roll invariant there is a slight modification of surface scattering power observed.

Chapter 4

Polarimetry in Siberian Forests

In this chapter, in order to assess the potentiality of ALOS L-band full polarimetric radar data, a number of polarimetric radar techniques will be analysed to characterise the polarisation response for forest cover on different meteorological conditions. Polarisation signatures and polarisation phase difference between HH and VV polarisations will be discussed in section 4.1 and 4.2 respectively in order to understand the scattering mechanisms. The analysis of the behaviour of the polarimetric coherence measurements as a function of growing stock volume (GSV) at different weather conditions, topographic variations and forest stand structures will be presented in section 4.3. Similar investigation for the polarimetric decomposition powers will be discussed in section 4.4. The important part of this section is to determine the existence of correlation between the polarimetric decomposition power and GSV and to examine the seasonal variability. Subsequently, an approach for estimating the GSV based on polarimetric decomposition powers will be discussed. The impact of tree species on polarimetric parameters will be presented in section 4.5. Finally, the concluding remarks will be pointed out in section 4.6.

4.1 Polarimetric signatures

Polarimetric signature is the visualization of behaviour of the target as a function of different polarisations. The shape of the polarimetric signatures provides information on the dominant scattering mechanism as well as the type of the polarisation (linear, circular) and also the target of the orientation by means of orientation angle. Figure 4.1 shows the L-band co-polarisation signatures of forest and non-forest areas in Shestakovsky-N. The co-polarisation signatures of other test sites are depicted in Figure B.1.1 (Appendix B). All the signatures shown in Figure 4.1 are derived from the Stokes matrix (Equation 2.10). The matrix is normalised to 1. For measuring polarimetric signatures, an area of 5625m² (3x3 pixels) are averaged. This would be a sufficient amount of pixels for reducing the statistical uncertainties on this analysis. It also reduces the speckle affect though the data already have been multi-looked before. The radar response is taken on homogenous stands where only one tree species are available.

In Shestakovsky-N, at thawing (10.04.2009) condition for aspen, birch, larch, and pine the highest power is observed at tau (ellipticity angle) =0º and at phi (orientation angle)=0º, ±90º which means that maximum co-polarised signature occurs at both HH- and VV-polarisation. The areas which are dominated by the birch forest also show similar co-polarisation signature except VV is slightly lower than HH. In all cases, the co-polarisation signatures are suggesting the dominance of multiple branch scattering combined with a weak double bounce component. Clear-cut areas show the characteristics similar to the forested area but with low pedestal height. The low pedestal height indicates the low unpolarised component due to the greater return from the ground surface and a smaller amount of volume scattering. Pedestal height, obtained from the polarimetric signature, is a useful parameter for better interpretation. The pedestal height is the minimum value of the intensity found on the polarimetric signature. If the signature is calculated from single scatterer the pedestal height becomes zero and if several samples are considered for measurement of polarimetric signature then pedestal height becomes nonzero. The pedestal height depends on the spatial variations of the radar backscatter properties and indicates the different types of scattering mechanism found in the averaged sample. The entire area which covered by the tree species are shown in Figure 4.1 has higher pedestal height except pine. The lower pedestal height from the pine forest areas confirms the large amount of surface scattering from the ground. At thawing condition, the decrease in the dielectric constant of the forest canopy results in a decrease in the contribution of diffuse scatterers. HH/VV is higher on frozen days. HV is lower in frozen days. This demonstrates that the decrease in the relative contribution of branch scattering (volume scattering) and increase in the relative contribution of direct return from the ground (surface scattering).

On the other hand at unfrozen (21.05.2007) condition, different polarisation signatures for aspen and pine have been observed. The backscattered power is maxima at tau=0º and at phi=0º (horizontal polarisation) and minima at phi=±90º which means the dominance of ground-trunk (double-bounce) scattering for this forest. In this case, the polarisation is horizontally oriented and targets are also horizontally oriented. This could be happened due to the wetter ground surface and moisture in the target which increases its dielectric constant. 0.2 cm precipitation is recorded one day before the SAR acquisition (21.05.2007). Birch and larch show the similar signatures as on thawing condition (10.04.2009). Pine forest has the higher pedestal height whereas on thawing condition lower pedestal height has been observed. The higher pedestal observed in the forest areas indicates the small amount of return from the ground surface. No difference of polarimetric signatures has been observed for clear-cut area at both thawing and unfrozen conditions.

The pedestal height is related to the degree of polarisation of the scattered wave. As the growing stock volume (GSV) increases, the degree of polarisation (DoP) decreases. This indicates that a larger amount of backscattered signal is unpolarised. The DoP is given by:

$$DoP = \frac{P_{max} - P_{min}}{P_{max} + P_{min}} \tag{4.1}$$

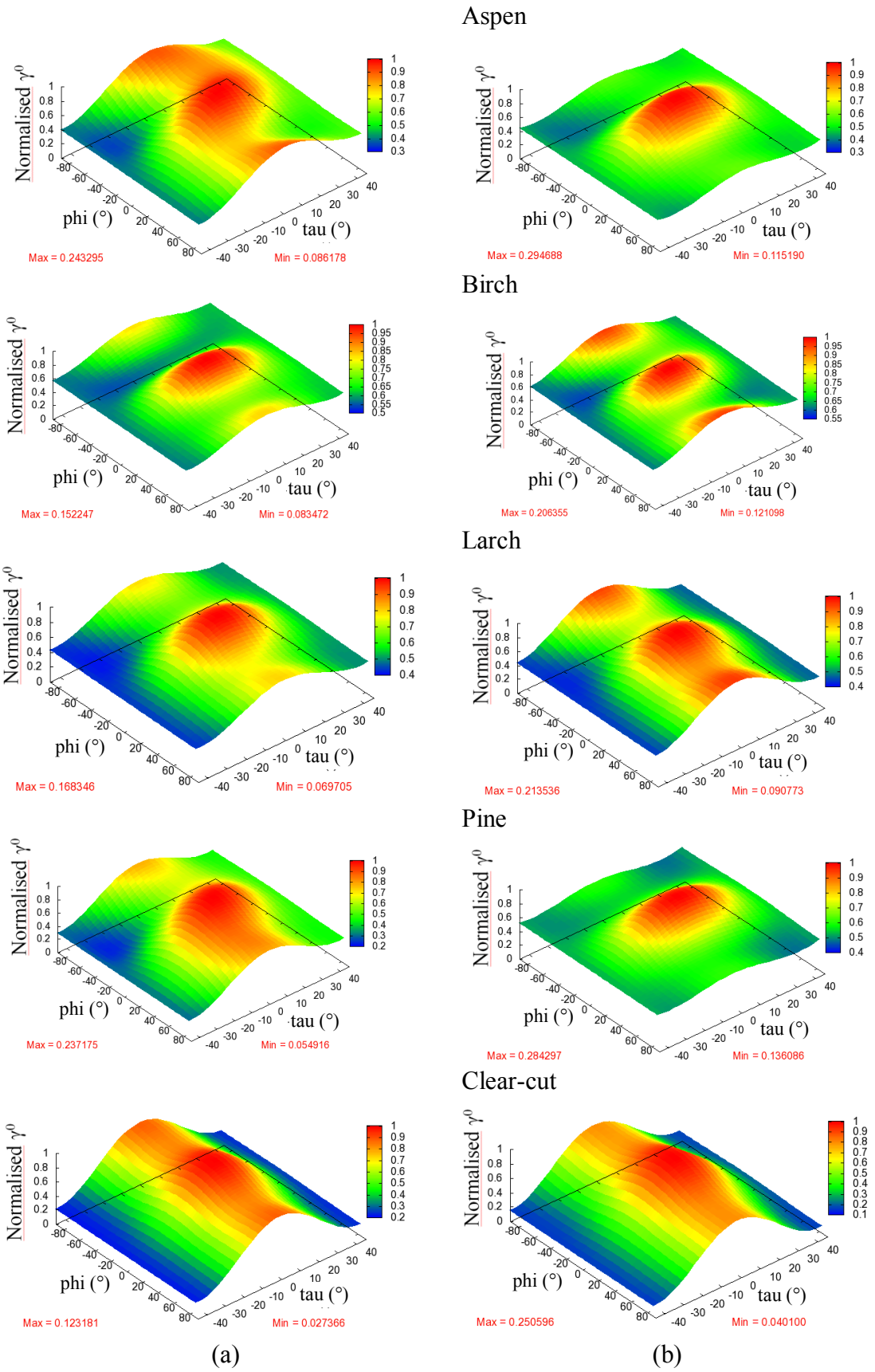

Figure 4.1 Observed ALOS PALSAR L-band co-polarisation signatures for aspen, birch, larch, pine and clear-cut areas at (a) thawing (10.04.2009) and (b) unfrozen (21.05.2007) conditions in Shestakovsky-N. "Max" and "Min" represent P_{max} and P_{min} respectively.

where P_{max} and P_{min}, are the minimum and maximum power obtained from the co-polarisation signatures. In Figure 4.1, "Max" and "Min" represent P_{max} and P_{min} respectively. When DoP = 1, the averaged return is completely polarised. On the other hand when DoP = 0, it is completely depolarised.

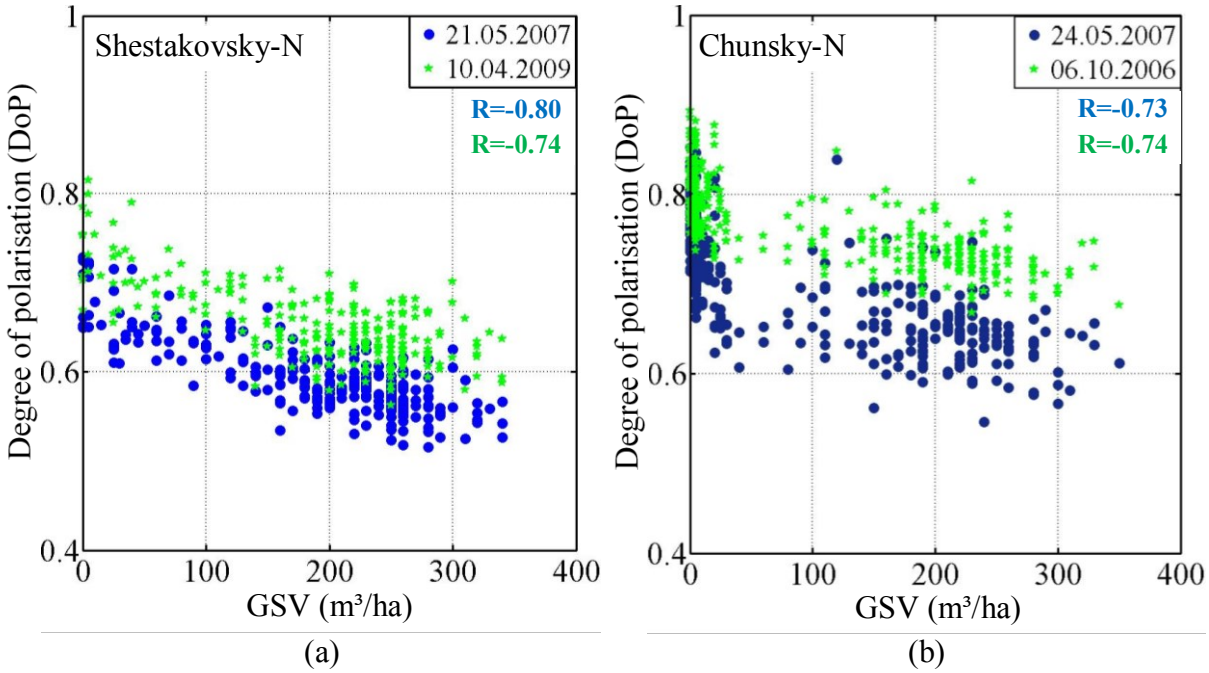

Figure 4.2 Observed degree of polarisation as a function of growing stock volume in (a) Shestakovsky-N and (b) Chunsky-N at different weather conditions.

Figure 4.2 depicts the strong correlation between the DoP and the GSV at different weather conditions in Shestakovsky-N and Chunsky-N. The DoP decreases with the increase of GSV in both test sites. This indicates that the non-polarised component increases as a function of GSV. In both test sites the DoP is appreciably higher at thawing and frozen conditions than at unfrozen condition. The effect of weather conditions on polarisation signatures using L-band data was also investigated by (Kwok *et al.* 1994). The authors investigated the change of L-band polarisation signatures caused by freezing for different forest types near Fairbanks, Alaska, U.S.A and found under unfrozen conditions, the DoP was noticeably reduced against frozen conditions. Low values of DoP indicate a considerable amount of received signal is non-polarised and also indicate the dominance of volume scattering.

4.2 Polarisation phase difference

A non-zero co-polarisation phase difference between HH and VV polarisation would be a consequence of a (i) bistatic reflection by the trunks, (ii) delay between H-polarised and V-polarised wave as the travel through the canopy and (iii) phase difference caused by the scattering of the target. Every scattering event adds 180° phase shift between the vertically and horizontally polarised electric field. A phase difference of 180° is characterised by ground-trunk interaction which is defined by double-bounce scattering, while values close

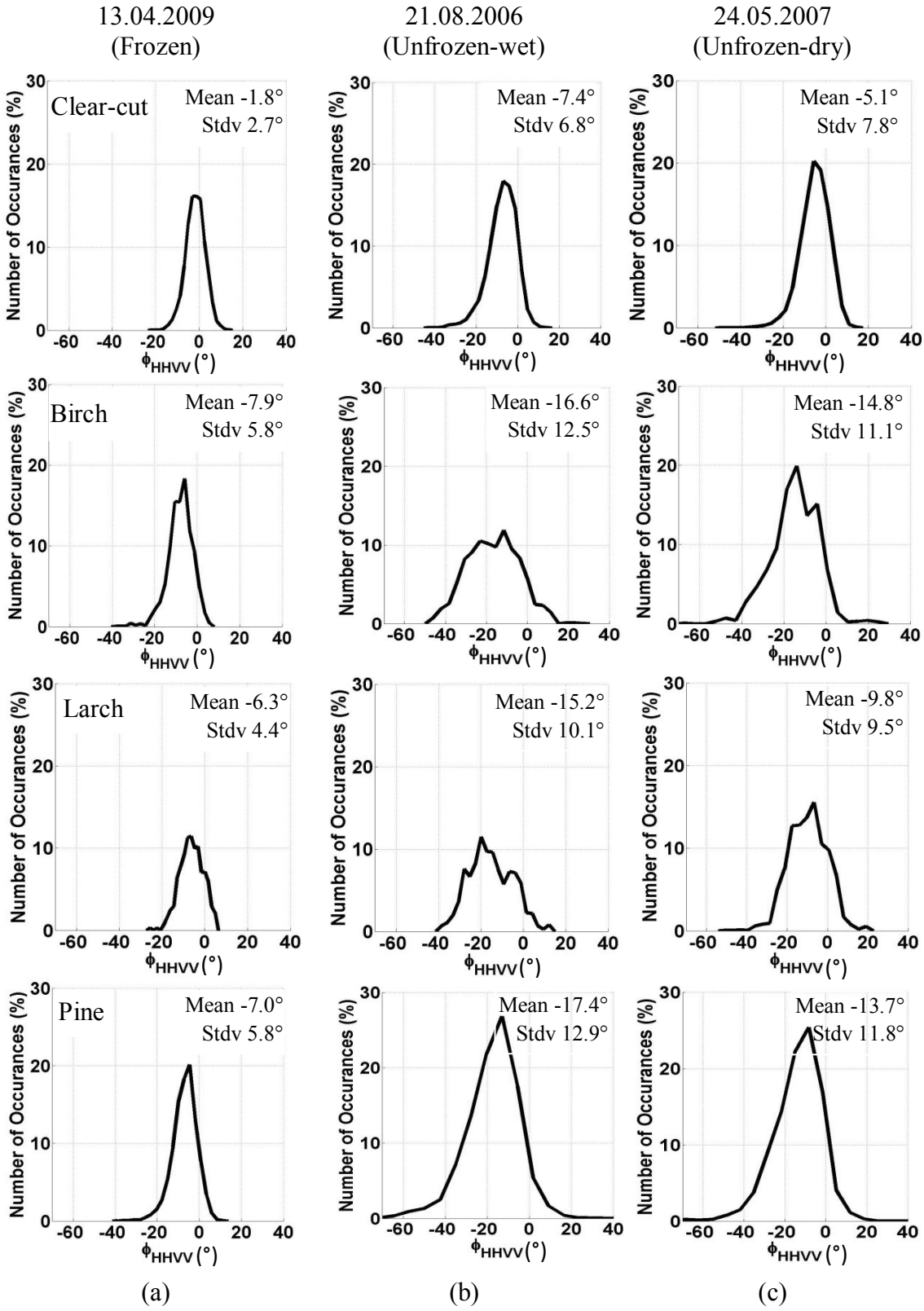

Figure 4.3 Observed changes of ALOS PALSAR L-band HHVV-phase differences at (a) frozen (13.04.2009), (b) unfrozen-wet (21.08.2006) and (c) unfrozen-dry (24. 05.2007) conditions in Chunsky-N. The figure shows the mean and standard deviations of the clear-cut and different tree species.

to 0° indicates surface scattering.

The polarisation phase difference (PPD) histograms for clear-cut and different types of tree species birch, larch, and pine in Chunsky-N at frozen, unfrozen-wet and unfrozen-dry conditions are illustrated in Figure 4.3. The other examples of PPD histogram for non-forest and forest areas of Shestakovsky-N and Primorsky-E are shown in Figure B.2.2 and Figure B.2.3 (Appendix B) respectively. Only the tree species which contribute at least 70% of GSV in each stand are considered for the investigations. The changes of mean and standard deviations during frozen and unfrozen conditions are measured. The standard deviation represents the variability of the PPD. Regardless the weather conditions, the histograms for clear-cut areas feature a sharp peak at which mean value is close to zero. This indicates the dominance of surface scattering mechanism at any weather conditions. The PPD of forest areas, dominated by vertical structure, are found to be different compare to clear-cut areas. The PPD distributions of aspen, birch, larch, and pine forests are much wider than the non-forest areas. The spread of PPD distribution indicates the high variability in the scattering property due to the contribution of multiple branch scattering (or volume scattering).

During freezing (13.04.2009) the mean and standard deviation of PPD has been observed to be smaller than at unfrozen conditions on both 24.05.2007 and 21.08.2006. The PPD difference between frozen and unfrozen conditions indicates an impact of the meteorological conditions. Furthermore, the comparatively low standard deviation of PPD during freezing means less depolarisation of the returned signal. Within the forest areas, larch shows, especially in unfrozen-dry condition lower variability (smaller standard deviation of PPD) than the other tree species.

The mean values of PPD and their standard deviations are computed for different classes of GSV. The results are illustrated in Figure 4.4 where mean values are shown as '*' and vertical bars represent the standard deviation of the PPD of the stands within the GSV classes. As the GSV increases PPD also increase. In both test sites, the negative PPD have been observed for different weather conditions. At L-band the two-way attenuation by the vegetation layer of backscatter from the ground below the vegetation layer results in a negative phase difference, whereas the backscatter from the plant-ground double bounce reflection results in a positive phase difference (Ulaby *et al.* 1987).

In Shestakovsky-N, polarisation phase difference is found to increase from -5° (clear-cut, bog areas) to -18° for 150-180 m^3/ha GSV class at frozen conditions whereas at unfrozen condition (21.05.2007) PPD varies from -10° to -23°. The results show that as the GSV increases the PPD moves away from the zero degree and standard deviation of PPD increases. For the GSV class 0-30 m^3/ha, surface scattering is the main contributor as mean PPD more close to the zero. A linear correlation has been found between PPD and GSV up to 180 m^3/ha. The results show that as the vegetation increases, the multiple scattering from trunk and primary branches also are increased. For GSV greater than 180 m^3/ha, the PPD values are randomly distributed. This could be due to the negligible ground contribution beyond this point.

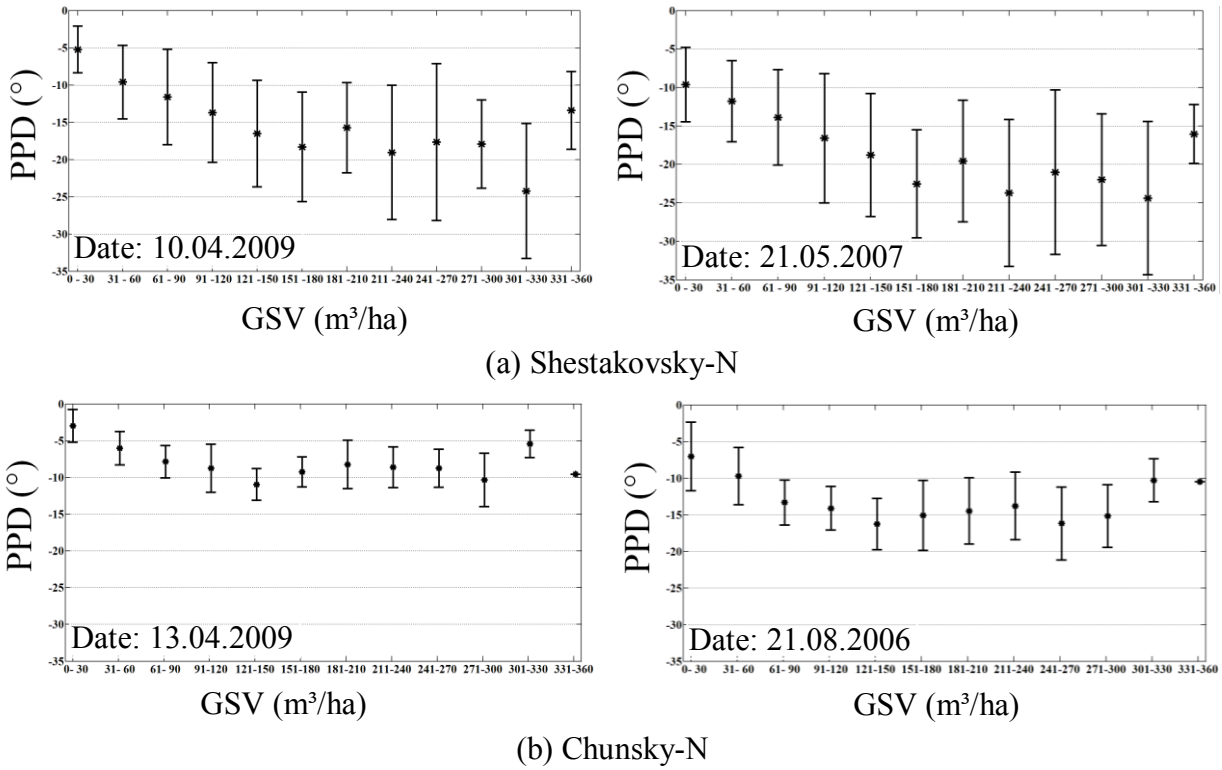

Figure 4.4 Mean polarisation phase difference between HH and VV polarisations as a function of GSV under (a) thawing (10.04.2009) and unfrozen (21.05.2007) conditions in Shestakovsky-N and (b) frozen (13.04.2009) and unfrozen (21.08.2006) conditions in Chunsky-N.

Similar trends are also found in Chunsky-N for frozen (13.04.2009) and unfrozen (21.08.2006) conditions. The results show that as GSV increases the PPD also increase. For the GSV class 0-30 m³/ha surface scattering is the main contributor so mean PPD more close to the zero degree. Standard deviation of this GSV class is relatively higher compare to other higher GSV classes. This could be due to (i) unfrozen condition and (ii) a large number of heterogeneous stands are considered on that class.

Mean PPD monotonically increases from -7º to -16º for GSV class 121-150. After GSV class 121-150, the PPD values are randomly distributed. On unfrozen day the mean values of PPD for each GSV class standard deviations are higher.

Therefore, observable increase of mean and deviations of PPD suggesting a high variability in the scattering properties due to the contribution of branch scattering at unfrozen condition. Further support to this assumption is found in the investigation by Kwok *et al.* (1994).

4.3 Polarimetric coherences

To investigate the dependency of polarimetric coherence (or HHVV-coherence) on growing stock volume, scatter plots of GSV versus HHVV-coherence are produced for Shestakovsky-N, Primorsky-E, Chunsky-E, Chunsky-N and Bolshe-NE (Figure 4.5). The

coherence values are measured by averaging all the pixels within each forest stand. The clear decrease of coherence for the increasing GSV with small spread has been observed for different weather conditions. To allow a quantitative analysis between the GSV and polarimetric coherence, Pearson's correlation coefficient has been calculated for all plots. Pearson's correlation coefficient and regression parameters are reported in Table B.1 (Appendix B). The highest correlation R= -0.87 between coherence and GSV is obtained under unfrozen condition in Shestakovsky-N. The significant differences of the scatter plots of these three test sites, Primorsky-E, Chunsky-E and Chunsky-N, are the large spread of coherence values over the GSV. Large dynamic range and little spread have been observed in Shestakovsky-N whereas Primorsky-E and Chunsky-N are affected by small dynamic range and larger spread respectively. The stands of GSV below 10 m³/ha in Chunsky-N, the coherence spreads over half of the whole dynamic range. The possible reason can be the discrepancies between forest inventory data and radar acquisition. The level of coherence is high in Chunsky-N. This could be due to the environmental conditions.

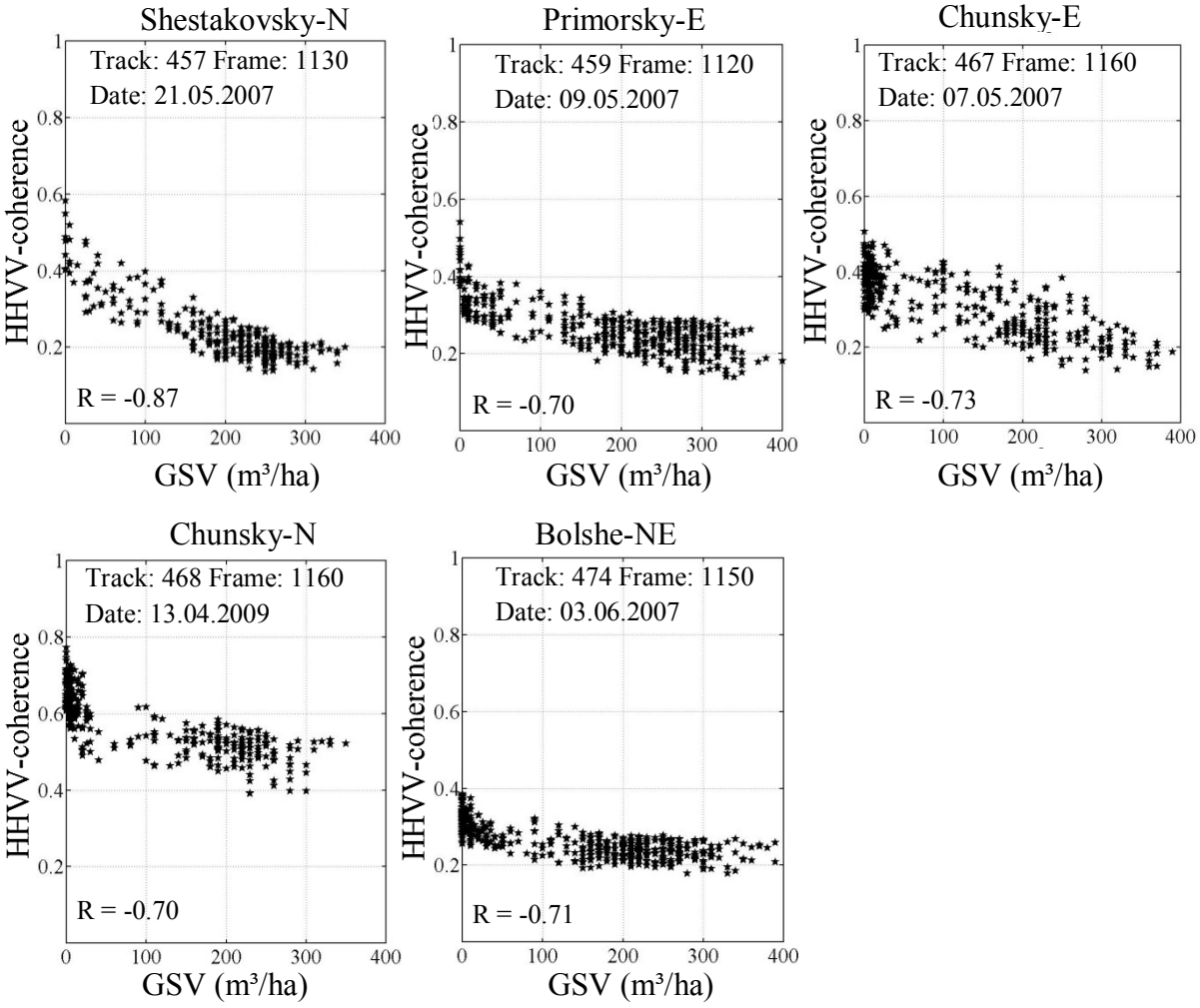

Figure 4.5 Observed coherence versus growing stock volume in m³/ha for Shestakovsky-N, Primorsky-E, Chunsky-E Chunsky-N, Bolshe-NE and Bolshe-SE. The figure shows the track and frame number of ALOS PALSAR L-band data. The asterisk '*' shows the stand-wise mean coherence.

The saturation level of coherence for GSV is defined using the following scheme (Thiel *et al.* 2012):

i) Calculate the mean coherence $\gamma_{\Delta 50GSV}$ for 50 m³/ha *GSV* classes (e.g. GSV_{class1} = 0-50 m³/ha, GSV_{class2} = 50-100 m³/ha etc.);

ii) Compute the normalised mean coherence $\gamma_{\Delta 50GSVnorm}$ by dividing $\gamma_{\Delta 50GSV}$ by standard deviation of coherence, σ_{coh} for each 50 m³/ha *GSV* classes.

iii) Compute the normalised mean coherence difference $\Delta\gamma_{\Delta 50GSVnorm}$ between all adjacent 50 m³/ha *GSV* classes, at which the coherence of the lower *GSV* class is the minuend.

iv) Measured the slope, $\theta_{sat} = tan^{-1}(\Delta\gamma_{\Delta 50GSVnorm}/50)$ between the two 50 m³/ha *GSV* adjacent classes.

Since the mean coherence is normalised by the standard deviation of within 50 m³/ha *GSV* classes, the spread of the coherence has a negative impact on the saturation level. The larger the spread the lower the saturation level for GSV.

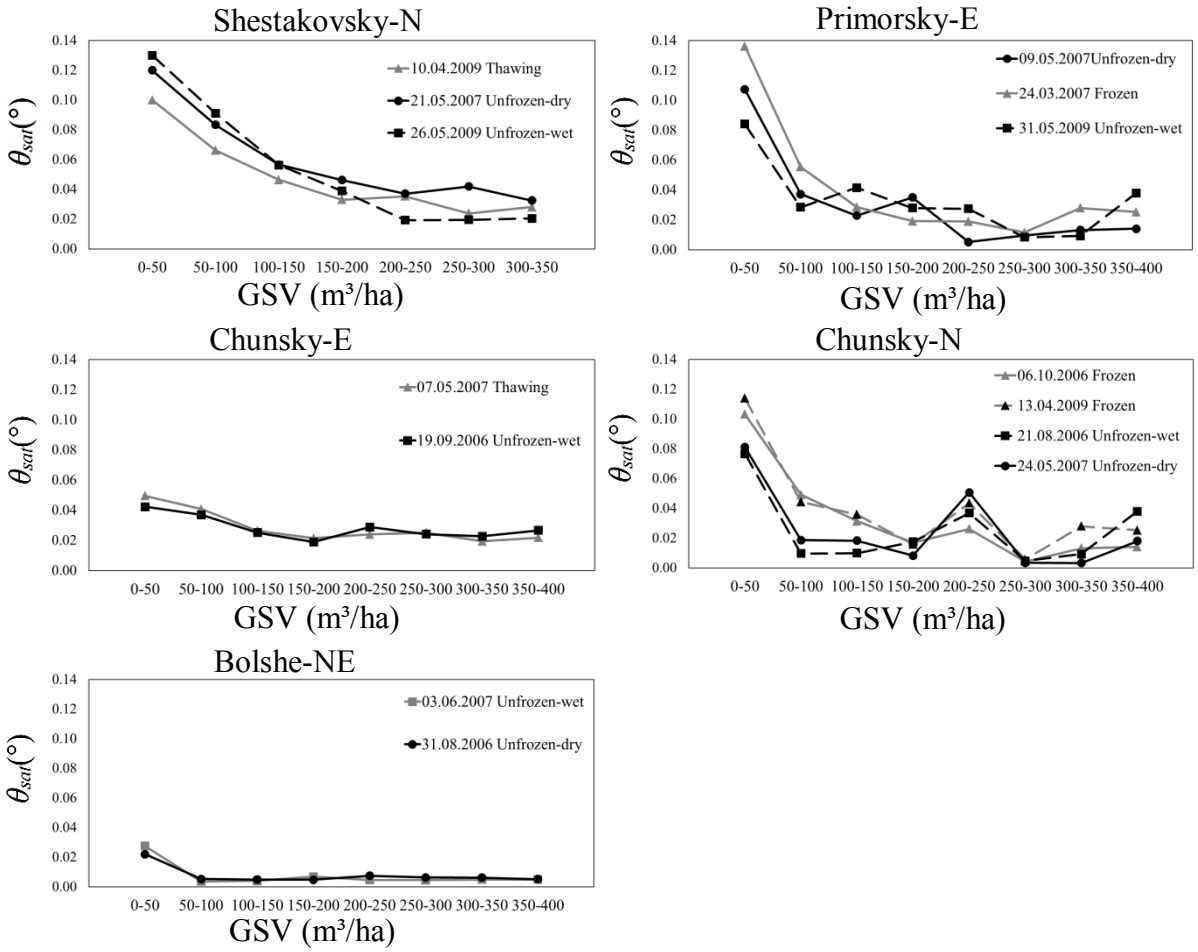

Figure 4.6 Observed saturation levels for forest growing stock volume using ALOS PALSAR L-band HHVV-coherence in Shestakovsky-N, Primorsky-E, Chunsky-E Chunsky-N and Bolshe-NE.

Figure 4.6 depicts the saturation level for forest GSV using HHVV-coherence at all the test sites in Siberian forests. The slope between the two classes of GSV has been measured. The highest saturation level at ~250 m³/ha achieved for unfrozen condition (21.05.2007 and 26.05.2009) in Shestakovsky-N. One has to keep in mind that no image has been acquired at frozen condition in Shestakovsky-N. The images acquired at frozen condition show higher level of saturation than for image at unfrozen condition in Primorsky-E and Chunsky-N. The lowest saturation at ~100 m³/ha has been observed in Bolshe-NE. Previous studies (Eriksson *et al.* 2003,Thiel and Schmullius 2009) have shown that saturation for GSV using L-band coherence in Siberia commonly occurs at GSV values < 200 m³/ha. Eriksson *et al.* (2003) found the saturation level for winter coherence images between 100 and 130 m³/ha in Bolshe.

In previous chapter it has been discussed that due to the speckle affect, the stands which are less than 2 ha and the standard deviation of stand-wise coherence greater than 0.1 are excluded. When screening the forest parameters in the inventory data for erroneous measurements, obvious discrepancies with the satellite data are found. For some stands, the inventory data indicates high stem volume although the coherence is very high. This was most likely the consequence of a failed update of the inventory data after logging has been done. Extreme outliers in the GSV-coherence relationship are discarded by identifying all the stands with a coherence more than two standard deviations of all stand-wise coherence measurements above or below the main trend, which is identified by means of a simple regression model that is fitted to the data: To remove the extreme outliers a non-linear equation which describes the relationship between GSV and coherence is applied, as shown in Equation 4.2.

$$\gamma_{HHVV} = a.exp^{-b*GSV} + c \tag{4.2}$$

where *a, b, c* are the regression parameters and γ_{HHVV} is the HHVV-coherence. This expression was applied by Eriksson, (2004) to describe the relationship between GSV and interferometric coherence. The stands which are outside of the two standard deviation of the regression line are removed. A much larger standard error indicates very heterogeneous forest cover (e.g. partial cut, fire scars and logging) for which the inventory data is probably erroneous.

In the following sub sections, the investigations will be carried out for the relationship between coherence and GSV in terms of weather conditions, forest stand structure i.e. relative stocking and forest stand size. The rationale behind the impact of stand size is that larger stands include more pixels on the coherence can be averaged, thus reducing the speckle effect as well as noise in the measurements. Fransson *et al.* (2001) and Santoro *et al.* (2002) investigated the retrieval of GSV from ERS-1/2 coherence has higher accuracy for stands larger than 2 ha. Santoro *et al*. (2002) showed that the estimation of GSV at stand level has significantly lower error than at plot level (circle of 7 – 10 m radius). Askne and Santoro, (2005) observed that not only the stand size but also other factors such as forest structural homogeneities play a signification role for defining the retrieval accuracy.

Since the coherence is determined by the ground and the vegetation scatterers within a pixel area, it is reasonable to assume that tree density plays a significant role.

4.3.1 Multi-temporal consistency

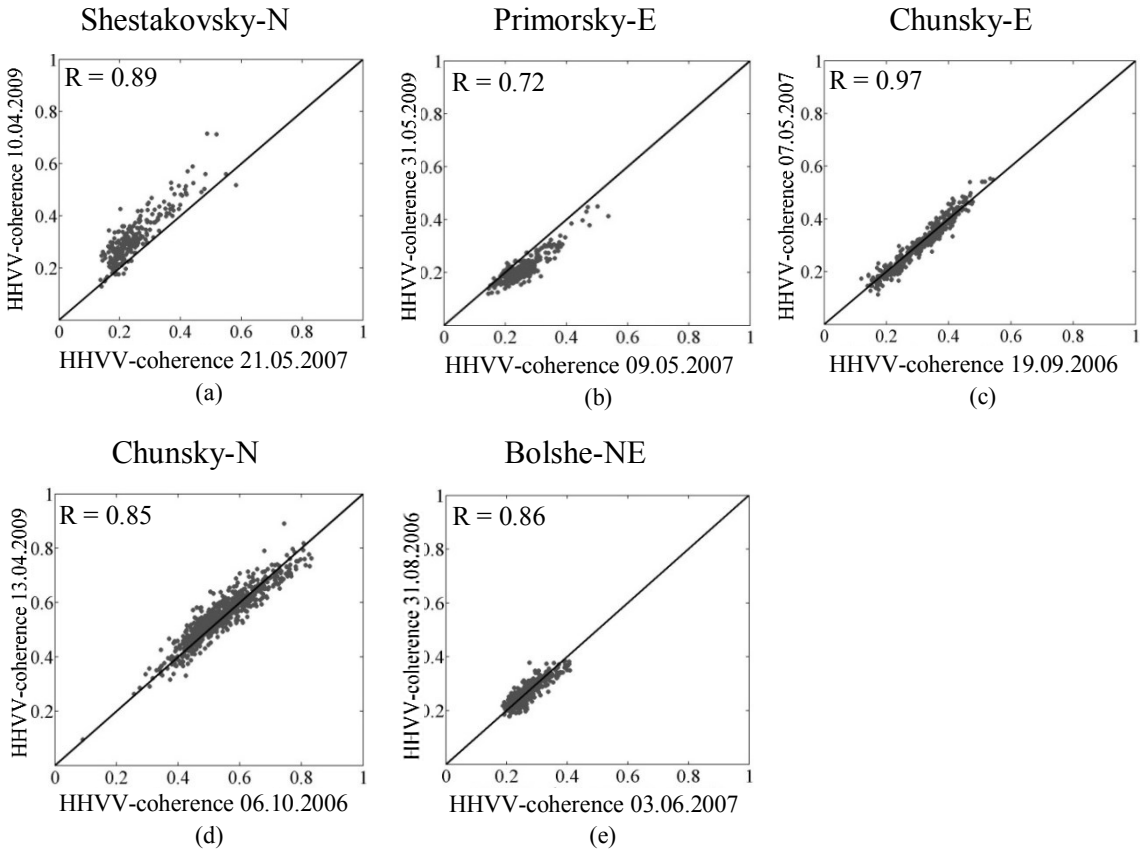

Figure 4.7 ALOS PALSAR L-band HHVV-coherence from two different acquisition dates plotted against each other for (a) Shestakovsky-N, (b) Primorsky-E, (c) Chunsky-E, (d) Chunsky-N and (e) Bolshe-NE.

The consistencies of the HHVV-coherence over the years on same weather conditions are investigated. Five scatter plots for the stand-wise coherence of the two different dates are displayed in Figure 4.7. The temporal consistency of the coherence is high with Pearson's correlation coefficients between 0.86 and 0.97. These high correlations indicate the degree to which coherence change consistently that may be related to the robustness of using coherence to characterise GSV. A slight positive offset with respect to the 1:1 line, caused by the differing environmental conditions, is observed in Figure 4.7(a). This indicates that the environmental conditions are different on these dates. It has been snowed during the acquisition of the image acquired on 10.04.2009 (thawing condition) and on 21.05.2007 (unfrozen condition) no precipitation recorded by the weather stations. In Primorsky-E, two images acquired at similar weather conditions have been compared. The temperatures on both days were almost similar but 1.6 cm precipitation recorded by the weather station on 31.05.09 whereas no precipitation has been reported during one week before 09.05.2007. This result shows that the coherence value is lower during the moderate

rainfall in forest where the dielectric properties are higher for the forest ground and vegetation. No offset is found for Chunsky-N, Chunsky-E and Bolshe-NE because the two images of each forest compartments acquired under the same environmental conditions. The Pearson's correlation coefficients between the fourteen acquisitions in Shestakovsky-N, Primorsky-E, Chunsky-N, Chunsky-E and Bolshe-NE are greater than 0.80 (one acquisition is 0.72). No outliers have been observed in Figure 4.7. This indicates that the considered forest stands are not affected by the disturbances between two acquisition dates of ALOS PALSAR L-band coherence images.

4.3.2 Seasonal variations

In this section seasonal behaviour of HHVV-coherence observations for both sparse and dense forests are discussed in terms of different environmental conditions. It has been widely known that the SAR system does not suffer from cloudiness or day-night cycle but SAR image is affected by the meteorological conditions. Both intensity and coherence images are strictly depended on the weather condition. Figure 4.8 and Figure 4.9 show the coherence values for sparse and dense forest at Shestakovsky-N, Primorsky-E, Chunsky-E, Chunsky-N and Bolshe-NE.

The sparse forests, where the forest canopy is characterised by large gaps, represent the stands with GSV from 0 to 20 m^3/ha. Dense forest comprises all stands with a GSV above 250 m^3/ha. By choosing these GSV ranges, a sufficient number of stands are available for each forest class. For the different test sites, the mean GSV for sparse forest varies between 6 m^3/ha and 10 m^3/ha. For dense forest it varies between 273 m^3/ha and 300 m^3/ha. In Shestakovsky-N, the coherence value for sparse forest is 0.53 at thawing condition (10.04.2009) whereas at unfrozen-dry (21.05.2007) and unfrozen-wet conditions (25.05.2009) a mean coherence of ~0.40 is observed. The difference of mean coherence values for sparse forest between unfrozen-dry (21.05.2007) and unfrozen-wet (25.05.2009) condition is not significant. The standard deviations of coherence for sparse forest are similar at all weather conditions in Shestakovsky-N. Primorsky-E shows similar mean coherence values like Shestakovsky-N for sparse forest at frozen (24.03.2007) and unfrozen-dry (09.05.2007) conditions. At unfrozen-wet (31.05.2009) condition the coherence value is ~0.31 which is lower than the same weather condition in Shestakovsky-N. This could be happened due to the wetter ground. Since 1.6 cm rained before the acquisition of SAR, the dielectric constant on the ground is high. The two coherence images for Bolshe-NE are acquired on unfrozen-dry (31.08.2006) and unfrozen-wet (03.06.2007) conditions. A slight difference of coherence value is observed for sparse forest. Bolshe-NE shows the lowest coherence value ~0.30 for sparse forest.

In Chunsky-E, the coherence for sparse forest is slightly higher at thawing (07.05.2007) condition than the coherence at unfrozen-wet (19.09.2006) condition. Four multi-temporal images are available for Chunsky-N. Two images acquired in winter, one in summer and other one in spring. In frozen conditions (06.10.2006 and 13.04.2009) the mean coherence for sparse forest are in the range between 0.63 and 0.65 whereas the images acquired at unfrozen conditions show the mean coherence nearly 0.47. The coherence value in

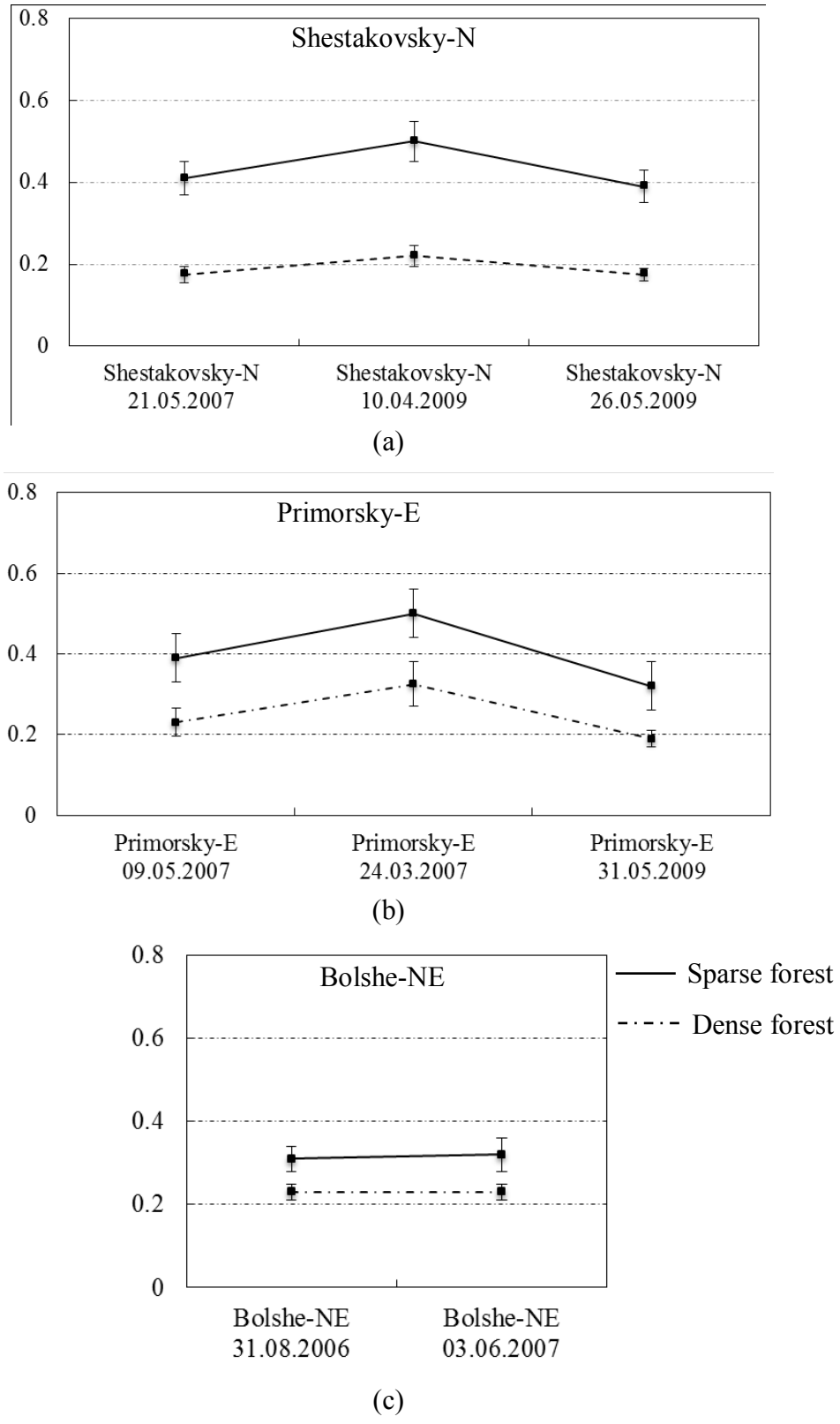

Figure 4.8 Seasonal behaviour of coherence observations for (a) Shestakovsky-N, (b) Primorsky-E and (c) Bolshe-NE. The average coherence values for each test sites are shown as "box" and the vertical bars represent the standard deviation. The solid line presents the coherence values for sparse forest and the dashed line presents dense forest.

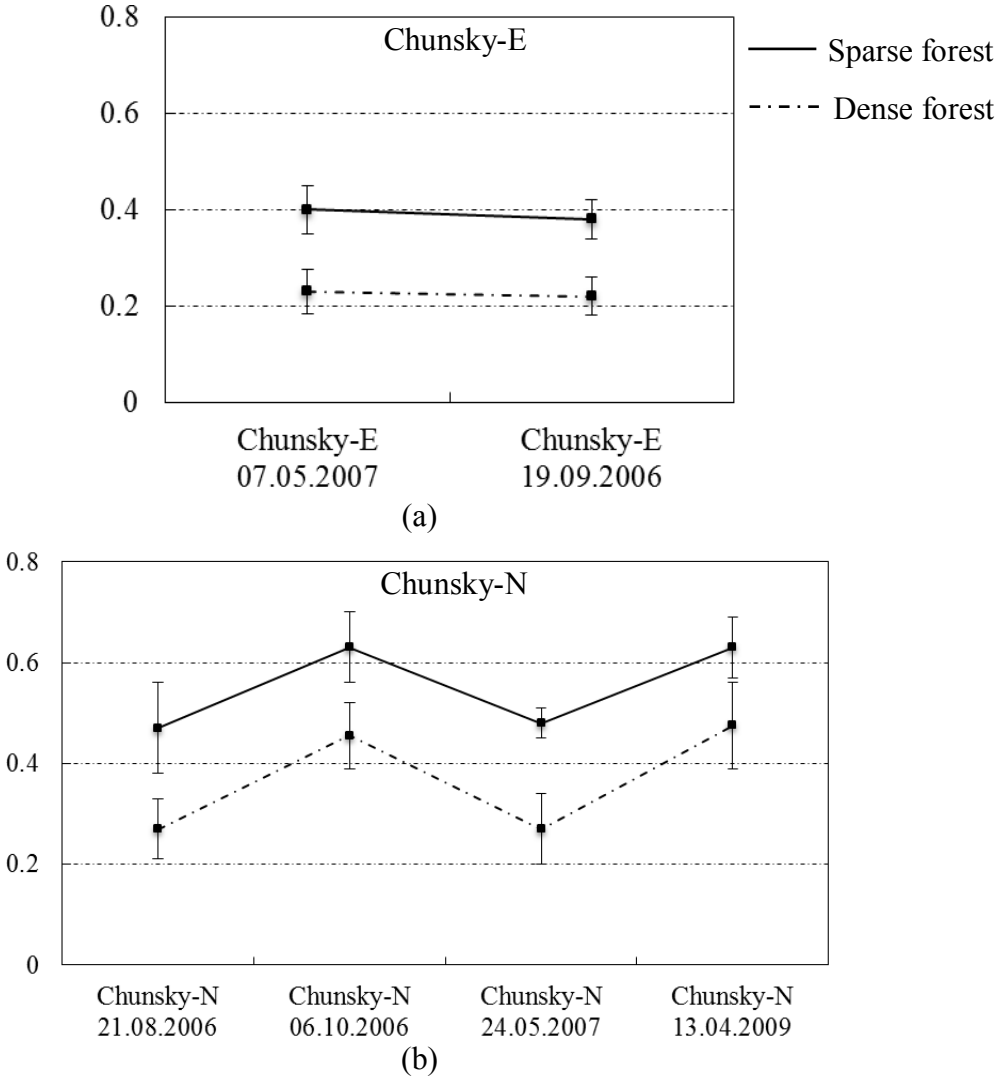

Figure 4.9 Seasonal behaviour of coherence observations for (a) Chunsky-E and (b) Chunsky-N. The average coherence values for each test sites are shown as "box" and vertical bars represent the standard deviation. The solid line presents the coherence values for sparse forest and the dashed line presents dense forest.

Chunsky-N for frozen condition is higher than the coherence at same condition in Primorsky-E and Shestakovsky-N. This could be due to the presence of higher snow cover (20 cm snow depth is reported by the weather station).

In frozen condition, all the trees can be expected to be temporally stable. Geometric properties are also of less importance. Due to freezing the dielectric constant of the trees is reduced (Dobson *et al.* 1990; Way *et al.* 1994), resulting in decreased attenuation. Thus, the amount of scattering within the canopy is also decreased (Kwok *et al.* 1994).

Bolshe-NE shows the lowest mean coherence values of both images for sparse forest. 0.23 and 0.80 cm precipitation recorded three days before the acquisitions. In Santoro *et al.* (2007a), it was assumed to be consequence of differences in heterogeneous soil moisture variations. Bolshe-NE is located west of the Yenisei river where peat soils are

dominant. Therefore, peat soils still have been in drying process, accompanied by heterogeneous soil moisture variations dropping the coherence in sparse forest. Eriksson, (2004) and Cartus, (2010) also reported the lowest coherence values for sparse forest in Bolshe-NE.

Coherence in dense forest shows similar behaviour like the coherence in sparse forest at frozen, unfrozen and thawing conditions. The lower standard deviation in all the test sites except Chunsky-N indicates the less dispersion of coherence values in dense forests. The observed coherence is higher for sparse forest than for dense forest. Relatively high coherence has been observed at frozen condition.

Figure 4.10 is summarised by the interpretation of Figure 4.8 and Figure 4.9. In summary, a contrast between sparse forest and dense forest has been observed at all weather conditions. A highest dynamic range of coherence 0.3 is observed. The variations of absolute level of coherence for sparse forest are larger than for the dense forest at unfrozen condition. The coherence for sparse forest differs from one test site to another test site at unfrozen condition whereas coherence for dense forest does not differ. The soil moisture content of the forest floor in different test sites and forest understories can affect the coherence in sparse forest. No variation of coherence has been observed for both sparse and dense forest at frozen and thawing conditions.

The highest value of coherence has been observed at frozen condition in sparse forest and dense forest. In forest, frozen condition with snow cover results in a decrease of dielectric constant of both, vegetation and surface. The lower dielectric constant causes reduction of scattering from the branches and a higher contribution of ground scattering. The reduced attenuation and deeper penetration positively influence the coherence.

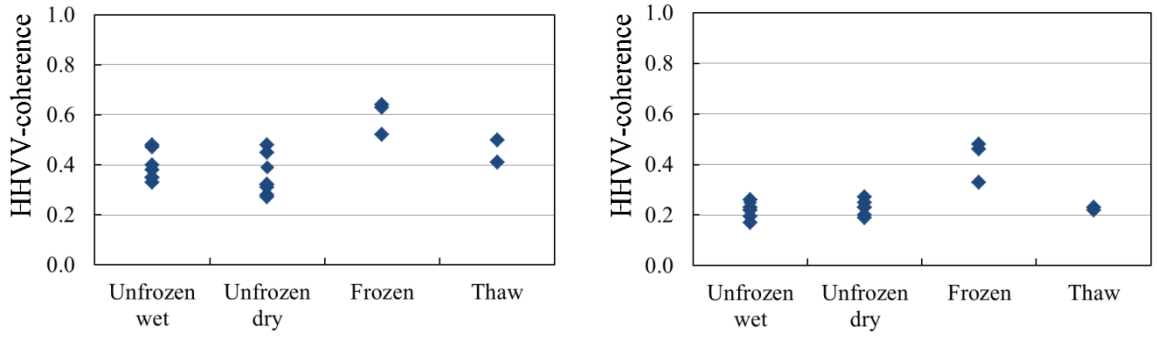

Figure 4.10 Polarimetric coherence values for (a) sparse forest and (b) dense forest at different weather conditions in Siberian forests.

No impact of topography on the relation between coherence and GSV has been observed. In previous chapter (section 3.1) it has been discussed that the topography in all the test sites in Siberia are mostly gentle. Almost 95% stands has slope less than 10º. The dependency of coherence upon stand size and relative stocking as a function of GSV has been investigated. Table 4.1 confirms that the correlation between HHVV-coherence and

Stand size (ha)	Number of stands	Dates		
		10.04.2009	21.05.2007	25.05.2009
2-10	42	-0.75	-0.84	-0.80
11-20	75	-0.80	-0.88	-0.87
21-30	47	-0.87	-0.84	-0.81
31-40	30	-0.78	-0.78	-0.79
41-50	26	-0.70	-0.75	-0.80
51-135	36	-0.95	-0.89	-0.91

Table 4.1 Pearson's correlation coefficients between stand-wise HHVV-coherence and GSV as a function of different stand size in Shestakovsky-N.

GSV does not depend on the size of the stands in Shestakovsky-N. Although the highest correlation achieved in largest stands (51-135 ha), there is no increase or decrease trend is observed as a function of stand size. Although only one example, this is also observed in other test sites in Siberian forests at different weather conditions. Concerning the trend of coherence as function of growing stock volume, an impact of the forest stand structures (relative stocking (RS)) has been found. A slightly higher correlation between HHVV-coherence and GSV is observed for stands with RS>70% compare to the stands with RS<70%.

4.4 Polarimetric decomposition powers

Yamaguchi *et al.* (2005) proposed a four-component scattering model based on the coherency matrix $[T]$ for the polarimetric SAR decomposition. This method is applied to ALOS PALSAR L-band data for both the coherency matrix $[T]$ and rotated coherency matrix $[T(\theta)]$ to obtain the decomposition powers, which consists of surface scattering P_s, double-bounce P_d, volume scattering P_v, and helix scattering P_h. After the rotation of coherency matrix the decomposition powers become $P_h(\theta), P_s(\theta), P_d(\theta),$ and $P_v(\theta)$. Here θ indicates the line of sight rotation (for details see section 3.5.2). Before applying the four-component decomposition powers to the ALOS PALASAR L-band data obtained from the Siberian forests to extract GSV information, the impact of line of sight rotation is investigated in the following section. The analysis is carried out mainly on different range of topographic areas (e.g. slope classes).

4.4.1 Impact of line of sight (LOS) rotation

Yamaguchi *et al.* (2011) published an approach of how the rotation of coherency matrix $[T]$, can be used to correct the polarimetric orientation angle (POA). The effect of this correction is particularly observable in urban areas, if buildings are not orthogonal to the radar LOS. In this study, the investigations will be carried on forest areas in Siberia. Figure

4.11 depicts the impact of applying the POA compensation to four-component decomposition powers. The mean values and the standard deviations of polarimetric

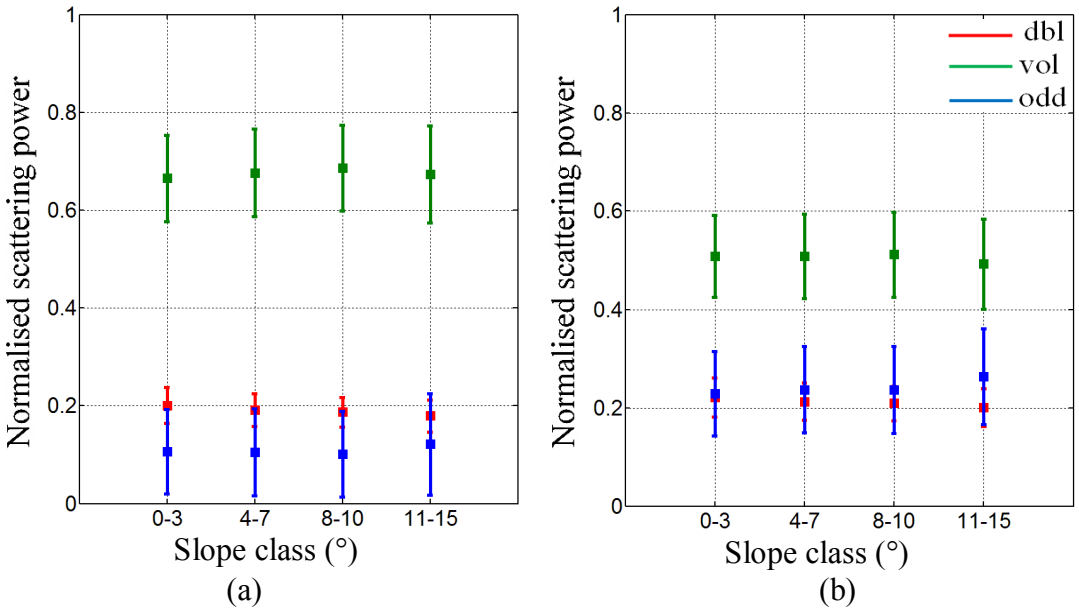

Figure 4.11 The mean decomposition scattering powers (a) before and (b) after the rotation of coherency matrix [T], for different slope classes in Shestakovsky-N. Red, green, blue, and black colours represent double-bounce, volume scattering, surface scattering, and helix scattering respectively.

Slope class (°)	Mean GSV (m³/ha)	Stdv GSV(m³/ha)	Mean POA (°)	Stdv POA (°)
0-3	193	78	±3.9	2.3
4-7	208	78	±4.3	2.7
8-10	205	74	±4.5	2.9
11-15	202	87	±4.8	3.3

Table 4.2 Mean and standard deviations (stdv) of GSV and polarisation orientation angles (POA) which are derived by circular polarisation algorithm (Equation 3.11) for different slope classes.

decomposition powers P_d, P_s, P_v, and $P_d(\theta), P_s(\theta), P_v(\theta)$, have been computed for different slope classes in Shestakovsky-N test site. The mean values are shown as squares and the vertical bars represent the standard deviation of the mean decomposition powers within the slope classes. The mean GSV and their standard deviations of the corresponding slope classes are given in Table 4.2. The mean GSV of all slope classes varies between 193 m³/ha and 208 m³/ha. The standard deviations range from 54 m³/ha to 67 m³/ha. The derived polarimetric OAs vary between -3.9° and +4.8° for all the investigated areas. The

POA extracted from polarimetric data shows a high standard variation mainly due to the phase noise. The POA compensation results in a decrease of volume scattering and an increase of double-bounce and surface scattering. The amount of the decrease of volume scattering is equal to the amount of the increase of double-bounce and surface scattering. The double-bounce and surface scattering power increase between 7 and 13%, whereas volume scattering power decreases between 13 and 25% over all studied areas. The POA of images show slight sensitivity to the topography under the forest at frozen conditions than at unfrozen conditions. This could be due to the deeper penetration to forest ground at frozen condition.

4.4.2 Growing stock volume and polarimetric decomposition powers

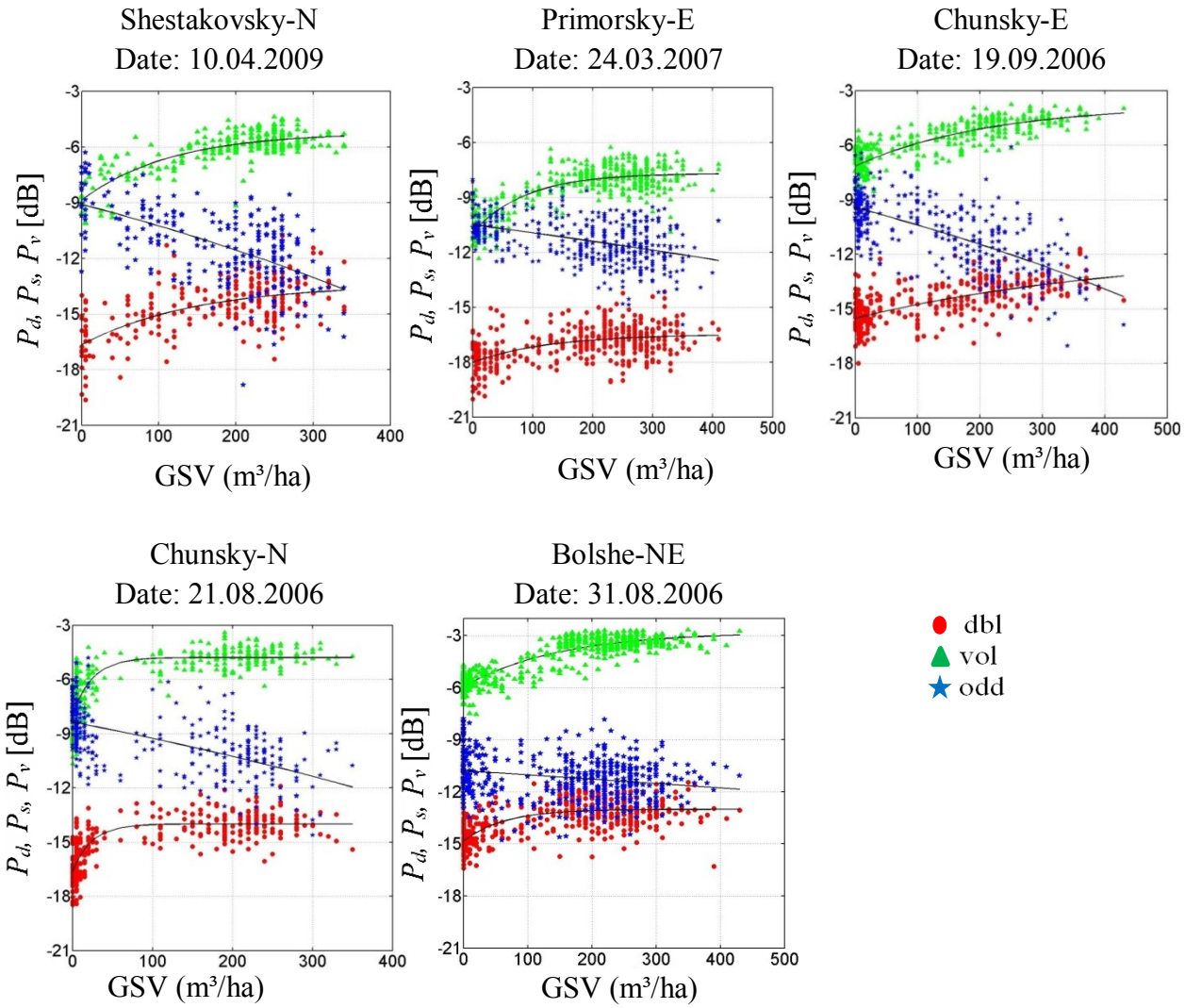

Figure 4.12 Relationship of GSV and decomposition powers, derived without rotation of coherence matrix [T]. Red, green, and blue represent the double-bounce, volume, and surface scattering power respectively.

The relationships between GSV and stand-wise polarimetric decomposition powers P_s, P_d, and P_v are illustrated in Figure 4.12 for Shestakovsky-N, Primorsky-E, Chunsky-E,

Chunsky-N and Bolshe-NE. Helix scattering power is not shown here since it characterises mainly the artificial targets (Yamaguchi *et al*. 2011). All analyses in this research have been done at forest stand level. Therefore, the decomposition powers are measured by averaging all the pixels within each stand. In all cases, the stand-wise average of $P_{d,}$ P_v increases and P_s decreases with the increasing of GSV.

Similarly, Figure 4.13 shows the same trend for $P_s(\theta), P_d(\theta)$, and $P_v(\theta)$. To allow a quantitative analysis between the GSV and polarimetric decomposition powers, Pearson's correlation coefficient has been calculated for all plots. Pearson's correlation coefficients are reported in Table 4.3. The $P_d(\theta)$ correlation is significantly better than P_d for the entire test sites for all the acquisitions. On the other hand the correlation between $P_s(\theta)$ and GSV decreases. Especially for all the acquisitions in Primorsky-E and for one acquisition (21.08.2006) in Chunsky-N, the $P_s(\theta)$ correlation declines noticeably compared to P_s. P_v and $P_v(\theta)$ remain almost same.

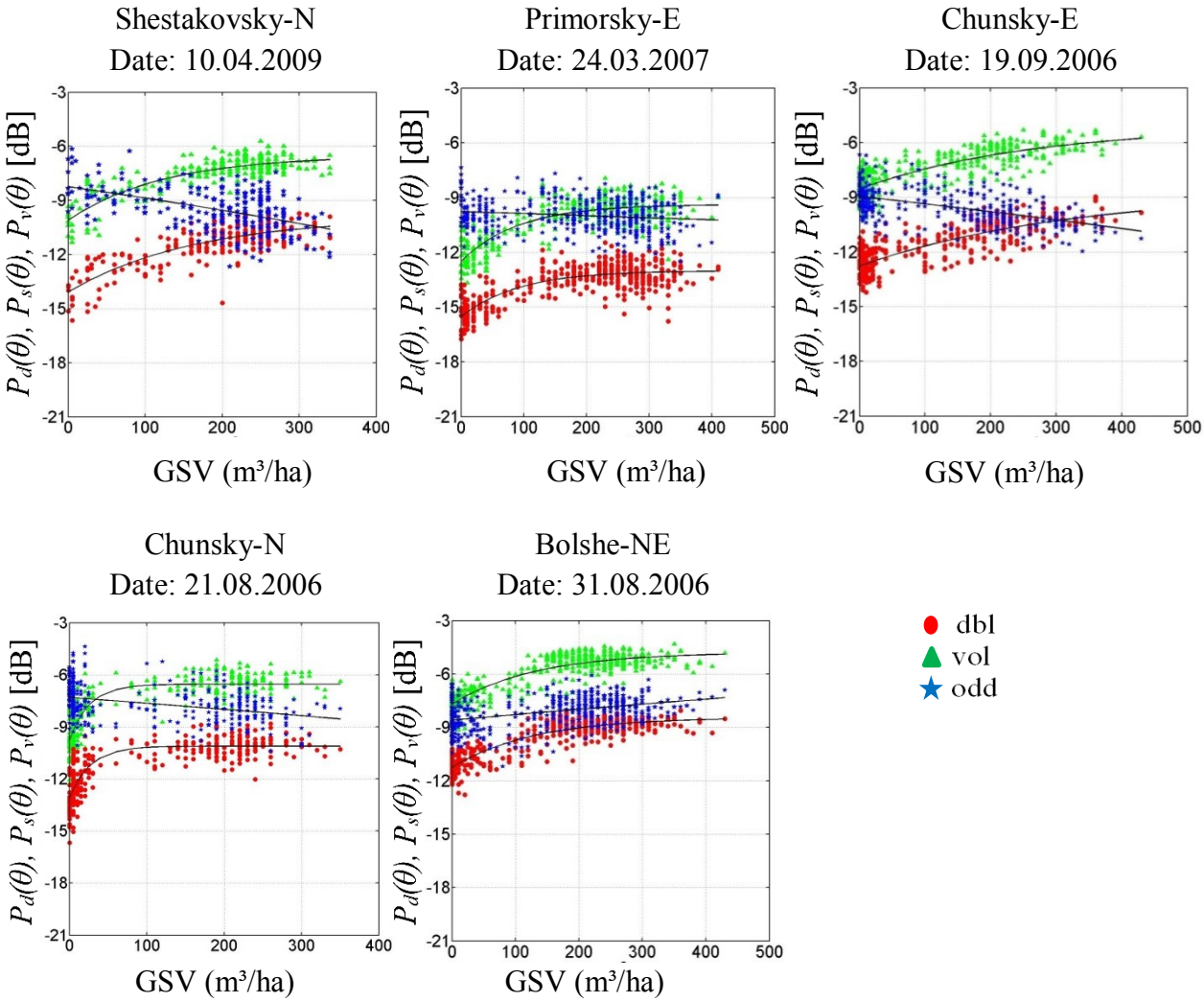

Figure 4.13 Relationship of GSV and decomposition powers, derived with rotation of coherence matrix [$T(\theta)$].

From the Table 4.3 it can be seen that both, volume and double-bounce scattering power have positive correlation and surface scattering has negative correlation with GSV.

Test Sites	Dates	P_d	$P_d(\theta)$	P_s	$P_s(\theta)$	P_v	$P_v(\theta)$
Shestakovsky-N	21.05.2007	0.26	0.70	-0.72	-0.61	0.70	0.73
Shestakovsky-N	10.04.2009	0.67	0.79	-0.56	-0.50	0.76	0.78
Shestakovsky-N	26.05.2009	0.31	0.71	-0.71	-0.61	0.75	0.76
Primorsky-E	09.05.2007	0.22	0.63	-0.54	-0.33	0.66	0.66
Primorsky-E	24.03.2007	0.48	0.70	-0.43	-0.15	0.74	0.74
Primorsky-E	31.05.2009	-0.15	0.46	-0.54	-0.37	0.58	0.61
Chunsky-E	07.05.2007	0.38	0.70	-0.50	-0.53	0.76	0.76
Chunsky-E	19.09.2006	0.64	0.80	-0.67	-0.52	0.81	0.81
Chunsky-N	06.10.2006	0.16	0.56	-0.65	-0.60	0.65	0.67
Chunsky-N	13.04.2009	0.34	0.61	-0.64	-0.58	0.63	0.63
Chunsky-N	21.08.2006	0.61	0.77	-0.60	-0.36	0.74	0.76
Chunsky-N	24.05.2007	0.49	0.69	-0.68	-0.62	0.72	0.73
Bolshe-NE	31.08.2006	0.25	0.84	-0.07	0.38	0.32	0.84
Bolshe-NE	03.06.2007	0.21	0.79	-0.14	0.08	0.30	0.82

Table 4.3 Pearson's correlation coefficients for GSV-decomposition powers relationships, derived with and without rotation of coherency matrix. P_d, P_s, and P_v indicate double-bounce, surface and volume scattering power before the rotation of coherency matrix [T], whereas $P_d(\theta), P_s(\theta)$ and $P_v(\theta)$ refer double-bounce, surface and volume scattering power after the rotation of coherency matrix [$T(\theta)$].

Based on these findings, an empirical relationship between the GSV and polarimetric decomposition powers is derived. This empirical relationship can be expressed as:

$$GSV = f\left(\frac{P_d(\theta) * P_v(\theta)}{P_s(\theta)}\right) \tag{4.3}$$

To simplify the Equation 4.3, it is assumed that GSV is a function of ground-to-volume scattering ratio. For lower GSV or sparse forest, the numerator ($P_d(\theta) * P_v(\theta)$) of Equation 4.3 is smaller and denominator ($P_s(\theta)$) is larger and vice versa for dense forest. In a brief, when ground-to-volume scattering ratio is large, the *GSV* is low due to gaps in the forest and when ground-to-volume scattering ratio is small, *GSV* is high. Figure 4.14 shows the relationship between GSV and ground-to-volume scattering ratio for all the

studied areas. A regression line between GSV and ground-to-volume scattering ratio has been derived. The model proposed by Wagner *et al.* (2003) is used to describe this relation, as shown in Equation 4.4:

$$\sigma^0(GSV) = \sigma_\infty + (\sigma_0 - \sigma_\infty) * e^{-\frac{GSV}{GSV_\infty}} \tag{4.4}$$

where σ_0 and σ_∞ are the backscatter coefficients at GSV = 0 m³/ha (non-forest) and for maximum values of GSV (dense forest) respectively, and GSV_∞ is the value of GSV at which the exponential function has increased by e. The regression coefficients R^2 have been obtained by fitting an exponential function to the decomposition power. The combination of the polarimetric decomposition powers by means of ratio results increased Pearson's correlation coefficients (compare Table 4.3 with Table 4.4).

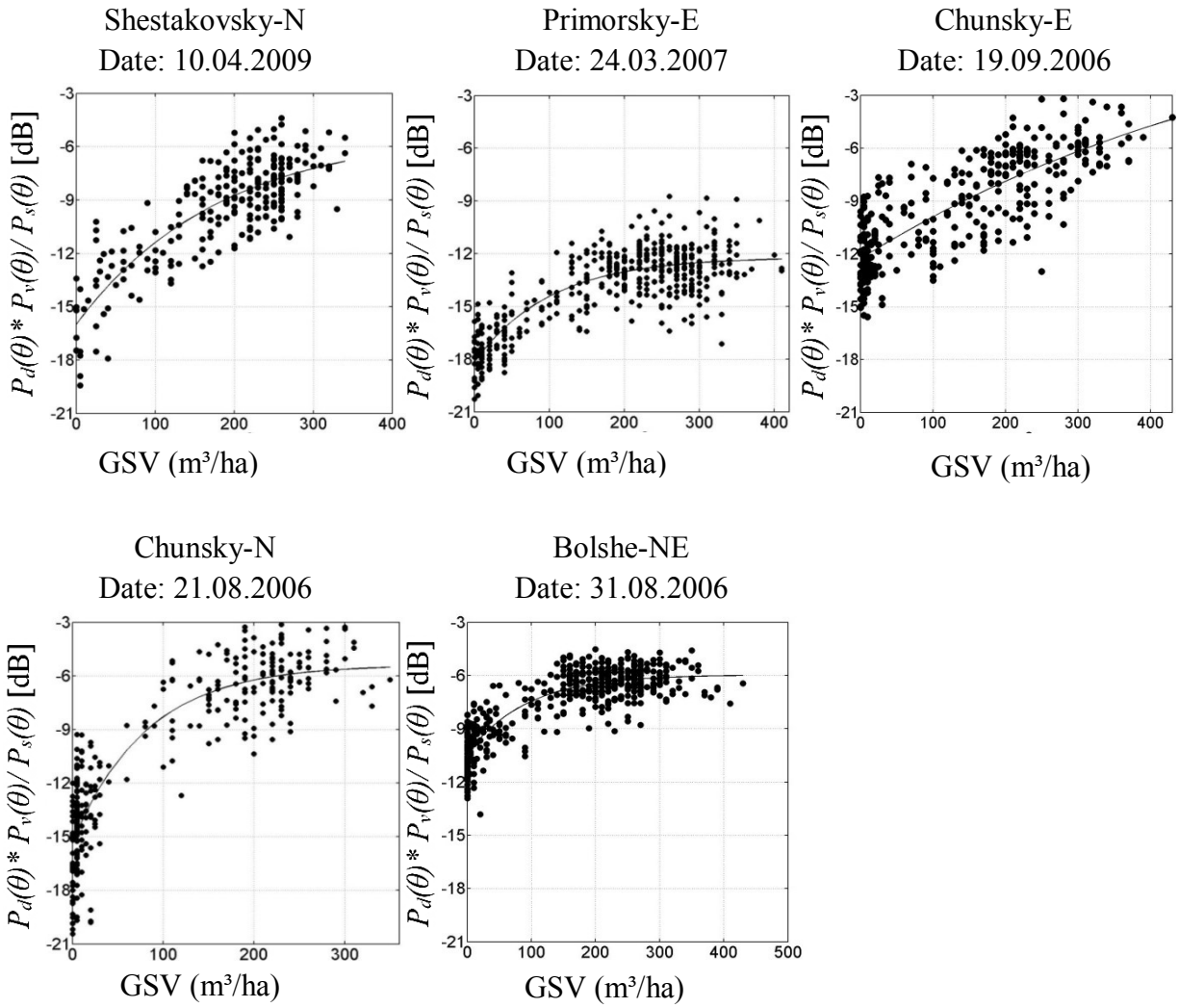

Figure 4.14 Regression between GSV and the ratio of double-bounce times volume scattering and surface scattering. Regression parameters are provided in Table 4.4.

The dynamic range between sparse forest and dense forest is relatively higher. However, the level of ground-to-volume scattering ratio varies from test site to test site.

This could be due to the weather influence which will be discussed in the following section.

Test Sites	Dates	σ_0 (dB)	σ_∞ (dB)	GSV_∞ (m³/ha)	R^2	Weather conditions
Shestakovsky-N	21.05.2007	-12.6	-3.9	177	0.70	Unfrozen, dry
Shestakovsky-N	10.04.2009	-15.9	-5.1	190	0.68	Thaw, wet
Shestakovsky-N	26.05.2009	-11.8	-3.1	126	0.75	Unfrozen, wet
Primorsky-E	09.05.2007	-10.9	-6.0	114	0.64	Unfrozen, dry
Primorsky-E	24.03.2007	-18.2	-12.2	103	0.69	Frozen
Primorsky-E	31.05.2009	-10.2	-5.7	101	0.55	Unfrozen, wet
Chunsky-E	07.05.2007	-11.8	+1.15	594	0.61	Thaw, wet
Chunsky-E	19.09.2006	-12.3	+3.1	595	0.67	Unfrozen, wet
Chunsky-N	06.10.2006	-20.3	-12.2	128	0.79	Frozen
Chunsky-N	13.04.2009	-20.0	-12.3	126	0.82	Frozen
Chunsky-N	21.08.2006	-15.3	-5.4	82	0.81	Unfrozen, wet
Chunsky-N	24.05.2007	-15.2	-6.7	80	0.80	Unfrozen, dry
Bolshe-NE	31.08.2006	-10.4	-5.9	97	0.75	Unfrozen, wet
Bolshe-NE	03.06.2007	-9.5	-5.6	74	0.67	Unfrozen, dry

Table 4.4 Estimated regression coefficients for decomposition powers and GSV. For better interpretation, a brief summary of weather conditions is provided also in this table. Detailed weather conditions are listed in Chapter 3 (Table 3.4).

Kobayashi *et al.* (2012) applied Yamaguchi's four-component decomposition scheme to ALOS PALSAR L-band data to compare the decomposition powers with the forest parameters tree height, tree diameter, and stand volume in tropical forest. The authors showed that surface and volume scattering powers are slightly better positively correlated with the forest parameters after the rotation of coherency matrix. The surface scattering is negatively correlated and volume scattering is positively correlated with forest parameters. They found that there is no correlation between double-bounce and forest parameters. This could be due to the vestigial canopy effects in tropical forest. Different direction of correlation between GSV and decomposition power has been observed by Goncalves *et al.* (2011). They used airborne L-band SAR data to apply the Freeman-Durden decomposition (Freeman & Durden, 1998) and showed that all the decomposition scattering powers were positively correlated with the stem volume of a tropical forest.

In our work, the rotation of the coherency matrix resulted in increased correlation between $P_d(\theta)$ and GSV in all study areas. Regarding the other polarimetric parameters, the rotation of the coherency matrix had almost no impact. This could be due to the fact that at L-band the penetration of the wave through the canopy is not sufficient, resulting in

noisy POAs in forest areas (Lee *et al.* 2011). The authors investigated the POA measurements by applying JPL AIRSAR C-, L- and P-band data over the forest in Freiburg, Germany on 15.06.2001. They found that P-band data has deeper penetration than the C- and L-band in the forest areas. Thus, the OA cannot be estimated accurately with ALOS PALSAR L-band in forest areas with varying topography.

Goncalves *et al.* (2011) set up a model by using multi-linear regression model of several incoherent and coherent attributes including volume scattering power of Freeman-Durden decomposition (Freeman & Durden, 1998). They showed that the GSV can be retrieved up to 308 m³/ha. Also in our work the high correlation coefficients for double-bounce and volume scattering provides the possibility to estimate the GSV in Siberian forests. Since the correlation for the surface scattering power (R < 0.65) is not consistent and not high enough for all the test sites, it should not be considered separately for GSV estimation. The inconsistent behaviour of surface scattering could be due to the (i) soil moisture variations, (ii) growth of small trees or forest understories and (iii) potential differences between forest inventory data from 1998 and the GSV at the time of the SAR acquisition.

Despite the considerable effects of meteorological (unfrozen/frozen/thawing conditions, precipitation) and environmental (soil moisture variations, snow properties) conditions, the temporal consistency of the polarimetric decomposition powers is high. To demonstrate this, the Pearson's correlation coefficient is computed between the images acquired at different weather conditions (unfrozen, frozen, thaw) on a pixel (25m) basis. All correlation coefficients are above 0.70. This high correlation indicates the robustness of the polarimetric decomposition powers.

The correlation between ALOS PALSAR L-band polarimetric decomposition powers and GSV is improved if the ratio of $P_d(\theta)$ times $P_v(\theta)$ and $P_s(\theta)$ is used instead of individual polarimetric decomposition powers. The relations shown in Figure 4.14 and also listed in Table 4.4 indicate that the higher sensitivity of the ground-to-volume scattering ratio for GSV as it is increased and a large dynamic range is observed for all test sites. The spread in the data shown in Figure 4.14 can depend on the spatial distribution of trees, canopy architecture, canopy moisture content, soil roughness and moisture. Further support to the assumption is found in a study carried out in Siberian forest areas by Santoro *et al.* (2006) and Eriksson *et al.* (2003). The R^2 values vary between 0.65 and 0.82 for all the test sites. The only exception (R^2=*0.55*) has been found for the image acquired on 31.05.2009 in Primorsky-E. This could be due to heavy impact of weather conditions. According to the weather data records (Table 3.4) it is not raining on the day of the acquisition, however moderate rain (1.6 cm) is observed during the past three days before the acquisition. The high values of R^2 for Chunsky-N are due to the high proportion of stands with low GSV.

4.4.3 Impact of weather conditions

To get an overview of how the contribution of polarimetric decomposition powers $P(\theta)$ change at different meteorological conditions, the normalised values of $P_s(\theta), P_d(\theta),$ and $P_v(\theta)$ have been plotted for the corresponding acquisition dates. Figure 4.15 illustrates the

mean values for sparse and dense forests. In sparse forest, surface scattering $P_s(\theta)$ is more dominant than volume scattering $P_v(\theta)$, and double-bounce $P_d(\theta)$. Exceptions are observed at unfrozen and rainy conditions where $P_v(\theta)$ is higher than $P_s(\theta)$ for sparse forest in Primorsky-E (31.05.2009) and in Chunsky-E (19.09.2006). During the frozen conditions $P_s(\theta)$ is more dominant than at unfrozen conditions. As $P_s(\theta)$ increases $P_d(\theta)$ and $P_v(\theta)$ decrease at frozen conditions.

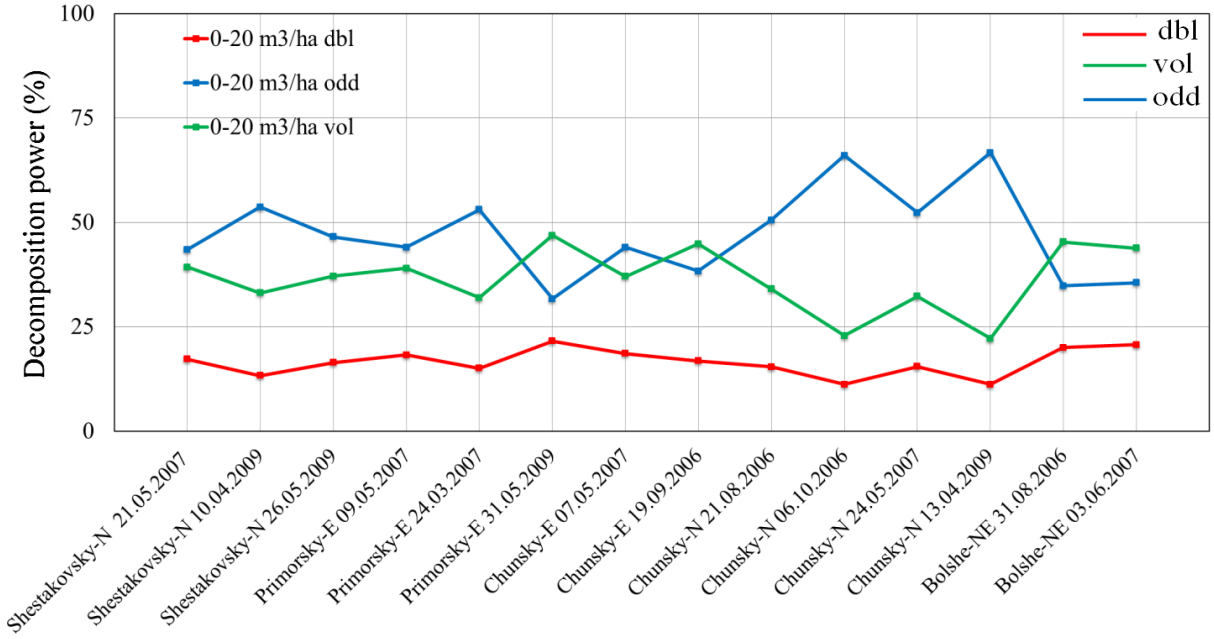

(a)

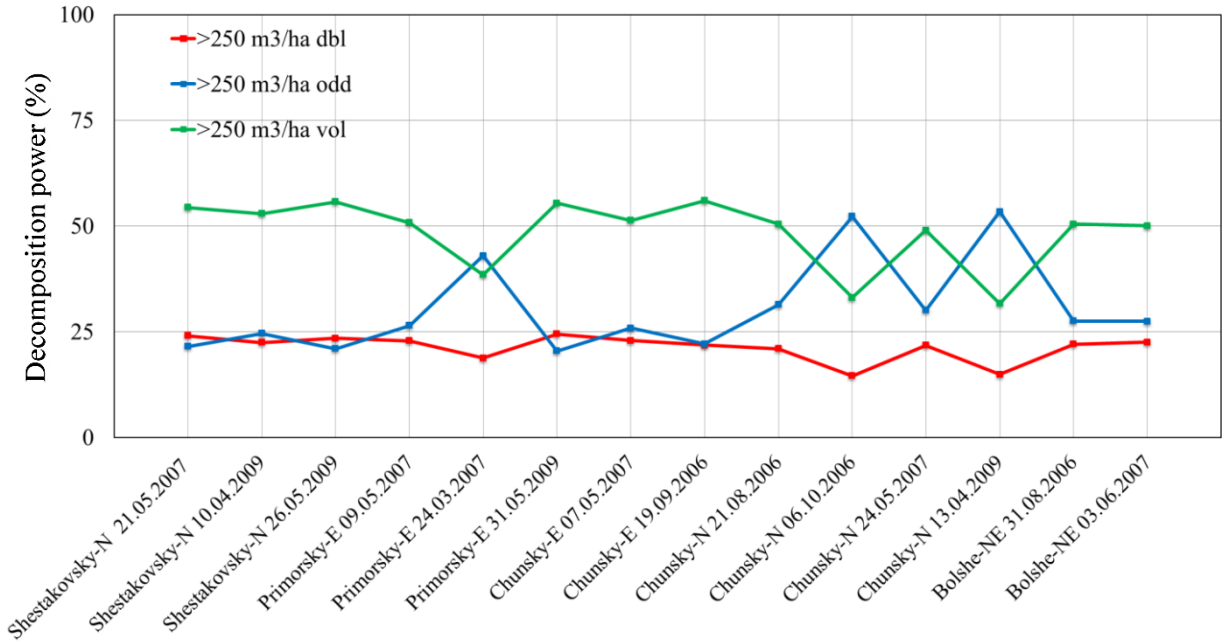

(b)

Figure 4.15 Mean polarimetric decomposition powers for all acquisition dates in Siberian forests. Red, green, and blue colours represent double-bounce, volume and surface scattering respectively for (a) sparse forest and (b) dense forest.

In dense forest, $P_v(\theta)$ in general exceeds $P_s(\theta)$ or $P_d(\theta)$. At unfrozen conditions volume scattering and double-bounce scattering is stable in general. At frozen conditions, $P_v(\theta)$ is reduced and increased $P_s(\theta)$ has been observed. $P_s(\theta)$ shows the highest scattering power for sparse forest at frozen conditions. $P_d(\theta)$ decreases slightly at frozen conditions.

The contribution of decomposition scattering power depends on the environmental conditions at the time of acquisition. In sparse and dense forests, the behaviour of the surface scattering power and volume scattering power are opposed. At all the test sites, surface scattering power is dominant in sparse forest at unfrozen and dry conditions, while in dense forest the volume scattering power is dominant.

At unfrozen-wet conditions, in sparse forests the volume scattering is higher than the surface scattering. This could be due to the increased moisture content of the canopy resulting in decreased penetration and more attenuation from the branch of the tree. Therefore, the ground contribution is decreased. Under these circumstances, the volume scattering power can be as high as for dense forest.

At frozen conditions, in dense forest the surface scattering power is higher than the volume scattering power. The differences between the contributions of scattering power from sparse and dense forests are nearly the same. In winter, canopies are frozen. Thus, the transmitted electromagnetic wave penetrates deeper into the canopy and a great amount of backscatter comes from the ground. However, radar backscatter is strongly influenced by the variations of snow parameters: snow grain size and shape, snow density, free liquid water content, stratification, snow depth; sensor parameters: frequency, polarisation, incidence angle; and subsurface parameters: surface roughness, dielectric constant (Koskinen, 2001). Snow is composed of ice crystal, air and liquid water. Dry snow is a combination of ice and air. If the snow has water in liquid form then the snow is called wet snow. The scattering mechanisms for snow are divided into three components (Ulaby *et al.* 1986): (i) backscattering from air-snow interface, (ii) backscattering from the snow volume and (iii) backscattering from the underlying ground surface. The points (i) and (iii) represent surface scattering mechanism and (ii) characterises the volume scattering mechanism. The dielectric constant from dry snow is low and the volume scattering is small. In case of wet snow, where the liquid water content increases the dielectric constant, the volume scattering increases and can be dominant at C-band. The longer wavelength at L-band makes the volume scattering from wet snow significantly lower than C-band (Ulaby *et al.* 1981). A thick snow layer and high snow density, which increase the dielectric constant, affect the incidence angle and the wavelength of the electromagnetic wave. The refraction within the snow makes the incidence angle smaller and the incident wavelength is shortened due to the increase dielectric constant. The wavelength of L-band is still considerably larger than the snow grain size and therefore, no significant volume scattering is generated by snowpack. The reduction of wavelength makes the surface rougher and the dielectric contrast between the snow and ground is smaller than between air and snow (Shi & Dozier, 1986). Thus, the rougher surface and the smaller dielectric constant decrease the volume scattering and increase the surface scattering. Though the

impact of snow is not thoroughly investigated it is assumed that at L-band the impact of dry snow can be neglected.

Although several studies have shown the importance of the double-bounce scattering mechanism at L-band (Sun *et al.* 1991; Saatchi *et al.* 1997) but in this study, the double-bounce contribution is in general smaller than the volume and surface scattering power. If the forest floor is smooth, ground-trunk interactions can significantly contribute to the total backscatter. However, in the forest many factors influence this kind of scattering mechanism: slope, dead wood, understories etc. In Siberian forests, the floor often exhibits small bushes and trees, which can reduce the double-bounce scattering power. Double-bounce is also reduced, if the angle between trunk and ground surface is not equal to 90°. This occurs in areas with pronounced topography and if the trunks are tilted. Further supports to the assumption have been reported by Pulliainen *et al.* (1999) and Ranson & Sun, (1994). The authors have found the double-bounce term in boreal forests is negligible because of rough surface ground and strong attenuation in coniferous and broadleaf types of forest. Baker & Luckman, (1999) have investigated the importance of double-bounce, surface and volume scattering in boreal forests with EMISAR L-band airborne sensor. They showed the dominance of volume scattering relative to the double-bounce scattering. Watanabe *et al.* (2006) applied Freeman-Durden three-component scattering model (Freeman & Durden, 1998) to the cool-temperate forest in northern Japan. They calculated and plotted the contributions of three scattering components (surface, double-bounce and volume scattering) against the biophysical parameters (weighted tree height, basal area, above ground biomass). The model indicated that the volume scattering contributes 80%-90% when the above ground biomass exceeds 50 tons/ha or the weighted tree height exceeds 5 m. The surface scattering components for young stands are increased to 20%, and the volume scattering components are reduced to 70%. The contributions of double-bounce are less than 10% for both young and mature forest.

Figure 4.16 shows the one example of saturation level for GSV using double-bounce scattering power in Shestakovsky-N and Chunsky-E. At unfrozen (21.05.2007 and 26.05.2009) conditions saturation occurs at 150 m^3/ ha GSV whereas at thawing condition the saturation reaches at 200 m^3/ ha. The saturation level for GSV increases to 250 m^3/ ha and 300 m^3/ ha using the double-bounce after the rotation of coherency matrix and also the ratio of ground-to-volume scattering power. The JERS backscatter in Swedish and Finnish boreal forests saturates between 150 and 225 m^3/ ha (Israelsson *et al.* 1995; Fransson & Israelsson, 1999; Kurvonen, *et al.* 1999). In Chunsky-E the saturation increases from 100 m^3/ ha to 250 m^3/ ha GSV. The slopes are not observed as high as in Shestakovsky-N. This could be due to the larger spread of double-bounce scattering power resulting a high standard deviation within each 50 m^3/ ha GSV classes. The volume scattering power after the rotation of coherency matrix has no positive affect for the saturation and remains same (Figure B.4.1 in Appendix B). In summary, the saturation level for GSV increases by using polarimetric decomposition powers but no improvements have been observed for GSV at Bolshe-NE. The saturation level at very low GSV in Bolshe-NE could have been due to (i) errors in the inventory data, (ii) forest structural diversity and (iii) soil moisture variations.

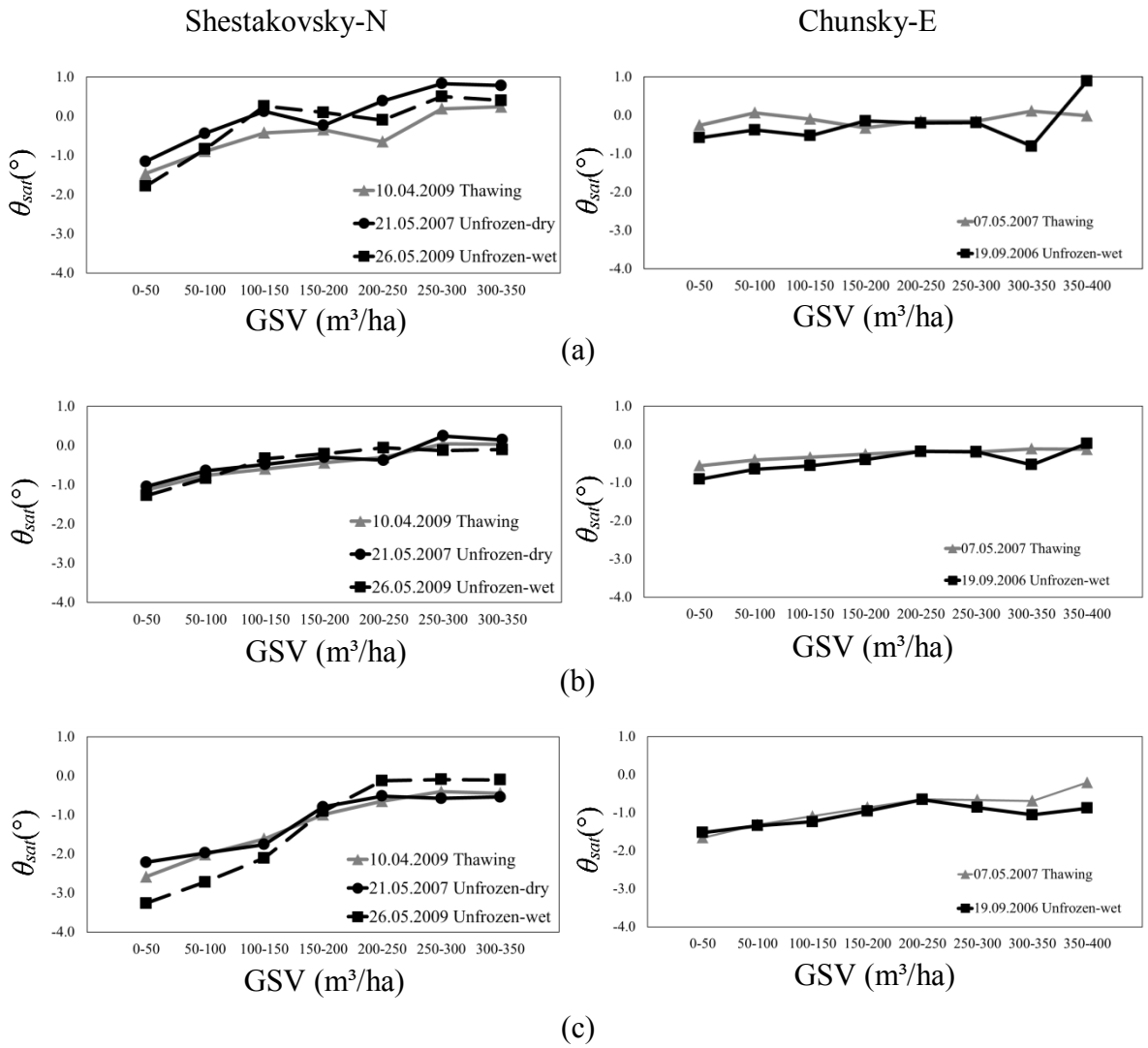

Figure 4.16 Observed saturation levels for forest growing stock volume at different weather conditions using ALOS PALSAR L-band double-bounce scattering power (a) without rotation of coherency matrix [T] and (b) with rotation of coherency matrix [$T(\theta)$], for Shestakovsky-N and Chunsky-E. (c) The ratio of ground-to-volume scattering power for same test sites.

4.5 Impact of tree species on polarimetric parameters

The impact of tree species on $P(\theta)$ at three different meteorological conditions has been investigated. All analyses are conducted on forest stand level. The stands with a GSV above 150 m³/ha have been selected. The four tree species aspen, birch, larch and pine are considered here in this study. Due to the low amount of samples cedar, fir and spruce are not considered. One problematic issue of this work is that pure stands (only one single species) are very rare. Therefore, all stands with a minimum areal coverage of 70% of the dominating species are considered. The observed impact of species is, therefore, disturbed by the other tree species growing in the stands. In Chunsky-N aspen is not occurring. The investigation is carried out for dense forest to reduce the ground contribution of the signal

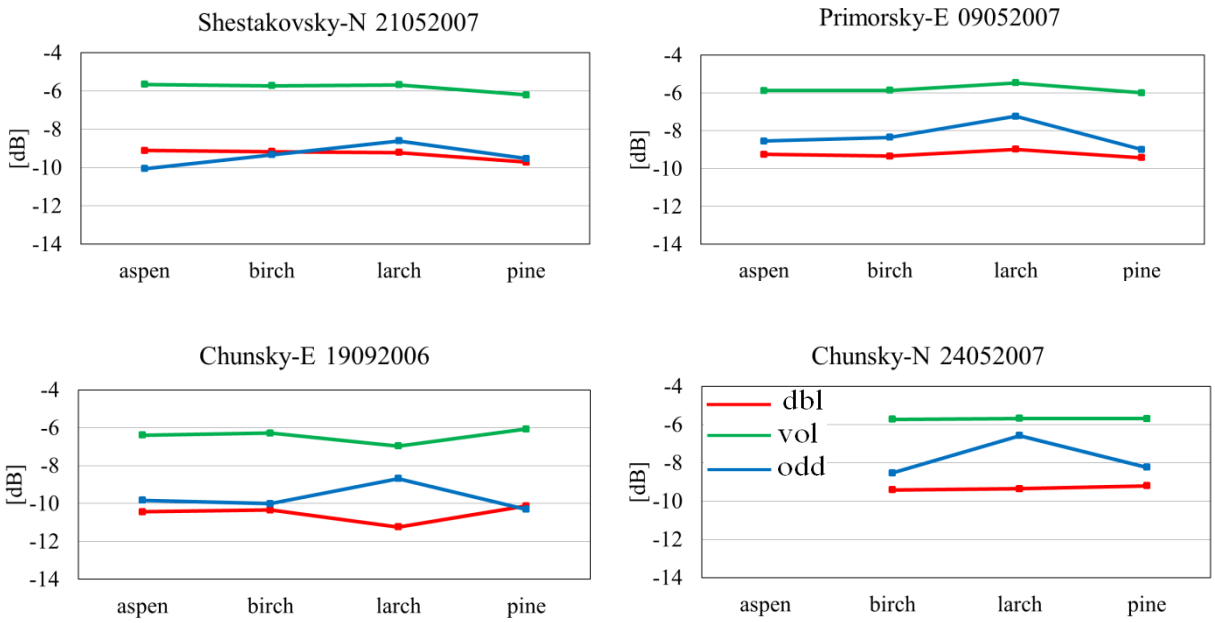

(a) Unfrozen conditions

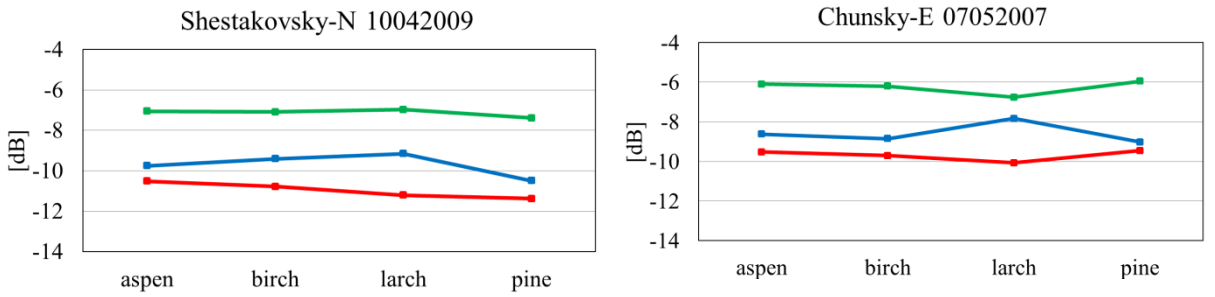

(b) Thawing conditions

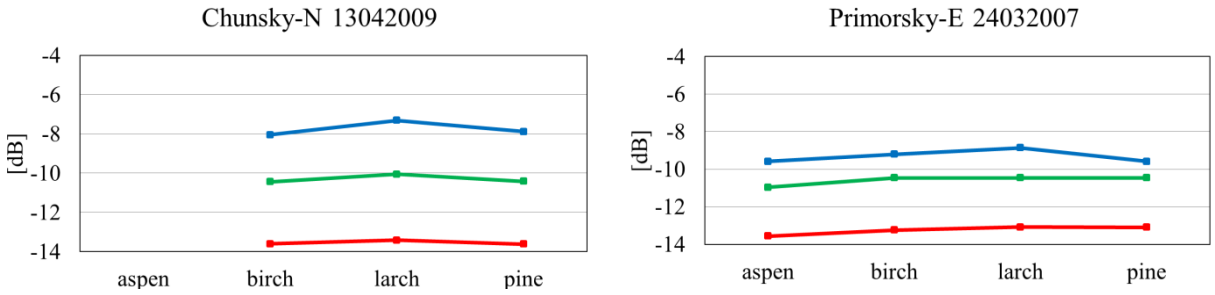

(c) Frozen conditions

Figure 4.17 Mean decomposition powers over dense forests (GSV > 150 m³/ha) separated by tree species at (a) unfrozen, (b) thawing and (c) frozen conditions. Red, green, and blue colours represent double-bounce, volume and surface scattering respectively.

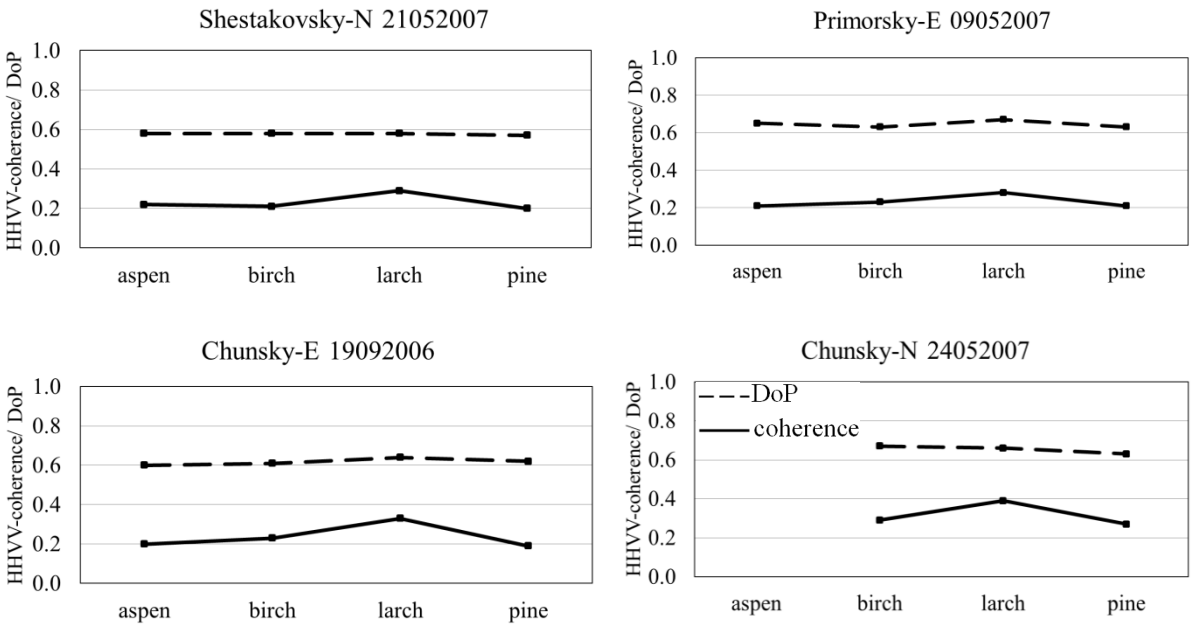

(a) Unfrozen conditions

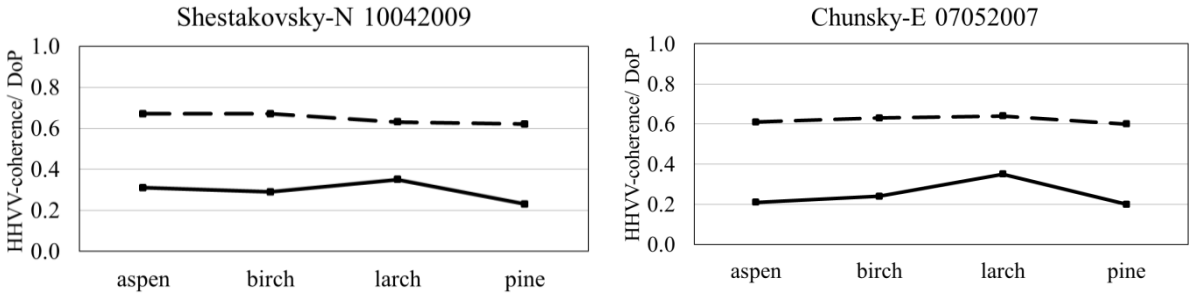

(b) Thawing conditions

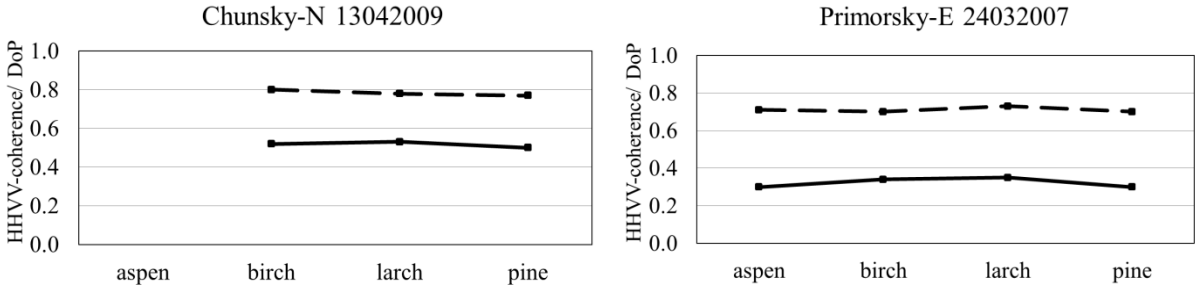

(c) Frozen conditions

Figure 4.18 Mean coherence and degree of polarisation values over dense forests (GSV > 150 m³/ha) separated by tree species at (a) unfrozen, (b) thawing and (c) frozen conditions. The dashed line indicates degree of polarisation and solid line presents polarimetric coherence.

and pronounce the impact of the trees. The mean and standard deviation of GSV of selected stands (> 150 m³/ha GSV) are given in Table 4.5. The mean GSV of each test site is either above or close to the saturation level. Thus, the variations of GSV in dense forest are assumed to have negligible effects on polarimetric parameters. The stand-wise mean values of $P_s(\theta), P_d(\theta), P_v(\theta)$, DoP and HHVV-coherence for aspen, birch, larch and pine are depicted in Figure 4.17 and Figure 4.18. For better interpretation the data set is divided by unfrozen, thawing, and frozen conditions. The impact of tree species on polarimetric parameters for Bolshe-NE has been shown in Figure B.3.1 (Appendix B). At unfrozen and thawing conditions it has been observed (Figure 4.18a) that the scattering decomposition powers are not very sensitive to tree species. Nevertheless, larch always shows the highest surface scattering. At thawing conditions, double-bounce shows only 0.5 dB difference between deciduous trees and coniferous trees in Shestakovsky-N.

Test sites	Aspen		Birch		Larch		Pine	
	Mean	Stdv	Mean	Stdv	Mean	Stdv	Mean	Stdv
Shestakovsky-N	267	28	201	23	242	37	259	46
Primorsky-E	290	48	205	26	239	53	278	46
Chunsky-E	266	55	212	24	198	17	302	38
Chunsky-N	—	—	172	13	225	30	250	52
Bolshe-NE	209	43	177	52	220	28	257	93

Table 4.5 Mean and standard deviations of GSV for aspen, birch, larch, and pine.

Two images in Chunsky-N and one image in Primorsky-E are acquired at frozen conditions (Figure 4.17(c)). $P_s(\theta)$ is higher than $P_v(\theta)$ at both test sites, $P_d(\theta)$ has the lowest contribution. Compared to unfrozen conditions, $P_v(\theta)$ and $P_d(\theta)$ are clearly reduced. During frozen conditions, the impact of the tree species on $P(\theta)$ is even smaller than at unfrozen conditions.

The geometrical properties of trees (e.g. crown shape, alignment of tree components) and environmental conditions (undergrowth, water consumption, interception, wind susceptibility etc.) affect the polarimetric decomposition scattering composition. In this study, the impact of polarimetric decomposition powers for aspen, birch, larch, and pine have been investigated at three different meteorological conditions: unfrozen (dry and wet), thawing and frozen. Spatiotemporal variability of environmental conditions during the growing season (precipitation, soil moisture change, growth etc.) result in increased spread (inter and intra species) variance of decomposition powers. At unfrozen conditions, the impact is increased in particular for larch. In Chunsky-N larch differs from other tree species by +2 dB surface scattering power at unfrozen conditions. At the other sites the

same behaviour is also observed, however the difference is slightly smaller than +2 dB. The higher surface scattering power from larch forest can indicate that the canopy are more transparent to the electromagnetic wave and a large part of the radar backscatter power comes from the ground. This could be due to the different canopy structures, different needles arrangement, less dense canopy. Moreover, there could be fewer understories in the larch forest stands and the surface is smoother.

HHVV-coherence shows similar values for aspen, birch and pine forest whereas the impact of larch is increased by a magnitude of +0.05 to +0.17 at unfrozen and thawing conditions. Watanabe *et al.* (2006) investigated the contributions of polarimetric coherence, double-bounce, surface and volume scattering power for spruce, fir, and larch forest in cool-temperate forest in northern Japan. The results showed higher coherence value and surface scattering powers for larch forest. However, the physical significance of observed results is not discussed.

The impact of tree species on polarimetric decomposition power and polarimetric coherence is very low at frozen conditions. The values of polarimetric parameters are almost similar at frozen conditions. This could be due to the frozen canopy the structural differences or geometrical properties between the tree species cannot be distinguished and volume scattering strengths for these four tree species are basically the same. Moreover, the forest ground is more exposed and the dielectric constant of the tree is reduced (Dobson *et al.* 1990; Way *et al.* 1994), resulting in decreased attenuation. This results in a higher ground contribution, which is in principle independent of the tree species and reduce of scattering within the canopy (Kwok *et al.* 1994). The DoP is of little value for tree species discrimination at different weather conditions.

4.6. Conclusions

The scope of this chapter is to investigate the behaviour of polarimetric parameters as a function of forest GSV. The investigations are carried out the effect of the different weather conditions, topography, forest stand structure and tree species in Siberian forests. Fourteen ALOS PALSAR L-band PLR scenes have been considered for the investigation at Shestakovsky-N, Primorsky-E, Chunsky-E, Chunsky-N and Bolshe-NE.

Polarimetric signatures are analysed over the forest and non-forest areas. The three dimensional co-polarisation signatures clearly distinguish the clear-cut, bogs from the forests. The type of polarisations, linear and circular, and the orientation of the target can extract from the polarimetric signatures. The scattering behaviour has been recognised. It is difficult to separate the tree species from the scattering mechanisms because of the similar distributed scattering behaviour of the target for all the tree species. Thus, polarisation signatures provide information on the scattering mechanism but not sensitive to the structure of the target.

Polarisation phase differences clearly distinguish the clear-cut, bogs from forest. The scattering behaviour (volume scattering, surface scattering) is recognised by the polarisation phase differences from forest and non-forest areas. The sensitivity of the

polarimetric phase differences for changing environmental conditions is clearly demonstrated. Comparison of the polarimetric phase differences at different weather conditions indicate relatively higher contribution of branch scattering at unfrozen condition than at frozen condition. Larch shows the less variability than other tree species at both, frozen and unfrozen conditions. The clear increase of mean polarisation phase differences accompanied by a slow increase of standard deviation for increasing GSV up to 180 m³/ha has been observed. After that point, PPD loses the sensitivity for GSV.

This study has shown a clear correlation between the ALOS PALSAR L-band polarimetric coherence and the GSV in Siberian forest. Independent of weather conditions, a high correlation (R= -0.87) between coherence and GSV is found. The highest saturation level at ~250 m³/ha is observed in Shestakovsky-N whereas in Bolshe-NE lowest saturation at ~100 m³/ha is obtained.

A contrast between coherence values of sparse forest and of dense forest has been observed at all weather conditions. The variations of absolute level of coherence for sparse forest are larger than for the dense forest at unfrozen condition. The coherence for sparse forest differs from one test site to another test site at unfrozen condition whereas coherence for dense forest does not differ. No variation of coherence has been observed for both sparse and dense forest at frozen and thawing conditions. Highest coherence obtained during winter in the presence of snow cover.

Topography effects such as direction of slopes are not observed. The correlation between HHVV-coherence and GSV does not depend on the size of the stands. No increase or decrease trend is observed as a function of stand size. A slightly higher correlation between coherence and GSV is observed for fully stocked stands.

The four-component power decomposition method has been applied to the ALOS PALSAR L-band fully polarimetric data to compare the decomposition powers to the GSV and the impact of different meteorological conditions. The surface scattering decreases as the exposure of the bare ground decreases, the volume scattering increases as the canopy expands and cover the forest floor and the double-bounce scattering, which is supposed to physically reflect the stem or stand volume, increases as the growing stock volume increases. Double-bounce and volume scattering powers show significant correlation with GSV. The correlation between GSV and surface scattering is found to be inconsistent. The importance of the LOS rotation has been demonstrated, as the correlation between double-bounce scattering power and GSV could be significantly improved. The correlation between polarimetric decomposition parameters and GSV is enhanced if the ratio of ground-to-volume scattering, which is the ratio of volume scattering times double-bounce and surface scattering, is used instead of considering polarimetric decomposition powers separately. When the ground-to-volume scattering ratio is large, the GSV is low due to gaps in the forest and when the ground-to-volume scattering ratio is small, GSV is high. The ratio of ground-to-volume scattering powers shows a high sensitivity to GSV and higher dynamic range between sparse forest and dense forest is observed for all the

investigated areas in Siberia. The average R^2 between growing stock volume and ground-to-volume scattering power is observed 0.72.

The contribution of decomposition powers over the sparse and dense forest depends on the weather conditions. At unfrozen conditions, surface scattering is dominant in sparse forests while in dense forests volume scattering is dominant. During thawing conditions, volume scattering in sparse forests is increased. The scenario is totally different at frozen conditions for dense forest, where the surface scattering power is higher than the volume scattering power.

The saturation level for GSV increases by using polarimetric decomposition parameters but no improvements have been observed for GSV at Bolshe-NE. The saturation level of GSV increases to ~300 m³/ha using polarimetric decomposition powers in particular, double-bounce and volume scattering power under unfrozen condition.

The dependence of decomposition powers, polarimetric coherence and degree of polarisation on the different tree species such as aspen, birch, larch and pine is also investigated. In this study the impact of tree species on polarimetric parameters has been assessed at unfrozen, frozen and thawing conditions. The stands dominated by larch species show higher surface scattering power than other tree species. Larch differs from aspen, birch and pine by +2 dB surface scattering power at unfrozen conditions. Double-bounce and volume scattering power remains unchanged for all the tree species. An impact of tree species on coherence is also observed. This impact is larger at unfrozen and thawing conditions. The largest coherence difference of +0.17 is observed between larch and other tree species. At frozen conditions, the impact of the tree species on the coherence and decomposition powers is small. The tree species' influence on the shape and structure of the canopy has less impact on the degree of polarisation.

This study has shown a clear correlation between GSV and ALOS PALSAR L-band polarimetric coherence as well as polarimetric decomposition powers. Regardless the weather conditions, the polarimetric coherence and polarimetric decomposition powers give the higher correlation and seem to be the most suitable parameters for GSV estimation in Siberian forests.

Chapter 5

Growing Stock Volume Retrieval

The objective of this chapter is to assess the accuracy of growing stock volume retrieval in Siberian forests from ALOS PALSAR L-band polarimetric parameters. For this purpose, two empirical statistical models will be introduced. Section 5.1 and 5.2 describe the models for polarimetric coherence and polarimetric decomposition powers respectively as function of growing stock volume. The estimations of unknown parameters of the models will be illustrated in these sections also. Models parameters will be estimated from a set of training forest stands. Once the parameters are measured, it is possible to invert the model for the retrieval of growing stock volume. Section 5.3 presents the methodology adopted for estimating growing stock volume from polarimetric coherence and polarimetric decomposition powers. In section 5.4, performance of the retrieval from the inversion of the models will be discussed with respect to environmental conditions, forest stand structures and dominant tree species. Finally, the results will be summarised and conclusions will be drawn in Section 5.5.

5.1 Polarimetric coherence modelling

It has been shown in section 4.3 that high correlation (R = -0.87) exist between the HHVV-coherence and growing stock volume (GSV). For the retrieval it is necessary to have a model that describes the HHVV-coherence as a function of GSV accurately and the preferred model should be characterised as a function of few parameters as possible. The following section describes the coherence model which will be used to estimate the GSV.

5. 1. 1 Model selection

In previous studies it has been proved that the relationship between GSV and SAR L-band coherence is exponential (Askne *et al.,* 1997; Koskinen *et al.,* 2001; Wagner *et al.,* 2003). The scatter plots of Figure 4.5 are suggesting that exponential model is more suitable than linear model. An empirical model of exponential form proposed by Wagner *et al.*(2003) is considered here, as shown in Equation 5.1:

$$\gamma_{HHVV}(GSV) = \gamma_{\infty} + (\gamma_{gr} - \gamma_{\infty}).e^{-GSV_{\gamma}.GSV} \quad (5.1)$$

In Equation 5.1, the γ_{gr} is given by the coherence of the sparse forest and γ_{∞} represents the coherence of dense forest. GSV_{γ} is the rate of coherence with increasing growing stock volume. A high value of γ_{gr}, small value of γ_{∞} and slow decrease of coherence with increasing forest *GSV* will be expected for estimating of GSV. The large difference between γ_{gr} and γ_{∞} i.e. higher dynamic range and also large value of GSV_{γ} i.e. slow decrease of coherence with increasing *GSV* will be expected for the retrieval of GSV.

5.1.2 Model training

The model is trained to understand the behaviour of model parameters and to allow the retrieval of GSV. In order to retrieve GSV, a set of known forest stands, used as training stands, are need to determine the model parameters by regression procedure. With these measured model parameters the coherence observations for a set of unknown forest stands, the testing group, can be inverted. The three unknown parameters of the empirical coherence model in Equation 5.1 need to be measured. The regression between coherence and GSV is used to determine the unknown parameters: γ_{gr}, γ_{∞} and GSV_{γ}. Part of the forest stands reported in the Table 3.1 is used to drive the models for training. Depending on the number of stands, the forest compartments are separated by five or six parts in terms of uniformly distributed growing stock volume as possible. The main aim of this procedure is to represent the growing stock volume distribution by the training sets. The model training has been performed at each compartment separately. The training has been performed at the stand level in order to minimize the effect of noise in the coherence measurements. One part of the stands is used to train the model and the remaining stands form the test set for validation. This procedure has been repeated for each test area. 16% to 21% of the total forest stands are used to train the model for all the test sites.

5.1.3 Model parameters estimation

Figure 5.1 illustrates the modelled coherence behaviour as a function of GSV using the Equation 5.1. The "black" solid lines show the model fit obtained from the three unknown parameters and the response of coherence to increase in GSV is nonlinear. Additionally, the obtained model parameters from the curve fitting for all test sites in Siberia are listed in Table 5.1.

Temporal variations of the HHVV-coherence for the training stands are analysed. The correlation coefficient between training sets of coherence for different dates are higher than R=0.89. The higher Pearson's correlation coefficient indicates that coherence data from ALOS PALSAR L-band shows good temporal stability. Figure 5.1 depicts that the level of coherence highly depends on the weather conditions.

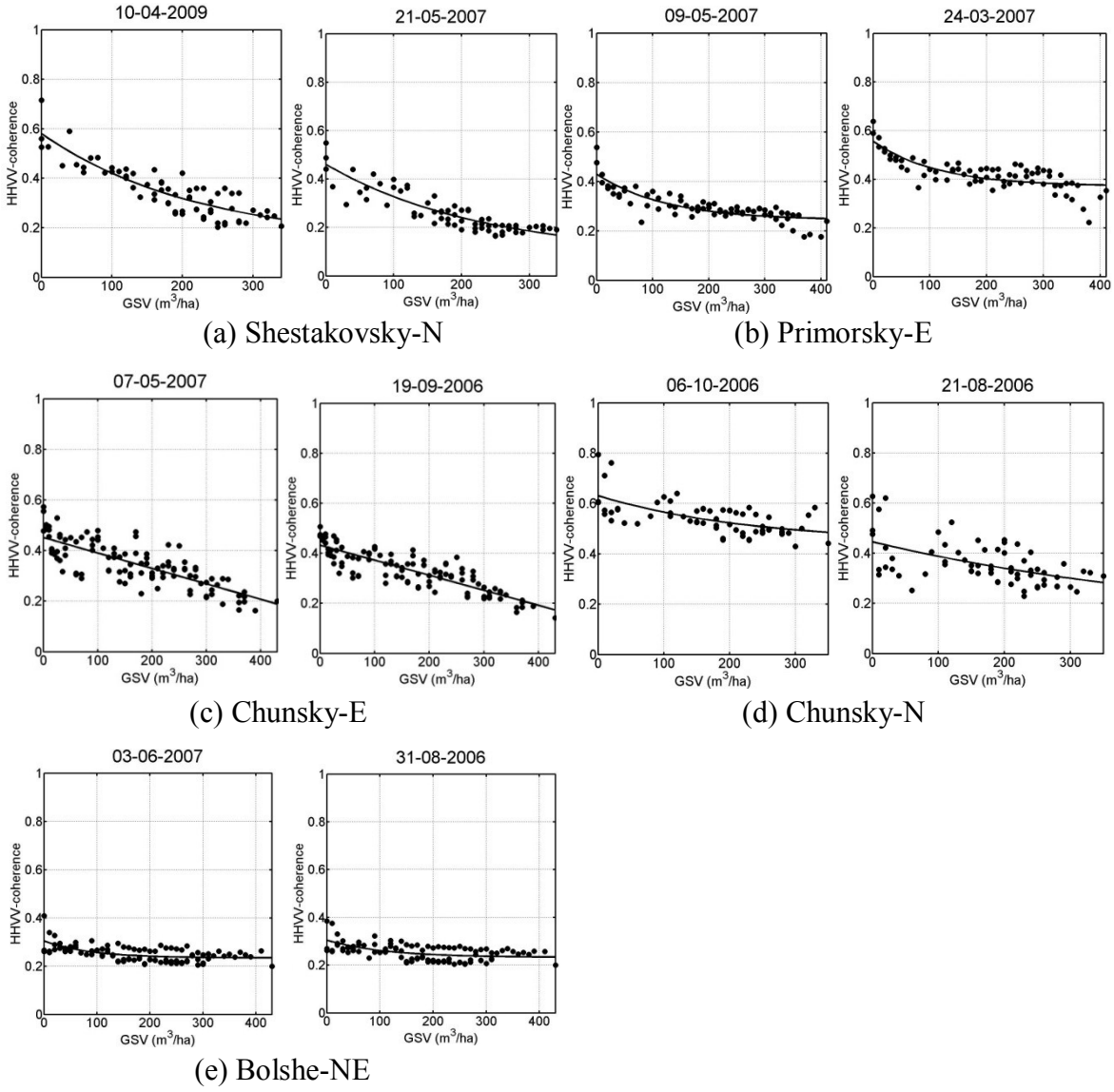

Figure 5.1 Behaviour of ALOS PALSAR L-band HHVV-coherence as a function of GSV for (a) Shestakovsky, (b) Primorsky-E, (c) Chunsky-E, (d) Chunsky-N and (e) Bolshe-NE. The filled circles show the ALOS PALSAR L-band HHVV-coherence observations and the solid lines represent the corresponding fittings of the model obtained by Equation 5.1. The number of stands for training sets varies between 16% and 21% of total forest stands.

The modelled coherence shows higher sensitivity for GSV in Shestakovsky-N, Chunsky-E and Chunsky-N. No saturation is observed in Chunsky-E. According to Table 5.1 and Figure 5.1, the images acquired under frozen conditions (24.03.2007) at Primorsky-E and on 06.10.2006 at Chunsky-N, the HHVV-coherence shows higher values for sparse and dense forest. During these acquisitions the forest is fully covered by snow. For increasing GSV in particular, after 100 m³/ha the slope becomes almost flat and the sensitivity of coherence to GSV decrease in Bolshe-NE. The coherence of the ground, γ_{gr}, has values between 0.31 and 0.32 and the coherence of the dense forest, γ_{∞}, has values between 0.21 and 0.22. The eastern forest compartments of Bolshe i.e. Bolshe-NE and

Bolshe-SE show the coherence values for sparse forest less than 0.4 and significantly dropped in slightly denser forest (~100 m³/ha), reaching a saturation level. On the other hand, the coherence values are between 0.41 and 0.45 for sparse forest in Bolshe-SW and Bolshe-NW (not shown in Figure 5.1) but the saturation reach at ~100 m³/ha like the eastern compartments of Bolshe. To explain this behaviour it can be assumed that the soil moisture contents at the non-forested ground and the forest ground floor can differ because of the effects of evapotranspiration and rainfall interception over forest. The possibility of low coherence values for the sparse forest in Bolshe-NE and Bolshe-SE can be the large amount of mixed type of forest i.e. non-homogeneity.

Bolshe-NE is located on eastern bank of the Yenisei where peat soils dominate but on the other hand the soils are mostly sandy in Bolshe-NW located on the western side of the river. The sandy soils absorbs the water and dried up quickly whereas high soil moisture exist in peat soils which lowering the coherence.

Test Sites	Dates	γ_{gr} (dB)	γ_{∞} (dB)	GSV_{γ} (ha/m³)
Shestakovsky-N	21.05.2007	0.46	0.08	227
Shestakovsky-N	10.04.2009	0.59	0.14	221
Shestakovsky-N	26.05.2009	0.45	0.10	210
Primorsky-E	09.05.2007	0.43	0.24	127
Primorsky-E	24.03.2007	0.56	0.37	113
Primorsky-E	31.05.2009	0.38	0.19	119
Chunsky-E	07.05.2007	0.46	0.20	450
Chunsky-E	19.09.2006	0.44	0.19	450
Chunsky-N	06.10.2006	0.63	0.44	236
Chunsky-N	13.04.2009	0.63	0.47	177
Chunsky-N	21.08.2006	0.45	0.31	184
Chunsky-N	24.05.2007	0.41	0.32	143
Bolshe-NE	03.06.2007	0.31	0.22	87
Bolshe-NE	31.08.2006	0.32	0.21	104

Table 5.1 Coherence modelled parameters for Shestakovsky-N, Primorsky-E, Chunsky-E, Chunsky-N and Bolshe-NE.

5.2 Polarimetric decomposition modelling

The Freeman-Durden decomposition (Freeman & Durden, 1998) is a technique for fitting a physically based, three-component scattering mechanisms model to the polarimetric SAR observations, without utilizing any ground-truth measurements. The general idea for this approach is to identify the dominant scattering components to any backscattering scenario. The total average backscatter is then determined from a 3 × 3 coherency matrix $[T]$ composed of three scattering components: surface scattering, m_s, double-bounce, m_d and volume scattering, m_v, as shown in Equation 5.2:

$$\begin{aligned}[T] &= [T_s] + [T_d] + [T_v] \\ &= m_s \begin{bmatrix} \cos^2 \alpha_S & \cos \alpha_S \sin \alpha_S e^{i\varphi_S} & 0 \\ \cos \alpha_S \sin \alpha_S e^{-i\varphi_S} & \sin^2 \alpha_S & 0 \\ 0 & 0 & 0 \end{bmatrix} \\ &+ m_d \begin{bmatrix} \cos^2 \alpha_d & \cos \alpha_d \sin \alpha_d e^{i\varphi_S} & 0 \\ \cos \alpha_d \sin \alpha_d e^{-i\varphi_S} & \sin^2 \alpha_d & 0 \\ 0 & 0 & 0 \end{bmatrix} \\ &+ m_v \begin{bmatrix} F_P & 0 & 0 \\ 0 & 1 & 0 \\ 0 & 0 & 1 \end{bmatrix}\end{aligned} \tag{5.2}$$

where $[T_s]$, $[T_d,]$ and $[T_v]$ are the surface scattering, double-bounce and volume scattering matrix. α is the dominant scattering mechanism. φ is the scattering phase, can be estimated, as shown in Equation 5.3:

$$\begin{cases} \varphi_d = \arg(T_{12}), \varphi_s = 0 \; if \; \alpha_d > \dfrac{\pi}{4} \\ \varphi_s = \arg(T_{12}), \varphi_d = 0 \; if \; \alpha_d < \dfrac{\pi}{4} \end{cases} \tag{5.3}$$

The Equation 5.2 has seven unknowns $m_s, m_d, m_{v,} \alpha_s, \alpha_{d,} \varphi_s$, and φ_d. In this model $F_P = 2$ which corresponds to the dipole cylinder cloud model. In general either surface scattering or double-bounce scattering dominates and the α parameter can be known to set the minor mechanism without too much loss of accuracy. If the double-bounce scattering dominant, then $\alpha_s = 0$ and $\alpha_s = \frac{\pi}{2}$, if the surface scattering is dominant. Now the model has five unknown parameters and can be possible to invert.

5.2.1 Model selection

In the Freeman-Durden model (Freeman & Durden, 1998), nothing is mentioned about the orthogonality of the surface and double-bounce component, but it has already been seen that for any surface scattering mechanism α_s, the double-bounce scattering mechanism has $\alpha = {}^{\pi}/_{2} - \alpha_s$. Therefore, it can be assumed that the surface and double-bounce mechanisms are orthogonal and it is allowed to express $\alpha_s, \alpha_{d,}$ in terms of α. The

Equation 5.2 has now five unknowns and five measurements. This model is called the hybrid Freeman/ eigenvalue technique (Cloude, 2010), as shown in Equation 5.4.

$$
\begin{aligned}
[T] &= m_s \begin{bmatrix} \cos\alpha \\ -\sin\alpha \\ 0 \end{bmatrix} [\cos\alpha \quad -\sin\alpha \quad 0] \\
&\quad + m_d \begin{bmatrix} \sin\alpha \\ \cos\alpha \\ 0 \end{bmatrix} [\sin\alpha \quad \cos\alpha \quad 0] \\
&\quad + m_v \begin{bmatrix} F_P & 0 & 0 \\ 0 & 1 & 0 \\ 0 & 0 & 1 \end{bmatrix} \\
&= \begin{bmatrix} m_s\cos^2\alpha + m_d\sin^2\alpha & \cos\alpha\sin\alpha(m_d - m_s) & 0 \\ \cos\alpha\sin\alpha(m_d - m_s) & m_d\cos^2\alpha + m_s\sin^2\alpha & 0 \\ 0 & 0 & 0 \end{bmatrix} \\
&\quad + \begin{bmatrix} F_P m_v & 0 & 0 \\ 0 & m_v & 0 \\ 0 & 0 & m_v \end{bmatrix} \\
[T] &= [T_{sd}] + [T_v]
\end{aligned}
\tag{5.4}
$$

where α is predominantly surface or double-bounce scattering, depending on the dominant eigenvalue of a 2×2 sub-matrix as shown and $[T_{sd}]$ is the dominant "surface" component, modelled as either a surface scattering or double-bounce scattering contribution, and $[T_v]$ is the volume component. This model is entirely consistent with the RVoG model which is the simplest form of two-layer approach, with a volume layer of particles above a non-penetrable boundary or surface (Cloude, & Papathanassiou, 2003).

Since the model is physical based therefore Equation 5.4 is to enable inversion of model directly from the data. The first step is to use the HV-polarization channel to estimate the volume scattering component, m_v, as shown in Equation 5.5. Second step, the calculation of surface scattering component, m_s and double-bounce component, m_d are given by the eigenvalues of the rank 2 matrix $[T_{sd}]$ and then using these values to obtain the estimation of α parameter, as shown in Equation 5.7:

$$
m_v = T_{33} \tag{5.5}
$$

$$
\begin{aligned}
m_{d,s} &= \frac{(T_{11} + T_{22} - (F_P + 1)T_{33})}{2} \\
&\quad \pm \frac{\sqrt{(T_{11} - T_{22} - (F_P - 1)T_{33})^2 + 4|T_{12}|^2}}{2}
\end{aligned}
\tag{5.6}
$$

$$\alpha_{d,s} = \cos^{-1}\left[\left(1 + \left|\frac{T_{12}}{T_{22} - T_{33} - m_{d,s}}\right|^2\right)^{-\frac{1}{2}}\right] \tag{5.7}$$

The maximum surface component is selected from the maximum of the pair m_s and m_d as defined in Equation 5.6. The surface component includes both double-bounce and surface scattering contributions.

This model will be used to estimate the ratio of ground-to-volume scattering components, termed μ which is an important parameter for the development of polarimetric interferometry (section 1.3.4). By measuring maximum surface component from Equation 5.8 the corresponding α parameter can be calculated, as shown in Equation 5.9:

$$m_{max} = max(m_d, m_s) \tag{5.8}$$

$$\alpha_{max} = \cos^{-1}\left[\left(1 + \left|\frac{T_{12}}{T_{22} - T_{33} - m_{max}}\right|^2\right)^{-\frac{1}{2}}\right] \tag{5.9}$$

The volume shape parameter F_P is measured by Equation 5.10.

$$F_P = \frac{T_{11}}{T_{33}} - \frac{|T_{12}|^2}{T_{33} * (T_{22} - T_{33})} \tag{5.10}$$

where $\begin{cases} 0 \leq F_P \leq 2 & -\text{Multiple scattering} \\ 2 \leq F_P \leq \infty & -\text{Single scattering} \end{cases}$

The ratio of ground-to-volume scattering can be obtained by assuming a scattering mechanism for α parameter, as shown in Equation 5.11:

$$\mu = \frac{surface}{volume} = \frac{\underline{w}^{*T}[T_S]\underline{w}}{\underline{w}^{*T}[T_V]\underline{w}}$$

$$= \frac{m_{max}}{m_v}\frac{1}{(1 + (F_P - 1)\cos^2\alpha_{max})} \tag{5.11}$$

The Equation 5.11 is not the maximum ground-to-volume scattering ratio. This can be achieved by finding the largest eigenvector of the matrix $[T_v]^{-1}[T_{sd}]$, as shown in Equation 5.12:

$$\frac{m_{max}}{m_v}\begin{vmatrix} \frac{\cos^2\alpha_{max}}{F_P}-\mu & \frac{\cos\alpha_{max}\sin\alpha_{max}}{F_P} \\ \cos\alpha_{max}\sin\alpha_{max} & \sin^2\alpha_{max}-\mu \end{vmatrix}=0$$

$$\mu_{max}=\frac{m_{max}}{m_v}\left(\sin^2\alpha_{max}+\frac{1}{F_P}\cos^2\alpha_{max}\right) \tag{5.12}$$

In Equation 5.12, μ_{max} is a function of the surface scattering mechanism α, the volume shape parameter F_P, and the ratio of backscatter amplitude components. When μ_{max} is large, the idea is that GSV is low (due to gaps in the forest or low level vegetation) and when μ_{max} is small, GSV is high due to high canopy covers which increase volume scattering. This idea has been developed quantitatively using the two-layer approach of surface and volume scattering in Askne *et al.* (2003). It leads to a classical relationships between GSV and μ_{max}, as shown in Equation 5.13:

$$\mu_{max}=\frac{\sigma^0_{gr}}{\sigma^0_\infty}\frac{e^{-\beta*GSV}}{1-e^{-\beta*GSV}}=\frac{re^{-\beta*GSV}}{1-e^{-\beta*GSV}} \tag{5.13}$$

where $r=\frac{\sigma^0_{gr}}{\sigma^0_\infty}$ and σ^0_{gr} and σ^0_∞ define the backscatter coefficient of the sparse forest and the backscattering coefficient of the dense forest respectively. The model of Equation 5.13 contains two unknowns r and β that need to be estimated. It is found that the two-way forest transmissivity is exponentially related to the GSV with coefficient β (Askne *et al.* 2003). The following expression where the forest backscatter is describes as a function of GSV, has been used to measure r and β.

$$\sigma^0_{for}=\sigma^0_{gr}e^{-\beta V}+\sigma^0_\infty\left(1-e^{-\beta V}\right) \tag{5.14}$$

In Equation 5.14 σ^0_{gr}, σ^0_∞ and β are unknown and need to be estimated using the training set of backscatter and GSV measurements.

5.2.2 Model training and model parameters estimation

The four unknown parameters μ_{max}, σ^0_{gr}, σ^0_∞ and β have to be measured. The μ_{max} is estimated without using any training set of stands. It is computed directly from the Equation 5.12. Figure 5.2 shows one example of ratio of ground-to-volume scattering μ_{max}, for frozen condition (13.04.2009) and unfrozen-dry condition (21.08.06) in Chunsky-N. Here μ_{max} is mapped in a color-coded form as shown between 0 dB and +24 dB. Hence blue areas are where surface scattering dominates and yellow where volume scattering dominates. The most forested areas are seen in yellow colour corresponding to a μ_{max} in the range 0 to -5dB. At frozen condition μ_{max} is higher than at unfrozen condition. The reciprocal of μ_{max} i.e. volume-to-ground scattering ratio can be used as a substitution for GSV map. One should keep in mind that as this ratio involves information from the off-diagonal elements of coherency matrix $[T]$ i.e. polarimetric phase, it is potentially more sensitive to growing stock volume variations than backscatter intensities alone.

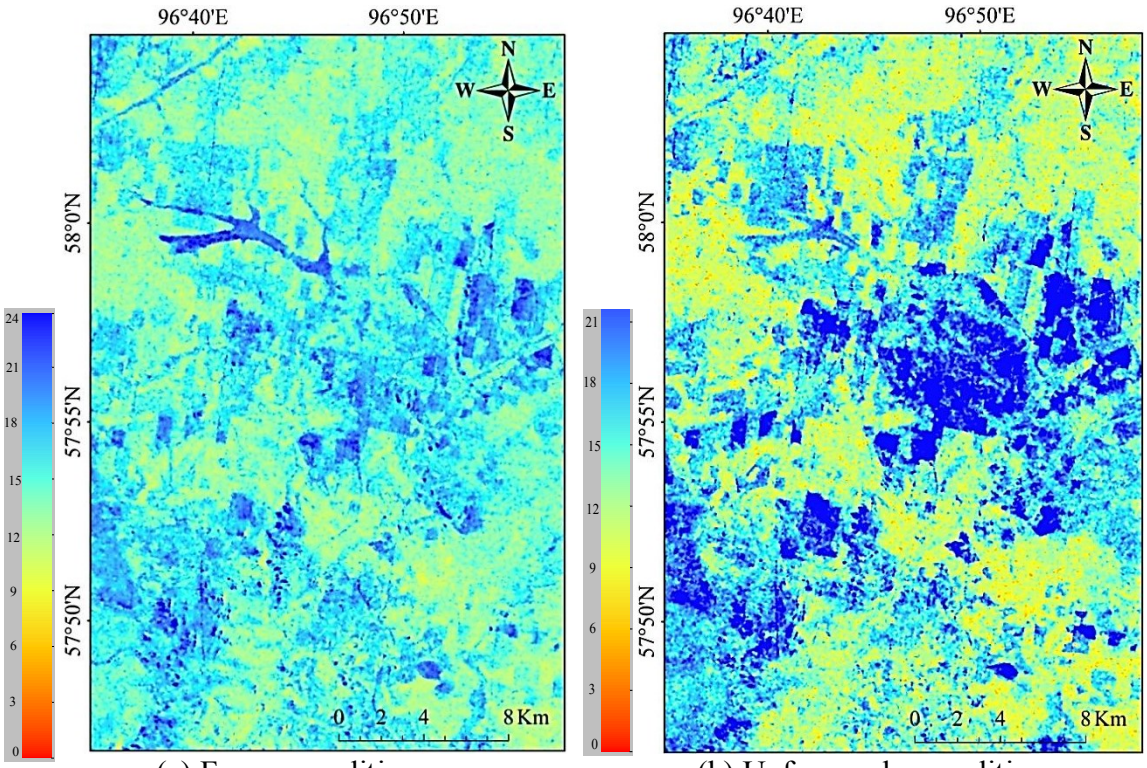

(a) Frozen condition 13.04.2009

(b) Unfrozen-dry condition 21.08.2006

Figure 5.2 Image of ground-to-volume scattering ratio μ_{max} in dB for Chunsky-N under (a) frozen (13.04.2009) and (b) unfrozen (21.08.2006) conditions.

The sparse forest and dense forest backscatter coefficients ($\sigma_{gr}^0$and σ_{∞}^0) and the two way transmissivity β, can be estimated with a non-linear regression using a least square approach which minimise the sum of the squared differences between measured HV-backscatter $\sigma_{m,i}^0$ and the modelled backscatter, σ_i^0 for each training sample:

$$\sum_{i=1}^{N}\left[\sigma_{m,i}^0 - \sigma_i^0\left(\sigma_{gr}^0, \sigma_{\infty}^0, \beta\right)\right] = min \tag{5.15}$$

where N represents the number of forest stands in the training set, $\sigma_{m,i}^0$ is the measured backscatter for the i^{th} stand whereas σ_i^0 is the corresponding modelled backscatter value. β is empirically defined coefficient. The uncertainty of backscatter measurement must be as small as possible to obtain a correct fit. The same training sets of coherence modelling has been used for the estimation of three unknown parameters, σ_{gr}^0, σ_{∞}^0 and β. The shortcoming of this approach is that if the backscatter data is affected by a large spread, these three unknown parameters will suffer from significant uncertainty.

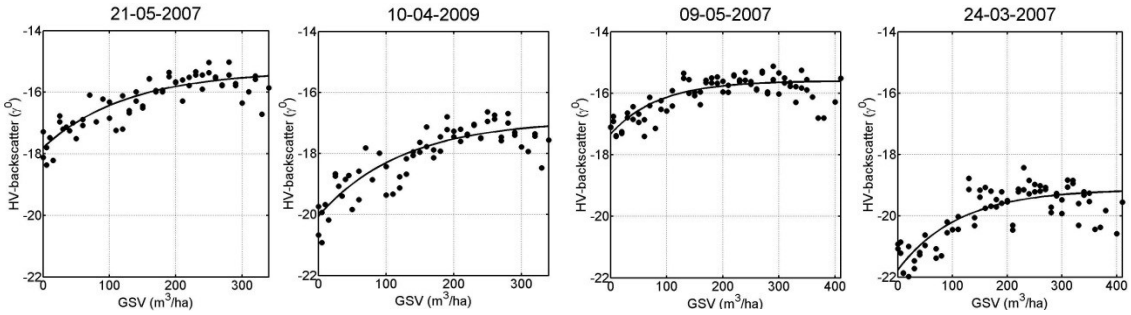

(a) Shestakovsky-N (b) Primorsky-E

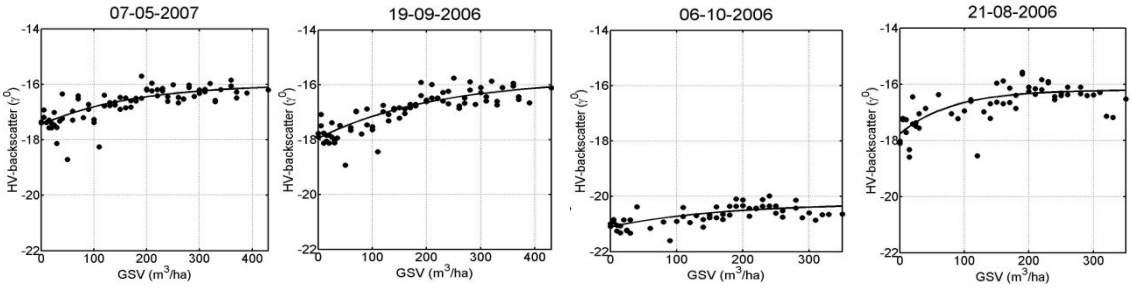

(c) Chunsky-E (d) Chunsky-N

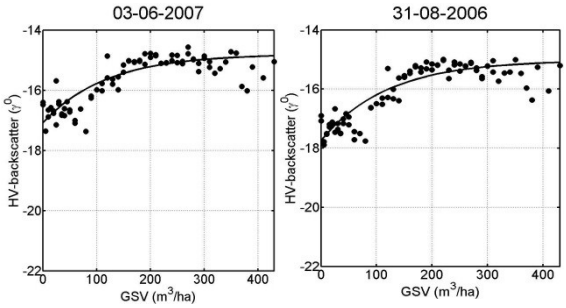

(e) Bolshe-NE

Figure 5.3 Behaviour of ALOS PALSAR L-band HV-backscatter (σ^0) as a function of GSV for (a) Shestakovsky, (b) Primorsky-E, (c) Chunsky-E, (d) Chunsky-N and (e) Bolshe-NE. The filled circles show the ALOS PALSAR HV-backscatter observations and the solid lines represent the corresponding fittings of the model obtained by Equation 5.14. The number of stands for training sets varies between 16% and 21% of total forest stands.

Figure 5.3 illustrates the results of regression between modelled backscatter and GSV and Table 5.2 highlights the modelled backscatter which shows higher sensitivity than coherence for changing weather conditions. Even though the spread of stand-wise observations from modelled curves are high, the average level of backscatter for different GSV class is well described by the model. Saturation level of backscatter has been occurred between 102 and 222 m³/ha. The dynamic range varies between 0.7 dB and 3.8 dB depending on the weather conditions. Lowest dynamic range has been achieved under frozen condition whereas highest dynamic range achieved under unfrozen conditions. The

difference of dynamic range between unfrozen-dry and unfrozen-wet condition is less than 0.6 dB for all the test sites. One exception has been observed in Primorsky-E. Comparing

Test Sites	Dates	σ^0_{gr} (dB)	σ^0_{∞} (dB)	β (ha/m³)	$r=\frac{\sigma^0_{gr}}{\sigma^0_{\infty}}$
Shestakovsky-N	21.05.2007	-20.05	-16.9	192.3	0.48
Shestakovsky-N	10.04.2009	-17.8	-15.3	163.9	0.56
Shestakovsky-N	26.05.2009	-14.6	-10.8	197.0	0.42
Primorsky-E	09.05.2007	-17.3	-15.5	102.0	0.66
Primorsky-E	24.03.2007	-21.7	-19.1	126.6	0.55
Primorsky-E	31.05.2009	-15.6	-14.1	113.6	0.71
Chunsky-E	07.05.2007	-17.7	-15.9	178.6	0.66
Chunsky-E	19.09.2006	-18.0	-15.7	222.2	0.59
Chunsky-N	06.10.2006	-21.1	-20.2	166.7	0.81
Chunsky-N	13.04.2009	-20.5	-19.8	161.3	0.85
Chunsky-N	21.08.2006	-17.7	-16.2	120.5	0.71
Chunsky-N	24.05.2007	-16.8	-15.2	128.2	0.69
Bolshe-NE	03.06.2007	-17.1	-14.7	140.8	0.58
Bolshe-NE	31.08.2006	-17.7	-15.0	144.9	0.54

Table 5.2 HV-backscatter modelled parameters for Shestakovsky-N, Primorsky-E, Chunsky-E, Chunsky-N and Bolshe-NE

different weather conditions in Primorsky-E, a highest dynamic range (2.6 dB) is found for frozen conditions.

5.3 GSV Retrieval procedure

After determining the unknown model parameters from the model training, it is possible to retrieve the growing stock volume based on HHVV-coherence GSV_{HHVV}, and ratio of ground-to-volume scattering GSV_{gv}, for an independent set of stands (test set) by the inversion of the models (Equation 5.1 and Equation 5.13). More than 80% of the total forest stands have been used for the validation of the models. The retrieval of GSV has been performed at stand level. The estimated growing stock volume based on polarimetric coherence, GSV_{HHVV} and ratio of ground-to-volume scattering, GSV_{gv} are expressed as:

$$GSV_{HHVV} = \frac{1}{v_\infty}\log\left(\frac{\gamma_\infty - \gamma_{HHVV}(v)}{\gamma_\infty - \gamma_0}\right) \tag{5.16}$$

$$GSV_{gv} = \frac{1}{\beta}\log\left(1 + \frac{r}{\mu_{max}}\right) \tag{5.17}$$

The GSV can only be retrieved if the coherence values are within the range between γ_0 and γ_∞. Since the model used here is essentially exponential, they approach an asymptotic limit and in some cases the retrieved values are fallen outside the range determined by the model would result in either infinite or negative growing stock volume. Therefore, if coherence measurements are outside the interval of the modelled values, from Equation 5.16 the following strategies are taken into account:

- The stands with coherence values above the modelled ground coherence γ_0 are set to 0 m³/ha GSV.
- The stands with coherence values below the modelled dense forest coherence γ_∞ are set to highest growing stock volume of the test site.
- The coherence values which are at least two standard deviations distant from modelled coherence, the corresponding stands are classified as outliers and are excluded (Santoro *et al.* 2002).

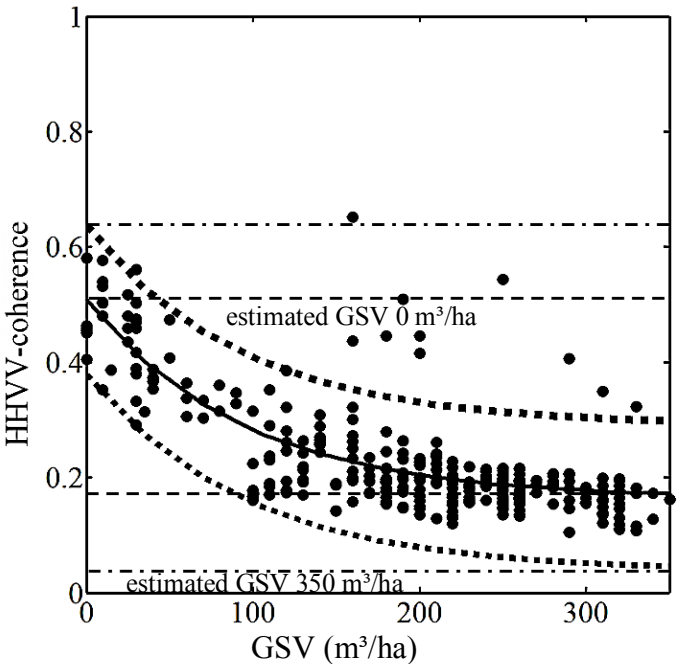

Figure 5.4 Example of regression curve for Shestakovsky-N. The dashed lines represent the upper and lower limits of the regression curve. The dotted lines resemble the two standard deviation distances from the curve and the dash-dotted lines are the limits for removal of outliers.

Figure 5.4 illustrates the above procedures for Shestakovsky-N. The two-standard deviations of coherence from the modelled curve are measured for each training set of the stand. The two dotted lines in Figure 5.4 represent the two standard deviations from the curve. If any coherence values outside these dotted lines are observed, the stands of these coherence values are removed from the training set.

To quantify the performance of the GSV retrieval, the following statistical measurements are used:

- The Root mean square error (RMSE).
- Relative RMSE which is defined as the ratio between RMSE and the mean value of ground-truth GSV. It allows to inter-comparison of results between different test sites. The value is multiplied by 100 to get it in percent.
- Coefficient of determination R^2 between ground-truth GSV and predicted GSV are used.
- Estimation bias which is defined as:

  $$\text{Estimation bias} = \text{mean}(GSV_{es}) - \text{mean}(GSV_{rf})$$

  where GSV_{es} and GSV_{rf} signifies the estimated GSV and the reference or ground-truth GSV for the specific study area.

The RMSE is calculated as shown in Equation 5.18 (Fransson *et al.* 2001):

$$\text{RMSE} = \sqrt{\left[\frac{1}{N_{test}}\sum_{i=1}^{N_{test}}\left(\left(GSV_i^{es} - GSV_i^{rf}\right)\right)^2 - 0.5\frac{1}{N_{test}}(SE_i)^2\right]} \quad (5.18)$$

N_{test} represents the number of samples in the test set, GSV_i^{es} and GSV_i^{rf} are the retrieved and ground-truth growing stock volume respectively for stand i , SE_i is the standard error for stand i and factor 0.5 is a correction due to systematic sampling design in accordance with the empirical investigations (Lindgren, 1984). The inventory accuracy for growing stock volume is 15% for stands which are ready to be harvested and 20% for all other stands (Schmullius, *et al*. 2001; Stolbovoi & Mccallum, 2002). In this study, standard error, *SE*, is calculated by 20% of the mean ground-truth growing stock volume of the test set.

5.4 Assessment of GSV retrieval

The computed values of RMSE, relative RMSE, R^2 and estimation bias for all the analysed coherence images and ratio of ground-to-volume scattering images are listed in Table 5.3 and Table 5.4 respectively for Shestakovsky-N, Primorsky-E, Chunsky-E, Chunsky-N and Bolshe-NE. Using coherence images, the RMSE varies between 38 and 119 m^3/ha and R^2 between 0.35 and 0.73. The best RMSE 38 m^3/ha is reported for Shestakovsky-N whereas the worst RMSE 119 m^3/ha is obtained for Bolshe-NE. Both best and worst RMSE are achieved at unfrozen-wet condition. Eriksson, (2004) and Santoro *et*

al. (2004) also reported that the lower retrieval accuracies achieved with interferometric coherence images acquired under unfrozen conditions.

The relative RMSE are within the range between 18 and 76%. Comparing the values of RMSE and relative RMSE, high relative RMSE has been observed for Chunsky-N at frozen and unfrozen conditions. The high R^2 value for Chunsky-N is due to the large number of stands with low GSV. The bias is more sites dependent rather on weather conditions. The retrieved mean GSV is over estimated at Shestakovsky-N and Chunsky-E. On the other hand, under estimation of retrieved mean GSV is observed for Primorsky-E, Chunsky-N and Bolshe-NE.

Test Sites	Dates	RMSE (m^3/ha)	Relative RMSE (%)	R^2	Estimation bias
Shestakovsky-N	21.05.2007	41	20	0.67	36
Shestakovsky-N	10.04.2009	60	31	0.61	22
Shestakovsky-N	26.05.2009	38	18	0.73	5
Primorsky-E	09.05.2007	96	53	0.36	-38
Primorsky-E	24.03.2007	107	57	0.45	-43
Primorsky-E	31.05.2009	108	57	0.36	-25
Chunsky-E	07.05.2007	84	69	0.66	24
Chunsky-E	19.09.2006	71	57	0.70	10
Chunsky-N	06.10.2006	71	68	0.60	-8
Chunsky-N	13.04.2009	70	71	0.62	-33
Chunsky-N	21.08.2006	75	72	0.58	-2
Chunsky-N	24.05.2007	78	73	0.56	-8
Bolshe-NE	03.06.2007	119	76	0.35	-23
Bolshe-NE	31.08.2006	115	73	0.39	-18

Table 5.3 Growing stock volume retrieval accuracy expressed in terms of RMSE, relative RMSE, R^2 and estimation bias from ALOS PALSAR L-band HHVV-coherence for all the investigated forest areas. The (+) positive values in estimation bias indicate the overestimation and the negative (-) values represent the underestimation of retrieved mean GSV.

Test Sites	Dates	RMSE (m^3/ha)	Relative RMSE (%)	R^2	Estimation bias
Shestakovsky-N	21.05.2007	44	23	0.62	3
Shestakovsky-N	10.04.2009	58	31	0.52	-12
Shestakovsky-N	26.05.2009	48	24	0.59	7
Primorsky-E	09.05.2007	71	35	0.41	12
Primorsky-E	24.03.2007	74	37	0.42	-25
Primorsky-E	31.05.2009	76	38	0.35	5
Chunsky-E	07.05.2007	77	58	0.52	-11
Chunsky-E	19.09.2006	72	54	0.59	12
Chunsky-N	06.10.2006	77	72	0.56	-7
Chunsky-N	13.04.2009	78	73	0.58	-9
Chunsky-N	21.08.2006	81	76	0.56	53
Chunsky-N	24.05.2007	86	81	0.54	45
Bolshe-NE	03.06.2007	85	54	0.40	8
Bolshe-NE	31.08.2006	87	55	0.38	10

Table 5.4 Growing stock volume retrieval accuracy expressed in terms of RMSE, relative RMSE and R^2 from ALOS PALSAR L-band ground-to-volume scattering ratio for all the investigated forest areas.

The RMSE spans between 44 and 87 m^3/ha for the retrieval of GSV from ratio of ground-to-volume scattering power images. Likewise retrieval of GSV from coherence images, Shestakovsky-N shows the best RMSE and Bolshe-NE shows the worst RMSE and both under unfrozen-dry conditions. In contrast to the retrieval of GSV based on HHVV-coherence, the bias is dependent on weather conditions. The retrieved mean GSV is underestimated from 7 to 25 m^3/ha at frozen and thawing conditions whereas at unfrozen conditions the retrieved GSV is overestimated.

The poor quality of retrieval GSV based on coherence has been observed for Primorsky-E and Bolshe-NE. The RMSE is always greater than 100 m^3/ha in Primorsky-E, except for one case when the error is 96 m^3/ha. The situation is even worse in Bolshe-NE where RMSE is between 115 and 119 m^3/ha (Table 5.3). The relative RMSE shows higher inaccuracy for the estimation of GSV in Bolshe-NE. The reason behind the high retrieval

error is low sensitivity to GSV i.e. smaller dynamic range, and large dispersion of the coherence measurements (Figure 4.5 and Figure 4.6).

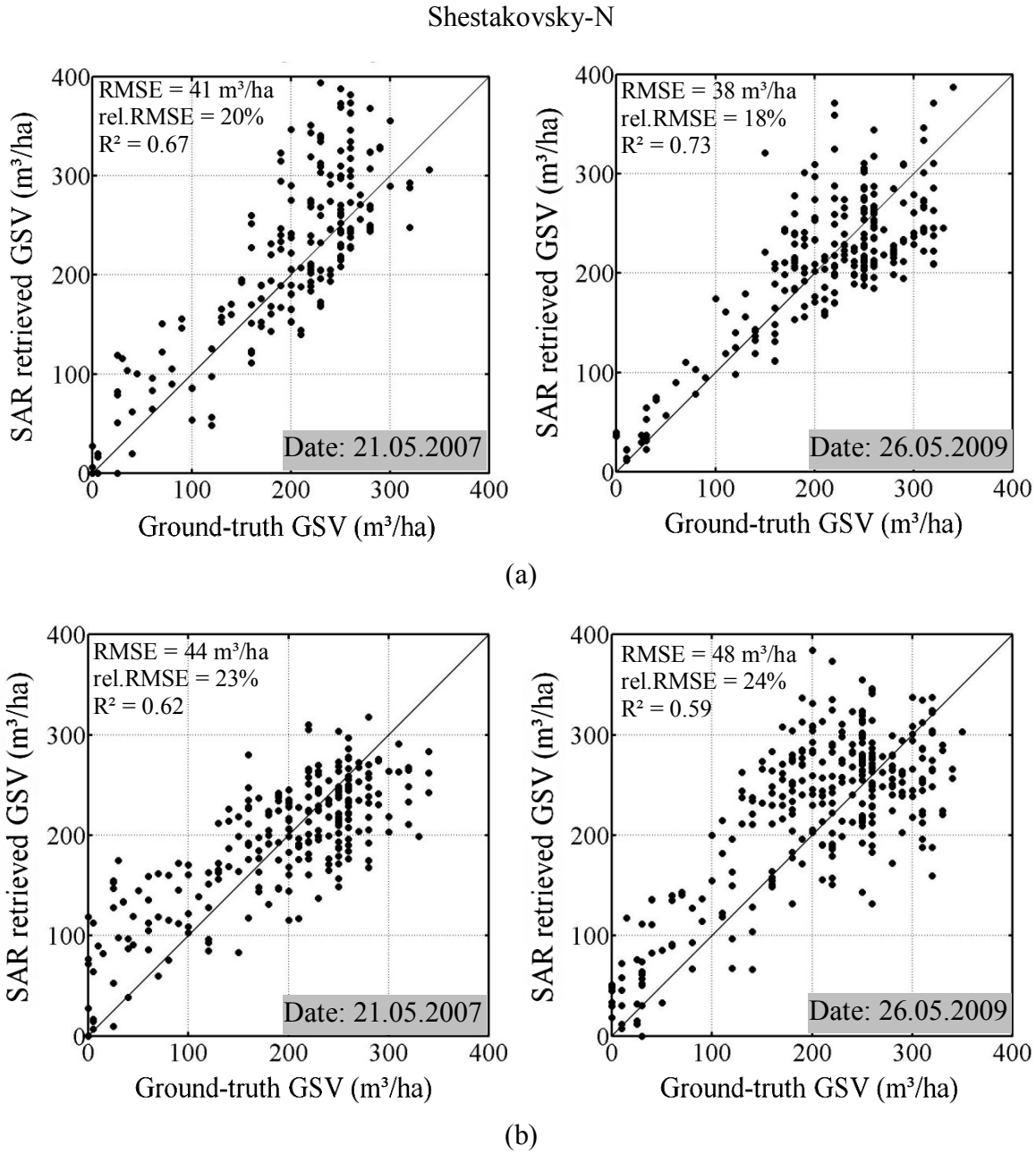

Figure 5.5 Comparison between growing stock volume from forest inventory data and growing stock volume retrieved from L-band ALOS PALSAR (a) HHVV-coherence and (b) ratio of ground-to-volume scattering for Shestakovsky-N.

In Figure 5.5(a), the examples of scatter plots for ground-truth GSV against the retrieved GSV using ALOS PALSAR L-band polarimetric coherence are illustrated. In Appendix C.1 and C.2, the retrieved growing stock volume has been plotted against forest growing stock volume for all available images. The majority of stands are clustered along 1:1 line up to almost 250 m³/ ha but there are some stands with high GSV (between 200

and 300 m³/ ha) which are significantly overestimated. The retrieved GSV from the coherence image acquired under unfrozen-wet (26.05.2009) condition has shown the saturation at ~220 m³/ ha. The results are good for young and intermediate stands of GSV, but there are few stands with high GSV are underestimated. Such behaviours can be due to the effect of coherence estimation and lower sensitivity of coherence at high GSV. In Figure 4.6 it has been seen the saturation level is between 200 and 250 m³/ha under unfrozen-wet condition at Shestakovsky-N. At thawing condition (26.05.2009), the GSV between 200 and 300 m³/ha are both overestimated and underestimated (Figure C.1.1 in Appendix C).

Figure 5.5(b) shows the comparison of ground-truth GSV and retrieved growing stock volume based on the ratio of ground-to-volume scattering. In contrast to the estimation of using coherence data at unfrozen-dry (21.05.2007) condition, the estimation errors for stands with high GSV values are not significant but there are some stands with low GSV are overestimated. The retrieval of GSV under unfrozen-wet condition has shown the good agreement with young and intermediate forests but stands with high GSV are overestimated. It is therefore, difficult to judge which of the two models that is most suitable for GSV prediction.

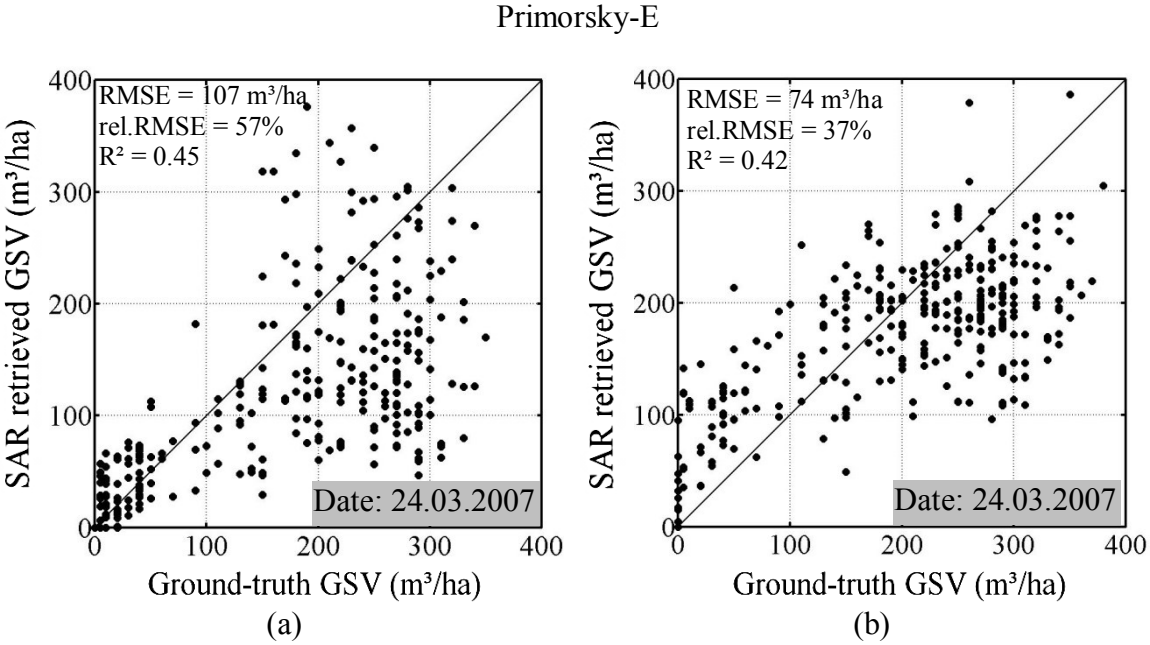

Figure 5.6 Comparison between growing stock volume from forest inventory data and growing stock volume retrieved from L-band ALOS PALSAR (a) HHVV-coherence and (b) ratio of ground-to-volume scattering for Primorsky-E.

The estimation of GSV from coherence model shows slightly better for frozen conditions while the ratio of ground-to-volume scattering model performs better for unfrozen-dry condition. The high retrieval error of RMSE=107 m³/ha for frozen condition at Primorsky-E does not agree with that statement (Figure 5.6(a)). In fact, the RMSE is between 96 and 108 m³/ha for Primorsky-E at frozen and unfrozen conditions. The one

reason for such results are probably error in the ground truth data but then the question will be raised on why comparatively low retrieval error (RMSE between 71 and 76 m^3/ha) for estimating GSV using the ratio of ground-to-volume scattering (Figure 5.6(b)). The most possible reason is that the coherence for the test sets or validation stands does not entirely coincide with the true coherence. Primorsky-E and Bolshe-NE might have strongly affected by the model training, and ground-truth errors are also considered responsible for the low accuracy than other test sites.

Comparing the retrieval results from the models of the two polarimetric parameters for all the test sites, it is seen that at the stand level, RMSE is better for ratio of ground-to-volume scattering than for polarimetric coherence. Retrieval of GSV is characterised by smaller errors when it is based on ground-to-volume ratio rather than on coherence. The standard deviations of estimated GSV using ratio of ground-to-volume scattering is always smaller than the standard deviations of estimated GSV using coherence for all the test sites (Figure C.3.1 in Appendix C).

The retrieval error is strongly site-dependent. Shestakovsky-N shows the best results and Bolshe-NE shows the worst result. The reasons for the large spread and the different behaviours have to be attributed to the different test site properties, as well as to the ground data accuracy. In Siberia, heterogeneity of the dielectric properties, the effect of forest structural features on the relationship between backscatter and GSV and local inaccuracies in the ground data could explain the large errors. The training should encompass the best possible distribution of stem volumes in the area under investigations. Askne & Santoro *et al.* (2005) have shown the importance of having both training and validation sets a uniform distribution of growing stock volume, being furthermore similar.

Since the overall accuracy of the retrieval GSV based on ratio of ground-to-volume scattering is slightly better than the HHVV-coherence, the remaining analysis will focus only on ratio of ground-to-volume scattering. The estimation of GSV based on the ratio of ground-to-volume scattering has been investigated on the dependency of forest stand structure such as stand size and forest density which in particular is assumed to be expressed by means of the relative stocking (RS) parameter. To take into account of different distribution of ground-truth GSV in the test set, the relative RMSE gives the better idea of retrieval accuracy. For the investigation the RS is separated by three classes: 0-50%, 51-70% and 71-100%. The plot in Figure 5.7 depicts the clear decrease of relative RMSE by increasing relative stocking i.e. for forests with more managed type of structure. Except in Chunsky-N the relative RMSE has obtained between 17 and 40% for RS greater than 70%. The retrieval error for Chunsky-N reduces considerably when RS = 51-70% has been considered. For RS=71-100% a slight decrease of relative RMSE has been achieved for the retrieval of GSV. Santoro *et al.* (2007a) also found the high value of relative RMSE for RS = 71-100% in the case of Chunsky-N. The authors assumed that high values for RS = 71-100% is because of few stands with mostly high volumes are included in the test set. The assumption is agreed with the investigation of this work. The other possible reasons for the higher relative RMSE could be due to the fact that (i) several stands had been partially or totally clear-felled between the collection of the in situ measurements and the

acquisition of SAR data and (ii) almost 60% are heterogeneous stands of four or five tree species are considered here for the investigations. One should keep in mind that KOMPSAT-2 data which is used to update the forest inventory data for recent logging and disturbances are not available in Chunsky-N.

It has been observed that large stand size has a slight impact to obtain accurate retrieval. The results show that relative RMSE of 16-40% is achieved when the forest stands size is larger than about 40 ha.

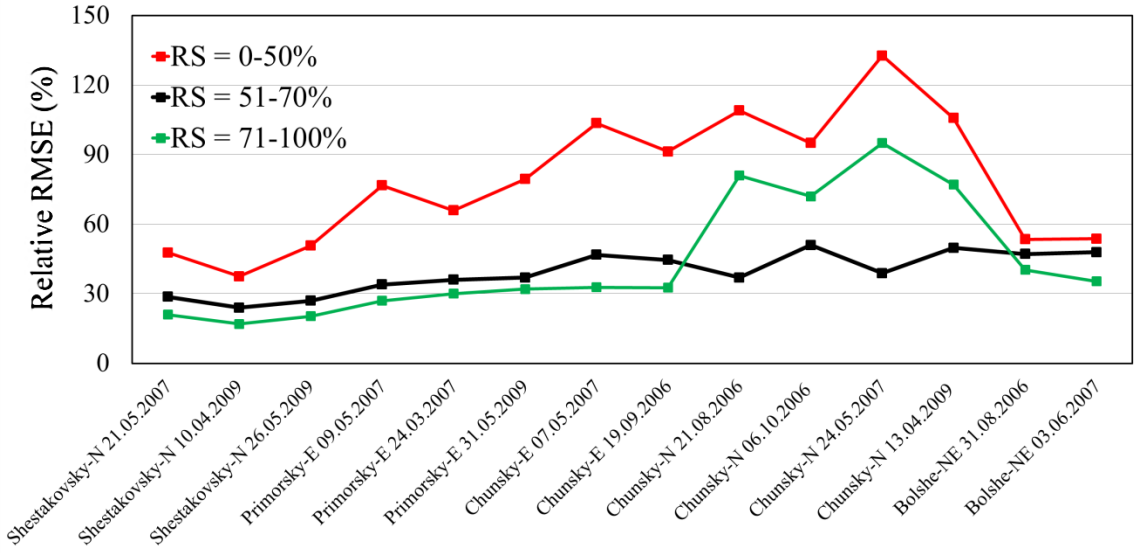

(a)

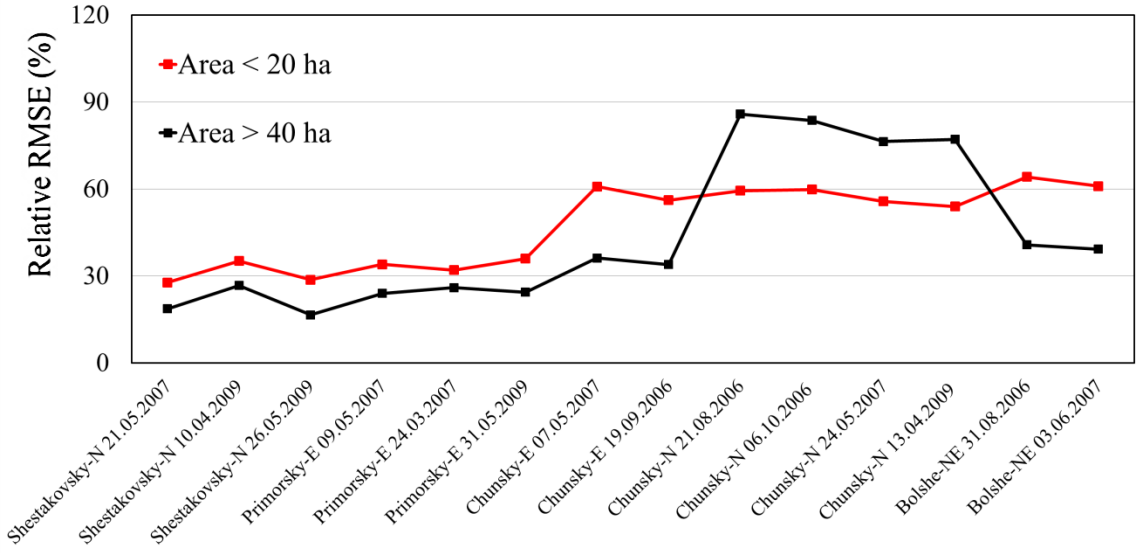

(b)

Figure 5.7 The relative RMSE for the estimation of GSV as a function of (a) relative stocking and (b) stand size from ratio of ground-to-volume scattering images in Siberian forests.

Test Sites	Dates	Aspen	Birch	Larch	Pine	Weather conditions
Shestakovsky-N	21.05.2007	12	44	49	44	Unfrozen, dry
Shestakovsky-N	10.04.2009	73	61	57	45	Thaw, wet
Shestakovsky-N	26.05.2009	15	51	28	41	Unfrozen, wet
Primorsky-E	09.05.2007	47	48	41	79	Unfrozen, dry
Primorsky-E	24.03.2007	43	46	67	86	Frozen
Primorsky-E	31.05.2009	79	52	35	82	Unfrozen, wet
Chunsky-E	07.05.2007	84	36	59	93	Thaw, wet
Chunsky-E	19.09.2006	77	30	50	93	Unfrozen, wet
Chunsky-N	06.10.2006	—	40	108	120	Frozen
Chunsky-N	13.04.2009	—	36	106	110	Frozen
Chunsky-N	21.08.2006	—	71	43	61	Unfrozen, dry
Chunsky-N	24.05.2007	—	81	26	60	Unfrozen, wet
Bolshe-NE	03.06.2007	66	46	17	128	Unfrozen, wet
Bolshe-NE	31.08.2006	55	43	49	127	Unfrozen, dry

Table 5.5 Growing stock volume retrieval accuracy for aspen, birch, larch and pine forests expressed in terms of RMSE from ALOS PALSAR ratio of ground-to-volume scattering.

The RMSE for the retrieval of growing stock volume as a function of dominant tree species: aspen, birch, larch and pine are listed in Table 5.5. Relative RMSE and estimation bias have been provided in Table C.4.1 and Table C.4.2 (Appendix C) respectively. The selection criteria for the dominant tree species are measured according to section 4.5. The retrieval accuracy varies from test sites to test site. The best RMSE for aspen (12 m^3/ha), birch (30 m^3/ha), larch (17 m^3/ha) and pine (41 m^3/ha) has been reported for Shestakovsky-N, Chunsky-E, Bolshe-NE and Shestakovsky-N respectively.

Four different weather conditions: unfrozen-dry, unfrozen-wet, frozen and thawing, have been reported in this investigation. Unfortunately SAR images of these four weather conditions are not available for each test sites. Therefore, it would be difficult to find which will be the best possible weather condition to retrieve specific species. Aspen is retrieved more accurately (12 m^3/ha) under unfrozen-dry conditions for Shestakovsky-N, Chunsky-E and Bolshe-NE but there is no image available under frozen condition. The images are available at frozen and unfrozen conditions for Primorsky-E and the best 43 m^3/ha RMSE for the retrieval of GSV for aspen forest has been achieved under frozen

condition. Images acquired under thawing condition (10.04.2009) for Shestakovsky-N and unfrozen-wet condition (31.05.2009) for Primorsky-E show larger RMSE compare to other images on that test sites under different meteorological conditions. One explanation is that the snow is melting at Shestakovsky-N and 1.6 cm precipitation recorded by the weather stations at Primorsky-E. Therefore, the forest ground is wet and the canopies are moist which makes the higher dielectric constant. The dynamic range of radar backscatter between sparse forest and dense forest becomes smaller because of the high dielectric constant. Moreover, the surface of the forest floor turned into rougher which creates the surface scattering higher. As a result, the ratio of ground-to-volume scattering, μ_{max} are smaller and it is difficult to separate ground component from the volume component for dense forest.

Birch shows similar kind of results like aspen for all test sites but the model is less sensitive for the retrieval of birch forest due to the changes of dielectric constant. The RMSE increases slightly for the retrieval of GSV under thawing condition (10.04.2009) and unfrozen-wet condition (31.05.2009). The retrieval accuracy for birch forest at Chunsky-N is different than other test sites. Under frozen condition, the best RMSE 36 m³/ha is measured for birch forest but the error increased to 71 m³/ha RMSE under unfrozen-wet condition and also for unfrozen-dry condition. If the best RMSE for the retrieval of GSV for larch forest is sorted out, the sequential order will be unfrozen-wet, unfrozen-dry, thawing, frozen conditions.

The retrieval accuracy for pine forest changes slightly (less than 7 m³/ha) due to the change of meteorological conditions for all the test sites except Chunsky-N. Under frozen condition, the error is between 110 and 120 m³/ha RMSE. The RMSE for the retrieval of GSV for pine forest from images acquired under unfrozen (wet and dry) condition decreases almost 50%.

In a brief, the retrieval accuracy of GSV for larch tree species has been observed to be consistently sensitive to the weather conditions. High accuracy has been obtained under unfrozen condition whereas low accuracy for frozen condition.

5. 5 Conclusions

In this chapter, the stand-wise retrieval of GSV based on polarimetric coherence and ratio of ground-to-volume scattering is assessed in Siberian forests. The relationships between coherence and ratio of ground-to-volume scattering with respect to growing stock volume are described in terms of simple and robust models. The model parameters are measured by the regression between polarimetric coherence and growing stock volume from the training sets. Almost 16 to 21% of the total stands have been used for the training. Ground-to-volume scattering ratio has been computed directly from the ALOS PALSAR L-band data.

The model parameters show the sensitivity to the weather conditions. Higher dynamic range is observed for coherence at frozen condition than at unfrozen condition whereas

vice versa for HV-backscatter coefficients. Higher magnitude of ground scattering component is observed at frozen condition than at unfrozen condition.

To assess the growing stock volume retrieval accuracy, the RMSE, relative RMSE and coefficient of determination R^2 are computed. A best RMSE of 38 m^3/ha and R^2=0.73 is obtained based on polarimetric coherence. On the other hand, using ratio of ground-to-volume scattering the best retrieval accuracy is 44 m^3/ha and R^2=0.62. The best results for both SAR parameters are observed under unfrozen condition at Shestakovsky-N. Though the best RMSE is slightly higher for coherence but it is possible to partially improve the retrieval accuracy using ratio of ground-to-volume scattering. Regardless the weather conditions, the best results are obtained in Shestakovsky-N. In Shestakovsky-N, at the stand level GSV up to 250 m^3/ha is possible to estimate with an error 38 m^3/ha (relative RMSE 18%). Several studies (Fransson *et al.* 2001; Santoro *et al.* 2002; Askne *et al.* 2003) reported relative RMSE less than 20% for the retrieval of growing stock volume. But these results are achieved for multi-temporal stack of ERS-1/2 C-band images acquired under frozen conditions and preferably with shorter baseline. Fransson & Israelsson, (1999) stated RMSE of 54 m^3/ha when estimating growing stock volume of boreal forests using multi-temporal JERS-1 L-band data. Similar results are found by Santoro *et al.* (2006), who reported RMS errors ranging from 36 m^3/ha (relative RMSE 25%) to 152 m^3/ha (relative RMSE 59%), when investigating JERS-1 data from test sites in the boreal zone using a model-based approach. For L-band SAR the saturation of growing stock volume estimation showed at about 150 m^3/ha (Rauste *et al.* 1994; Fransson & Israelsson, 1999). In tropical forest, saturation effects for estimating growing stock volume are not observed up to 308 m^3/ha (Goncalves, 2011). However no formal assessment of saturation is possible due to the small number of observations, and the lack of forest stands with GSV less than 155 m^3/ha and greater than 308 m^3/ha. The authors set up a model by using multi-linear regression model of several incoherent and coherent attributes including volume scattering power of Freeman and Durden decomposition (Freeman, 1998). The results of our study appear promising though high retrieval of error and low level of saturation for estimating growing stock volume in some test sites makes it difficult to have a final statement for Siberian forest. This should be investigated in greater detail in further studies.

The retrieval error is strongly site-dependent. Shestakovsky-N shows the best results and Bolshe-NE shows the worst result. The reason for the large spread and the different behaviours have to be attributed to the different test site properties, as well as to the ground data accuracy. In Siberia, heterogeneity of the dielectric properties, the effect of forest structural features on the relationship between backscatter and GSV and local inaccuracies in the ground-truth data could explain the large errors. The training data should encompass the best possible distribution of growing stock volume in the area under investigations.

The estimation bias measured by using polarimetric coherence is more sites dependent rather depending on weather conditions. The estimated mean GSV is over estimated at Shestakovsky-N and Chunsky-E. On the other hand, under estimation of retrieved mean GSV is observed for Primorsky-E, Chunsky-N and Bolshe-NE. In contrast, based on ground-to-volume scattering ratio the bias is mainly dependent on the weather conditions.

The estimated mean GSV is underestimated from 7 to 25 m³/ha at frozen and thawing conditions whereas at unfrozen conditions the retrieved GSV is overestimated.

Coherence is slightly better for retrieval of GSV at frozen condition whereas the ratio of ground-to-volume scattering is better for unfrozen condition. Since the ALOS PALSAR L-band full polarimetry images are not available for all kinds of weather conditions in each test site, it is difficult to say which condition is best suited for the retrieval of growing stock volume.

The estimation of GSV based on ratio of ground-to-volume scattering has been investigated on the dependency of forest stand structure such as stand size and forest density which in particular is assumed to be expressed by means of the relative stocking (RS) parameter. The growing stock volume retrieval error decrease with increase of relative stocking and stand size. For relative stocking of at least RS=70%, a relative RMSE 17-40% is obtained and a relative RMSE of 16-40% is achieved when the forest stands size is larger than about 40 ha. One should note that forest stands with higher relative stocking represents a more homogeneous and managed type of forest.

Based on the ground-to-volume scattering ratio, the retrieval accuracy of GSV as a function of tree species has been analysed. The retrieval accuracy of GSV for larch tree species is observed to be consistently sensitive to the weather conditions. High accuracy is obtained under unfrozen condition whereas low accuracy for frozen condition.

To conclude, it has been shown that a method based on polarimetric coherence and ratio of ground-to-volume scattering power, can be used for growing stock volume retrieval in Siberian forests at the stand level up to 250 m³/ha. Note that this estimation does not require multi-temporal data as required in POLINSAR and so enables better tracking of temporal changes in growing stock volume. The selection of training stands for measuring the models parameters are the major drawback of these two retrieval methods. The growing stock volume distributions of both training and validation stands should be as similar as possible.

Chapter 6

Conclusions

6.1 Summary of the results

The objective of this work is concerned with the development of new quantitative space-borne SAR remote sensing technique for forestry applications. In particular to assess the potentiality of ALOS PALSAR L-band quadpol radar data for the retrieval of forest growing stock volume. Before estimating the growing stock volume, the potentiality of polarimetric parameters, especially polarimetric signatures, degree of polarisation, polarisation phase difference, polarimetric coherence and polarimetric decomposition powers are investigated to characterise the polarisation response of forest cover at different weather conditions, forest stand structures and tree species. Based on the availability of ground-truth data and SAR data the work is limited to the study of Siberian forest. Fourteen ALOS PALSAR L-band quadpol data over forest areas in Siberia have been considered here for the evaluation.

The shape of the co-polarised signatures provides information on the dominant scattering mechanism. Given a polarimetric signature, the scattering parameters such as type of the polarisation (linear, circular or elliptical) and the orientation angle at which the target is oriented are extracted. From these parameters the scattering behaviour of the forest target is recognised. The polarimetric signatures have been analysed over forest and non-forest areas. The pedestal height associated with co-polarisation signatures discriminate the forest and non-forest. The scattering mechanisms for aspen, birch, larch and pine forest stands are not distinguishable from each other because of the similar distributed scattering behaviour of the target for all the tree species. Therefore, polarimetric signature is not sensitive to the structure of target. Based on the degree of polarisation, a fine distinction could be made among different GSV classes. The degree of polarisation has shown the significant negative correlation (R=-0.80) with growing stock volume.

Polarisation phase difference clearly distinguishes the clear-cut, bogs from the forest areas. The scattering behaviour (volume scattering, surface scattering) is recognised by the polarisation phase difference from forest and non-forest areas. The sensitivity of the polarimetric phase difference for changing environmental conditions is clearly

demonstrated. Comparison of the polarimetric phase differences at different weather conditions, relatively higher contribution of branch scattering at unfrozen condition has been observed than at frozen condition. Larch shows the less variability than other tree species at both, frozen and unfrozen conditions. The clear increase of mean polarisation phase difference accompanied by a slow increase of standard deviation for increasing growing stock volume up to 180 m³/ha has been observed. After that point, polarisation phase difference loses the sensitivity for growing stock volume. This could be due to the negligible ground contribution beyond this point.

The relationship between forest growing stock volume and ALOS PALSAR L-band polarimetric coherence is analysed in Siberian forests. The trend and spread of coherence as a function of growing stock volume is mainly depend on the weather conditions. Independent of weather conditions, a high correlation (R= -0.87) between polarimetric coherence and growing stock volume is achieved. Topography effects such as direction of slopes are not observed. The correlation between HHVV-coherence and GSV does not depend on the size of the stands. No increase or decrease trend is observed as a function of stand size. A slightly higher correlation between coherence and growing stock volume is observed for fully stocked stands.

The coherence in sparse forest is always higher than in dense forest. The coherence level and the dynamic range, i.e. the difference between coherence in sparse and dense forests, strongly depends on the weather conditions, since these affect the dielectric properties of the forest floor and the vegetation. The mean coherence is consistently highest in both sparse and dense forests under frozen conditions and lowest at unfrozen conditions. The coherence for sparse forest differs from one test site to another test site at unfrozen condition whereas coherence for dense forest changes slightly. Soil moisture variations in different test sites and forest understory can affect the coherence in sparse forest.

The four-component decomposition parameters have been applied to the ALOS PALSAR L-band data to compare the decomposition powers to the growing stock volume. The decomposition powers of surface scattering, double-bounce and volume scattering, derived with and without rotation of coherency matrix, are compared with growing stock volume. To compensate for topographic effects an adaptive rotation of the coherency matrix has been accomplished. After the rotation, the correlation between growing stock volume and double-bounce increase significantly. Volume scattering remains the same and surface scattering power slightly decreases. In general, the volume scattering power and double-bounce power increase as the GSV increases, whereas the surface scattering power decreases. The physical explanations for the observed relationships are (i) at low GSV there are many gaps in the canopy which increase the surface scattering, (ii) as the vegetation grows the canopy covers most of the ground which increases the volume scattering and decreases the surface scattering and (iii) the growth of the tree trunk increases the double-bounce scattering power. The significant relationship between the decomposition powers and the growing stock volume can potentially be used to estimate the growing stock volume.

Regarding the other polarimetric parameters, the rotation of the coherency matrix compensated by polarisation orientation angle has almost no impact. This could be due to the fact that at L-band the penetration of the wave through the canopy is not sufficient, showing in noisy polarisation orientation angle in forest areas. Thus, the polarisation orientation angle cannot be estimated accurately in forest areas with varying topography.

The correlation between polarimetric decomposition parameters and growing stock volume is enhanced if the ratio of ground-to-volume scattering, which is the ratio of volume scattering times double-bounce and surface scattering, is used instead of considering polarimetric decomposition powers separately. The idea has been developed quantitatively using the two layer approach of surface and volume scattering in forest. When ground-to-volume scattering ratio is large, the growing stock volume is low due to gaps in the forest and when ground-to-volume scattering ratio is small, growing stock volume is high. The sensitivity of ground-to-volume scattering ratio has been increased significantly for growing stock volume and achieved a relatively high correlation (R^2 values vary between 0.65 and 0.82 for all the test sites). A relatively higher dynamic range is observed for all the test sites.

In sparse forest, at unfrozen conditions the surface scattering is higher than the volume scattering, while volume scattering is dominant in dense forest. The scenario is different at frozen conditions. For dense forest, the surface scattering is higher than volume scattering. Decomposition would suggest that Siberian forest scattering is dominated by surface and volume scattering. The double-bounce scattering mechanism appears to contribute only a small fraction of the overall decomposition power.

The saturation level for growing stock volume increases by using polarimetric decomposition parameters but no improvements have been observed for GSV at Bolshe-NE. In Shestakovsky under unfrozen condition, the saturation level of GSV increases to ~300 m³/ha using polarimetric decomposition power in particular, double-bounce, volume scattering and ground-to-volume scattering power.

The impact of tree species on polarimetric decomposition powers, polarimetric coherence and degree of polarisation have been investigated at three different meteorological conditions: unfrozen (dry and wet), frozen and thawing. The stands with a growing stock volume above 150 m³/ha have been selected. The four tree species aspen, birch, larch and pine are considered in this study. Due to the low amount of samples cedar, fir and spruce are not considered for the investigations. Therefore, all the stands with a minimum areal coverage of 70% of the dominating species are selected. The observed impact of species is, therefore, disturbed by the other tree species growing in the stands. The investigation is carried out for dense forest to reduce the ground contribution of the signal and pronounce the impact of the trees. The mean growing stock volume of selected stands are above or close to the saturation level. Thus, the variations of GSV in dense forest are assumed to have negligible effects on polarimetric parameters. The impact is increased in particular for larch which differs from other tree species by +2 dB surface scattering power at unfrozen conditions. The higher surface scattering power from larch

forest can indicate that the canopies are more transparent to the electromagnetic wave and a large part of the radar backscatter power comes from the ground. Moreover, this could be due to the different canopy structures, different needles arrangement, less dense canopy and fewer understories in forest floor. The impact of tree species on polarimetric decomposition is very low at frozen conditions. Larch is also differed from other tree species by the magnitude of +0.17 polarimetric coherence. Aspen, birch, larch and pine do not affect in a different way by degree of polarisation at any weather conditions.

To give an answer of the first question mentioned in the first chapter (section 1.4), the polarimetric coherence, polarimetric decomposition powers such as double-bounce, surface scattering, volume scattering and also ground-to-volume scattering ratio can contain complementary information for estimating forest growing stock volume and therefore, the use of these parameters can beneficial for the observations of Siberian forests.

Based on the observations of Siberian forests, two empirical models have been developed that describe the ALOS PALSAR L-band polarimetric coherence and ground-to-volume scattering ratio as a function of forest growing stock volume. The model parameters are computed by the regression between polarimetric coherence and forest growing stock volume from a training set. HV-backscatter is also used to measure the model parameter. Almost 16 to 21% of the total forest stands are used as training set. The models have been proved to fit both polarimetric coherence and HV-backscatter data under different weather conditions. Higher dynamic range is observed for coherence at frozen condition than at unfrozen condition whereas vice versa for HV-backscatter coefficients. Higher magnitude of ground scattering component is observed at frozen condition than at unfrozen condition.

To quantify the performance of the growing stock volume retrieval accuracy, the RMSE, relative RMSE, coefficient of determination R^2 and bias are computed. The best RMSE of 38 m^3/ha and R^2=0.73 is obtained based on polarimetric coherence. On the other hand, using the ratio of ground-to-volume scattering the best retrieval accuracy of 44 m^3/ha and R^2=0.62 is achieved. The best retrieval results for both SAR parameters are observed under unfrozen condition at Shestakovsky-N. Though the best RMSE is slightly higher for coherence but it is possible to partially improve the retrieval accuracy for all the test sites using ratio of ground-to-volume scattering. Regardless the weather conditions, best result obtained in Shestakovsky-N. In Shestakovsky-N, at the stand level, growing stock volume up to 250 m^3/ha is possible to estimate with an error of 38 m^3/ha. The retrieval error is strongly site-dependent. Shestakovsky-N shows the best results and Bolshe-NE shows the worst result.

The reason for the large spread and the different behaviours have to be attributed to the different test site properties, as well as to the ground data accuracy. In Siberia, heterogeneity of the dielectric properties, the effect of forest structural features on the relationship between backscatter and GSV and local inaccuracies in the ground data could explain the low retrieval accuracy. The training should encompass the best possible growing stock volume distribution in the area under investigations. Despite the different

levels of growing stock volume accuracy has been achieved in Siberian forests the accuracy can be improved if information about the site conditions in some way could be taken into account.

Coherence is slightly better for the retrieval of GSV at frozen condition whereas the ratio of ground-to-volume scattering is better for unfrozen condition. Since the ALOS PALSAR L-band full polarimetry images are not available for all kinds of weather conditions in each test site, it is difficult to say which weather condition is best suited for the retrieval of growing stock volume.

The estimation of growing stock volume based on the ratio of ground-to-volume scattering has been investigated on the dependency of forest stand structure such as stand size and forest density which in particular is assumed to be expressed by means of the relative stocking (RS) parameter. To take into account of different distribution of forest growing stock volume in each test site, the relative RMSE gives the better idea for the retrieval accuracy. The relative stocking has a positive impact on the estimation of growing stock volume. The forest growing stock volume retrieval error decreases with increasing stand size and relative stocking. The results are consistent for all the test sites except Chunsky-N under different weather conditions. For relative stocking of at least 70%, a relative RMSE 17-40% is considered the effective retrieval error in Siberian forests. Comparatively lower relative RMSE indicates that retrieval performs best at intensively managed forest structure. It has been observed that large stand size is a major factor to obtain accurate retrieval. The results show that relative RMSE of 16-40% is achieved when the forest stands size is larger than about 40 ha. The overall assessment of the model is suggesting that polarimetric data provides more accurate estimation of forest growing stock volume, in particular over well managed forest structure and larger stands.

Based on the ground-to-volume scattering ratio, the RMSE of the retrieval of growing stock volume for aspen, birch, larch and pine forests are investigated. The best RMSE for aspen (12 m^3/ha), birch (30 m^3/ha), larch (17 m^3/ha) and pine (41 m^3/ha) has been reported. In Siberian forests, the retrieval accuracy of GSV for larch tree species has been observed to be consistently sensitive to the weather conditions. High accuracy has been obtained under unfrozen condition whereas low accuracy for frozen condition.

The selection of training stands for measuring the models parameters are the major drawback of these two retrieval methods, in particular for polarimetric coherence. The growing stock volume distributions for both training and validation stands should be as similar as possible. Based on ratio of ground-to-volume scattering the parameter of the model is measured by using regression procedure between HV-backscatter and forest growing stock volume from the training set. This drawback can overcome by means of Cloude-Pottier decomposition (Cloude & Pottier, 1997), entropy, which is the good discriminator between forest and non-forest regions.

Summarising the findings, the results are obtained in this study confirms the hypothesis that ALOS PALSAR L-band quadpol data can be used to quantify the growing stock volume at stand level with a reasonable accuracy in Siberian forests, although the forest

site conditions play a fundamental role for the final accuracy. The growing stock volume estimation based on polarimetric data does not require multi-temporal data, as required for POLINSAR techniques and so enables better tracking of temporal changes in growing stock volume. Furthermore, thanks to PALSAR polarimetric L-band data are already available for many areas on the globe, while suited POLINSAR datasets are still missing.

6.2 Future outlook

In ground-to-volume ration scattering power, the surface response is in fact modified by propagation through the upper medium, the vegetation layer. So, far, such propagation effects are ignored, on the assumption that the volume is random and hence acts as a scalar attenuation of all polarisations equally, which has no effect on the alpha parameters of surface and double-bounce components. A model can be developed which considers the propagation distortions into the medium followed by scattering.

In this study, it has been stated that different test sites have different retrieval accuracy regardless the weather condition. The variations could be different soil moisture effects. This can be the upcoming work how GSV changes in terms of soil moisture.

Another issue that deserves some attention is the effect of seasonality on tree species identification. The tree species have a different backscatter response in different weather conditions and the degree of this change could possibly be exploited to assist with species discrimination techniques. With the launch of ALOS-2 PALSAR L-band data coverage with 14 days revisited time and higher resolution can be suitable for identification of tree species.

The investigations mostly carried out on relatively flat terrain areas. The future study will be to apply these polarimetric parameters to high topographic areas, in particular Thüringer Wald, Germany.

Chapter 7

References

Askne, J., & Smith, G. (1996). Forest InSAR decorrelation and classification properties. *Proceedings of Fringe'96*, Zurich, ESA SP-406, 95-103.

Askne, J., Santoro, M., Smith, G., & Fransson, J.E.S. (2003). Multitemporal repeat-pass SAR interferometry of boreal forests. *IEEE Transactions on Geoscience and Remote Sensing*, 41, 1540-1550.

Askne, J., & Santoro, M. (2005). Multitemporal repeat pass SAR interferometry of boreal forests. *IEEE Transactions on Geoscience and Remote Sensing*, 43, 1219-1228.

Askne, J., & Santoro, M. (2007). Boreal forest stem volume estimation from multitemporal C-band InSAR observations. *ESA Envisat Symposium*, Montreux, Switzerland.

Balzter, H., Baker, J. R., Hallikainen, M., & Tomppo, E. (2002). Retrieval of timber volume and snow water equivalent over a Finnish boreal forest from airborne polarimetric Synthetic Aperture Radar. *International Journal of Remote Sensing,* 23, 3185–3208.

Balzter, H., Skinner, L., Luckman, L., & Brooke, R. (2003). Estimation of tree growth in a conifer plantation over 19 years from multi-satellite L-band SAR. *Remote Sensing of Environment,* 84, 184-191.

Baker, J. R., & Luckman, A. J. (1999). Microwave observations of boreal forests in the NOPEX area of Sweden and a comparison with observations of a temperate plantation in the United Kingdom. *Agricultural and Forest Meteorology,* 98-99, 389-416.

Beer, C., Lucht, W., Schmullius, C., & Shvidenko, A. (2006). Small net carbon dioxideuptake by Russian forests during 1981–1999. *Geophysical Research Letters*, 33, L15403, doi:10.1029/2006 GL026919.

Bickel, S. H., & Bates, R. H. T. (1965). Effects of magneto-ionic propagation on the polarization scattering matrix. *Proceedings IRE,* 53,1089-1091.

Boerner, W. M., & El-Arini, M.B. (1981). Polarization dependence in electromagnetic inverse problem. *IEEE Transactions on Antennas and Propagation*, 29(2), 262–271.

Boerner, W. M., Foo, B. Y., & Eom, H. J. (1987). Interpretation of the polarimetric co-polarization phase term in radar images obtained with the JPL airborne L-band SAR system. *IEEE Transactions on Geoscience and Remote Sensing,* 25, 77-82.

Cameron, W.L., & Leung, L.K. (1990). Feature motivated polarization scattering matrix decomposition. *Proceedings of IEEE International Radar Conference*, Arlington, VA.

Cartus, O. (2010). Large area forest stem volume mapping using synergy of space borne interferometric radar and optical remote sensing: a case study of Northeast China. Ph.D. thesis, Friedrich-Schiller- Universität Jena, Jena, Germany.

Castel, T., Martinez, J. M., Beaudoin, A., Wegmüller, U., & Strozzi, T. (2000). ERS INSAR data for remote sensing hilly forested areas. *Remote Sensing Environment,* 73, 73–86.

Castel, T., Beaudoin, A., Stach, N., Stussi, N., Toan, T. Le., & Durand, P. (2001). Sensitivity of space-borne SAR data to forest parameters over sloping terrain. Theory and experiment. *International Journal of Remote Sensing,* 22, 2351-2376.

Cloude, S. R. (1986). Group theory and polarization algebra, OPTIK, 75(1), 26–36.

Cloude, S. R. (2010). *Polarisation application in remote sensing,* Oxford University Press. ISBN: 978-0-19-956973-1.

Cloude, S. R., & Papathanassiou, K. P. (2003). Three-stage inversion process for polarimetric SAR interferometry.*Proceedings. Institute of Electrical Engineering—Radar, Sonar Navigation,* 150, 125–134.

Cloude, S. R., & Pottier, E. (1996). A review of target decomposition theorems in radar polarimetry. *IEEE Transactions on Geoscience and Remote Sensing,* 34, 498-518.

Cloude, S. R., & Pottier, E. (1997). An entropy based classification scheme for land applications of polarimetric SAR. *IEEE Transactions on Geoscience and Remote Sensing,* 35, 68-78.

Cloude, S. R., Lumsdon, P., Cassells, G. F., Woodhouse, I. H., & Tembo, M. (2009). An assessment of ALOS L-band polarimetry for land-use monitoring in Malawi. *IEEE International Geoscience and Remote Sensing Symposium IGARSS,* 947-950.

Dobson, M. G., McDonald, K., & Ulaby, F.T. (1990). Effects of Temperature on Radar Backscatter from Boreal Forests. *IEEE International Geoscience and Remote Sensing Symposium IGARSS*, Collegepark, Maryland, USA. 2481-2484.

Dobson, M. C., Ulaby, F. T., Le Toan, T., Beaudoin, A., Kasischke, E. S., & Christensen, N. (1992). Dependence of radar backscatter on coniferous forest biomass. *IEEE Transactions on Geoscience and Remote Sensing*, 30, 412-415.

Durden, S. L., Van Zyl, J. J., & Zebker, H. A. (1989). Modelling and observation of the radar polarization signature of forested areas. *IEEE Transactions on Geoscience and Remote Sensing,* 27 (3), 290-301.

Eriksson, L. E. B., Santoro, M., Wiesmann, A., & Schmullius, C. (2003). Multitemporal JERS repeat-pass coherence for growing-stock volume estimation of Siberian forest. *IEEE Transactions on Geoscience and Remote Sensing*, 41, 1561-1570.

Eriksson, L. E. B. (2004). Satellite-borne L-band interferometric coherence for forestry applications in the boreal zone. Ph.D. thesis, Friedrich-Schiller- Universität Jena, Jena, Germany.

Fransson, J. E. S., & Israelsson, H. (1999). Estimation of stem volume in boreal forests using ERS-1 C- and JERS-1 L-band SAR data. *International Journal of Remote Sensing.* 20, 123–137.

Fransson, J. E. S., Walter, F., & Ulander, L. H. M. (2000). Estimation of forest parameters using CARABAS-II VHF SAR Data. *IEEE Transactions on Geoscience and Remote Sensing,* 38 (2), 720-727.

Fransson, J. E. S., Smith, G., Askne, J., & Olsson, H. (2001). Stem volume estimation in boreal forest using ERS-1/2 coherence and SPOT XS optical data. *International Journal of Remote Sensing,* 22, 14, 2777-2791.

Fraser, R. H., & Li, Z. (2002). Estimating fire-related parameters in boreal forest using SPOT VEGETATION. *Remote Sensing Environment,*82, 95–110.

Freeman, A., & Durden, S. L. (1998). A three-component scattering model for polarimetric SAR data. *IEEE Transactions on Geoscience and Remote Sensing,* 36, 963-973.

Freeman, A. (2004). Calibration of linearly polarized polarimetric SAR data subject to Faraday rotation. *IEEE Transactions on Geoscience and Remote Sensing,* 42(8), 1617–1624.

Freeman, A., & Saatchi, S. S. (2004). On the detection of Faraday rotation in linearly polarized L-band SAR backscattering signatures. *IEEE Transactions on Geoscience and Remote Sensing,* 42(8), 1607-1616.

Freeman, A. (2007). Fitting a two-component scattering model to polarimetric SAR data from forests. *IEEE Transactions on Geoscience and Remote Sensing,* 45(8), 2583–2592.

Garestier, F., Dubois-Fernandez, P. C., Guyon, D., & Le Toan, T. (2009). Forest biophysical parameter estimating using L-band and P-band polarimetric SAR data. *IEEE Transactions on Geoscience and Remote Sensing,* 47, 3379-3388.

Gaveau, D. L .A. (2002). Modelling the dynamics of ERS-1/2 coherence with increasing woody biomass over boreal forests. *International Journal of Remote Sensing*, 23 (18), 3879–3885.

Goncalves, F., Santos, J, & Treuhaft, R. (2011). Stem volume of tropical forests from polarimetric radar. *International Journal of Remote Sensing,* 32, 503-522.

Hajnsek, I., Pottier, E., & Cloude, S. R. (2003). Inversion of surface parameters from polarimetric SAR. *IEEE Transactions on Geoscience and Remote Sensing.*41, 727-744.

Häme, T., Salli, A., & Lahti, K. (1992). Estimation of carbon storage in boreal forests usingremote sensing data. In M. Kanninen, & P. Anttila (Eds.), *Pilot study.The Finnish research program on climate change, progress report.*250−255, Helsinki, Finland: Academy of Finland.

Harrell, P. A., Bourgeau-Chavez, L. L., Kasischke, E. S., French, N. H. F., & Christensen, N. L. (1995). Sensitivity of ERS-1 and JERS-1 radar data to biomass and stand structure in Alaskan boreal forest. *Remote Sensing of Environment,* 54, 247-260.

Harrell, P. A., Kasischke, E. S., Bourgeau-Chavez, L. L., Haney, E. M., & Christensen, N. L. (1997). Evaluation of approaches to estimating aboveground biomass in southern pine forests using SIR-C data. *Remote Sensing of Environment,* 59, 223-233.

Healy, S. P., Cohen, W. B., Zhiqian, Y., & Krankina, O. (2005). Comparison of Tasseled Cap-based Landsat data structures for use in forest disturbance detection. *Remote Sensing of Environment,* 97, 301-310.

Hellmann, M. (2000). Classification of fully polarimetric SAR-data for cartographic applications. Ph.D. thesis, TU Dresden, Germany.

Henderson, F. M., & Lewis, A. J. (1998), *Principles and Applications of Imaging Radar*, Vol. 2 of Manual of Remote Sensing, (R.A. Reyerson, Ed.), 3rd ed., John Wiley & Sons, New York.

Hoekman, D. H., & Quiñones, M. J. (2000). Land cover type and biomass classification using AIRSAR data for evaluation of monitoring scenarios in the Colombian Amazon. *IEEE Transactions on Geoscience and Remote Sensing*. 38 (2), 685-696.

Hoekman, D. H., & Quiñones, M. J. (2002). Biophysical forest type characterization in the Colombian Amazon by airborne polarimetric SAR. *IEEE Transactions on Geoscience and Remote Sensing,* 40, 1288-1300.

Huynen, J. R. (1970). Phenomenological theory of radar targets. Ph.D. thesis, University of Technology, Delft, The Netherlands.

Huynen, J. R. (1990). The Stokes parameters and their interpretation in terms of physical target properties, *Proceedings of the International Workshop on Radar Polarimetry*, JIPR-90, Nantes, France.

Hyyppa, J., & Hallikainen, M. (1996). Applicability of airborne profiling radar to forest inventory. *Remote Sensing of Environment*, 57, 39-57.

Imhoff, M. L., Johnson, P., Holford, W., Hyer, J., May, L., Lawrence, W., & Harcombe, P. (2000). BioSAR™: An inexpensive airborne VHF multiband SAR system for vegetation biomass measurement. *IEEE Transactions on Geoscience and Remote Sensing,* 38 (3), 1458-1462.

Israelsson, H., Askne, J., & Sylvander, R. (1994). Potential of SAR for forest bole volume estimation. *International Journal of Remote Sensing*, 15, 2809-2826.

Israelsson, H., Askne, J., Fransson, J., & Sylvander, R. (1995). JERS-1 SAR analysis of boreal forest biomass.Volume II, Ministry of International Trade and Industry, National Space Development Agency of Japan, Tokyo.

Israelsson, H., Ulander, L. H. M., Askne, J. L. H., Fransson, J. E. S., Frölind, P. O., Gustavsson, A., & Hellsten, H. (1997). Retrieval of forest stem volume using VHF SAR. *IEEE Transactions on Geoscience and Remote Sensing*, 35, no. 1, 36–40.

Ito, Y., & Omatu, S. (1998). Polarimetric SAR data classification using competitive neural networks. *International Journal of Remote Sensing,* 19, 2665-2684.

Karam, M. A., Amar, F., Fung, A. K., Mougin, E., Lopes, A., Levine, D. M., & Beaudoin, A. (1995). A microwave polarimetric scattering model for forest canopies based on vector radiative-transfer theory. *Remote Sensing of Environment,* 53, 16-30.

Kellndorfer, J. M., Dobson, M. C., Vona, J. D., & Clutter, M. (2003). Toward precision forestry: plot-level parameter retrieval for slash pine plantations with JPL AIRSAR. *IEEE Transactions on Geoscience and Remote Sensing*, 41(7), 1571-1582.

Kononov, A. A., & Ka, M. H. (2008). Model-associated forest parameter retrieval using VHF SAR data at the individual tree level. *IEEE Transactions on Geoscience and Remote Sensing*. 46. 69-84.

Koskinen, J. (2001). Snow monitoring using microwave radars. Ph.D. thesis, Laboratory of Space Technology, Helsinki University of Technology, Espoo, Finland.

Koskinen, J. T., Pulliainen, J. T., Hyyppä, J. M., Engdahl, M. E., & Hallikainen, M. T. (2001). The seasonal behaviour of interferometric coherence in boreal forest. *IEEE Transactions on Geoscience and Remote Sensing,* 39(4), 820-829.

Kostinski, A. B., & Boerner, W. M. (1986). On foundations of radar polarimetry, *IEEE Transactions on Antennas and Propagation*, 34, 1395–1404.

Krogager, E. (1990). New decomposition of the radar target scattering matrix. *Electronics Letters,* 26, 1525-1527.

Krogager, E., & Madsen, S. N. (1996). Comparison of various decompositions for analysis, interpretation and classification of polarimetric SAR images. *European Conference on Synthetic Aperture Radar, EUSAR '96*, 105-108, Königswinter, Germany.

Kuplich, Salvatori, V., & Curran, P. J. (2000). JERS-1/SAR backscatter and its relationship with biomass of regenerating forests. *International Journal of Remote Sensing,* 21, 2513-2518.

Kwok, R., Rignot, E. J. M., Way, J., Freeman, A., & Holt, J. (1994). Polarization signatures of frozen and thawed forests of varying environmental state. *IEEE Transactions on Geoscience and Remote Sensing*, 32, 371-381.

Kobayashi, S., Omura, Y., Sanga-Ngoie, K., Widyorini R., Kawai, S., Supriadi, B., & Yamaguchi, Y. (2012). Characteristics of decomposition powers of L-band multi-polarimetric SAR in assessing tree growth of industrial plantation forests in the tropics. *Remote Sensing,* 4(10), 3058-3077.

Krogager, E. (1990). A new decomposition of the radar target scattering matrix, *Electronics Letter*, 26(18), 1525–1526, 1990.

Kurvonen, L., Pulliainen, J., & Hallikainen, M. (1999). Retrieval of biomass in boreal forests from multitempotalERS-1 and JERS-1 SAR images. *IEEE Transactions on Geoscience and Remote Sensing,* 37(1), 198-205.

Lebedev, A. (2005). Siberian and Russian far east timber for China legal and illegal pathways, players and trends. Bureau for Regional Outreach Campaigns, Forest Trends, CIFOR, DFID.

Lee, J. S., Grunes, M. R., & Grandi, G. De. (1999). Polarimetric SAR speckle filtering and its implication for classification. *IEEE Transactions on Geoscience and Remote Sensing*, 37(5), 2363-2373.

Lee, J. S., Schuler, D. L., & Ainsworth, T. L. (2000). Polarimetric SAR data compensation for terrain azimuth slope variation. *IEEE Transactions on Geoscience and Remote Sensing*, 38, 2153-2163.

Lee, J. S., Grunes, M. R., Pottier, E., & Ferro-Famil, L. (2001). Segmentation of polarimetric SAR images. *IEEE International Geoscience and Remote Sensing Symposium IGARSS*, Sydney, Australia.

Lee, J. S., Schuler, D. L., Ainsworth, T. L., Krogager, E., Kasilingam, D., & Boerner, W.M. (2002). On the estimation of radar polarization orientation shifts induced by terrain slopes. *IEEE Transactions on Geoscience and Remote Sensing*, 40, 30-41.

Lee, J. S., & Pottier, E. (2006). *Polarimetric radar imaging: from basics to applications*. CRC Press. ISBN: 13: 978-1-4200-5497-2.

Lee, J. S., & Ainsworth, T. L. (2011). The effect of orientation angle compensation on coherency matrix and polarimetric target decomposition. *IEEE Transactions on Geoscience and Remote Sensing,* 49(1-1), 53-64.

Lee, S. K., Kugler, F., Hajnsek, I., & Papathanassiou, K. (2009). The impact of temporal decorrelation over forest terrain in polarimetric SAR interferometry. *POLINSAR, Frascati, Italy.*

Lee, S. K., Kugler, F., Hajnsek, I., & Papathanassiou, K. (2010). Multi-baseline PolInSAR forest height estimation in the presence of temporal decorrelation. *EUSAR, Aachen,*829-832.

Lindgren, O. (1984). A study on circular plot sampling of Swedish forest compartments. Department of Biometry and Forest Management, Swedish University of Agricultural Sciences, Umeå, Sweden, Report 11.

Lozano, F. J., Suarez-Seoane, S., Kelly, M., & Luis, E. (2008). A multi-scale approach for modelling fire occurrence probability using satellite data and classification trees: A case study in a mountainous Mediterranean region. *Remote Sensing Environment,* 112,708-719.

Lucas, R. M., Moghaddam, M., & Cronin, N. (2004). Microwave scattering from mixed-species forests, Queensland, Australia. *IEEE Transactions on Geoscience and Remote Sensing,* 42 (10), 2142-2159.

Lucas, R. M., Cronin, N., Lee, A., Moghaddam, M., Witte, C., & Tickle, P. (2006). Empirical relationships between AIRSAR backscatter and LIDAR-derived forest biomass, Queensland, Australia. *Remote Sensing Environment,*100, 407 – 425.

Luckman, A., Baker, J., Kuplich, T. M., Yanasse, C. D. C. F., & Frery, A.C. (1997). A study of the relationship between radar backscatter and regenerating tropical forest biomass for spaceborne SAR instruments. *Remote Sensing Environment,* 60, 1-13.

Lüneburg, E. (1995). Principles of radar polarimetry, *Proceedings of the IEICE Transactions on the Electronic Theory*, E78-C, 10, 1339–1345.

Lüneburg, E. (1996). *Radar polarimetry: A revision of basic concepts, in Direct and Inverse Electromagnetic Scattering*, Serbest, H., & Cloude, S. R. (Eds.), Pittman Research Notes in Mathematics Series 361, Addison Wesley Longman, Harlow, United Kingdom.

Manninen, A. T., & Ulander, L. H. M. (2001). Forestry parameter retrieval from texture in CARABAS VHF-band SAR images. *IEEE Transactions on Geoscience and Remote Sensing,* 39 (12), 2622-2633.

Massonnet, D., Rossi, M., Carmona, C., Adragna, F., Peltzer, G., Feigl, K., & Ragaute, T. (1993). The displace field of Landers earthquake mapped by radar interferometry. *Nature,* 364, 138-142

McNeill, S., & Pairman, D. (2005). Stand age retrieval in production forest stands in New Zealand using C-band and L-Band polarimetric radar. *IEEE Transactions on Geoscience and Remote Sensing,* 43, 2503-2515.

Melon, P., Martinez, J. M., Toan, T. L., Ulander, L. M. H., & Beaudoin, A. (2001). On the retrieving of forest stem volume from VHF SAR data: observation and modelling. *IEEE Transactions on Geoscience and Remote Sensing,* 39 (11), 2364-2372

Mette, T., Papathanassiou, K., Hajnsek, I., Pretzsch, H., & Biber, M. (2004). Applying a common allometric equation to convert forest height from Pol-InSAR data to forest biomass. *IEEE International Geoscience and Remote Sensing Symposium IGARSS'04*, Anchorage, Alaska, USA**,** 270-272.

Mougin, E., Proisy, C., Marty, G., Fromard, F., Puig, H., Betoulle, J. L., & Rudant, J. P. (1999). Multifrequency and multipolarization radar backscattering from mangrove forests. *IEEE Transactions on Geoscience and Remote Sensing,* 37, 94-102.

Nilsson, S., Shivdenko, A., Stolbovoi, V., Gluck, M., Jonas, M., & Obersteiner, M. (2000). Full carbon account for Russia.International Institute for Applied System Analysis (IIASA), Vienna, Austria.

Neumann, M., Saatchi, S. S., Ulander, L. M. H., & Fransson, J. E. S. (2012). Assessing performance of L- and P-band polarimetric interferometric SAR data in estimating boreal forest above-ground biomass. *IEEE Transactions on Geoscience and Remote Sensing,* 50, 714-726.

Papathanassiou, K. P., Marotti, L., Schneider, R. Z., & Hajnsek, I. (2007). Pol-InSAR results from ALOS-PALSAR. *IEEE Geoscience and Remote Sensing Symposium*, Barcelona, Spain.

Praks, J., Kugler, F., Papathanassiou, K. P., Hajnsek, I., & Hallikainen, M. (2007). Height estimation of boreal forest: interferometric model-based inversion at L- and X-band versus HUTSCAT profiling scatterometer. *IEEE Geoscience and Remote Sensing Letters*, 4, no. 3, 466–470.

Pretzsch, H. (2002). *Grundlagen der Waldwachstumsforschung*. PareyVerlag, Berlin, Germany.

Proisy, C., Mougin, E., Lopes, A., Sarti, F., Dufrêne, E., & Ledantec, V. (1999). Temporal variations of interferometric coherence over a deciduous forest in Harris, R.A., and

Ouwehand, L. (Eds.).*SAR Workshop: CEOS Committee on Earth Observation Satellites.* Paris: European Space Agency, Toulouse, France.

Pulliainen, J. T., Kurvonen, L., & Hallikainen, M. T. (1999). Multitemporalbehavior of L-band and C-band SAR observations of boreal forests. *IEEE Transactions on Geoscience and Remote Sensing*, 37, 927-937.

Quiñones, M. J., & Hoekman, D. H. (2004). Exploration of factors limiting biomass estimation by polarimetric radar in tropical forests. *IEEE Transactions on Geoscience and Remote Sensing,* 42, 86-104.

Ranson, K. J., & Sun, G. (1994). Mapping biomass of a northern forest using multifrequency SAR data. *IEEE Transactions on Geoscience and Remote Sensing,* 32, 388-396.

Ranson, K. J., & Sun, G. (1997). An evaluation of AIRSAR and SIR-C/X-SAR images for mapping northern forest attributes in Maine, USA. *Remote Sensing of Environment,* 59, 203-222.

Rauste, Y., Häme, T., Pulliainen, J., Heiska, K., & Hallikainen, M. (1994). Radar-based forest biomass estimation. *International Journal of Remote Sensing*, 15, 2797–2808.

Rauste, Y. (2005). Multi-temporal JERS SAR data in boreal forest biomass mapping. *Remote Sensing Environment*, 97, 263 – 275.

Rignot, E., Salas, W. A., & Skole, D. L. (1997). Mapping deforestation and secondary growth in Rondonia, Brazil, using imaging radar and thematic mapper data. *Remote Sensing Environment*, 59.167-179.

Rignot, E. (2000). Effect of Faraday rotation on L-band interferometric and polarimetric synthetic aperture radar data. *IEEE Transactions on Geoscience and Remote Sensing,* 38, 383-390.

Saatchi, S. S., & McDonald, K. C. (1997). Coherent effects in microwave backscattering models for forest canopies. *IEEE Transactions on Geoscience and Remote Sensing,* 35, 1032-1044.

Saatchi, S. S., & Moghaddam, M. (2000). Estimation of crown and stem water content and biomass of boreal forest using polarimetric SAR imagery. *IEEE Transactions on Geoscience and Remote Sensing,* 38, 697-709.

Saksa, T. Uuttera, J., Kolström, T., Lehikoinen, M., Pekkarinen, A., & Sarvi, V. (2003). Clear-cut detection in boreal forest aided by remote sensing. *Scandinavian Journal of Forest Research,* 18(6), 537-546.

Santoro, M., Askne, J., Smith, G., & Fransson, J. (2002). Stem volume retrieval in boreal forests from ERS-1/2 interferometry. *Remote Sensing of Environment*, 81, 19-35.

Santoro, M., Eriksson, L., Askne, J., & Schmullius, C. (2006). Assessment of stand-wise stem volume retrieval in boreal forest from JERS-1 L-band SAR backscatter. *International Journal of Remote Sensing*, 27, 3425–3454.

Santoro, M., & Cartus, O. (2010). *STSE BIOMASAR: Validating a novel biomass retrieval algorithm based on hyper-temporal Wide-Swath and Global Monitoring ENVISAT ASAR datasets.* Final Report, ESA ESRIN contract No. 21892/08/I-EC.

Santoro, M., Shvidenko, A., McCallum, I., Askne, J., & Schmullius, C. (2007a). Properties of ERS-1/2 coherence in the Siberian boreal forest and implications for stem volume retrieval. *Remote Sensing Environment*, 106, 154–172.

Santoro, M., Werner, C., Wegmüller, U., & Cartus, O. (2007b). Improvement of interferometric SAR coherence estimates by slope-adaptive range common band filtering, *IEEE International Geoscience and Remote Sensing Symposium IGARSS*, Barcelona, Spain.

Santoro, M., Fransson, J. E. S., Eriksson, L. E. B., Magunsson, L., Ulander, L. H. M., & Olsson, H. (2009). Signatures of ALOS PALSAR L-band backscatter in Swedish forest. *IEEE Transactions on Geoscience and Remote Sensing,* 47, 4001-4019.

Santos, J. R., Lacruz, M. S. P., Araujo, L. S., & Keil, M. (2002). Savanna and tropical rainforest biomass estimation and spatialization using JERS-1 data. *International Journal of Remote Sensing,* 23, 1217–1229, 2002.

Santos, J. R., Freitas, C. C., Araujo, L. S., Dutra, L. V., Mura, J. C., Gama, F. F., Soler, L. S., & Sant'Anna, S. J. S. (2003). Airborne P-band SAR applied to the aboveground biomass studies in the Brazilian tropical rainforest. *Remote Sensing of Environment,* 87, 482–493, 2003.

Schmullius, C., & Rosenquist, A. (1997). Closing the gap - A Siberian boreal forest map with ERS-1/2 and JERS-1. *Proceedings of third ERS symposium on space at the service of our environment*, Florence, 14–21 March. ESA SP-414 (1885–1890). Noordwijk, The Netherlands: ESA Publications Division, ESTEC.

Schmullius, C., Baker, J., Balzter, H., Davidson, M., Eriksson, L., Gaveau, D., Gluck, M., Holz, A., Letoan, T., Luckman, A., Marschalk, U., McCallum, I., Nilsson, S., Orrmalm, S., Quegan, S., Rauste, Y., Roth, A., Rozhkov, V., Sokolov, V., Shvidenko, A., Sirro, L., Skuding, V., Strozzi, T., Tansey, K., Utsi, R., Vietmeier, J., Voloshuk, L., Wagner, W., Wegmüller, U., Westin, T., Wiesmann, A., & Yu, J. J. (2001). *SIBERIA - SAR Imaging for Boreal Ecology and Radar Interferometry Applications*. Final report, EC-Center for Earth Observation, project reports, contract no. ENV4-CT97-0743-SIBERIA.

Schuler, D. L., Lee, J. S., Kasilingam, D., & Nesti, G. (2002). Surface roughness and slope measurements using polarimetric SAR data. *IEEE Transactions on Geoscience and Remote Sensing,* 40, 687-698.

Shi, J., & Dozier, J. (2000). Estimation of snow water equivalence using SIR-C/X-SAR – Part I: inferring dry snow density and subsurface properties. *IEEE Transactions on Geoscience and Remote Sensing*, 8, 6, 2465-2474.

Shimada, M., Isoguchi, O., Tadono, T., & Isono, K. (2009). PALSAR radiometric and geometric Calibration. *IEEE Transactions on Geoscience and Remote Sensing*, 47, 3915-3932.

Shvidenko, A., Shepashenko, D., Nilsson, M., & Bouloui, Y. (2007). Semi-empiricalmodels for assessing biological productivity of Northern Eurasian forests. *Ecological Modelling*, 204, 163−179.

Smith, G., & Ulander, L. H. M. (2000). A model relating VHF-Band backscatter to stem volume of coniferous boreal forest. *IEEE Transactions on Geoscience and Remote Sensing,* 38 (2), 728-740.

Stokes, G. G. (1852). On the composition and resolution of streams of polarized light from different sources. *Transactions of the Cambridge Philosophical Society*, 9, 399–416.

Stolbovoi, V., & Mccallum, I. (2002). Land Resources of Russia. International Institute for Applied Systems Analysis and the Russian Academy of Science, Laxenburg, Austria, CD-ROM.

Stratton, J. A. (1941). *Electromagnetic Theory*, McGraw-Hill, New York, USA.

Sun, J. G., Simonett, D. S., & Strahler, A. H. (1991). A radar backscatter model for discontinuous coniferous forests. *IEEE Transactions on Geoscience and Remote Sensing*, 29, 639-650.

Tansey K. J., Luckman, A. J., Skinner, L., Balzter, H., Strozzi, T., & Wagner, W. (2004). Classification of forest volume resources using ERS tandem coherence and JERS backscatter data. *International Journal of Remote Sensing,* 25, 751–768.

Thiel, C. J. (2004). Extrahierung hydrologisch relevanter parameter aus hochaufgelösten polarimetrischen L-Band sowie interferometrischen X-Band SAR-daten. Ph.D. thesis, Lehrstuhl für Fernerkundung, Friedrich-Schiller-Universität Jena, Jena, Germany.

Thiel, C. J., Drezet, P., Weise, C., Quegan, S., & SchmulliuS, C. (2006). Radar remote sensing for the delineation of forest cover maps and the detection of deforestation. *Forestry - International Journal Forest Research,*79(5), 590-597.

Thiel, C. J, Thiel C., Reiche, J., Leiterer, R., Santoro, M., & Schmullius, C. (2007). Polarimetric PALSAR SAR data for forest cover mapping in Siberia. First Joint PI Symposium of ALOS Data Nodes for ALOS Science Program, Kyoto, Japan.

Thiel, C. J., Thiel, C., & Schmullius, C. (2009). Operational large-area forest monitoring in Siberia using ALOS PALSAR summer intensities and winter coherence. *IEEE Transactions on Geoscience and Remote Sensing*, 47, 3993-4000.

Thiel, C. J., Hüttich, C., & Schmullius, C. (2012). Impact of freezing on ALOS PALSAR coherence properties in central Siberia and its implication to forest growing stock volume assessment. *ForestSAT 2012***,** Corvallis, Oregon, USA.

Thornton, J., & Ziegler, C. (2002). The Russian far east in perspective. University of Washington Press, 165-192.

Titheridge, J. E. (1972). Determination of ionospheric electron content from the Faraday rotation of geostationary satellite signals. *Planetary and Space Science,* 20, 353-369.

Toan, T. Le., Beaudoin, A., Riom, J., & Guyon, D. (1992). Relating forest biomass to SAR data. *IEEE Transactions on Geoscience and Remote Sensing,* 30, 403-411.

Touzi, R., & Charbonneau, F. (2002). Characterization of symmetric scattering using polarimetric SARs. *Proceedings IGARSS*, 1, 414–416

Townsend, P. A. (2002). Estimating forest structure in wetlands using multitemporal SAR. *Remote Sensing Environment* 79, 288– 304.

Treter, U. (1993). *Die Borealen Waldländer*. Westermann, Braunschweig, Germany.

Trexler, M. C. (1991). *Minding the World's Carbon Store,* World Resources Institute. ISBN/EAN: 978-0-915825-48-6.

Tsolmon, R., Tateishi, R., & Tetuko, J. S. S. (2002). A method to estimate forest biomass and its application to monitor Mongolian Taiga using JERS-1 SAR data. *International Journal of Remote Sensing,* 23, 4971–4978.

Ulaby, F. T., & Stiles, W. (1981). Microwave response of snow, *Advance in Space Research,* 1, 10, 131-149.

Ulaby, F. T., Moore, R. K., & Fung, A. K. (1986). Microwave remote sensing, active and passive, volume III, Artech House, Dedham, MA.

Ulaby, F. T., Held, D., Dobson, M. C, McDonald, K. C., & Senior, T. B. A. (1987). Relating polarization phase difference of SAR signals to scene properties. *IEEE Transactions on Geoscience and Remote Sensing,* 25, 83-92.

Ulander, L. H. M. (1996). Radiometric slope correction of synthetic-aperture radar images. *IEEE Transactions on Geoscience and Remote Sensing,* 34, 1115-1122.

Ulander, L. H. M., Fransson, J. E. S., Gustavsson, A., Smith, G., & Walter, F. (2002). VHF-Band for Forest Stem Volume Applications. National Radio Science Meeting, Boulder, Colorado.

Van Zyl, J. J., Zebker, H. A., & Elachi, C. (1987). Imaging radar polarization signatures: Theory and observation. *Radio Science,* 22(4):529—543.

Van Zyl J. J. (1989). Unsupervised classification of scattering behavior using radar polarimetry data. *IEEE Transactions on Geoscience and Remote Sensing,* 27(1), 36–45.

Wagner, W., Luckman, A., Vietmeier, J., Tansey, K., Balzter, H., Schmullius, C., Davidson, M., Gaveau, D., Gluck, M., Toan, T. L., Quegan, S., Shvidenko, A., Wiesmann, A., & Yu, J. J. (2003). Large-scale mapping of boreal forest in SIBERIA using ERS tandem coherence and JERS backscatter data. *Remote Sensing Environment*, 85, 125–144.

Wang, J. R., & Mo, T. (1990). The polarization phase differences in orchard trees. *International Journal of Remote Sensing*, 11:7, 1255-1265.

Wang, Y., Day, J. L., & Davis, F. W. (1998). Sensitivity of modelled C- and L-Band radar backscatter to ground surface parameters in Loblolly pine forest. *Remote Sensing Environment*. 66, 331–342.

Watanabe, M., Shimada, M., Rosenqvist, A., Tadono, T., Matsuoka, M., Romshoo, S. A., Furuta, R., Nakamura, K., & Moriyama, T. (2006). Forest structure dependency of the relation between L-band σ^0 and biophysical parameters. *IEEE Transactions on Geoscience and Remote Sensing,* 44, 3154–3165.

Way, J., Rignot, E. J. M., Mcdonald, K. C., Oren, R., Kwok, R., Bonan, G., Dobson, M. C., Viereck, L. A., & Roth, J. E. (1994). Evaluating the type and state of Alaska taiga forests with imaging radar for use in ecosystem models. *IEEE Transactions on Geoscience and Remote Sensing*, 32, 353-370.

Wegmüller, U. (1999). Automated terrain corrected SAR geocoding. *Proceedings IEEE International Geoscience and Remote Sensing Symposium IGARSS,* Hamburg, Germany, 1712-1714.

Wegmüller, U., Werner, C., Strozzi, T., & Wiesmann, A. (2002). Automated and precise image registration procedure. *Analysis of Multi-Temporal Remote Sensing Images,* L. Bruzzone and P. Smits, Eds. Singapore: World Scientific, 2, 37-39.

White, J. C., Wulder, M. A., & Brooks, D. (2005). Detection of red attack stage mountain pine beetle infestation with high spatial resolution satellite imagery. *Remote Sensing Environment,* 96, 340-351.

Wright, P., Quegan, S., Wheadon, N., & Hall, D. (2003). Faraday rotation effects on L-band space-borne SAR data. *IEEE Transactions on Geoscience and Remote Sensing,* 41, 2735–2744.

Yamaguchi, Y., Moriyama, T., Ishido, M., & Yamada, H. (2005). Four-component scattering model for polarimetric SAR image decomposition. *IEEE Transactions on Geoscience and Remote Sensing,* 43, 1699-1706.

Yamaguchi, Y., Sato, A., Boerner, W. M., & Yamada, H. (2011). Four-component scattering power decomposition with rotation of coherency matrix. *IEEE Transactions on Geoscience and Remote Sensing,* 49, 2251-2258.

Yanasse, C. D. C. F., Sant'anna, S. J. S., Frery, A. C., Rennó, C. D., Soares, J. V., & Luckman, A. J. (1997). Exploratory study of the relationship between tropical forest regeneration stages and SIR-C L and C band data, *Remote Sensing Environment,*59, 180-190.

Yatabe, S. M., & Leckie, D. G. (1995). Clearcut and forest-type discrimination in satellite SAR imagery. *Canadian Journal of Remote Sensing*, 21, 456-467.

Zebker, H. A., & Goldstein, R. M. (1986). Topographic mapping from interferometric synthetic aperture radar observations. *Journal of Geophysical Research*, 91, 4993-4999.

Zebker, H. A., Madsen, S. N., Martin, J., Wheeler, K. B., Miller, T., Lou, Y., Alberti, G., Vetrella, S., & Cucci, A. (1992). The TOPSAR interferometric radar topographic mapping instrument. *IEEE Transactions on Geoscience and Remote Sensing,* 30, 933-940.

Zebker, H. A., Rosen, P. A., Goldstein, R. M., & Gabriel, A. (1994). On the derivation of coseismic displacement field using differential radar interferometry: the Lander earthquake. *Journal of Geophysical Research*, 99, 19617-19634.

Ziegler, V., Lüneburg, E., & Schroth, A. (1992). Mean back-scattering properties of random radar targets: A polarimetric covariance matrix concept. *IEEE International Geoscience and Remote Sensing Symposium IGARSS'92*, May 26–29, Houston Texas, 1992, 266–268.

Appendix A

Overview of KOMPSAT-2 and the results of polarisation orientation angle (POA) compensation for off diagonal elements of coherency matrix

A.1 KOMPSAT-2 mission and overview

The Second Korea Multi-Purpose Satellite (KOMPSAT-2) system consists of space segment and ground segment. The KOMPSAT-2 space segment consists of a single KOMPSAT-2 satellite flying on a sun-synchronous low earth orbit and the (Multi-Spectral Camera) MSC as a primary payload. The KGS consists of the (Korea Aerospace Research Institute) KARI site which is located in Daejeon. The KARI site is comprised of the primary mission and control element and the image data reception and processing element. In order to satisfy the overall missions of the KOMPSAT-2 system the KARI site provides the capability to monitor and control the KOMPSAT-2 satellite, to conduct KOMPSAT-2 mission planning, and to receive, process, and distribute image data.

The Mission orbit of the KOMPSAT-2 is a sun-synchronous circular orbit with an altitude of 685.13 km. The Orbit inclination is 98.127° and the eccentricity from 0°. The satellite operates with a nominal local time of ascending nodes of 10:50 AM +10/-15 min. The satellite passes Korean region during the day along ascending orbits and during the night along descending orbits. The KOMPSAT-2 satellite is designed for an operational service life of 3 years on the mission orbit.

KOMPSAT-2's instruments are designed to acquire high and very-high-resolution imagery with a footprint of 15 km. The satellite has the capacity to acquire 20 minutes of imagery on each orbit and it can steer its sensors both ways out to 30° off track. Panchromatic and multispectral images can be acquired at the same time. KOMPSAT-2 radiometer features:

mode	Channel	Spectral band	Spatial resolution	Footprint
Multispectral (MSC)	1	0,45 - 0,52 mm (blue)	4 m	15 km
	2	0,52 - 0,60 mm (green)	4 m	15 km
	3	0,63 - 0,69 mm (rouge)	4 m	15 km
	4	0,76 - 0,90 mm (near-infrared)	4 m	15 km
panchromatic (PAN)	P	0,50 - 0,90 mm (black and white)	1 m	15 km

Table A.1.1 KOMPSAT-2 radiometric parameters.

The KOMPSAT-2 will allow the generation of high resolution images better than 1 m for PAN data and 4 m for MS data with nadir viewing condition at the nominal altitude of 685 km. PAN imaging and MS imaging can be operated simultaneously during mission operations. The swath width is greater than or equal to 15 km at the mission altitude for PAN data and MS data.

A.2 Polarisation orientation angle (POA) compensation for off diagonal elements of 3 × 3 coherency matrix [*T*]

$$[T] = \begin{bmatrix} \langle |S_{HH} + S_{VV}|^2 \rangle & \langle (S_{HH} + S_{VV})(S_{HH} - S_{VV})^* \rangle & 2\langle (S_{HH} + S_{VV}){S_{HV}}^* \rangle \\ \langle (S_{HH} - S_{VV})(S_{HH} + S_{VV})^* \rangle & \langle |S_{HH} - S_{VV}|^2 \rangle & \sqrt{2}\langle S_{HV} S_{VV}^* \rangle \\ 2\langle S_{HV}(S_{HH} + S_{VV})^* \rangle & 2\langle S_{HV}(S_{HH} - S_{VV})^* \rangle & 4\langle |S_{HV}|^2 \rangle \end{bmatrix}$$

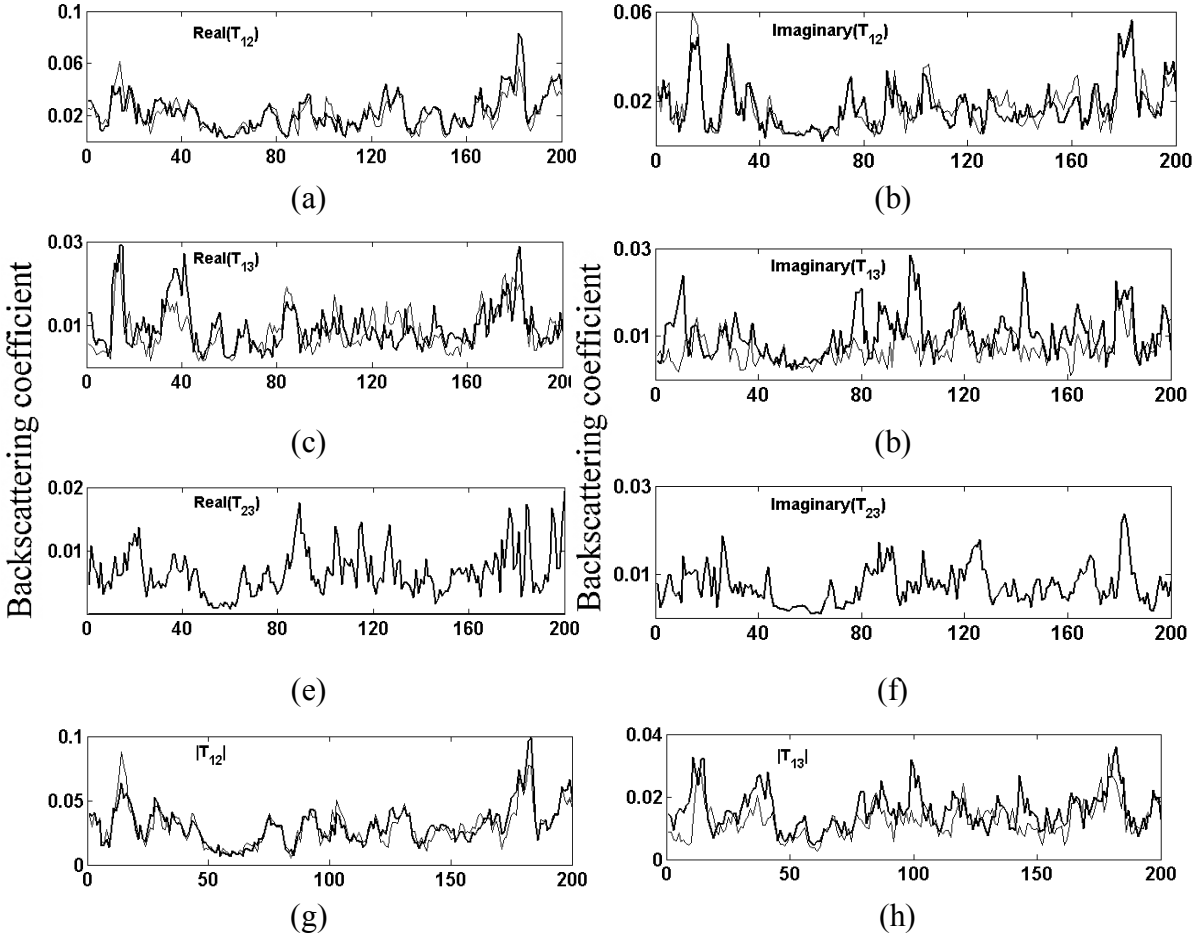

Figure A.2.1 These plots show the effects of POA correction for the real and imaginary parts of the off-diagonal coherency matrix [*T*] terms. The thin lines indicate the value before compensation and coarse lines for the value after compensation. As shown, the effect on the real and imaginary parts of T_{12} and T_{13}, which is shown in (a), (b), (c) and (d), cannot be consistently characterized. The real part of T_{23}, which is shown in (e) and the imaginary part of T_{23}, which is shown in (f), are roll invariant. The effect on the magnitudes of T_{12} and T_{13}, which is shown in (g) and (h), respectively, indicates that $|T_{12}|$ tends to decrease while $|T_{13}|$ tends to increase. (a) Re(T_{12}) before and after compensation. (b) Im(T_{12}) before and after compensation. (c) Re(T_{13}) before and after compensation. (d) Im(T_{13}) before and after compensation. (e) Re(T_{23}) before and after compensation. (f) Im(T_{23}) before and after compensation. (g) $|T_{12}|$ before and after compensation. (h) $|T_{13}|$ before and after compensation.

Appendix B

Polarimetric signatures and polarisation phase differences in Siberian forests

B.1 Polarimetric signatures in Primorsky-E

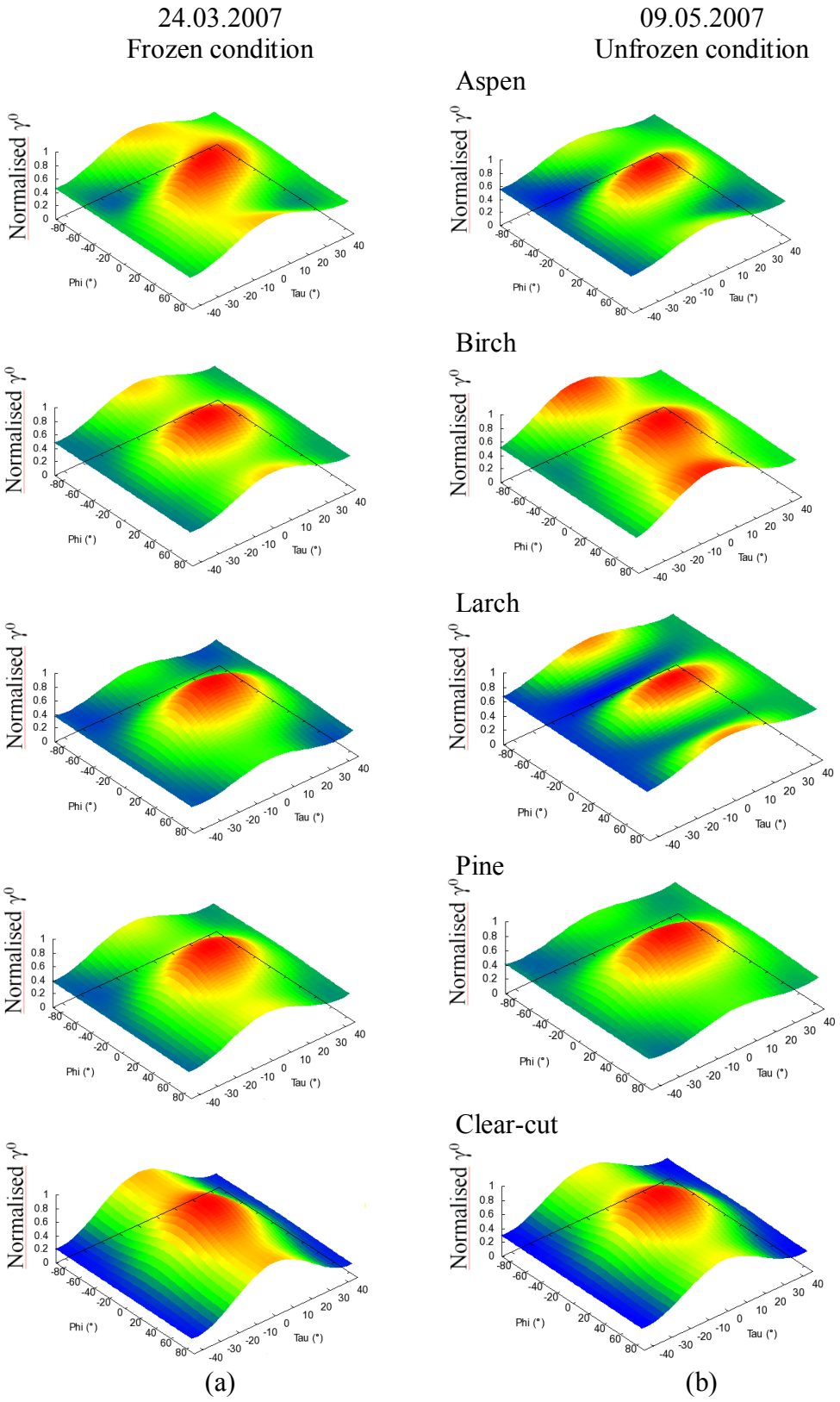

Figure B.1.1 Observed ALOS PALSAR L-band co-polarisation signatures for aspen, birch, larch, pine and clear-cut areas at (a) frozen (24.03.2007) and (b) unfrozen (09.05.2007) conditions in Primorsky-E.

B.2 Polarisation phase differences in Shestakovsky-N and Primorsky-E

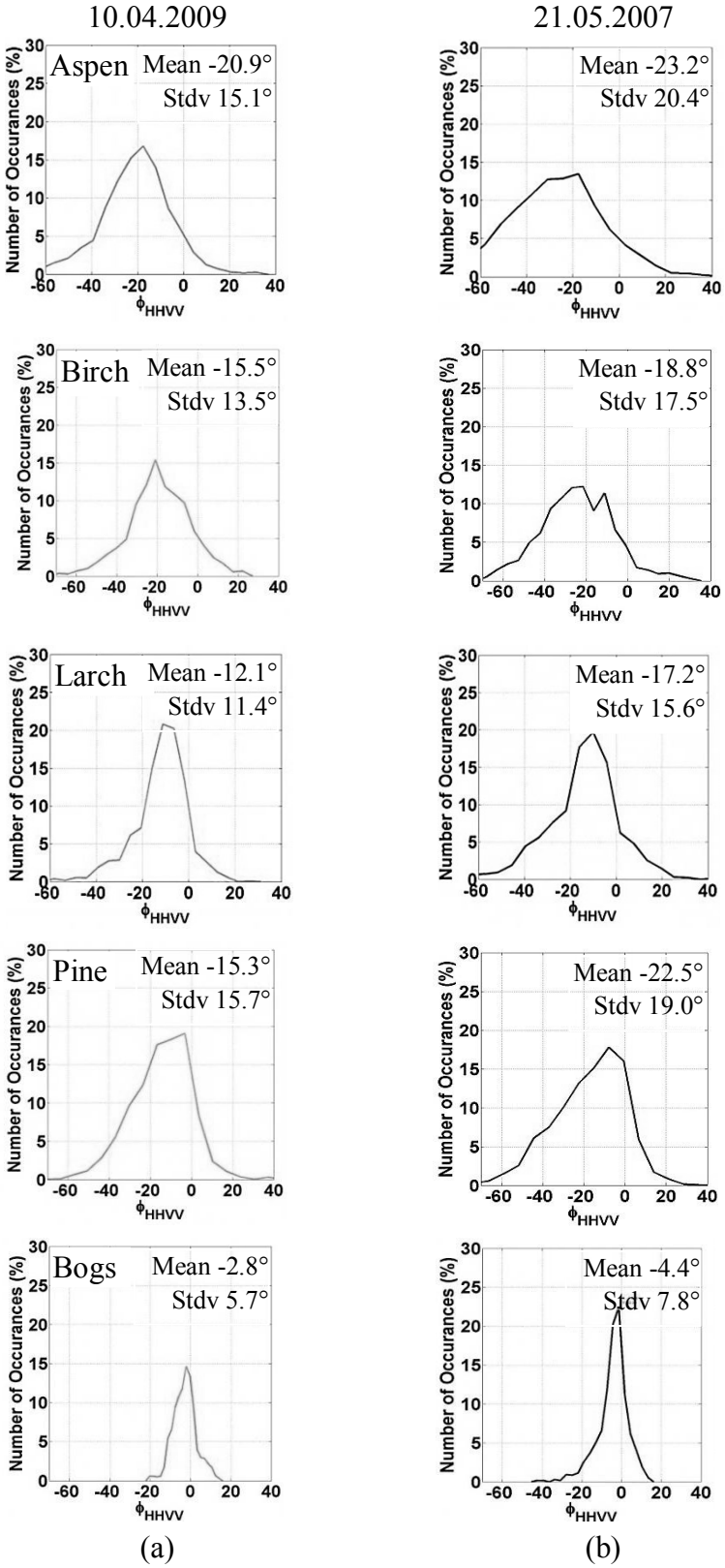

Figure B.2.2 Observed changes of polarisation phase differences at (a) thawing (10.04.2009) and (b) unfrozen (21.05.2007) conditions in Shestakovsky-N. The figure shows the mean and standard deviation (stdv) of the different tree species and bogs.

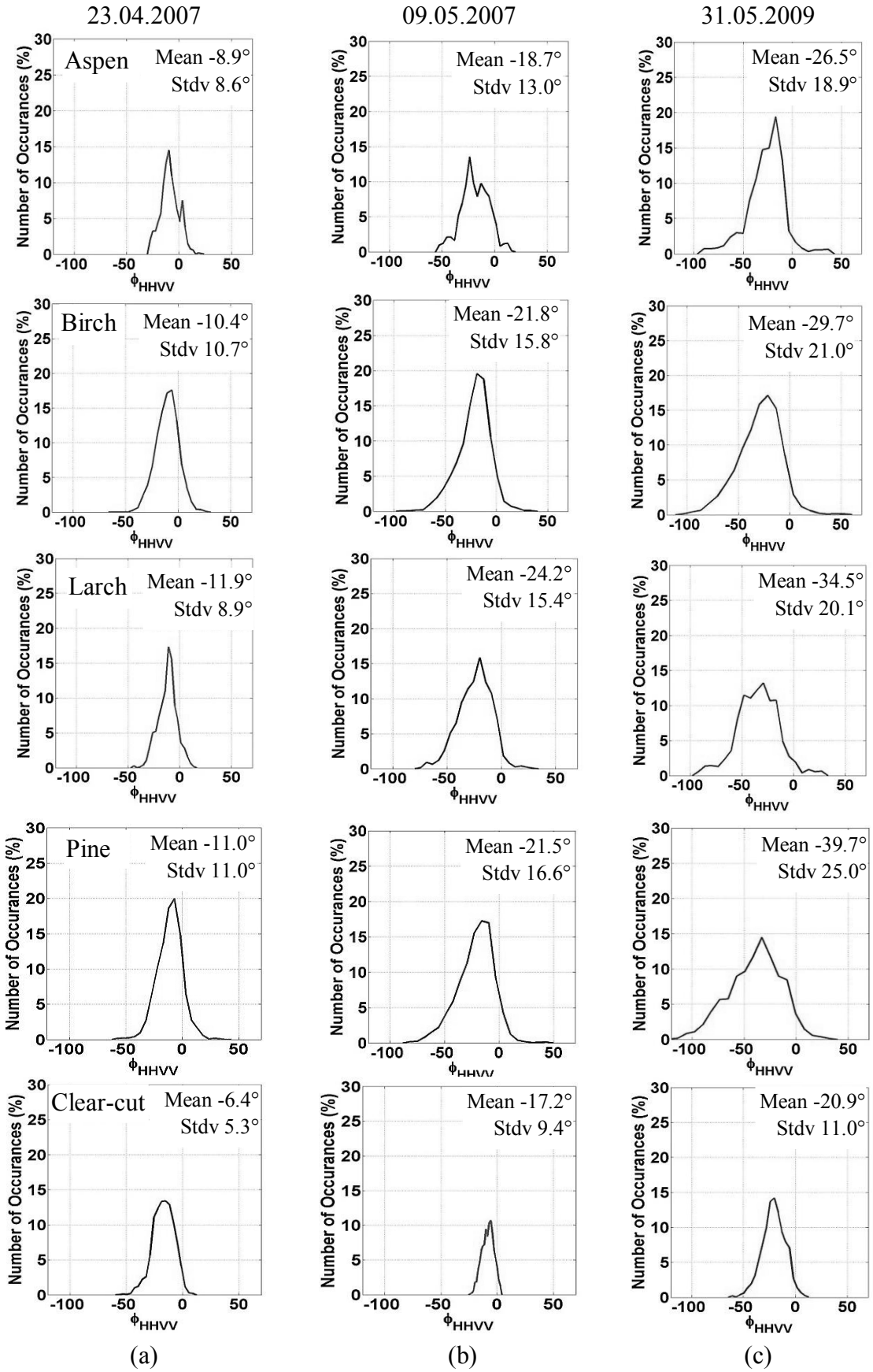

Figure B.2.3 Observed changes of HHVV-phase differences at (a) frozen (23.04.2007) (b) unfrozen-dry (09.05.2007) and (c) unfrozen-wet (31.05.2009) conditions in Primorsky-E. The figure shows the mean and standard deviation of the tree species and clear-cut.

B.3 Impact of tree species on polarimetric parameters in Bolshe-NE

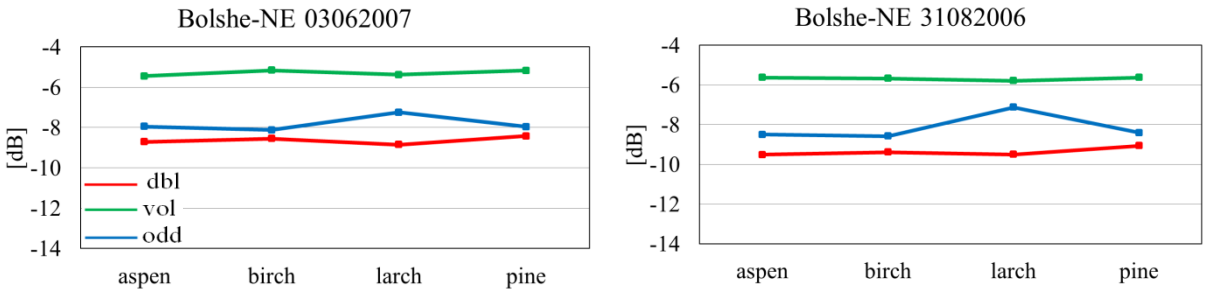

(a)

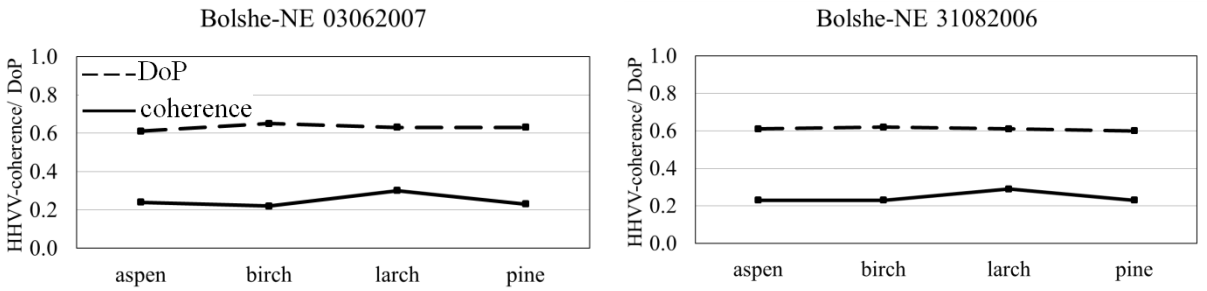

(b)

Figure B.3.1 (a) Mean decomposition powers and (b) Degree of polarisation (DoP) and HHVV-coherence over dense forests (GSV > 150 m³/ha) in Bolshe-NE separated by tree species at unfrozen conditions (03.06.2007 and 31.08.2006). Red, green, and blue colours represent double-bounce, volume and surface scattering powers respectively. The "black" dashed line indicates degree of polarisation (DoP) and solid line represents HHVV coherence.

B.4 Saturation levels for GSV in Shestakovsky-N and Chunsky-E

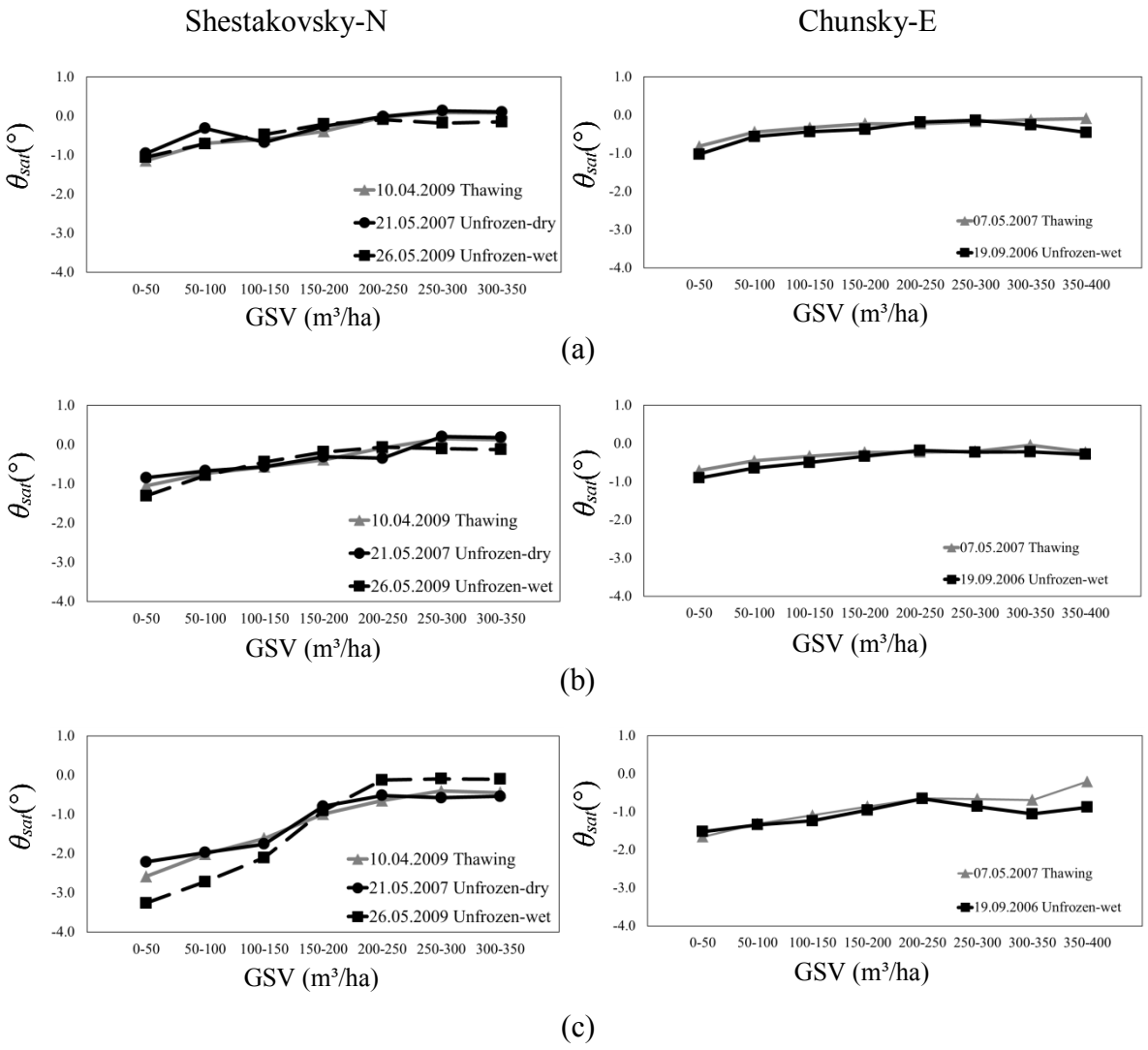

Figure B.4.1 Observed saturation levels for forest growing stock volume at different weather conditions using ALOS PALSAR L-band volume scattering power (a) without rotation of coherency matrix [T] and (b) with rotation of coherency matrix [$T(\theta)$], for Shestakovsky-N and Chunsky-E. (c) The ratio of ground-to-volume scattering power for same test sites.

B.5 Pearson's correlation coefficient between GSV and SAR parameters

Test sites	Dates	HH	HV	VH	VV	HH/HV	VV/HV	HHVV coherence	DoP	Alpha	Entropy
Shestakovsky-N	21.05.2007	0.23	0.72	0.73	0.24	0.56	0.60	-0.87	-0.80	0.78	0.76
Shestakovsky-N	10.04.2009	0.33	0.68	0.68	0.24	0.42	0.57	-0.74	-0.72	0.73	0.71
Shestakovsky-N	26.05.2009	0.26	0.72	0.76	0.33	0.50	0.58	-0.86	-0.81	0.79	0.79
Primorsky-E	09.05.2007	0.14	0.55	0.55	0.14	0.38	0.48	-0.70	-0.49	0.63	0.65
Primorsky-E	24.03.2007	0.32	0.67	0.67	0.34	0.47	0.46	-0.64	-0.57	0.65	0.68
Primorsky-E	31.05.2009	0.16	0.61	0.61	0.13	0.24	0.39	-0.65	-0.48	0.53	0.60
Chunsky-E	07.05.2007	0.14	0.76	0.76	0.20	0.55	0.63	-0.73	-0.72	0.69	0.67
Chunsky-E	19.09.2006	0.58	0.81	0.80	0.63	0.44	0.65	-0.77	-0.75	0.76	0.73
Chunsky-N	21.08.2006	0.53	0.76	0.76	0.49	0.44	0.58	-0.70	-0.72	0.71	0.68
Chunsky-N	06.10.2006	-0.40	0.64	0.63	-0.44	0.66	0.66	-0.71	-0.74	0.72	0.71
Chunsky-N	24.05.2007	-0.02	0.73	0.73	-0.21	0.60	0.67	-0.71	-0.73	0.70	0.69
Chunsky-N	13.04.2009	-0.23	0.59	0.59	-0.36	0.62	0.67	-0.70	-0.72	0.76	0.75
Bolshe-NE	31.08.2006	0.77	0.85	0.86	0.79	-0.12	-0.23	-0.72	-0.73	0.59	0.63
Bolshe-NE	03.06.2007	0.66	0.83	0.84	0.68	0.16	0.09	-0.71	-0.74	0.52	0.63

Table B.1 Pearson's correlation coefficient between SAR parameters and forest growing stock volume (GSV) in Siberian forests.

Appendix C

Growing stock volume retrieval results based on ALOS PALSAR L-band polarimetric coherence and ratio of ground-to-volume scattering power

C.1 GSV retrieval results from HHVV-coherence

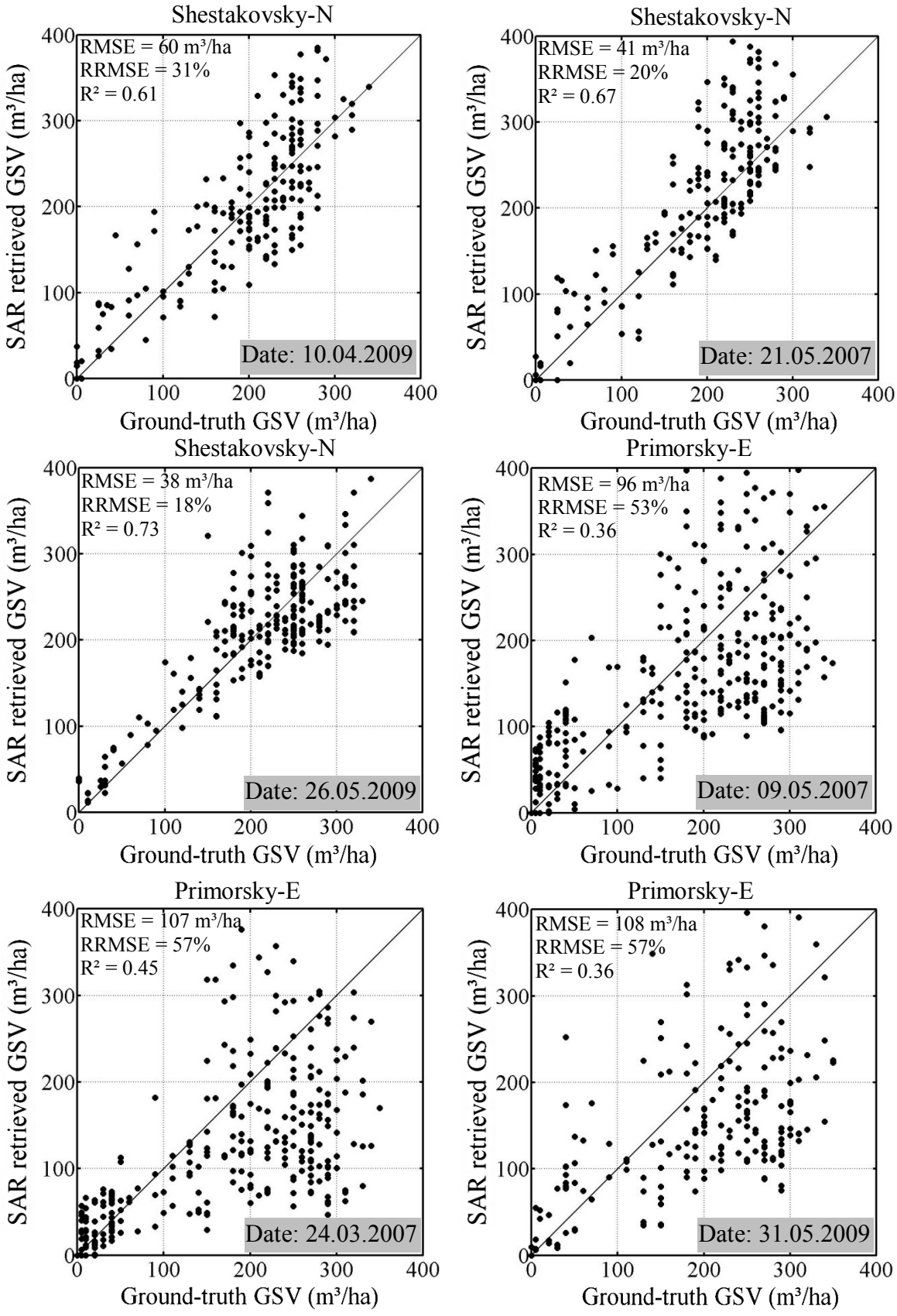

Figure C.1.1 Comparison between growing stock volume from forest inventory and growing stock volume retrieved from ALOS PALSAR L-band HHVV-coherence.

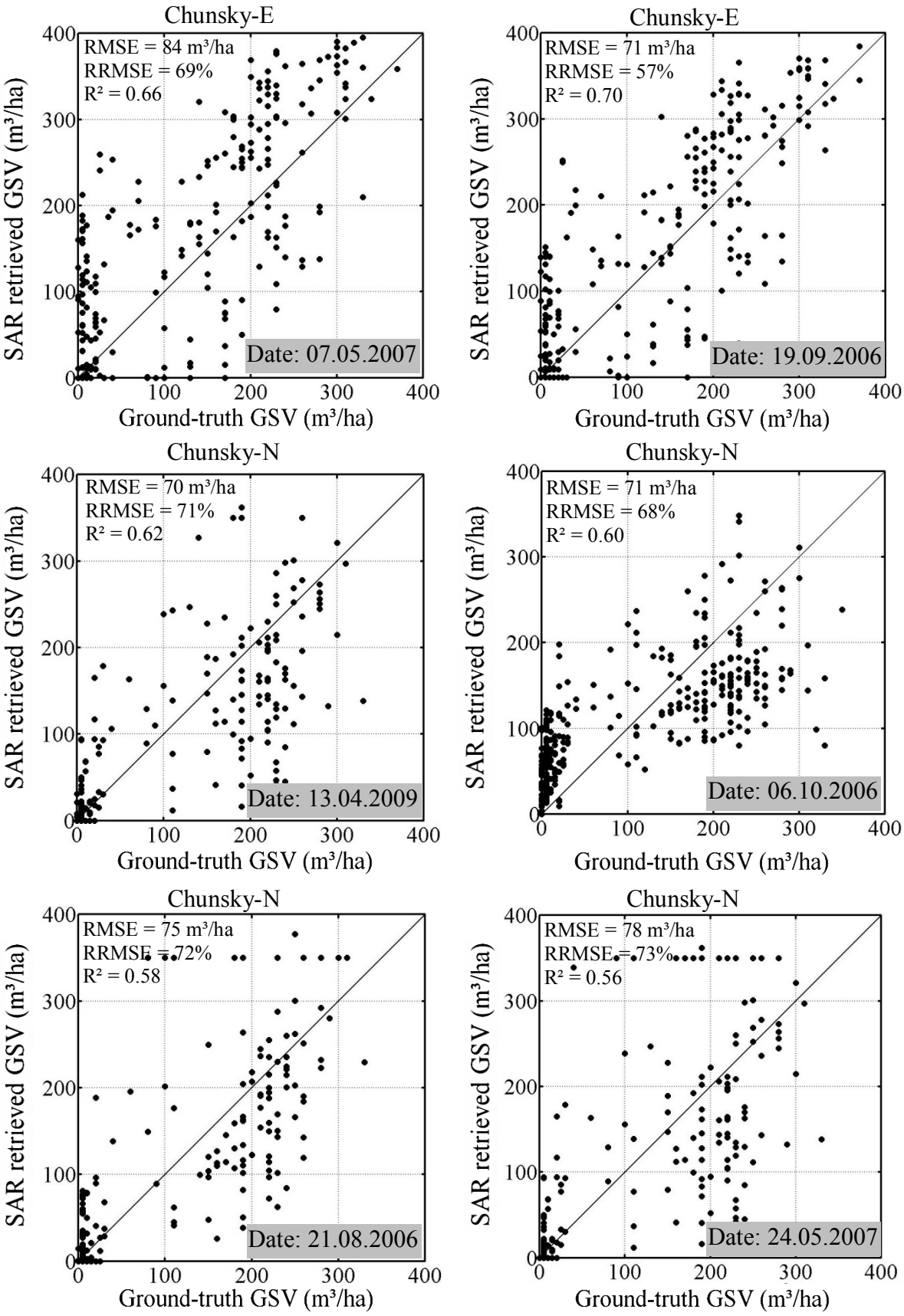

Figure C.1.2 Comparison between growing stock volume from forest inventory and growing stock volume retrieved from ALOS PALSAR L-band HHVV-coherence.

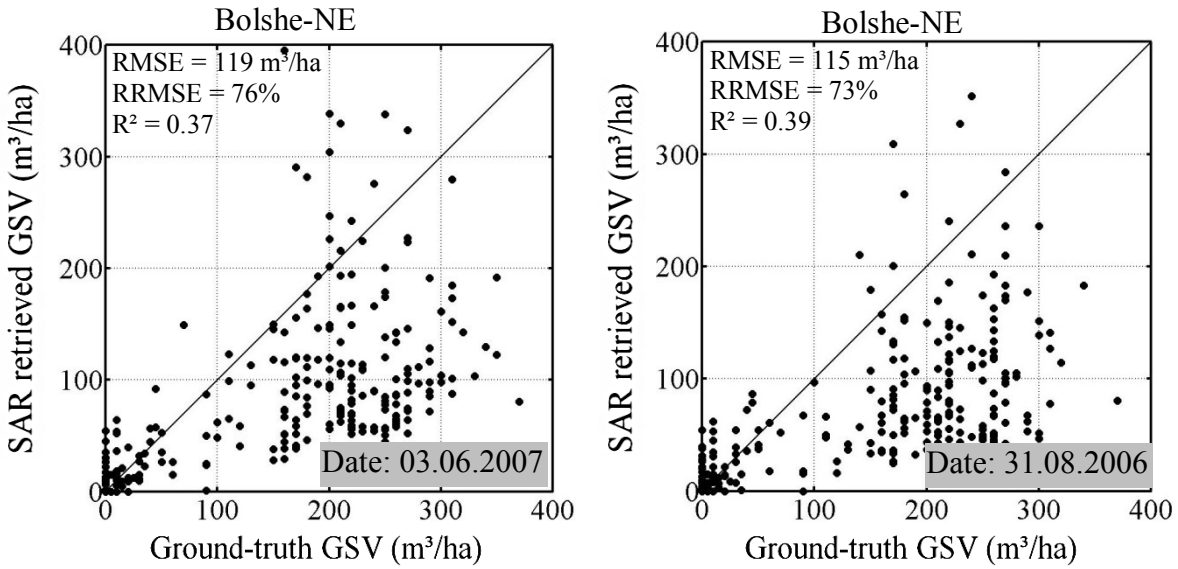

Figure C.1.3 Comparison between growing stock volume from forest inventory and growing stock volume retrieved from L-band ALOS PALSAR HHVV-coherence. RRMSE represents the short form of relative RMSE.

C.2 GSV retrieval results from ground-to-volume scattering ratio

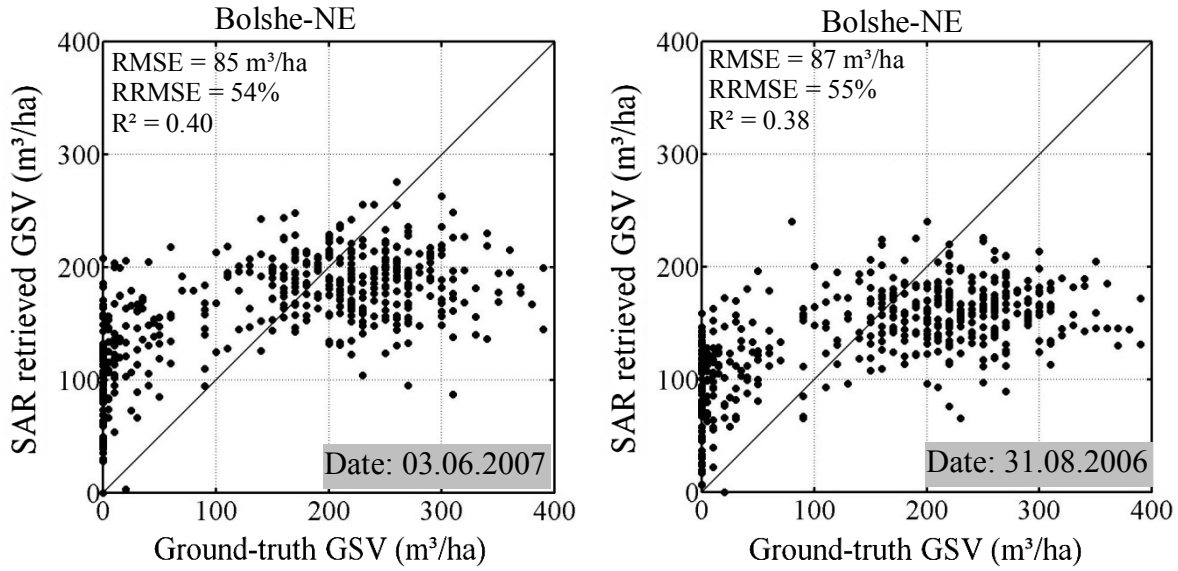

Figure C.2.1 Comparison between growing stock volume from forest inventory and growing stock volume retrieved from ALOS PALSAR L-band ground-to-volume scattering power ratio. RRMSE represents the short form of relative RMSE.

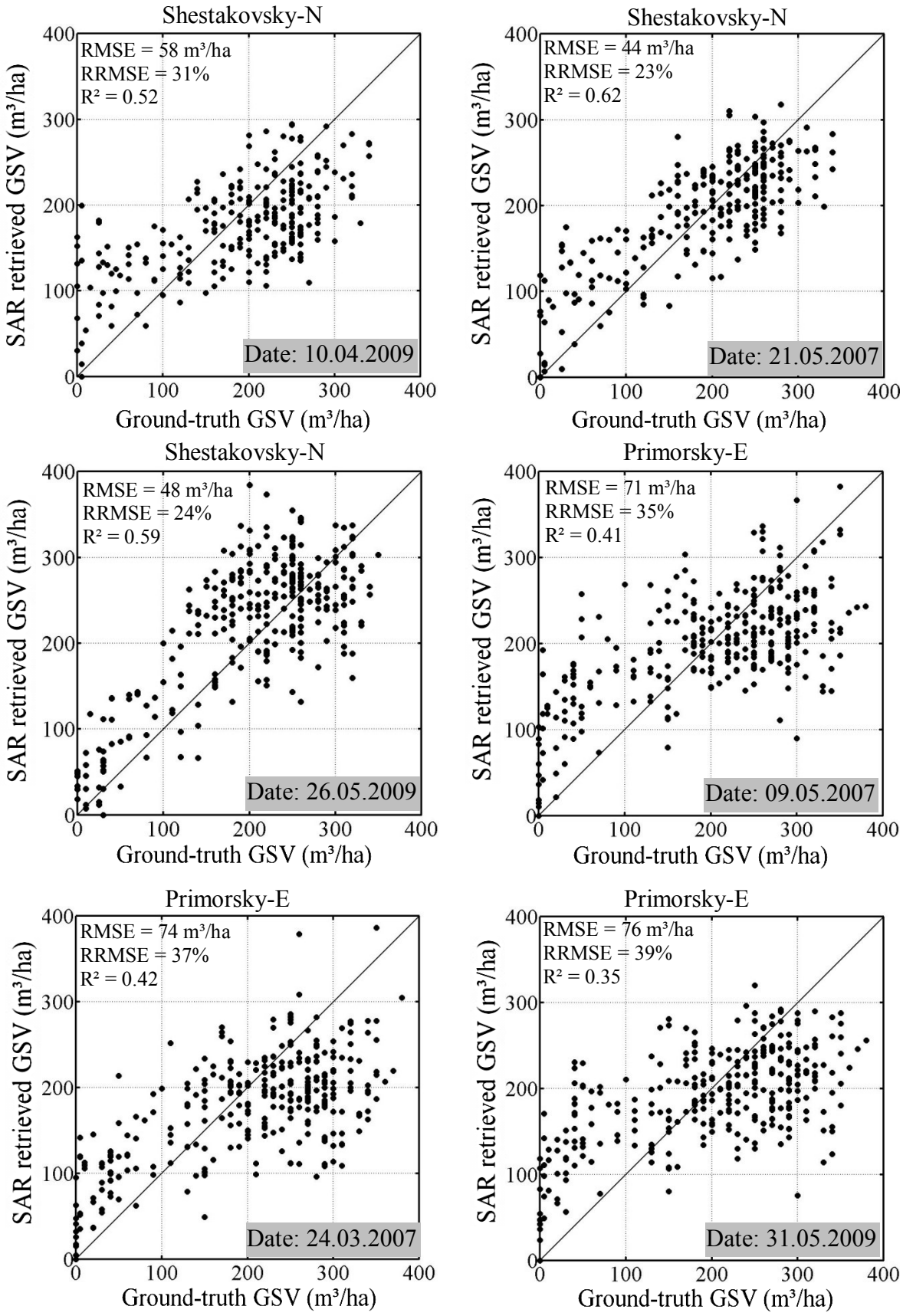

Figure C.2.2 Comparison between growing stock volume from forest inventory data and growing stock volume retrieved from ALOS PALSAR L-band ground-to-volume scattering power ratio. RRMSE represents the short form of relative RMSE.

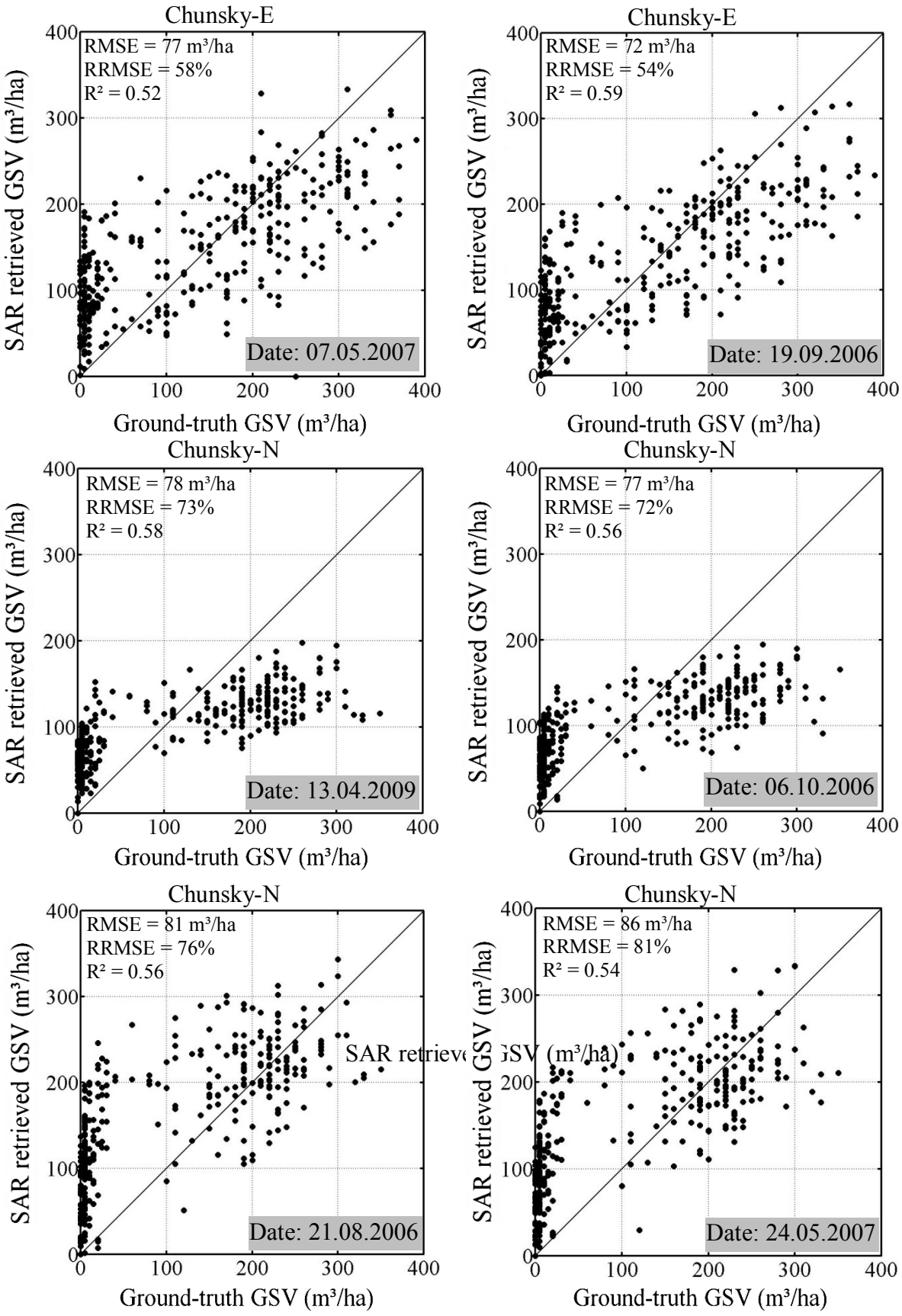

Figure C.2.3 Comparison between growing stock volume from forest inventory and growing stock volume retrieved from ALOS PALSAR L-band ground-to-volume scattering power ratio. RRMSE represents the short form of relative RMSE.

C.3 Comparison of mean retrieved GSV and mean ground-truth GSV

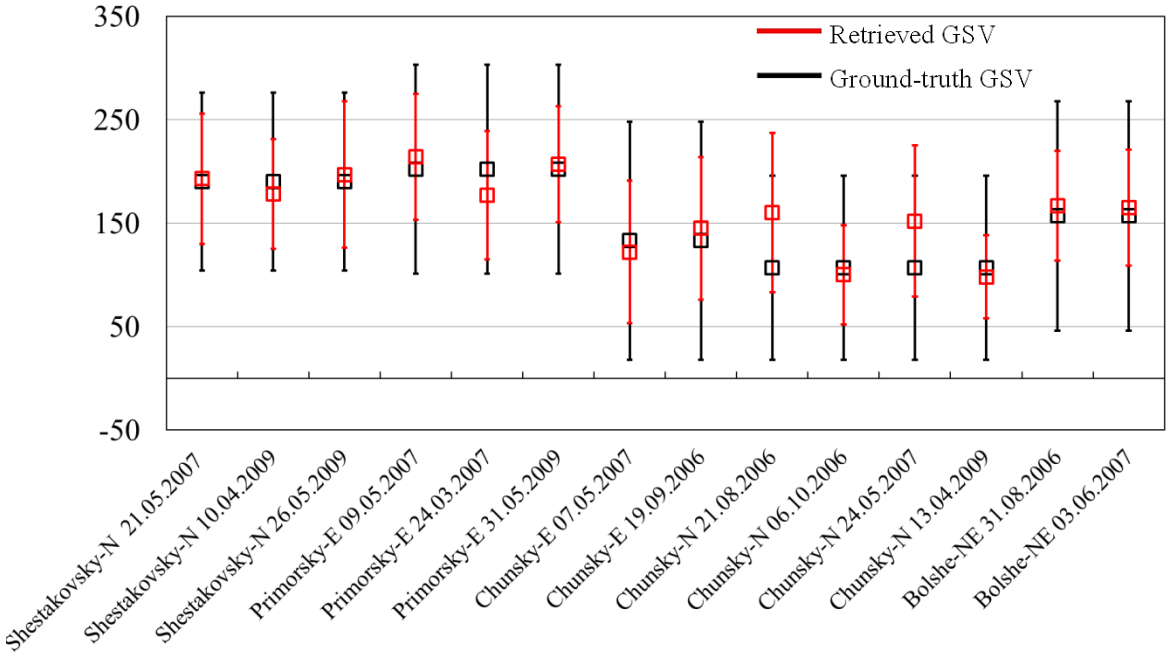

(a)

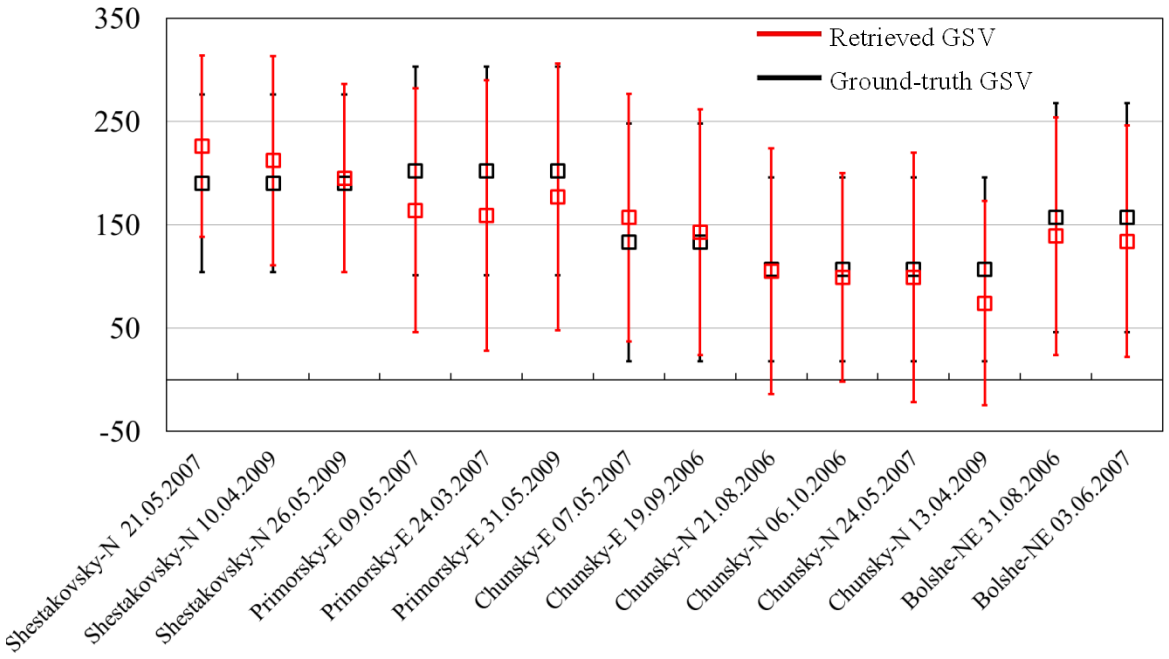

(b)

Figure C.3.1 Comparison of mean estimated GSV and mean ground-truth GSV based on ALOS PALSAR L-band (a) ground-to-volume scattering power ratio and (b) polarimetric coherence for Siberian forests. The estimated and ground-truth mean GSV values are shown as "rectangular box" and vertical bars represent the standard deviations.

C.4 GSV retrieval results for tree species

Test Sites	Dates	Aspen	Birch	Larch	Pine	Weather conditions
Shestakovsky-N	21.05.2007	5	22	21	17	Unfrozen, dry
Shestakovsky-N	10.04.2009	29	21	25	17	Thaw, wet
Shestakovsky-N	26.05.2009	12	44	12	22	Unfrozen, wet
Primorsky-E	09.05.2007	19	22	15	25	Unfrozen, dry
Primorsky-E	24.03.2007	17	23	27	28	Frozen
Primorsky-E	31.05.2009	31	25	15	26	Unfrozen, wet
Chunsky-E	07.05.2007	32	14	34	33	Thaw, wet
Chunsky-E	19.09.2006	35	17	34	33	Unfrozen, wet
Chunsky-N	06.10.2006	—	27	48	55	Frozen
Chunsky-N	13.04.2009	—	22	47	47	Frozen
Chunsky-N	21.08.2006	—	49	11	26	Unfrozen, dry
Chunsky-N	24.05.2007	—	43	19	25	Unfrozen, wet
Bolshe-NE	03.06.2007	26	29	8	50	Unfrozen, wet
Bolshe-NE	31.08.2006	32	26	22	49	Unfrozen, dry

Table C.4.1 Growing stock volume retrieval accuracy for aspen, birch, larch and pine expressed in terms of relative RMSE (%) based on ALOS PALSAR L-band ground-to-volume scattering power ratio for all the investigated forest areas in Siberia.

Test Sites	Dates	Aspen	Birch	Larch	Pine	Weather conditions
Shestakovsky-N	21.05.2007	-14	26	-43	-32	Unfrozen, dry
Shestakovsky-N	10.04.2009	-62	3	-53	-33	Thaw, wet
Shestakovsky-N	26.05.2009	33	50	-27	-17	Unfrozen, wet
Primorsky-E	09.05.2007	-55	14	-27	-52	Unfrozen, dry
Primorsky-E	24.03.2007	-47	1	-57	-80	Frozen
Primorsky-E	31.05.2009	-79	-6	-33	-69	Unfrozen, wet
Chunsky-E	07.05.2007	-31	-21	-37	-63	Thaw, wet
Chunsky-E	19.09.2006	-52	-31	-44	-69	Unfrozen, wet
Chunsky-N	06.10.2006	—	-48	-109	-119	Frozen
Chunsky-N	13.04.2009	—	-41	-105	-98	Frozen
Chunsky-N	21.08.2006	—	76	-28	-8	Unfrozen, dry
Chunsky-N	24.05.2007	—	68	-46	-10	Unfrozen, wet
Bolshe-NE	03.06.2007	-48	-2	-56	-113	Unfrozen, wet
Bolshe-NE	31.08.2006	-26	29	-6	-97	Unfrozen, dry

Table C.4.2 Growing stock volume retrieval accuracy for aspen, birch, larch and pine expressed in terms of bias estimation from ALOS PALSAR L-band ground-to-volume scattering power ratio for all the investigated forest areas in Siberia. The (+) positive values in estimation bias indicate the overestimation and the negative (-) values represent the underestimation of retrieved mean GSV.

Acknowledgements

I would like to express my gratitude to all those who gave me the possibility to complete this dissertation. First of all, I would like to thank my supervisor, Professor Dr. Christiane Schmullius for her unlimited help and support. Her sharp advice and guidance opened my eyes to the field of radar remote sensing. She has allowed me unrestricted freedom in pursuing my own ideas and interests.

I would also like to extend my appreciation and sincerest thanks to my second supervisor Dr. Christian Thiel for his valuable guidance, scholarly advice, consistent encouragement and precious assistance during my studies. His constructive comments and suggestions greatly improved my research work and scientific writing.

Apart from my supervisors there are many people who have great influences on my research work. I am obliged to many of my colleagues Oliver, Nicolas, Ralf, Claudia, Valerio, Nesrin, Martyna for giving me the opportunities to earn experiences in the field of radar remote sensing. I would like to show my gratitude to Dr. Christian Hüttich for sharing his experiences and suggestions about dissertation writing. Special thanks to Robert and Sina for their assistances to write "Zusammenfassung". Thanks to Marc for helping me to get rid of the virus from my PC. My deepest thanks to my all colleagues who create such a wonderful atmosphere in this institute.

I would like to thank the Deutsche Forschungsgemeinschaft (DFG) for providing the funding which allowed me to undertake this research.

I would like to thank my all friends in Jena with whom I spent a lot of joyful moments.

Finally, I would like to thank my parents and my sister for their patience and support during all these years.

Curriculum Vitae

Personal information

Name:	Tanvir Ahmed Chowdhury
Date of birth:	July 01, 1980
Place of birth:	Chittagong, Bangladesh
Nationality:	Bangladeshi
Marital status:	single

Professional experiences

05/2009 - present **Doctoral student position**
Dept. of Earth Observation, Friedrich-Schiller-University Jena , Germany
- Polarimetric SAR Data Analysis.
- Radar Backscatter Modeling.

07/2008 - 03/2009 **Scientific Assistant**
Dept. of Electronics, Politecnico di Torino, Italy
- Responsible for simulation of X-BAND RADAR data, building software for the interface between the user and the RADAR.
- Working on Radar Signal processing: filtering, noise reduction.

01/2008 - 07/2008 **Student Assistant**
Dept. of Electronics, Politecnico di Torino, Italy
- Worked as a student assistant in a FORALPS project "DEVELOPMENT OF A PORTABLE, LOW-COST X-BAND RADAR IN ALPINE VALLEYS".
- Design an FM network to cover the province of Torino,Italy with radio transmission at the frequency f = 99 MHz
- Design a Curtain Antenna for HF transmission at 13m band for very long distance communication.

08/2004 - 09/2006 **Lecturer**
Dept. of Computer Science & Engineering (CSE), Premier University, Bangladesh

04/2003 - 03/2004 **Student assistant**
Dept. of Computer Science & Engineering (CSE), Rajshahi University of Engineering and Technology, Bangladesh
- Developed software to interface the Industrial Robot (RB-5) with PC.

Educational background

05/2009 - present	**Ph.D. Student** Dept. of Earth Observation, Friedrich-Schiller-University Jena , Germany ▪ *Thesis*: Assessment of the Potentiality of L-band Quadpol Radar for the Retrieval of Forest Structural Parameters by means of polarimetric information in Central Siberia and Thüringer Wald.
09/2007 - 07/2008	**Master of Science in Electronic Engineering** Politecnico di Torino, Italy ▪ *Thesis:* Radar Meteorology-Analysis of echoes detected by a portable, low-cost, X-band radar for rainfall monitoring in Alpine Valleys.
10/2006 - 08/2007	**Master of Science in Electrical Engineering and Information Technologies** University of Karlsruhe, Germany
04/2000 - 03/2004	**Bachelor of Science in Computer Science and Engineering** Rajshahi University of Engineering and Technology (RUET), Bangladesh ▪ *Thesis:* Recognition of human faces using *KOHONEN SELF ORGANIGING MAP* of Artificial Neural Network Technique.

List of publications

Chowdhury, T. A., Thiel, C. J., & Schmullius, C. "Assessment of the potentiality of L-band quadpol radar for the retrieval of forest structural parameters by means of polarimetric information in central Siberia". *Proceedings of ESA living planet symposium*, Bergen, Norway, 28 June – 2nd July, 2010.

Chowdhury, T. A., Thiel, C. J., & Schmullius, C. "Forest structural parameters and growig stock volume retrieval in Thringian forest using L-band polarimetric radar". *Proceedings of POLINSAR 2011*, ESA-ESRIN, Frascati, Italy, 24 – 28 January, 2011.

Chowdhury, T. A., Thiel, C. J., & Schmullius, C. "Growing stock volume retrieval in boreal forest from ALOS L-band polarimetric coherence". *Proceedings of IEEE International Geoscience and Remote Sensing Symposium IGARSS 2012*, Munich, Germany, 22 – 27 July, 2012.

Jena, 21-02-2013 (Tanvir Ahmed Chowdhury)

Selbständigkeitserklärung

Ich erkläre, dass ich die vorliegende Arbeit selbstständig und unter Verwendung der angegebenen Hilfsmittel, persönlichen Mitteilungen und Quellen angefertigt habe.

Jena, 21-02-2013 Unterschrift des Verfassers/der Verfasserin

(Tanvir Ahmed Chowdhury)